Università degli Studi di Napoli

Federico II

SCUOLA POLITECNICA E DELLE SCIENZE DI BASE

Dipartimento di Scienze della Terra, dell'Ambiente e delle Risorse

DOTTORATO IN SCIENZE DELLA TERRA, DELL'AMBIENTE E DELLE RISORSE

XXXIV ciclo

Interaction between tectonics and volcanic activity in the Campi Flegrei caldera and northeastern sector of Roccamonfina

Ph.D. Thesis

Ph.D. candidate:

Jacopo Natale

Tutor: **Prof. Stefano Vitale**

Co-tutor: **Roberto Isaia, Ph.D.**

“I have nothing in common with lazy people
who blame others for their lack of success.
Great things come from hard work and perseverance.
No excuses.”
Kobe Bean Bryant

Summary

page intentionally left blank

Preface

This thesis was produced in the framework of the Doctorate Programme in Earth, Environmental and Resources Sciences (DiSTAR) at the University of Naples Federico II. The research activity was conducted at the DiSTAR, supervised by Prof. Stefano Vitale and co-supervised by Dr. Roberto Isaia of Osservatorio Vesuviano Sezione di Napoli of the Istituto Nazionale di Geofisica e Vulcanologia. The project was carried out with the cooperation of Prof. Luigi Ferranti of DiSTAR, Dr. Marco Sacchi of Institute of Marine Sciences of the National Research Council of Naples, and with German partners Dr. Lena Steinmann and Prof. Volkhard Spiess, of the Department of Geosciences of the University of Bremen. The research activity was sustained by the scholarship funded by the Minister of University and Research of Italy (MIUR). Unfortunately, due to the Covid pandemic, no visiting research period could be conducted. This thesis was written in the cumulative format and thus consists of three standalone research manuscripts published, submitted, or that will be submitted as first-author articles to international peer-reviewed journals.

The following general introduction underlines the context and background of the research and the aims and the methods followed in the manuscripts. Finally, a conclusive chapter is provided at the end of the manuscript, which involves a general outcome of the research activity, implications, future development, and opportunities.

Jacopo Natale

Napoli, February 2022

page intentionally left blank

Abstract

This thesis presents a study on two research areas: Campi Flegrei and Roccamonfina (southern Italy). The evolution of these volcanic areas results from the complex interplay between tectonics and volcanic processes. In particular, in the area of Campi Flegrei, the research was split into two main branches: (1) the reconstruction of an integrated stratigraphy of the last 15 kyr of the marine and volcaniclastic infill of the Pozzuoli Gulf, which represents over one-third of the overall volcanic field, and (2) the reconstruction of the structural pattern in the offshore caldera, to disentangle the formation of the caldera during significant volume eruptions.

This study has been performed analyzing a set of over 150 seismic profiles acquired in the Pozzuoli Gulf between 2008 and 2013 that investigate the submerged portion of the caldera down to the first 350 m. The interpretation of seismic data was integrated with the stratigraphic data of the thoroughly studied uplifted marine sequence of the La Starza unit and the most up-to-date tephrostratigraphy of the last 15 kyr. The following results were achieved in agreement with the stratal architecture, stacking patterns, and unit-bounding unconformities. The main results of this study consist of an integrated on-land-offshore stratigraphy, able to explain and detail the several volcano-tectonic processes that followed the collapse of the Neapolitan Yellow Tuff (NYT) eruption. In particular, the almost complete sedimentary record describes that ground deformation is coupled with volcanism and that large erupted magma volumes intra-caldera Plinian eruptions triggered the main ground movements, with a scale-invariant pattern resemblance. Both Agnano-Pomici Principali (12 ka) and Agnano-Monte Spina (4.55 ka) eruptions were followed by significant ground subsidence that favored marine transgression and then followed by roughly rapid uplift, which was locally recorded by erosional unconformities. It is important to stress that the general pattern of ground deformation in the last 10 kyr shows a radial symmetry, as observed today (i.e. bradyseism), with maximum uplift values and subsidence recorded near Pozzuoli town. The stratigraphy allowed to detail the stratigraphic position of debated coastal eruptions, such as Banco di Nisida and Nisida, to the East, and Bacoli, Porto Miseno, and Capo Miseno, to the West, respectively. Furthermore, two offshore intrusion features, namely the Bagnoli cryptodome and the Punta Pennata structure, were characterized both time and process-wise. This work is a robust attempt to overwhelm the lack of direct stratigraphic data (i.e., well-logs) within the offshore sector and substantially contribute to the comprehension of the recent evolution of Campi Flegrei caldera.

The same seismic reflection dataset was used for the second research branch concerning the offshore sector of the Campi Flegrei caldera. The aim was to thoroughly reconstruct the structural framework of the Campi Flegrei offshore and unravel a potential contribution from the tectonic field. As an outcome, two main fault systems were recognized: the ring fault system, furtherly divided into inner, medial, and outer fault zones, and the dome fault system. The ring fault system is a 2.5 km wide arcuate ring fault zone, massively involved by fluid uprise, which mainly down threw the central part of the caldera, joining with the continental structural highs of Posillipo and Monte di Procida, to the East and the West, respectively. Stratigraphic analysis corroborates that the collapse has occurred in two distinct episodes, first with the Campanian Ignimbrite (CI) eruption (40 ka), and then the same structures have been reactivated during the NYT collapse (15 ka), although with a lower amount of subsidence, ranging from one-third to one-quarter. For the NYT collapse, the structural analysis suggests that the process not only reactivated the main ring fault of the CI collapse but also occurred in a differential manner, with the sinking proceeding from outside-to-inside, showing hints of fault growth on the external rims, whereas depicting a late collapse on the innermost rim, in agreement with on-land studies. The dome fault system develops in the central part of the caldera, and it is the offshore continuation of a complex array of faults accommodating the volcano-tectonic collapses of the central sector. In particular, this area is a NE-SW to NNE-SSW trending, piece-meal-like high-angle normal fault array that accommodates the sudden subsidence that closely followed the Plinian eruption of Agnano-Monte Spina (4.55 ka). The structural analysis points out that this collapsed area is associated with discrete episodes of volcano-tectonic collapses instead of being ascribed to analog models-like resurgence-related graben formation.

Furthermore, over 220 fault plane data have been analyzed with the radial analysis, pointing out the influence of N-S tectonic field on the formation of the CI caldera and for volcano-tectonic collapses, as furtherly supported by the systematic reactivation of adequately oriented faults (i.e., E-W), and the formation of grabens within the fault zones. This work substantially contributes to the comprehension of the overall caldera structure and greatly addresses the volcano-tectonic processes following the major caldera collapse. Finally, this work highlights how the offshore fault zones may connect the surface to the deep-seated hydrothermal system, conveying considerable amounts of fluids on a much larger area than that currently monitored, and suggest that this area should not be ruled out as a potential eruption site.

Finally, as concerned the study conducted in the NE sector of Roccamonfina volcano, the aim was to investigate a beautifully exposed magmatic dike within an active cement quarry on the Mt Cesima ridge. During three years of excavations, the quarry cultivation progressively exposed more and more outcrops along the several excavation steps and fronts. Systematic structural and UAV-based (Unmanned Aerial Vehicles) surveys shed light on the complex interaction between preexisting and syneruptive fault zones, with dike intrusion and fissure eruption. In particular, the main outcome of this work is that a reasonably large magmatic dike of lc-tephrite composition has intruded within an E-W fault zone during a rifting event characterized by N-S extensional direction. The dike, minor segments, and fingers intruded within a Mesozoic limestone host rock, overlain by early Pleistocene slope breccia ("Breccia Mortadella"). Its lateral path was deflected during its propagation by a pre-existing NE-SW cataclastic fault zone. A large amount of extension and the vicinity to the surface caused the dike to thicken, reaching a width exceeding 25 m.

Nonetheless, the dike had managed to reach the surface and feed an Icelandic/Strombolian eruption that dispersed in the vicinity a 30 m thick pyroclastic succession constituted by scoriaceous spatters and lapilli. Large ballistics of carbonate lithics, lava blocks, and metric spatters characterize the proximal facies of this deposit. The eruption also built a series of welded spatters, ramparts, and cones, which are barely preserved from erosion. One of the most remarkable outcomes of this work is that the dike products overlay a series of paleosols and trachyte Plinian fallout deposits ascribable to the White Trachytic Tuff (WTT) eruptions of Roccamonfina, whose younger age is 230 ka. Furthermore, a thick reddish paleosol interposes between that pumice-lapilli layer with the proximal Strombolian succession, suggesting to have occurred way after it. The whole succession, including the host rock and Strombolian tephras, are intensely faulted, with a prevailing contribution from N-S and E-W faults. This tectonic phase is likely related to the uplift phase that exhumed the carbonate ridge of Mt Cesima, giving its present-day configuration. In previous petrological studies, these products were ascribed by inference to Epoch 1 of Roccamonfina, i.e., older than 350 ka due to similarity with the HKS products erupted in the early stages of the volcano activity. However, this study demonstrates that this remarkable extensional tectonic pulse occurred, hinted by the dike intrusion, to be younger than the last Plinian eruptions of Roccamonfina, the WTT, whose composition belong to the less alkaline KS series. Therefore, this study suggests that the rift-related extensional pulse managed to melt and involve HKS magma in this rejuvenation of the activity. Finally,

these results open the way to the comprehensive understanding of volcano-tectonic processes in the Tyrrhenian margin of the Campania coastal half-graben system.

Chapter 1: Introduction

1.1 Introduction

The analysis of deformation structures, such as fractures and faults, and their mutual relationships with the host rock, is a fundamental instrument to unravel the evolution of tectonic processes at local to regional scales. Understanding the structural setting of a study area massively helps to constrain its geological evolution. This approach is equally profitable and even more valid if applied to volcanic areas, where the juxtaposition of successive products may produce suitable exposure of such relationships. The combination of structural geology and volcanology methods is a relatively new scientific field in geology: volcano-tectonics.
Therefore, using the techniques specific of structural geology is possible to investigate the relationships between tectonic (far-field) and local (volcano-related) stress fields. A wide literature highlights the spatiotemporal relationships between tectonic structures and favorable tectonic regimes with the localization of volcanic vents (e.g., Bevilacqua et al., 2015). Hence, describing and characterizing the volcano-tectonic structures becomes a primary task for understanding volcanic system behavior and assessing future hazard scenarios. Two main test areas have been studied in this Ph.D. project, the Campi Flegrei caldera and the area to the North-East of Roccamonfina volcano in southern Italy. Both study areas belong to the Tyrrhenian margin of the southern Apennines, where volcanism shows close relationships to the back-arc extensional setting and evolved accordingly to the tectonic maturity (Peccerillo et al., 2017). The Campi Flegrei volcanic field occurs in the central sector of the Campania Plain and is one of three volcanic centers of the Neapolitan area, with Somma-Vesuvio and Ischia (Scandone et al., 1991). In this area, volcanism is at least 80 kyrs old (Pappalardo et al., 1999; Scarpati et al., 2013) and is characterized by scattered monogenetic volcanism, quiescence periods, and not least, large-magnitude caldera-forming ignimbrite eruptions. The two main ignimbrite eruptions are thoroughly described in the literature, the Campanian Ignimbrite at 40 ka (150-200 km^3 DRE; Giaccio et al., 2017; Silleni et al., 2020) and the Neapolitan Yellow Tuff at 15 ka (20-40 km^3 DRE, Orsi et al., 1992; Scarpati et al., 1993; Deino et al., 2004). Following the last caldera eruption, over 70 eruptions have occurred, clustered in time and space (Di Vito et al., 1999; Bevilacqua et al., 2016). One of the most remarkable phenomena is that volcanic activity is accompanied by significant ground deformation, morphologically expressed by a

central uplifted resurgent dome (Isaia et al., 2009; Vitale and Isaia, 2014; Di Vito et al., 2016; Isaia et al., 2019; Vitale et al., 2019). These, likewise other studies, have been performed in the continental and coastal part of the caldera, where pyroclastic and volcaniclastic rocks crop out (Di Vito et al., 1999, Orsi et al., 2004). In addition to the pyroclastic successions, of particular interest is the occurrence of uplifted marine sediments of La Starza Unit exposed in the central coastal sector, thoroughly described in the literature (Rodriquez, 1964; Cinque et al., 1985; Giudicepietro, 1993; Isaia et al., 2019; Vitale et al., 2019). Such studies, performed during several decades, took advantage of suitable exposition but were often short-lived or spatially limited due to scattered outcrops, intense urbanization, and potentially severe subaerial erosion. In this scenario, considering that over one-third of the caldera is submerged beneath the Gulf of Pozzuoli, many authors since 1970s investigated the offshore sector using seismic reflection data to overcome the aforementioned limitations. In fact, modern active geophysical methods, such as seismic reflection data, can be successfully used. Many studies, with datasets of different disciplines and vintages, explored the sedimentary infill of the Gulf to characterize the caldera structure and the stratal architecture (Colantoni, 1972; Pescatore et al., 1984; Milia et al., 1998; Sacchi et al., 2014; Steinmann et al., 2016; 2018). This Ph.D. research strand aims at bridging the gap between the offshore and on-land both stratigraphic and structural settings to investigate the volcano-tectonic processes occurring in the caldera and recorded in the infill, differently from all previous works. In this way, a new understanding of the complex evolution of such caldera floor deformation, volcanism, faulting, and the interplay with the sedimentary system was explored.

Concerning the other research line, near the Roccamonfina volcano, the main aim is to explore the relationships between regional tectonics and volcanic activity. In particular, this research line was focused on the outcrop located in the Taverna San Felice quarry, to the North-East of Roccamonfina. During the three years of the Ph.D. research, the digging activity at the quarry has progressively exposed the main features of one of the best exposure of a Pleistocene magmatic dike emplaced in a carbonatic host-rock in Europe. The Roccamonfina is a composite volcano active through the Middle-Upper Pleistocene, located within the peri-Tyrrhenic horst-graben structure of the Garigliano Plain. This volcano went through different stages of activity (Rouchon et al., 2008), which mainly built a central stratocone (Tedesco, 1965), with eccentric monogenetic vents, lava fields, and explosive Plinian eruptions. These stages were strongly influenced by the regional tectonics (De Rita and Giordano, 1996), with the Garigliano graben developing since at least the Middle Pleistocene (Giordano et al., 1995; Bosi and Giordano,

1997). The study has focused on Mt Cesima, located northeastward to the volcano. This relief consists of a succession of Jurassic to Cretaceous shallow-water limestones, covered by reworked slope Maastrichtian-Paleocene calcarenites and breccias, and finally sealed by Lower Pleistocene continental breccias. Several examples of monogenetic vents and dikes are reported in the literature in this area (Di Girolamo et al., 1972; 1991; De Rita and Giordano, 1996). The common thread of these two research lines is the interplay between deformation structures and volcanic activity.

1.2 Geological setting

The southern Apennines are a segment of the Alpine system in the central sector of the western Mediterranean Sea (Fig. 1.1a). It formed with the Calabria-Peloritani Terrain (CPT), a retreating thrust belt system where the subduction rate exceeds that resulting from the convergence (Doglioni, 1991; Doglioni et al., 1996; Royden, 1993; Jolivet et al., 1999; Faccenna et al., 2001; Patacca and Scandone, 2007; Carminati and Doglioni, 2012). The CPT includes remnants of the overriding plate (Europa Plate/CPT) partially involved in the subduction/exhumation process tectonically overlying the oceanic suture (Ligurian Ocean), in turn covering an orogenic wedge formed by Meso-Cenozoic thrust-sheets of the continental part of the Adria plate (subducting plate). The latter is made of metamorphic units on the top overlying the sedimentary cover units forming a thrust-and-fold belt defined by several stacked thrust-sheets, including successions of different paleoenvironments, from deep basin to shallow-water platform (Fig. 1.1b; e.g., Mostardini and Merlini, 1986; Casero et al., 1988; Doglioni et al., 1996; Menardi Noguera and Rea, 2000; Faccenna et al., 2001; Catalano et al., 2004; Shiner et al., 2004; Patacca and Scandone, 2007; Mazzoli et al., 2008; Bonardi et al., 2009; Cosentino et al., 2010; Scrocca, 2010; Roure et al., 2012; Vitale and Ciarcia, 2013, 2018; Vitale et al., 2020a,b). In the late 1960s, hydrocarbon exploration provided a significant leap in knowledge, furnishing a deep glance about the tectono-stratigraphic architecture of the orogenic wedge of the chain with the CROP project (e.g. Scrocca et al., 2003), featuring tens of kilometers long seismic lines that investigated down to about 15 km at depth. Although different and sometimes contrasting interpretations about the tectonic architecture have been proposed (e.g., Mostardini and Merlini, 1986; Casero et al., 1988; Doglioni et al., 1996; Menardi Noguera and Rea, 2000; Patacca and Scandone, 2007; Mazzoli et al., 2008), seismic and borehole investigations marked

the existence of a buried imbricated belt made of the Apulian Platform carbonates (APB) below the Apennines orogenic prism.

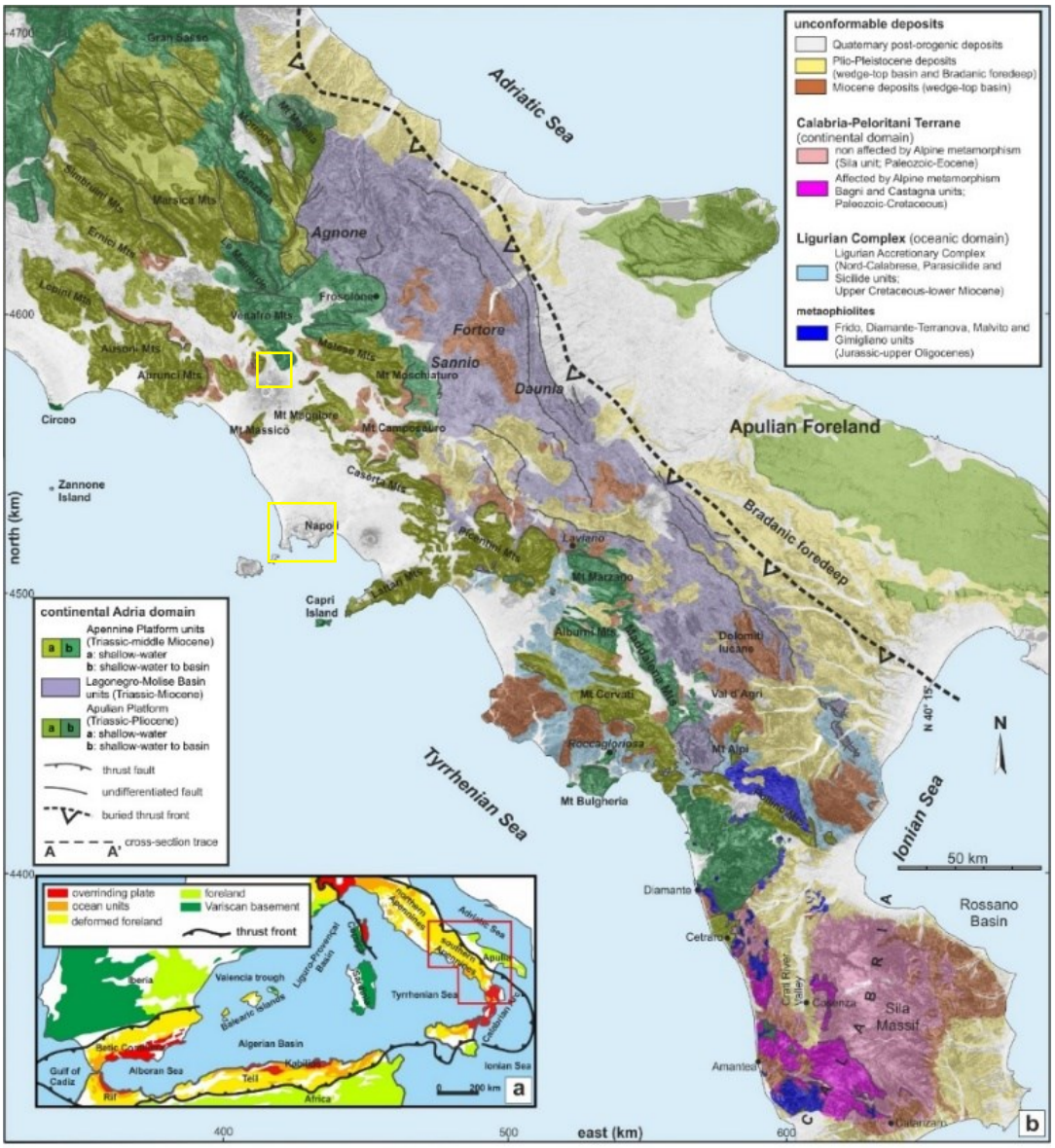

Figure 1.1. (a) Tectonic sketch of western-central Mediterranean Alpine belts (after Mazzoli and Martin-Algarra, 2011; modified). (b) Tectonic map of the southern Apennines (from Vitale and Ciarcia, 2021, modified). Yellow boxes indicate the two study areas.

Recent research (e.g., Mazzoli et al., 2008; Scrocca, 2010) depicts the southern Apennines as formed by dominated-flat thrusts separating major units crosscut by ramp-dominated thrusts affecting the APB. The temporal activity of the major thrust faults suggests a dominant thin-skinned tectonics occurred during the first stage of the orogenic shortening (early-late Miocene) and a thick-skinned deformation since the early Pliocene (Tozer et al., 2002; Mazzoli et al., 2006; Cardello et al., 2021). The synorogenic stratigraphic evolution results from the interplay

between tectonics and sedimentation in the foreland basin system, including back-bulge, forebulge, foredeep, and wedge-top basins (DeCelles and Busby, 2012). The foredeep sedimentation in the Apennine and Apulian platform domains was generally preceded by emersion and erosion of the carbonate successions related to the flexure of the subducting Adria plate (forebulge stage; Sabbatino et al., 2020, 2021). The thrust front-foredeep-forebulge system generally migrated toward E/SE (Vitale and Ciarcia, 2013). The youngest foredeep basin sediments constrain the lower timing for the thrust front migration, and the oldest overlying unconformable wedge-top basin deposits, locally sealing contacts between different thrust sheets, fix the upper temporal limit (Fig. 1.2; e.g., Storti and McClay, 1995; Cosentino et al., 2003; Bonardi et al., 2009; Roure et al., 2012; Vitale and Ciarcia, 2013, 2018). The southern Apennines were also characterized by a significant out-of-sequence thrusting associated with the early Pliocene thick-skinned tectonics that involved the wedge-top basin deposits younger and younger toward the Apulian foreland (Vitale et al., 2018; 2020a, 2020b).

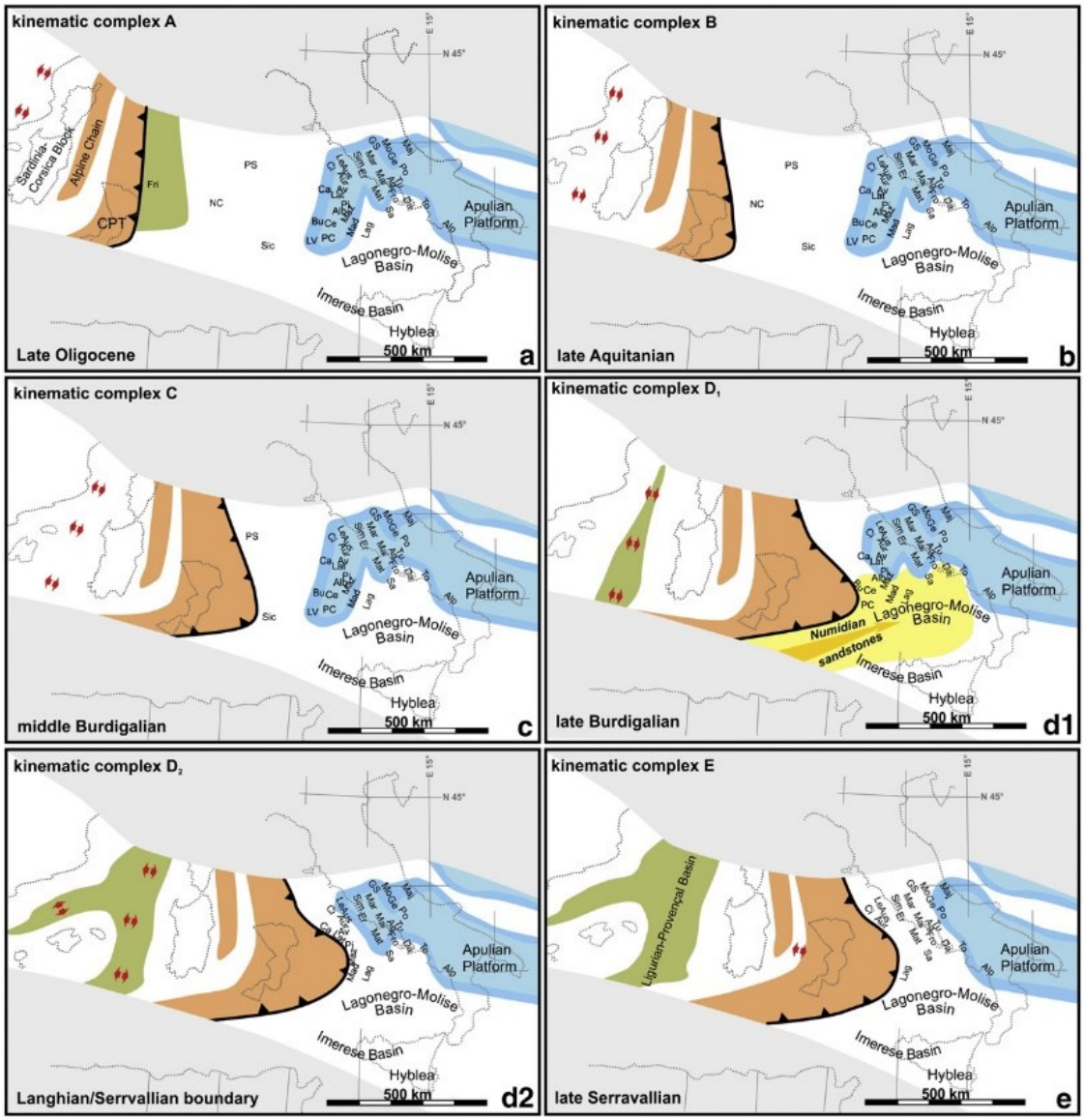

Figure 1.2. Orogenic evolution of the southern Apennine from Late Oligocene to Late Serravallian (after Vitale and Ciarcia, 2013).

The orogen has been subject to back-arc extension since the Late Miocene due to rapid slab roll-back of the Calabrian block, which produced two main extensional basins in the abyssal plain of the Tyrrenian sea, namely the Vavilov and the Marsili basin, located to NW and SE, respectively (Fig. 1.3; Trincardi and Zitellini, 1987; Guenguen et al., 1998). Consequently, the Tyrrhenian margin has undergone a large amount of extension (Turco et al., 2006), resulting in thinned and rifted continental crust, allowing the occurrence of several volcanic centers from Latium to Campania (Savelli, 2002).

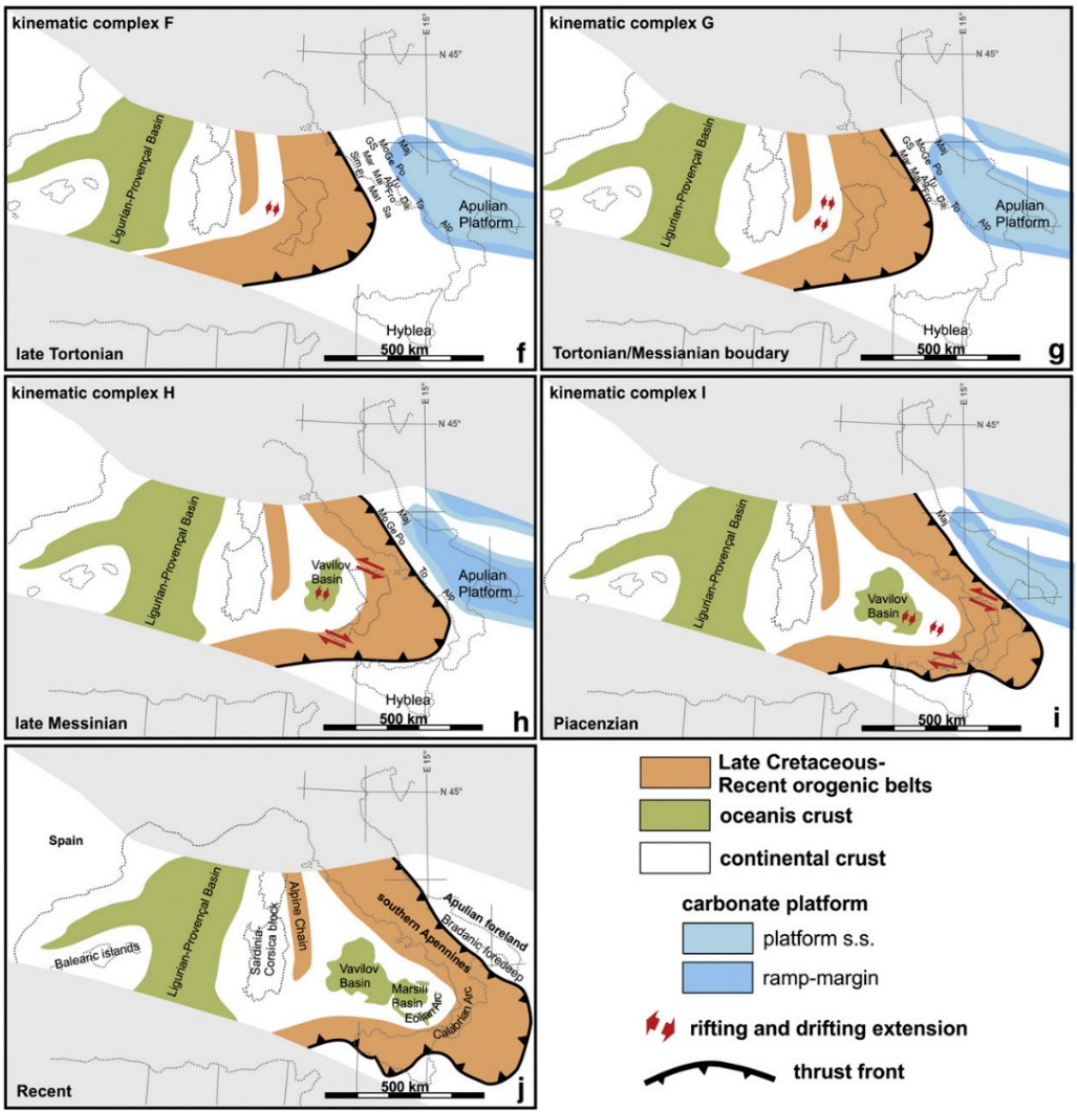

Figure 1.3. Orogenic evolution of the souther Apennine from Late Tortonian to recent, including the opening of the Tyrrhenian ocean and development of Vavilov and Marsili basins (after Vitale and Ciarcia, 2013).

This extensional tectonic field was accommodated first by N-S and NNW-SSE trending normal faults (from Late Miocene to Pliocene, Trincardi and Zitellini, 1987). In contrast, from the Pliocene through Quaternary, NE-SW, NW-SE, and E-W trending faults accommodated the extension with alternating contributions. In the western Tyrrhenian sea, this extension seems to have ceased and been replaced by compression in the late Pleistocene/Holocene, especially west of the Aeolian-Tindari-Letojanni fault (Zitellini et al., 2020). Nonetheless, the extension still occurs along the eastern Tyrrhenian and axial margin of the chain (Serpelloni et al., 2006). Many Pleistocene active back-arc volcanism occurrences are reported in the literature in this extensional context.

1.3 Tectonics and volcanism on the Tyrrhenian margin

The Tyrrhenian Sea is one of the most complex geological settings on Earth (e.g., Dewey et al., 1989; Faccenna et al., 2001; Cavazza and Wezel, 2003; Cavazza et al. 2004; Beltrando et al. 2010; Vitale and Ciarcia, 2013, and references therein). Such complexity is broadly the outcome of its position at the boundary between the converging plates of Europe and Africa/Adria (Dewey et al., 1989; Doglioni et al., 1996; Faccenna et al., 2001; Mazzoli et al., 2008). The magmatism occurrence dates back from Late Cretaceous-Eocene to the Present, with many volcanic centers in the coastal plains (Fig. 1.4, Savelli, 2002; Lustrino et al., 2011).

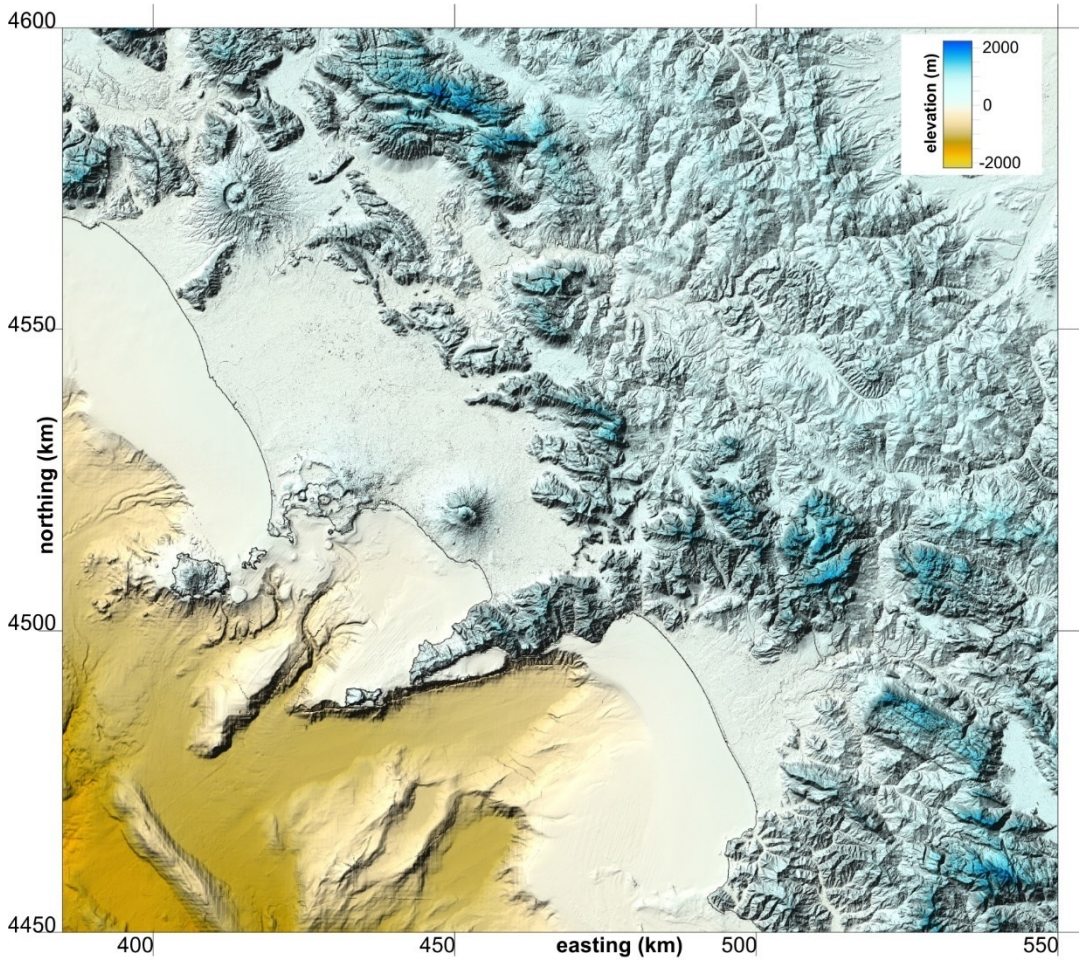

Figure 1.4. Shaded relief of the Tyrrhenian margin of the southern Apennines, indicating main volcanic centers, faults, and morphological features. Continental grid data are from ALOS Lidar data, 30 m resolution, bathymetry from EMODnet open-source database, 100 m resolution.

The magmatism on the Tyrrhenian margin of the Apennines broadly developed during the Late Pliocene-Pleistocene was coeval with the opening of the extensional basins and the formation of the Apennine-Maghrebian chain, having a close link with the subduction of Africa/Adria plates (Lustrino et al. 2011; Vitale and Ciarcia, 2013). On the Tyrrhenian margin of Campania,

where also calc-alkaline magmatism is dated back to 3.5 Ma (Fig. 1.5; Di Girolamo et al. 1976; Barbieri et al. 1979; Albini et al. 1980), the extension occurred along NW-SE and NE-SW lineaments, also affecting the nowadays Tyrrhenian basin (Cipollari et al., 1999; Palmiotto and Loreto, 2019).

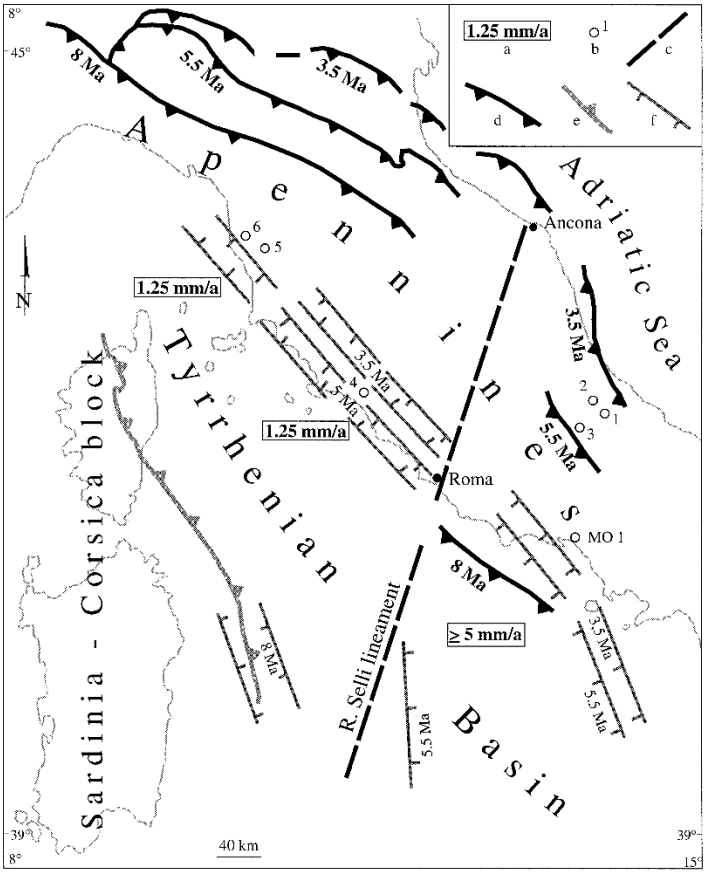

Figure 1.5. Paleogeographic reconstruction of the compressional and extensional fronts during the Late Tortonian-Middle Pliocene evolution of the Tyrrhenian-Apennines system. (a) total subsidence rate, (b) present position of the Messinian Lago-Mare sites: 1: Roccamorice; 2: Pescosansonesco; 3: Le Vicenne; 4: Tolfa Blera; 5: Volterra; 6: Val di Fine; MO 1: Mondragone 1 well; (c) lithosphere discontinuity; (d) active thrust front; (e) Alpine thrust front; (f) active front of the extensional tectonics. (modified after Cipollari et al., 1999).

During the early Pleistocene, extension in the axial zone replaced the previously prevailing crustal shortening (Vitale et al., 2017) along NW-SE structures. The coastal Garigliano and Campana plains formed through NE-SW and NW-SE Pleistocene horst-and-graben structures, locally alternated to NNW-SSE and NNE-SSW faults (Bosi and Giordano, 1997). This alternation of extensional directions affected the Plio-Quaternary volcanism allowing the establishment of central volcanoes such as Roccamonfina (De Rita and Giordano, 1996) and Somma-Vesuvius (Milia and Torrente, 2003; Acocella and Funiciello, 2006; Tramparulo et al.,

2018), and the development of broad volcanic fields in the horst-and-graben sectors, like Campi Flegrei, Ischia and Procida islands.

1.4 Campi Flegrei: previous knowledge

In central Italy, volcanic activity was recorded in the Roman Province, including major caldera-forming explosive events, has occurred since ca. 590-565 ka at the Vulsini, Monti Sabatini and Colli Albani volcanic districts (Fig. 1), and it seems to have ceased progressively from NW to SE since ca. 111 ka (Vulsini), 95 ka (Vico), 70 ka (Sabatini) and 36 ka (Colli Albani) (Perini et al., 2004; Palladino et al., 2010; Marra et al., 2016, 2019, 2020a, b).

In southern Italy, volcanism took place in the Campania plain (Roccamonfina, Ponziane, CVZ, Campi Flegrei and Vesuvius, whereas is recorded whitin the Apennines chain (Vulture), and in the Tyrrhenian sea, Aeolian archipelago and Etna and Sicily Channel.

Concerning the Campi Flegrei (CF), this volcanic field (Fig. 1.6) has been longly studied, starting from the pioneering works of De Lorenzo (1904) and Rittmann (1950), amongst the most important. The oldest activity of CF dates back to ~80 ka (Pappalardo et al., 1999; Scarpati et al., 2012). However, in the Campania Plain, volcanic activity is as old as 100-200 ka (De Vivo et al., 2001; Rolandi et al., 2003).

The CF volcanism was mainly monogenetic explosive magmatic and hydromagmatic alternated to minor effusive activity in the continental and marine portions (Di Girolamo et al., 1984). Periods of scattered volcanic activity, which erupted mainly K-alkaline magmas, were interrupted by large-magnitude caldera-forming eruptions dated back at 40 ka (Campanian Ignimbrite, Giaccio et al., 2018), 29 ka (Masseria del Monte Tuff, Albert et al., 2019), and 15 ka (Neapolitan Yellow Tuff, Orsi et al., 1992; Scarpati et al., 1993). Spatio-temporal distribution of volcanic activity has been studied with detailed stratigraphy of pyroclastic deposits of each stage (e.g., Rosi and Sbrana, 1987; Di Vito et al., 1999; Orsi et al., 2004; Isaia et al., 2015). The deeper part of the caldera has also been explored, taking advantage of deep geothermal boreholes perforated since the 1950s, which helped reconstruct the evolution of the volcanic field (Penta and Conforto, 1951; Rosi and Sbrana, 1983; 1987).

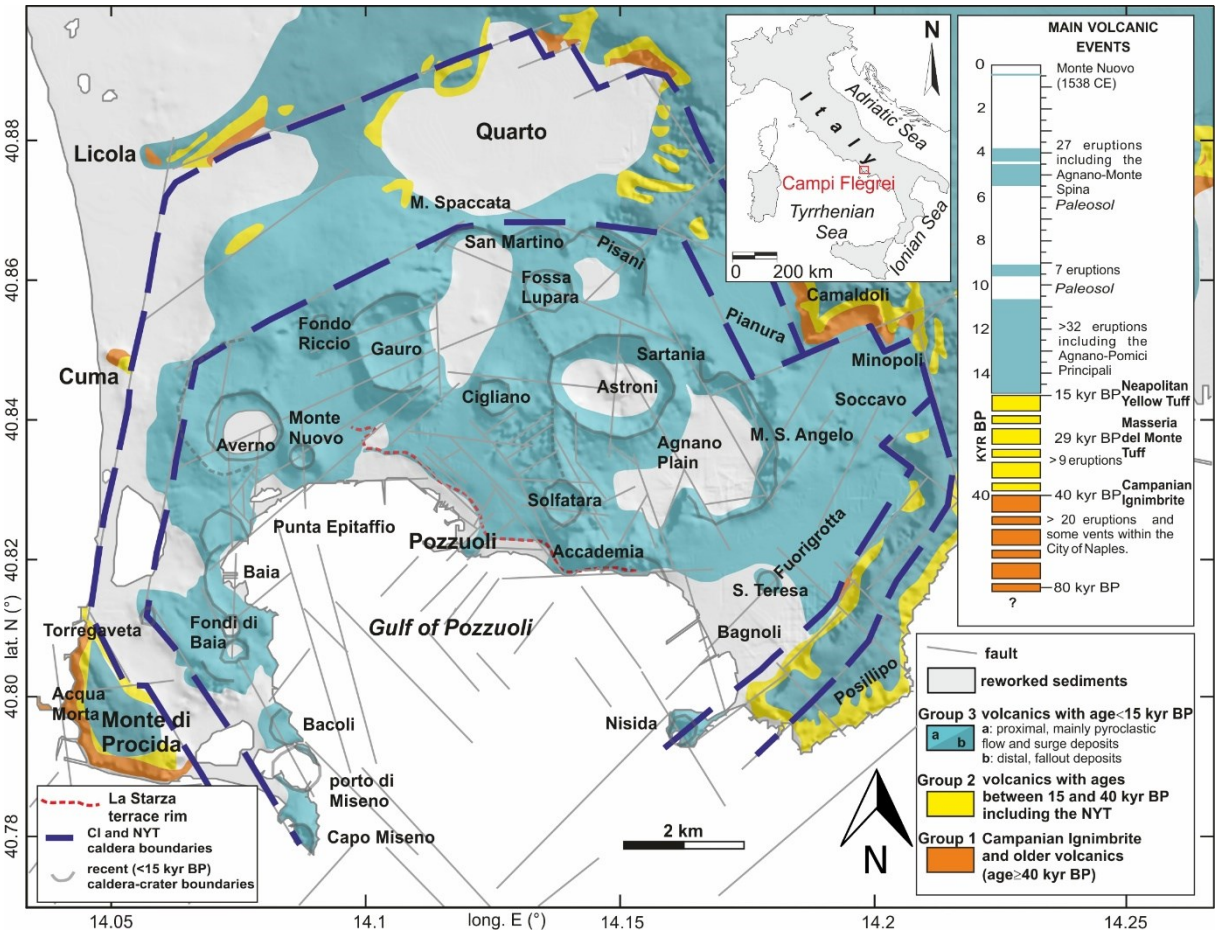

Figure 1.6. Simplified geological map of the Campi Flegrei caldera (modified after Vitale et al., 2019)

The vicinity of the vents to the coastline has interfered with the morphological evolution through time and acted as a proxy to retain information about eventual ground deformation. This is the case of the deeply studied coastal cliff of the La Starza (Rodriguez et al., 1964; Cinque et al., 1985; Amore et al., 1988; Giudicepietro, 1993; Isaia et al., 2009; Isaia et al., 2019). Nowadays, circa one-third of the volcano is submerged in the Gulf of Pozzuoli, and this offered through the decades the opportunity to explore the offshore sector with an available wide dataset (Colantoni, 1972; Pescatore et al., 1984; Milia, 1998; Milia and Torrente, 2000; Sacchi et al., 2014; Steinmann et al., 2016, 2018). the study of the volcano-tectonic structures has been attempted both in the on-land (Acocella et al., 2008; Vitale and Isaia, 2014; Vitale et al., 2019) and in the offshore (Colantoni, 1972; Sacchi et al., 2014; Natale et al., 2020) to fulfill the understanding of this volcanic system. In addition, the debated structure of the caldera has also been studied and inferred by geophysical methods (Florio et al., 1999; Secomandi et al., 2003; Zollo et al., 2004).

1.5 Roccamonfina: previous knowledge

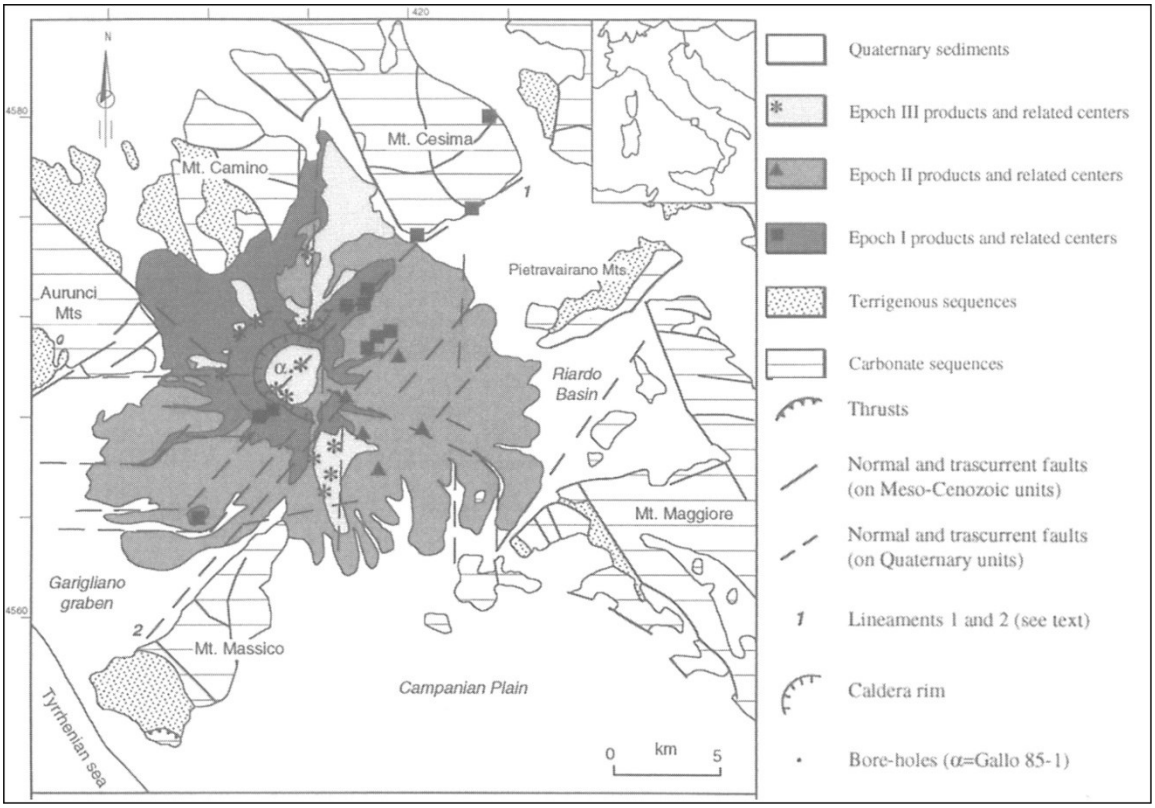

Figure 1.7. Simplified tectonic sketch of the Roccamonfina area highlighting the clustering of monogenetic vents of Epoch I and II on the NE lineaments 1 and 2, whereas Epoch 3 vents are aligned along N- trending tectonic lineaments (after De Rita and Giordano, 1996).

The volcano of Roccamonfina is a composite cone developed in the central part of the Garigliano graben between 550 and 150 ka (Tedesco, 1965; De Rita and Giordano, 1996). The activity of the Roccamonfina volcano, although poorly constrained geochronologically, seems to have spanned 696±49 to 148±18 ka with potential younger activity (i.e., 53±27 ka, Radicati di Brozolo, 1988; Rouchon et al., 2008). After the building of a large stratocone, the occurrence of large-Plinian eruptions (Rouchon et al., 2008) such as Brown Leucitic Tuff (353 ka), Lower White Trachytic Tuff (331 ka), Upper White Trachytic Tuff (230 ka), and Yellow Trachytic Tuff (227 ka), and the coeval tectonic extension (De Rita and Giordano, 1996), strongly influenced the morphology and structure of the volcano, as well as the distribution of ephemeral vents. In addition, many eccentric volcanic vents are reported in literature around the central volcano, with most of it found within 6-8 km from the center (De Rita and Giordano, 1996). Nonetheless, the cases of several volcanic vents further away from the volcano are not a few. These are reported around Mt Cesima, a carbonate relief to the North East of the volcano, near

Taverna San Felice (Di Girolamo et al., 1991; De Rita and Giordano, 1996), Presenzano town (Sgrosso and Aiello, 1963), Sesto Campano town (Di Girolamo et al., 1972), and a magmatic dike has been encountered during the excavations of the aqueduct galleries (Di Girolamo et al., 1991). The erupted products are mainly lavas and strombolian pyroclastics of Leucite-basanite to Leucite-tephrite composition (Di Girolamo et al., 1991). The relationships of such vents with the nearby Roccamonfina and with the regional tectonics is yet to be fully constrained.

1.6 Motivations

The general goal of this research is to try to answer some long-lived questions in the CF and Roccamonfina literature, including:

- Bridging the gap between on-land and offshore stratigraphy at Campi Flegrei.

  Despite the numerous attempts to reconstruct and constrain the different seismic units imaged in the caldera offshore, no direct correlation to the outcropping La Starza unit has been provided (Milia, 1998; Sacchi et al., 2014; Steinmann et al., 2016; 2018). This gap must be filled to constrain the different volcano-tectonic stages recorded by almost continuous sedimentation in the caldera offshore and only partially reconstructed on-land (Isaia et al., 2019). Addressing such lack might provide a detailed picture of the volcano-tectonic evolution and clarify the post-caldera deformation field and stratigraphic position of coastal eruptions/intrusions.

- Reconstructing offshore faults arrays to retrieve conceptual model of caldera structure and addressing literature ambiguities

  In the last decades, the offshore sector of the caldera offered the opportunity to study the structures affecting the volcanic rocks with greater detail than the on-land (Vitale and Isaia, 2014; Steinmann et al., 2016; Bevilacqua et al., 2020; Natale et al., 2020). This condition might allow dispelling the doubts on the existence of the caldera and whether it is single or multiple structures. Moreover, the constraint on the activation timing of intracaldera faults might unravel the role of faults in accommodating ground deformation during caldera stages. The resulting outcome might offer insights about the conceptual model also applicable to the on-land counterpart.

- What is the role between tectonics and magmatism in the emplacement of the most impressive example of dike intrusion in limestone host rock?

  Dike intrusions are common in tectonic rift settings and usually highlight the occurrence of major extensional events. Plio-Quaternary coastal plains of the Campania region are formed by graben and half-graben structural depression. The timing of these extensional events can be constrained by studying the few examples of monogenetic volcanism along the grabens borders. How does tectonics influence the parasitic activity of Roccamonfina? Is this marginal volcanism connected to this stratovolcano?

1.7 Thesis outline

Chapter 1: a general overview of the scientific context and research questions, including information on the geological background of the wider regional setting and a brief outlook to the two study areas, as well as the aims and objectives of this thesis.

Chapter 2: data and methods used in this thesis are presented, including seismic reflection datasets, software, survey methods, and handling of data.

Chapters 3 to 5: they represent the main matter of the thesis in the form of standalone research manuscripts that have been accepted/submitted/to be submitted to international peer-reviewed scientific journals. Such manuscripts are briefly outlined below.

Chapter 3: Integrated on-land-offshore stratigraphy of Campi Flegrei caldera: new insights on the volcano-tectonic evolution of the last 15 kyrs. It attempts to describe the almost continuous record of volcano-tectonic evolution and the thoroughly studied tephrostratigraphy of the post-NYT volcanic activity, reconstructing an integrated stratigraphy. The interplay between caldera floor motion, sea-level rise, and the evolving sedimentary system is discussed, resulting in a fine-tuned integrated on-land-offshore stratigraphy of Campi Flegrei caldera for the last 15 ka, which allows retrieving ages of seismic reflectors giving insights on the volcano-tectonic evolution in the last 15 ka. This research is published on Basin Research (https://onlinelibrary.wiley.com/doi/10.1111/bre.12643)

Chapter 4: Fault systems in the Campi Flegrei offshore sector: fault array geometry, nested caldera structure, dome resurgence, and tectonic field influences. It describes the faults affecting the Gulf of Pozzuoli, providing solid evidence of a multistage nested caldera structure associated with Campanian Ignimbrite and Neapolitan Yellow Tuff eruptions. This detailed mapping also evidences the effectiveness of a tectonic extensional stress field activity during inter-caldera periods. Another scientific outcome is the characterization of the sub-vertical faults affecting the offshore continuation of the resurgent dome, underlining that these faults are formed during discrete volcano-tectonic collapses.

Chapter 5: Middle Pleistocene volcano-tectonic activity in carbonate ridge northeast of Roccamonfina volcano (Italy): evidence of tectonic control on dike emplacement and implications for syn-eruptive carbonate assimilation. It describes and discusses the impressive exposure of a magmatic dike, hosted in a carbonate relief, feeding, and mild Strombolian eruption during a tectonic rifting event. A detailed field and UAV-based survey, along with

petrological analysis, provided insights into a groundbreaking example of the mutual relationships between magmatic and tectonic activity nearby the Roccamonfina volcano. The main results are that an important rifting phase is recognized in the middle Pleistocene exploited by E-W and NE-SW trending faults, allowed the uprise of magma along graben faults, and feeding monogenetic Strombolian eruption younger than 220 ka, thus younger than the last Plinian eruption of Roccamonfina.

Chapter 6: overarching conclusions and outlook for further research outlook.

Chapter 2: Materials and Methods

2.1 Seismic data

The stratigraphic and structural reconstruction of the Pozzuoli Gulf infill was based on three sets of high-resolution seismic profiles, namely Seistec_2013, Cafe 7/3, Marisk_2010. The Seistec dataset was acquired using the uniboom IKB-Seistec profiler (Simpkin and Davis, 1993, Mosher and Simpkin, 1999; Sacchi et al., 2019) by ISMAR-CNR of Naples in 2013. With a source frequency range between 1 and 20 kHz and a central frequency of 2 kHz, the theoretical vertical resolution is 0.2 m, with an average velocity of 1500 m/s. The horizontal resolution at central frequency is ~0.5 m at 150 ms TWT. The seismic signal penetration is strongly influenced by the high signal attenuation of the volcaniclastic rocks, especially in tuffs and fluid-saturated sediments, and it typically reaches Two Way Travel (TWT) depths between 100-150 ms. These lines are mainly NNE-SSW oriented with several oblique lines NE-SW and WNW-ESE oriented , covering the central and western part of the Pozzuoli Gulf (Fig. 2.1).

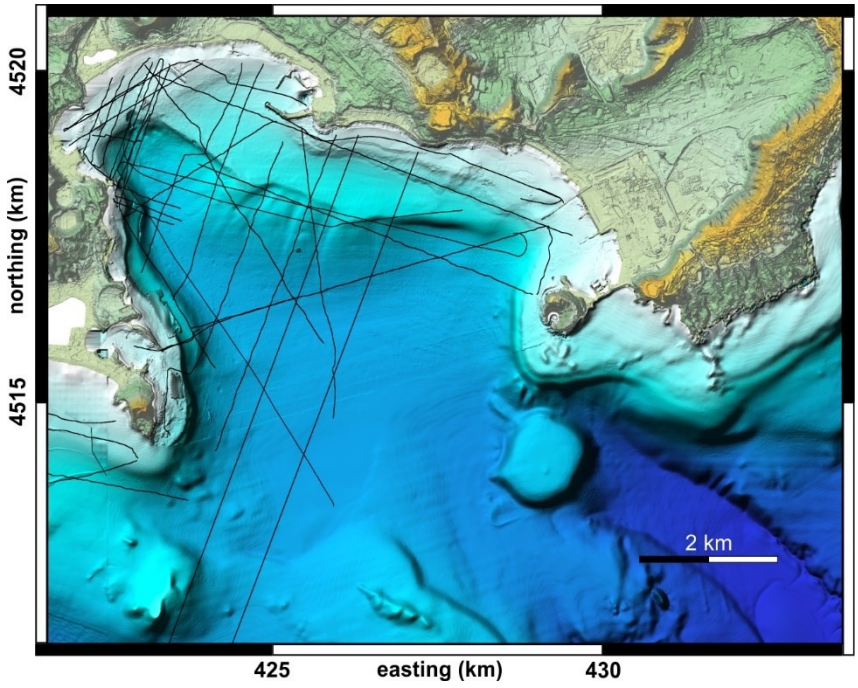

Figure 2.1 Distribution of Seistec single-channel high-resolution seismic lines within the Pozzuoli Gulf.

The Cafe 7/3 multichannel GeoB08 dataset (acquired during the CAFE-7/3 expedition in 2008; Steinmann et al., 2016) have a vertical resolution of ~2 m with a central source frequency of 250 Hz, out of 0.3-1 kHz range, with an average velocity of 1500 m/s. The horizontal resolution at central frequency is ~1 m at 150 ms, with a signal penetration exceeding

350 ms (Steinmann et al., 2016). The processing procedure of Steinmann et al. (2016) improved overall imaging depth compared to previous works in literature, allowing to follow seismic units beneath the shallow multiple reflections and the fluid-bearing layers. These lines are mainly N-S oriented with several oblique lines (both NE-SW and NW-SE) and a few ca. E-W oriented tie lines cover the central and the outer part of the Pozzuoli Gulf (Fig. 2.2). The third dataset is composed of sub-bottom chirp profiles (Marisk_2010 dataset). The Sub-Bottom Chirp profiler operated with a 16 transducer Benthos Chirp II system in a wide frequency band (2–7 kHz), with a long pulse (20–30 ms). Maximum signal penetration is down to 40-50 ms (TWT), enough to display the identified faults at shallow depths.

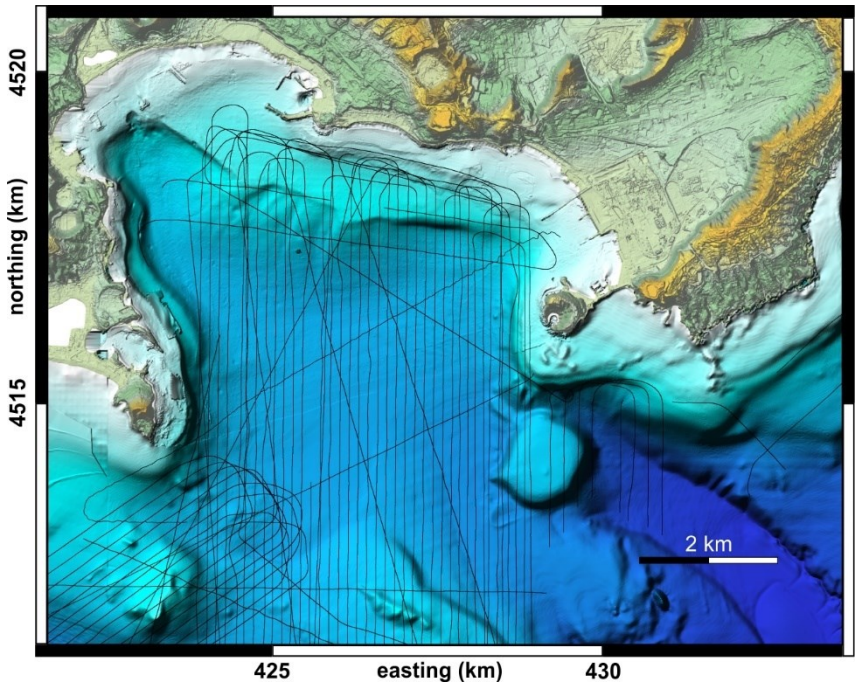

Figure 2.2 Distribution of Cafe multichannel high-resolution seismic profiles within the Pozzuoli Gulf.

Seismic lines belonging to the three datasets were imported and analyzed in the GeoSuite AllWorks (Geo Marine Survey System, 2012) and Eliis Paleoscan software packages (Eliis, 2018; Fig. 2.3). To estimate the thickness of seismic units, we used a two-way travel (TWT) time velocity of 1650 m/s, which is considered to be representative for shallow (<200 m), mostly unconsolidated volcaniclastic and marine deposits (Sacchi et al., 2014; Steinmann et al., 2018).

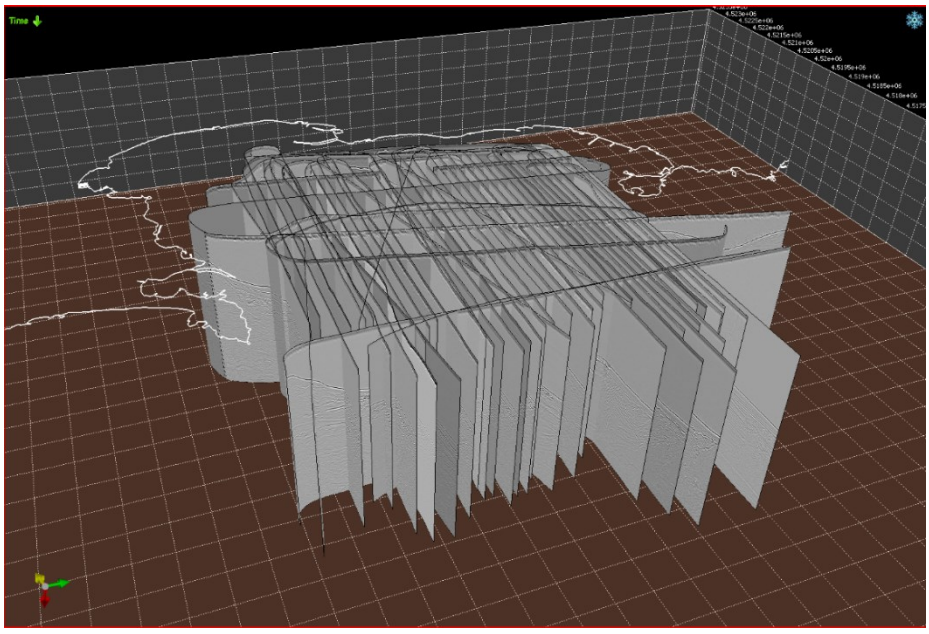

Figure 2.3 Example of 3D visualization of 2D seismic lines within the Eliis Paleoscan software environment.

To analyze the identified faults, the fault sticks were interpolated to retrieve fault orientation data, with a constant velocity of 1650 m/s. Every fault segment has been interpolated by joining up to 3 fault sticks (Fig. 2.4). The same approach has been adopted for the identified dikes.

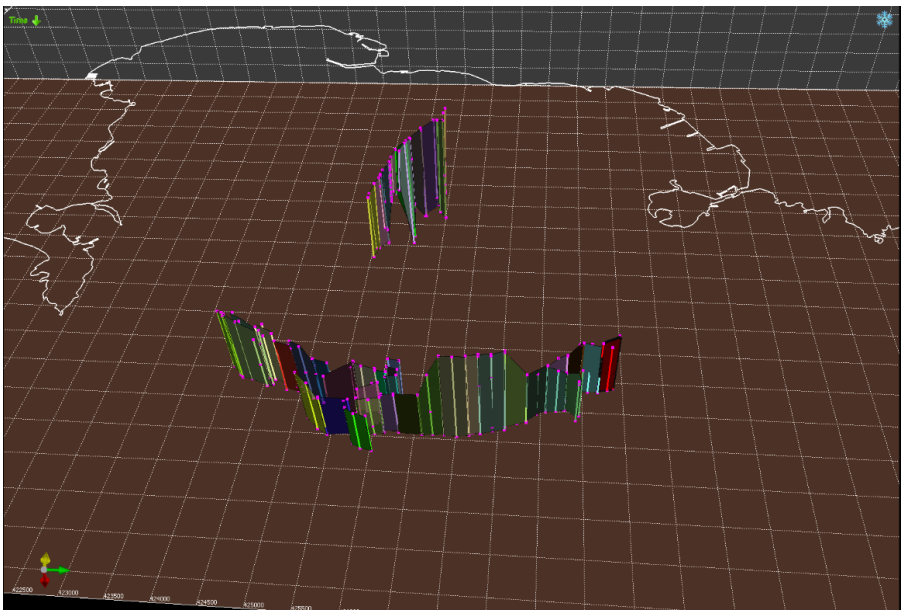

Figure 2.4 Example of 3D visualization of mapped faults picked in the 2D seismic dataset within the Eliis Paleoscan software environment.

2.2 Geospatial data

The high-resolution bathymetric map of the Pozzuoli Gulf (Somma et al., 2016); the bathymetric map of the Gulf of Naples (EMODnet), the Lidar DEM (SIT Napoli), and the global Lidar DEM ALOS were analyzed using Global Mapper software (Blue Marble Geographics) rendered using Surfer® software (Golden Software, LLC).

2.3 Structural data from seismic data

The measures of fault plane data were extracted from Eliis Paleoscan software packages (Eliis, 2018) and subsequently analyzed with Open Stereo (Grohmann and Campanha, 2010) and Tectonics FP (Reiter and Acs, 1996-2020) open-source software. Fault and dike orientation data were also analyzed through the radial analysis method to determine how their azimuth relates with a reference deformation center. This method (e.g., Tramparulo et al., 2018) consists in measuring the following three angular parameters (α, β, and δ). The angle α is defined as the angle (from 0° to 360°) between the north direction and the strike of the line connecting the reference point (i.e., the caldera center) to the fault plane centroid position (from 0° to 360°; Fig. 2c). The angle β, is defined as the angle between the north direction and the strike of the fault plane/dike (from 0° to 180°). The angle δ, which is the absolute value of the difference between α and β. The value of the δ angle, which ranges between 0 and 90°, allows us to classify the analyzed structures as i) radial ($\delta \leq 30°$); ii) oblique ($30° \leq \delta \leq 60°$) and iii) tangential ($\delta \geq 60°$) groups. Through the α-β diagram and d frequency histogram, the radial to tangential fault and dike geometry is evaluated.

2.4 Structural data from field and UAV survey

The collected structural data (fractures, faults, and slickenside lineations) have been subsequently analyzed with Open Stereo (Grohmann and Campanha, 2010) and Tectonics FP (Reiter and Acs, 1996-2020) open-source software. Fault data, including fault plane attitude, striation orientation, and kinematics, have been inverted through the PBT method (Angelier and Mechler, 1977) to provide information about the paleostress fields.

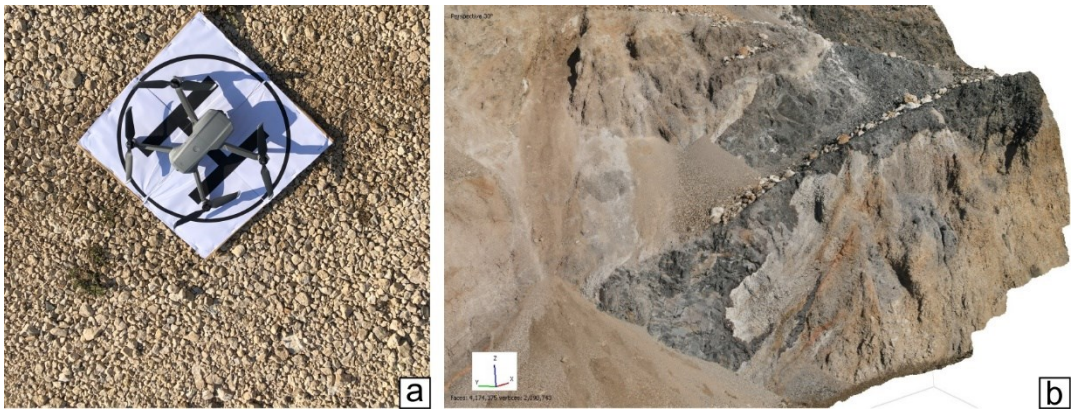

Figure 2.5 (a) take-off and landing platform of the DJI Mavic Air 2 used for the UAV acquisitions. (b) Example of 3D textured model of a detail of the dike of Taverna San Felice in the Agisoft Metashape software environment.

Furthermore, UAV aerial images captured by Unmanned Aerial Vehicles (UAV; Fig. 2.5a) were analyzed and processed to retrieve photogrammetric Structure from Motion (SfM) 3D models, using Agisoft Metashape software (Fig. 2.5b), and extract geometric geologic data utilizing the GeoVis3D software package (www.ausgeol.org\geovis3d; Fig. 2.6). This software is based on the texturized mesh output from Agisoft Metashape, exported in kmz file format, which is oriented in local coordinates. The software uses the orientation of the meshes to extract structural data, and/or the best fit plane of a traced section within the model.

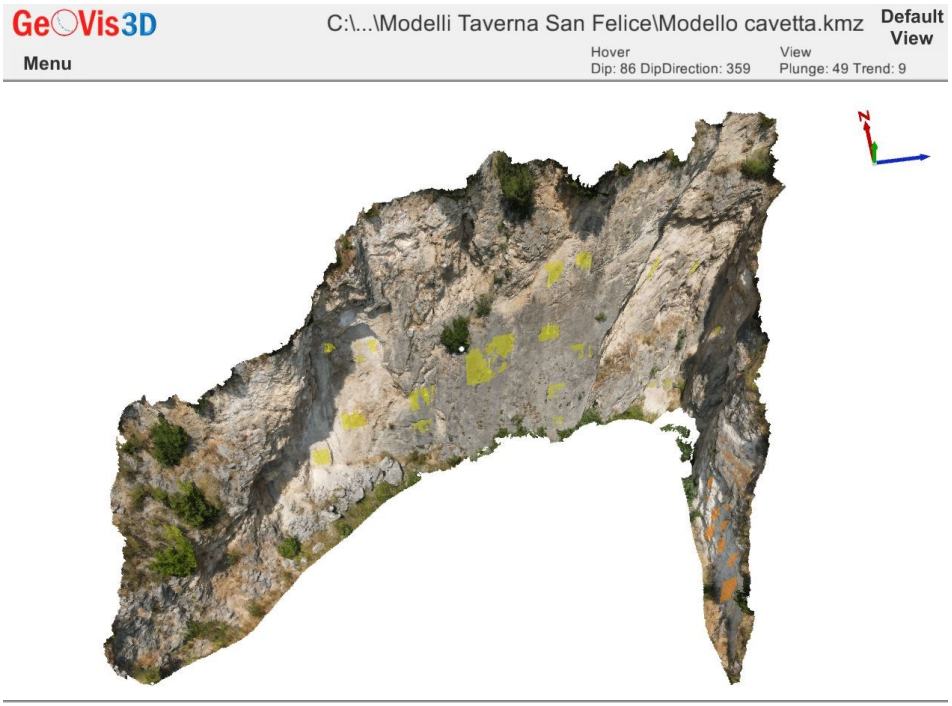

Figure 2.6 Example of structural analysis of Virtual Outcrop Models within the GeoVis3D software environment.

page intentionally left blank

Chapter 3: Integrated on-land-offshore stratigraphy of Campi Flegrei caldera: new insights on the volcano-tectonic evolution of the last 15 kyr

Abstract

Silicic calderas are volcanic systems whose unrest evolution is more unpredictable than other volcano types because they often do not culminate in an eruption. Their complex structure strongly influences the post-collapse volcano-tectonic evolution, usually coupling volcanism and ground deformation. Among such volcanoes, the Campi Flegrei caldera (southern Italy) is one of the most studied in literature. Significant long- and short-term ground deformations characterize this restless volcano. Several studies performed on the marine-continental succession exposed in the central sector of the Campi Flegrei caldera provided a reconstruction of ground deformation during the last 15 kyr. However, considering that over one-third of the caldera is presently submerged beneath the Pozzuoli Gulf, a comprehensive stratigraphic on-land-offshore framework is still lacking, making the previous seismo-stratigraphic studies detached from existing continental stratigraphy. This study aims at reconstructing the offshore succession through analysis of high-resolution single and multichannel reflection seismic profiles and correlates the resulting seismic stratigraphic framework with the stratigraphy reconstructed on-land. Results provide new clues on the causative relations between the intra-caldera marine and volcaniclastic sedimentation and the alternating phases of marine transgressions and regressions originated by the interplay between ground deformation and sea-level rise. The volcano-tectonic reconstruction, provided in this work, connects the major caldera floor movements to the large Plinian eruptions of Pomici Principali (12 ka) and Agnano Monte Spina (4.55 ka), with the onset of the first post-caldera doming at ~10.5 ka. We emphasize that ground deformation is usually coupled with volcanic activity, which shows a self-similar pattern, regardless of its scale. Thus, characterizing the long-term deformation history becomes of particular interest and relevance for hazard assessment and definition of future unrest scenarios.

3.1 Introduction

Caldera systems generally show complex ground deformation phenomena mainly associated with variations of magma production, uprise, storage, and migration in the volcano plumbing system through different timescales (e.g., Cashman and Giordano, 2014; Kennedy et

al., 2018). Overall, long-term ground deformation represents the surface expression of the incremental addition of magma and fluids within complex reservoirs (e.g., Marsh, 1984; Townsend et al., 2019; Acocella, 2019). Usually, the ground movements are coupled with volcanic activity and may either precede or follow eruptions. However, they can also occur with no associated eruptive activity, especially at silicic calderas (Newhall and Dzurisin, 1988; Acocella et al., 2015). Reconstruction of the complex interplay between volcanism and ground deformation is thus one of the main challenges in studying caldera systems, especially in active volcanic areas. Thus, an accurate tephrostratigraphic framework becomes the primary element in defining and quantifying the area affected by volcano-tectonic processes and reconstructing the main structures governing these phenomena and their evolution (e.g., Lucchi et al., 2007; Martì et al., 2018). The stratigraphic model, obtained by coupling the facies analysis of continental and marine sedimentary records with tephrochronology, allows reconstructing the timing of the constructive and destructive volcanic phases characterizing calderas, which may include large submerged portions (e.g., Santorini, Greece; Rabaul, Papua New Guinea; Deception Island, Antarctica; Campi Flegrei, Italy). Nonetheless, accurate reconstructions of the volcano-tectonic evolution are fundamental for any attempt to provide eruptive forecasting scenarios.

One of the most hazardous active volcanoes in the world is the Campi Flegrei caldera (CFc; Fig. 3.1a), which is carefully monitored due to its high urbanization (e.g., D'Auria et al., 2011; Chiodini et al., 2016; INGV, 2021). CFc recently recorded multiple unrest phases characterized by vertical and horizontal ground movements, seismicity, and hydrothermal activity (Woo and Kilburn, 2010; Chiodini et al., 2012; Amoruso et al., 2014, 2017; De Siena et al., 2017; Bevilacqua et al., 2020; Isaia et al., 2021). Historically, vertical ground movements (bradyseism) on the order of 1–10 m have been recorded since Roman times (more than 2000 years ago; e.g., Parascandola, 1947; Bellucci et al., 2006; Mohrange et al., 2006). At CFc, the Monte Nuovo eruption that occurred in 1538 CE is the only historical example of significant long-and short-term ground uplift (up to 15 m) culminated with an eruptive event (Guidoboni and Ciuccarelli, 2011; Di Vito et al., 2016).

The analysis of the marine sedimentary record provides a powerful tool for reconstructing both the stratigraphic framework and volcano-tectonic evolution of CFc. Notably, the study of the marine and volcanic succession exposed at La Starza coastal cliff nearby Pozzuoli town (Fig. 3.1a) allowed the reconstruction of the long-term caldera ground vertical movements over the last 15 kyr (Rodriquez, 1964; Cinque et al., 1985; Giudicepietro,

1993; Isaia et al., 2019; Vitale et al., 2019). However, because more than one-third of the caldera is currently submerged, marine geophysical data can significantly help to achieve a more detailed stratigraphic reconstruction, overwhelming primary issues like non-deposition, erosion, lateral continuity and secondary like urbanization, inaccessibility and limited exposure.

With this scope, several studies have assessed the stratigraphy of the offshore caldera basin-fill using seismic reflection datasets of different vintages and resolution (Pescatore et al., 1984; Fusi et al., 1991; Milia, 1998; Milia et al., 2000; Aiello et al., 2012, 2016; Sacchi et al., 2014, 2019; Steinmann et al., 2016, 2018; Natale et al., 2020). In this work, we benefit from a blend of high- and very-high-resolution seismic profiles, and provide a detailed stratigraphic framework for the submerged part of the caldera and integrate the marine record of the Pozzuoli Gulf with both the La Starza marine succession on-land and the whole continental tephrostratigraphic records of the caldera. Thus, this study significantly updates the stratigraphic framework of the Pozzuoli Gulf, giving rise to a renewed understanding of the long-term interplay between caldera floor motion and sea-level rise as a proxy for the volcano-tectonic events that accompanied the eruptive activity within the caldera.

3.2 Geological setting

3.2.1 Campi Flegrei caldera

The CFc is located along the Tyrrhenian Sea margin of southern Italy (Fig. 3.1; Vitale and Ciarcia, 2018 and reference therein). Volcanism in the broader CFc area started from at least 80 ka and was characterized by a scattered explosive activity associated with monogenetic cones, lava domes, and maars (Scarpati et al., 2013; Vitale and Isaia, 2014; Bevilacqua et al., 2015; Sbrana et al., 2015), including some volcanic edifices in the urban area of Naples. The present 12 km in diameter caldera (Fig. 3.1a) is the complex result of at least three very large explosive eruptions: the Campanian Ignimbrite (39.8 ka, up to about 250 km^3 DRE, Giaccio et al., 2008, 2017; Costa et al., 2012; Scarpati et al., 2016, 2020; Silleni et al., 2020); Masseria del Monte Tuff (29.3 ka, 17 km^3 DRE, Albert et al., 2019) and Neapolitan Yellow Tuff (NYT, 14.9 ka, 20-40 km^3 DRE, Orsi et al., 1992; Scarpati et al., 1993; Deino et al., 2004).

The current morphological layout chiefly derives from the NYT caldera collapse and subsequent intracaldera activity (e.g., Rosi and Sbrana, 1987; Orsi et al., 1996; Vitale and Isaia, 2014). Volcanism in the last 15 kyr mainly took place in distinct periods alternating with quiescence time lapses. Three main eruptive epochs ranging between 15–10.6 ka (Epoch 1),

9.6–9.1 ka (Epoch 2), and 5.5–3.5 ka (Epoch 3) have been set out in literature (Di Vito et al., 1999; Smith et al., 2011; Isaia et al., 2015). Most eruptions were distributed within the collapsed area and subordinately along its borders, varying in style and magnitude with a volume of erupted magma exceeding 1 km^3 during the major event of Pomici Principali (12.3 ka) and Agnano-Monte Spina (4.55 ka) (Orsi et al., 2004; Romano et al., 2019). Eruptions in the last 5 kyr mainly occurred in the eastern caldera sector (Neri et al., 2015; Bevilacqua et al., 2015, 2016), clustered along structural discontinuities (Isaia et al., 2004; Isaia et al., 2009; Vitale and Isaia, 2014) and, in at least one documented case, simultaneously occurred in different caldera sectors (Pistolesi et al., 2016). The estimated cumulative volume of erupted magma (DRE) varies during Epochs 1, 2, and 3, with values of 4.2 ± 0.7, 0.5 ± 0.1, and 2.6 ± 0.5 km^3, respectively (Bevilacqua et al., 2016).

Significant ground deformation and seismo-tectonic activity accompanied volcanic activity (Vitale et al., 2019). The ground deformation of the caldera floor is well-recorded in its central sector by the marine-transitional sedimentary sequence of the La Starza unit (Isaia et al., 2019; Vitale et al., 2019) that includes well-dated tephra layers. Presently, this succession crops out along the Pozzuoli coast, extending from Monte Nuovo volcano to the west and Bagnoli to the east (Fig. 3.1a), and it has been drilled by numerous wells (Di Vito et al., 1999; Isaia et al., 2019; Sbrana et al., 2015). The caldera floor motion usually preceded and accompanied volcanic activity (Isaia et al., 2019). Following the Agnano-Monte Spina Plinian eruption (AMS, 4.55 ka, De Vita et al., 1999; Smith et al., 2011), ground subsidence occurred rapidly, followed by an uplift phase that raised marine sediments to 20 m a.s.l. (Isaia et al., 2009). The last eruption, Monte Nuovo, occurred to the west of Pozzuoli town (Fig. 3.1a) in 1538 CE, following a few centuries of ground uplift (Guidoboni and Ciuccarelli, 2011).

In the early 1950s and the 1970-72 and 1982-84 periods, CFc experienced significant unrest (up to 1m/year of uplift and peaks of thousands of earthquakes per month), which is still ongoing today at slower rates (0.1 m/year of uplift; hundreds of earthquakes per month; INGV, 2021). Nevertheless, the normalized ground deformation shape (vertical and horizontal components) is remarkably constant regardless of the total displacement during uplift and subsidence phases. Furthermore, several works point out that the normalized deformation shows an axisymmetrical bell-shape, with a maximum at its center and radially decreasing from the caldera center to its periphery during uplift and subsidence phases (e.g., Bevilacqua et al., 2020). For this reason and in analogy with the historical monitoring data, we consider the uplift and subsidence phases as having this deformation shape.

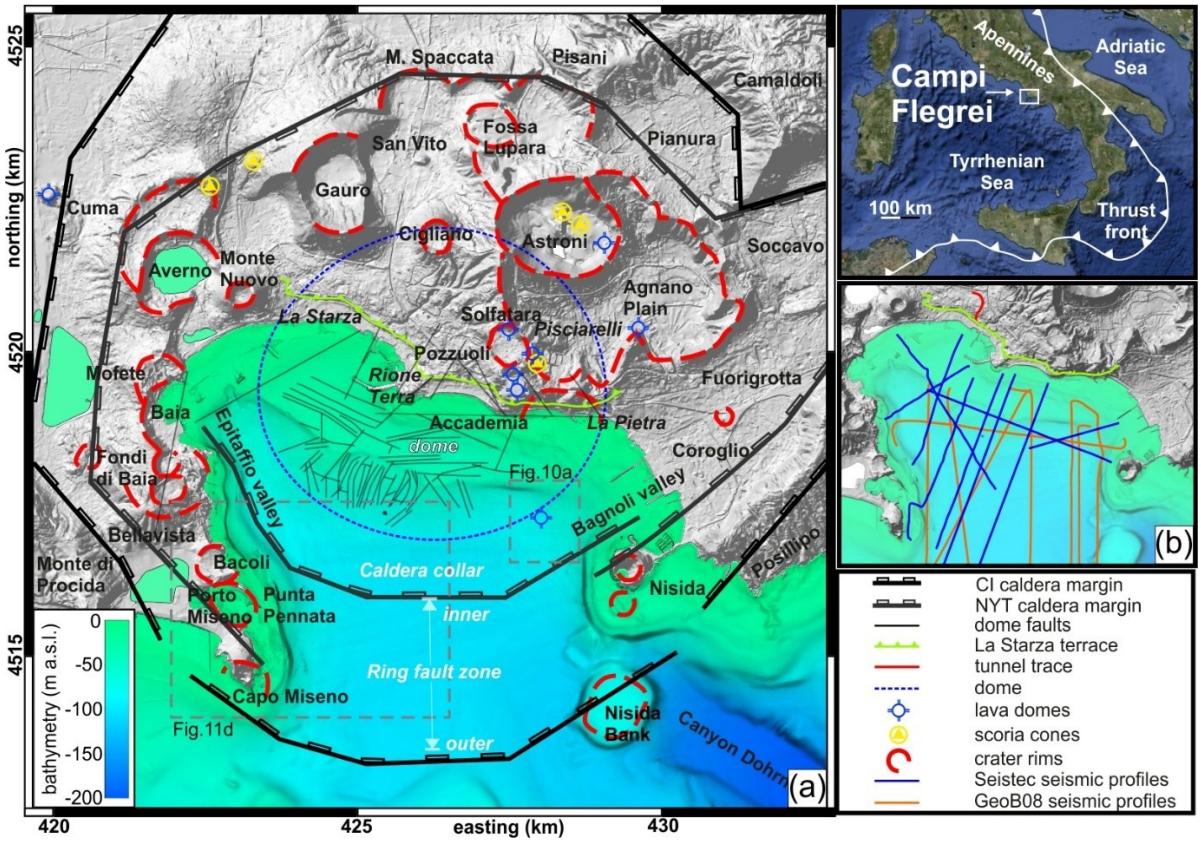

Figure 3.1. (a) Digital Elevation Model of the Campi Flegrei caldera, showing on-land caldera rims (modified after Vitale and Isaia, 2014; Steinmann et al., 2018), offshore ring fault zones (this work), dome surface area (Bevilacqua et al., 2020); dome faults (Natale et al., 2020), crater rims, scoria cones, and lava domes. Dashed boxes indicate the location of time-structure maps of Figures 10 and 11. (b) Locations of the seismic reflection lines used in this work.

3.2.2 Submerged caldera: the Pozzuoli Gulf

The Pozzuoli Gulf encompasses an area of ~40 km^2, covering a considerable part of the CFc (Fig. 3.1a). In the last 15 kyr, the interaction between sea-level rise, ground deformation, erosion, and sedimentation strongly affected its morphology (e.g., Versino, 1972; Sacchi et al., 2014; Somma et al., 2016). The offshore hosts the complementary portion of the subaerial caldera structures, including in the central sector a 5 km radius dome, roughly centered in Pozzuoli town, with the shallower sector (culmination) ranging between 20 and 40 m b.s.l. and bounded by a shelf break at variable depths (Fig. 3.1a). The peripheral area (caldera collar) encompasses the deepest part of the gulf, down to 120 m b.s.l, with the Epitaffio and Bagnoli valleys to the west and east, respectively. The caldera collar is an annular morpho-structural depression between the dome and the ring fault zone. This sector also comprises some morpho-

structural highs, made of remnants of monogenetic volcanic edifices, that bound the Pozzuoli Gulf from Capo Miseno to Punta Epitaffio to the west and from Nisida Island and Coroglio cliff to the east. The sector from Porto Miseno to Nisida localizes in correspondence of the caldera ring fault zone, which is confined by two main boundaries (Fig. 3.1a). The inner caldera boundary is defined by segmented normal faults with tens of meters of displacement associated with the NYT caldera collapse (Steinmann et al., 2016). The depth and the amount of the NYT down throwing are comparable to that estimated from on-shore drill holes (Rosi and Sbrana, 1987; De Natale et al., 2016). Southward, the outer caldera boundary is associated with the CI caldera collapse, with its footwall corresponding to the morpho-structural high made up of pre-CI volcanic banks (Steinmann et al., 2018). These fault strands join with the on-land lineaments associated with the CI caldera faults from Monte di Procida and Posillipo (e.g., Vitale and Isaia, 2014). Intense seafloor degassing and local intrusions localize in the area included by these two main fault zones, such as the Punta Pennata structure, along the coast of Bacoli, and the Bagnoli intrusion (Steinmann et al., 2018).

The most recent studies on the CFc offshore sector on stratigraphy and the interplay between caldera activity and sea-level fluctuations have been proposed by Steinmann et al. (2016, 2018). The authors used a 3D approach extending the identified bounding unconformities to the whole dataset to improve the previous 2D conceptual reconstruction (Steinmann et al., 2016). Their work also assessed an evolutionary model of the caldera system more thoroughly as recorded by their sedimentary units. In the present study, the original three units above the NYT defined by previous works have been deeply revised and detailed up to eleven units, with a different age interpretation, giving rise to a new understanding of the interplay between caldera floor motion, volcanic activity, and sea-level rise.

3.3 Materials and Methods

3.3.1 Seismic profiles

Our reconstruction of the Pozzuoli Gulf stratigraphy was mainly based on a set of high-resolution seismic profiles (Seistec_2013) acquired using the uniboom IKB-Seistec profiler (Simpkin and Davis, 1993, Mosher and Simpkin, 1999; Sacchi et al., 2019) by ISMAR-CNR of Naples in 2013 (Fig. 3.1b). With a source frequency range between 1 and 20 kHz and a central frequency of 2 kHz, the theoretical vertical resolution is 0.2 m, with an average velocity

of 1500 m/s. The horizontal resolution at central frequency is ~0.5 m at 150 ms TWT (Fig. 3.2a). The seismic signal penetration is strongly influenced by the high signal attenuation of the volcaniclastic rocks, especially in tuffs and fluid-saturated sediments, and it typically reaches Two Way Travel (TWT) depths between 100-150 ms.

To gather information on the deeper post-NYT reflectors, which are not adequately imaged in the Seistec dataset due to loss of signal, and to identify the base of the analyzed succession (top of NYT), we relied on the multichannel seismic lines from the GeoB08 dataset (Fig. 3.1b, acquired during the CAFE-7/3 expedition in 2008; Steinmann et al., 2016). These profiles have a vertical resolution of ~2 m with a central source frequency of 250 Hz, out of 0.3-1 kHz range, with an average velocity of 1500 m/s. The horizontal resolution at central frequency is ~1 m at 150 ms, with a signal penetration exceeding 350 ms (Steinmann et al., 2016). The processing procedure of Steinmann et al. (2016) improved overall imaging depth compared to previous works in literature, allowing to follow seismic units beneath the shallow multiple reflections and the fluid-bearing layers. Seismic lines belonging to the two datasets were imported and analyzed in the GeoSuite AllWorks (Geo Marine Survey System, 2012) and Eliis Paleoscan software packages (Eliis, 2018). To estimate the thickness of seismic units, we used a two-way travel (TWT) time velocity of 1650 m/s, which is considered to be representative for shallow (<200 m), mostly unconsolidated volcaniclastic and marine deposits (Sacchi et al., 2014; Steinmann et al., 2018).

3.3.2 Stratigraphic approach

The stratigraphic reconstruction proposed in this work is based on integrating on-land outcrop and borehole data retrieved from the literature (i.a., Isaia et al., 2019) with multiscale seismic reflection data (Fig. 3.1b). Concerning the offshore, we started our reconstruction on three reference units, which include the unit NYT (Steinmann et al., 2016), the well-dispersed transparent unit marker B (Natale et al., 2020), and the shallowest layers sampled by gravity corings (Sacchi et al., 2014). The methodological approach used to increase the stratigraphic resolution includes identifying the Unconformity Bounded Stratigraphic Units (UBSUs), particularly indicated for the volcanic environment (Lucchi et al., 2019). The UBSUs reconstructed offshore have been correlated with the corresponding marine successions (named "intervals") and their bounding unconformities defined on the La Starza on-land by Isaia et al. (2019). We emphasize that the application of UBSU correlations might suffer limitations due to different factors, including undersampling of on-land data due to incomplete records,

hiatuses, and erosion. Despite these limitations, this methodologic approach represents a valid alternative to overcome the lack of direct stratigraphic information (e.g., well-logs).

Using the correlation between gravity core data available from Sacchi et al. (2014) and seismic stratigraphic units, reflectors with high-amplitude and medium-frequency reflections were interpreted as coarse or poorly sorted volcaniclastic material intercalated within fine-grained, well-sorted marine sediments (Natale et al., 2020). The layered succession of marine deposits with different textures (e.g., lithology, grain size, matrix/particle ration, sorting) causes a significant variation of the acoustic impedance that produces strong reflection amplitudes. On the other hand, reflection-free bodies correlate to successions with prevailing homogeneous medium-fine grain-sized marine sediments (e.g., marker B of Natale et al., 2020). These deposits occasionally contain laterally discontinuous coarse beds likely represented by reworked volcaniclastic and marine deposits.

3.3.3 Sedimentation rates

In order to estimate the sedimentation rates for the main seismo-stratigraphic units identified here, we measured the thickness of each unit and sub-unit in a fixed area of the caldera collar on each seismic profile. Then, we averaged the thickness values and calculated the sedimentation rates by dividing the average thickness by the duration of the corresponding time interval. We performed the computation at the caldera collar insofar this area is less affected by volcano-tectonic motion, and thus potentially, all the seismostratigraphic units are recorded. Thus, the established rates are to be considered a maximum estimation. More details of this procedure are reported in the supplementary material.

3.4 Results

3.4.1 Definition of seismic units

To correctly display the recognized unconformities that bound the seismic units in different morphological settings, we show some full-length seismic profiles from the Seistec dataset, oriented about N-S and E-W (Figs. 3.2-3.4). We complemented the high-resolution profiles with three overlapping GeoB08 lines to highlight seismic interpretation consistency and further extrapolate the reconstructed stratigraphic framework at depth.

The first two complementary lines (Fig. 3.2) extend from the inner continental shelf of the central sector to the south of Pozzuoli bay for ~5 km. They illustrate the main seismic units,

with greater resolution at shallow depth for Seistec-402 (Fig. 3.2a) and higher penetration for the GeoB08-050 (Fig. 3.2b), where the main structural features of the dome and the ring fault zones are evident. The caldera faults in these lines do not cut units younger than the NYT.

Conversely, the 5 km long seismic profiles Seistec-401 (Fig. 3.3a) and GeoB08-121 (Fig. 3.3b) extend from Pozzuoli to Capo Miseno, crossing the Punta Pennata structure. The latter is an uplifted zone located south of the southwestern segments of the inner caldera ring (Steinmann et al., 2018). Furthermore, two ~W-E oriented seismic lines, 6 km long Seistec-801 (Fig. 3.4a) and 7 km long GeoB08-065 (Fig. 3.4b), broadly stretch from Baia, across the central dome, to Nisida Island. Finally, the submerged dome, the offshore extension of the continental dome (Bevilacqua et al., 2020), is strongly affected by high-angle normal faults (Natale et al., 2020), which lowered the dome culmination.

We identified different discontinuity surfaces (indicated, from bottom to top, H0 to H10) that, together with stratal architecture and seismic features, allowed us to distinguish eleven seismic units overlying the unit NYT (Table 3.1), which is the relative base of our high-resolution reconstruction. We labeled them as S0 to S10, with some of them including up to three subunits (Table 3.1). We used different criteria to identify these units, including, in order of priority: (i) boundary geometry; (ii) lateral continuity; (iii) seismic facies; and (iv) internal structure. The chronostratigraphy of S10 and the upper part of S9 has been calibrated with gravity cores (Sacchi et al., 2014; Natale et al., 2020). Unlike younger units, NYT, S0, and S1 are evident only on GeoB08 lines.

In the following paragraphs, we illustrate the main features of each seismic unit, as identified in the available seismic profiles and shown in Figure 3.5 and Table 3.1. To improve the readability of the seismic features, we indicate the unit-bounding horizon (Hn) with the same color code as the overlying unit.

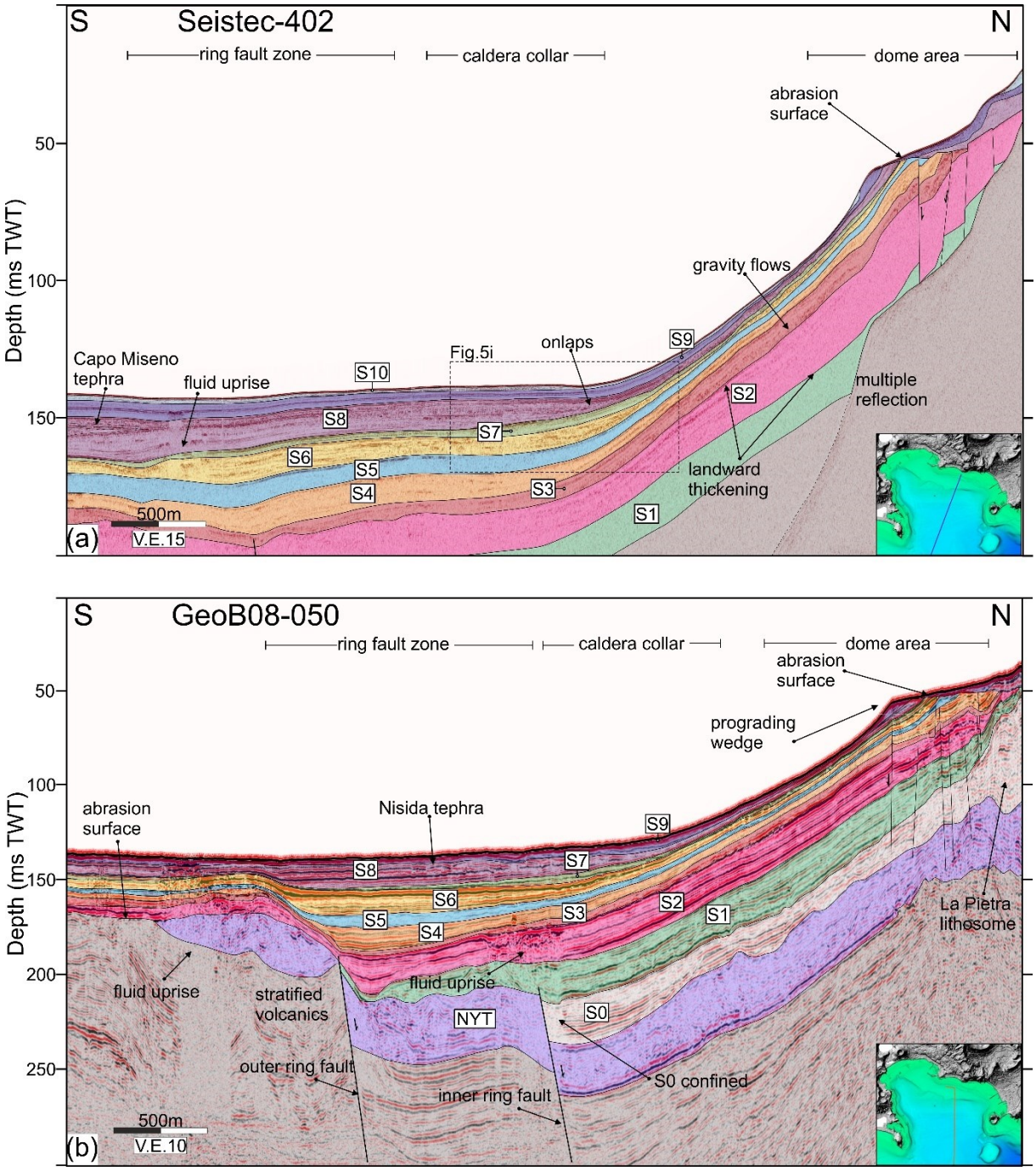

Figure 3.2. (a) Interpreted N-S trending seismic profile Seistec-402 showing the sedimentary infill of the offshore sector of the caldera and stratal relationships with the uplifted dome. Seismic units are indicated, as well as faults and fluid uprises. (b) Interpreted N-S oriented seismic profile GeoB08-050 highlighting the relationships between lower sequences and caldera ring faults. V.E.: Vertical Exaggeration. For locations, see bottom-right insets.

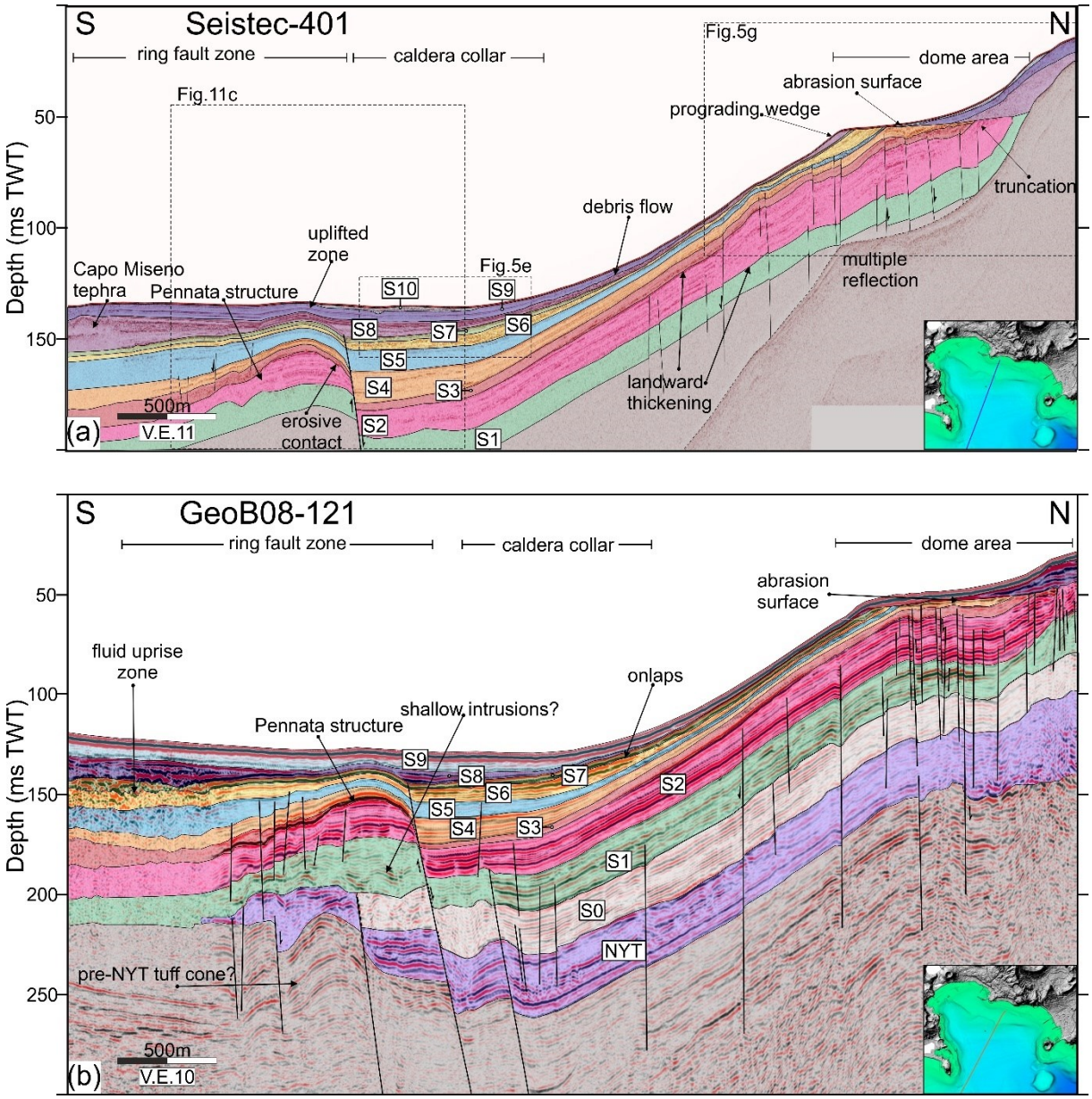

Figure 3.3. (a) Interpreted N-S trending seismic profile Seistec-401 showing the sedimentary infill of the offshore sector of the caldera and syn-sedimentary architecture of P.ta Pennata structure. Main erosive unconformities, seismic units, faults, and fluid uprises are indicated. (b) Interpreted N-S oriented seismic profile GeoB08-121. V.E.: Vertical Exaggeration. For locations, see bottom-right insets.

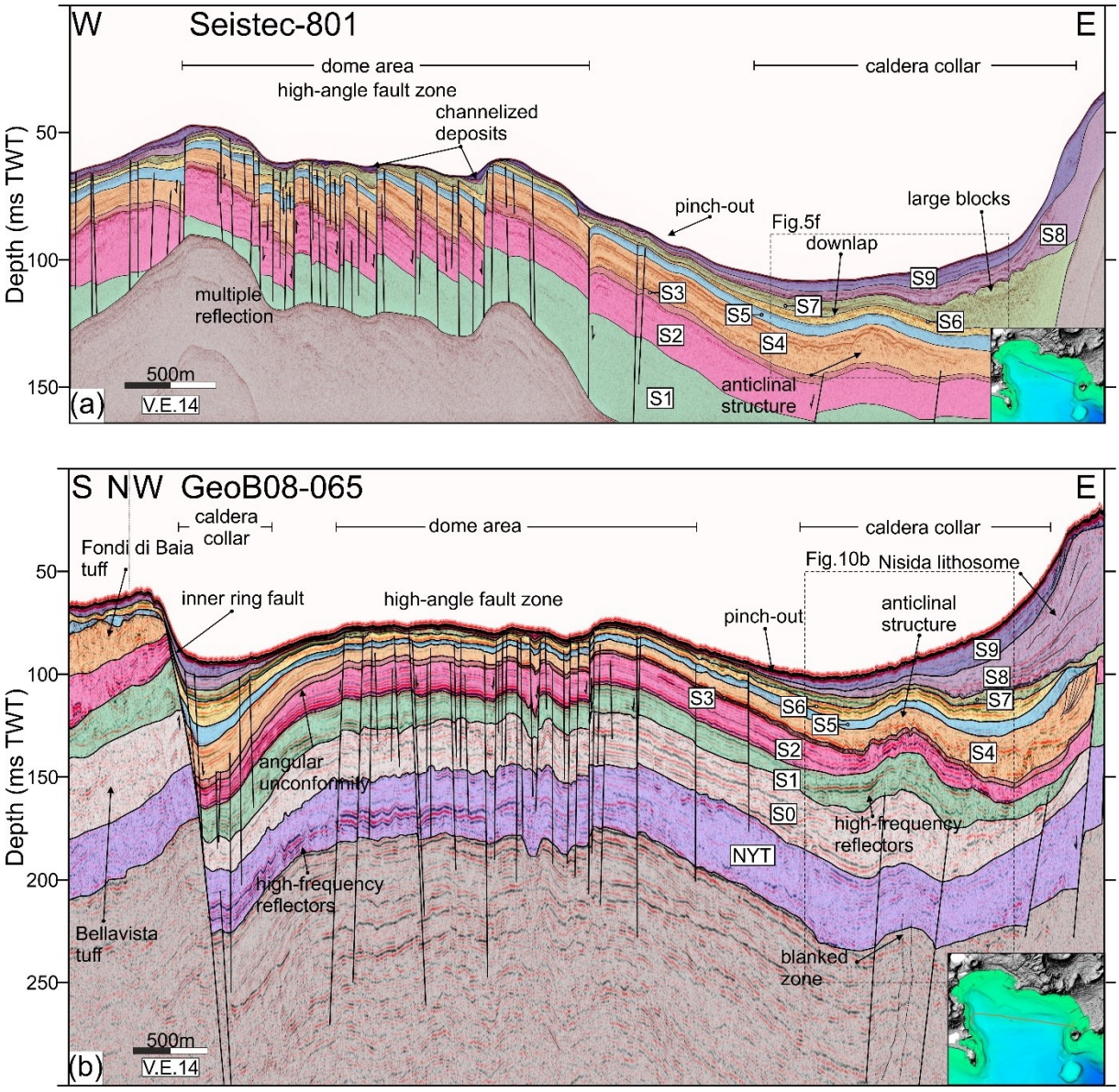

Figure 3.4. (a) Interpreted W-E trending seismic profile Seistec-801 showing the high-angle fault zone and its relationships with the syn-sedimentary infill and anticlinal folds. (b) Interpreted W-E oriented seismic profile GeoB08-065, showing the high-angle fault zone, the inner-ring fault, and the anticlinal structure. On both lines, seismic units are indicated. V.E.: Vertical Exaggeration. For locations, see bottom-right insets.

3.4.1.1 Unit NYT (Neapolitan Yellow Tuff)

Seismic unit NYT is the base of the post-caldera basin fill, as defined offshore by Steinmann et al. (2016). NYT generally exhibits chaotic seismic facies with mainly discontinuous, low to high amplitude reflections. To the west, the seismic facies evolves laterally to more layered medium amplitude reflectors (Fig. 3.4b). NYT overlays continuous high amplitude reflectors laterally and is capped by paraconformity H0 (U2 in Steinmann et al., 2016, 2018). The NYT unit is displaced by normal faults across the caldera ring zone, showing significant lateral thickness variations (Figs. 3.2b, 3.3b, 3.4b).

3.4.1.2 Units S0-S1

An overall sub-transparent facies characterizes unit S0 with the local occurrence of some medium-amplitude, more or less continuous reflectors. It has an average thickness of ~20 m, which keeps almost constant moving from the present shelf to the basin until the inner border of the caldera, where it is confined. Unit S0 is bounded upward by a sharp seismic amplitude and continuity variation, which defines unconformity H1.

Compared to S0, the overlying unit S1 is defined by increased amplitude and continuity and a slight decrease of the reflection frequency. The sequence has an average thickness of ~10 m with no significant lateral variations (Figs. 3.3b, 3.4b).

3.4.1.3 Unit S2

A sharp variation in reflection attributes characterizes the transition between S1 and S2 units across H2. Unlike the underlying units, S2 shows high-amplitude, high-frequency continuous reflectors. It includes three subunits, from bottom to top: S2a, S2b, and S2c (Table 3.1, Figs. 3.5a, b). The lowermost S2a subunit exhibits constant thickness (~8 m) with high-amplitude reflectors and upward frequency decrease (Figs. 3.2, 3.3). It is distributed throughout the Pozzuoli Gulf and represents a continuous seismostratigraphic marker for the two seismic datasets.

Seismic facies and geometric features sharply change within overlying subunit S2b, showing marked transparent facies with poor lateral continuity and, locally, some parallel reflectors. Its thickness is lesser than that of S2a and noticeably increases toward the northern part of the gulf (Figs. 3.2a, 3.3a, 3.5a, b).

The uppermost S2c subunit lies concordantly on top of S2b, showing more reflective facies, with continuous mid-amplitude and mid-frequency reflectors. Like the underlying subunit, S2c thickens landward, with values ranging between 2.5 m in the dome periphery to over 12 m in the apical dome area (Figs. 3.5a, b). The subunit is topped by paraconformity H3 (Figs. 3.5a, b). This contact is represented by a sharp, high amplitude, undulated to plane reflector.

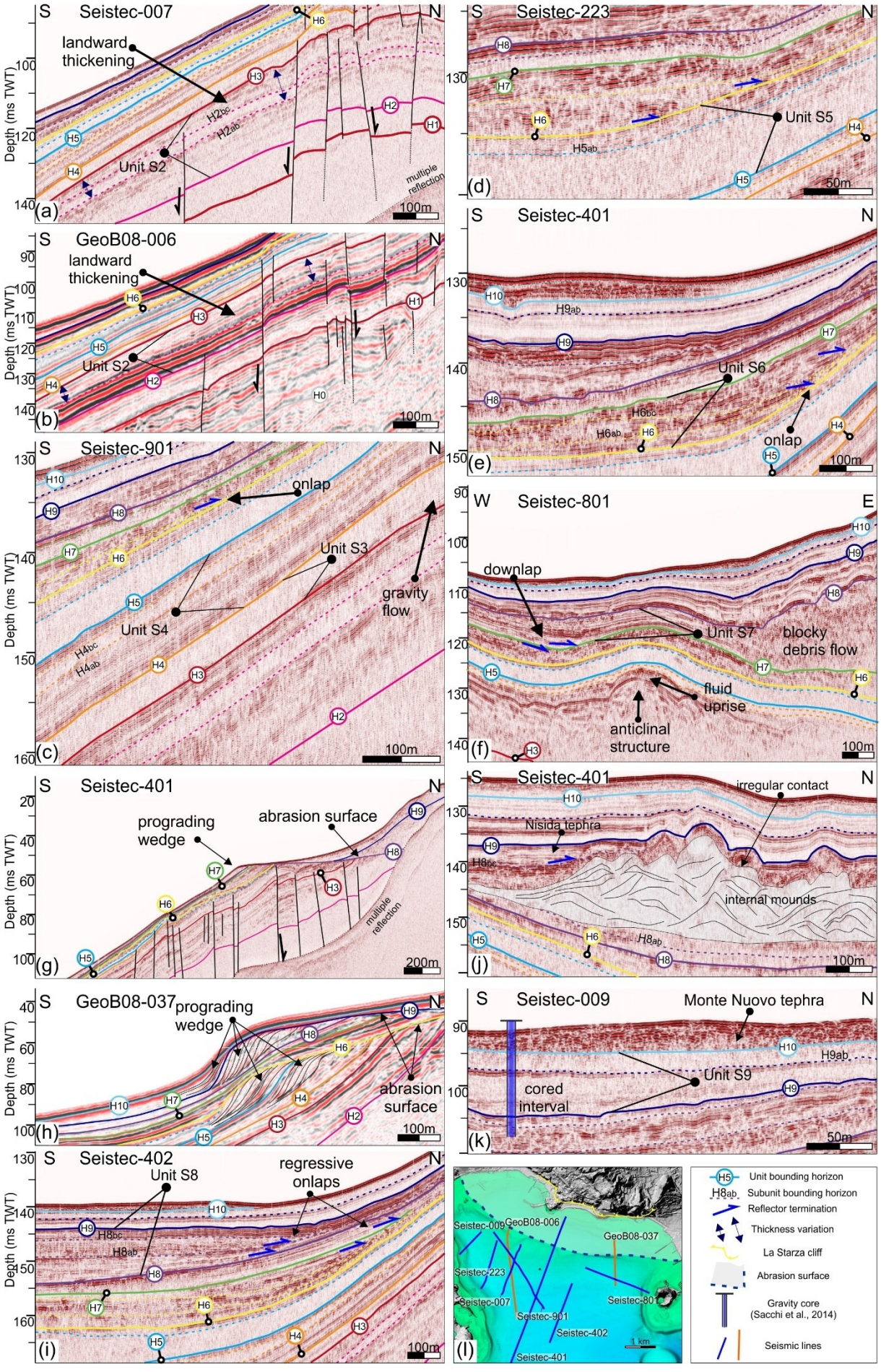
S
Seistec-007
N
landward thickening
Unit S2
multiple reflection
100m
(a)
S
GeoB08-006
N
landward thickening
Unit S2
H0
100m
(b)
S
Seistec-901
N
onlap
Unit S3
gravity flow
Unit S4
100m
(c)
S
Seistec-223
N
Unit S5
50m
(d)
S
Seistec-401
N
Unit S6
onlap
100m
(e)
W
Seistec-801
E
downlap
Unit S7
blocky debris flow
fluid uprise
anticlinal structure
100m
(f)
S
Seistec-401
N
prograding wedge
abrasion surface
multiple reflection
200m
(g)
S
GeoB08-037
N
prograding wedge
abrasion surface
100m
(h)
S
Seistec-402
N
Unit S8
regressive onlaps
100m
(i)
S
Seistec-401
N
irregular contact
Nisida tephra
internal mounds
100m
(j)
S
Seistec-009
N
Monte Nuovo tephra
Unit S9
cored interval
50m
(k)
Seistec-009
GeoB08-006
GeoB08-037
Seistec-223
Seistec-007
Seistec-801
Seistec-901
Seistec-402
Seistec-401
1 km
(l)
Depth (ms TWT)
Unit bounding horizon
Subunit bounding horizon
Reflector termination
Thickness variation
La Starza cliff
Abrasion surface
Gravity core (Sacchi et al., 2014)
Seismic lines

Figure 3.5. (a, b) Landward thickening of unit S2, bounded on top by horizon H3, passes landward from a paraconformity to an unconformity, as seen on Seistec GeoB08 lines, respectively. (c) Main characteristics of units S3 and S4. (d) Unit S5 as observed in dome-radial line Seistec-223, with the alternating amplitude reflectors. (e) Unit S6 and its three subunits and unit S9 seismic expression. (f) Anticlinal structure capped by chaotic blocky and boulder rich deposit. (g) Major abrasion surface (H8) topping the apical dome area and associated with S7 unit. (h) Two generations of abrasion surfaces and prograding wedges on the eastern part of the gulf. (i) Regressive stacking pattern marked by shifted onlap terminations and subdivision of S8 unit. (j) Stratigraphic position of Capo Miseno tephra located in the upper part of S8b subunit. Map inset showing the location of the seismic lines, dashed line encloses the extension of the abrasion surface.

3.4.1.4 Unit S3

S3 is identified by a sharp change of the internal characters of the seismic unit, featuring a 3.4 m thick sub-transparent facies with interspersed medium to high amplitude, discontinuous reflectors, particularly in its middle-top part (Figs. 3.5c, f). Unlike the underlying S2, this unit thickens toward the caldera collar area, reaching up to 4 m in thickness (Figs. 3.2-3.4).

3.4.1.5 Unit S4

S4 is composed of three subunits (S4a-c, Fig. 3.5c). S4a is located at the base and is characterized by stratified medium amplitude, mid-frequency reflectors, with higher amplitude upward, alternating with transparent reflectors mainly in its lower part with increasing thickness toward the collar area.

Subunit S4b is characterized by sub-transparent facies with locally poorly continuous reflectors mainly toward its top and shows a gentle decrease in thickness from the basin to the dome. Finally, a sharp contact characterizes the transition to the overlying S4c (Fig. 3.5c), represented by high amplitude continuous reflectors with significant thickening passing from the dome apical zone to the collar.

3.4.1.6 Unit S5

Sequence S5 features two sub-units (S5a-b). Subunit S5a is a well-recognizable stratigraphic marker in both Seistec and GeoB08 lines (Marker B in Natale et al., 2020) that exhibits transparent facies with discontinuous low amplitude reflectors toward the top (Figs. 3.2, 3.3, 3.4, 3.5c). It is characterized by marked thickness variations recording up to ~6 m in the collar zone. Notwithstanding the occurrence of erosive features in the dome area, the thickness of the unit is broadly preserved and is about 2 m.

Subunit S5b includes medium-to-high amplitude parallel to sub-parallel reflectors, with a slightly variable thickness (averagely around 0.5 m; Fig. 3.5d), generally preserved in the dome area.

3.4.1.7 Unit S6

Unit S6 overlies with a paraconformity horizon H6 and is characterized by high and very-high amplitude, continuous to chaotic reflectors in the basin. The basal contact evolves laterally to an angular unconformity toward the dome apical zone.

This unit encompasses subunits S6a-c, separated by internal unconformities and representing discrete depositional events (Table 3.1, Fig. 3.5e). Although they display similar facies and lobate geometry, the uppermost subunit shows larger thicknesses (up to 2.5 m) along the slope and the collar. All three subunits are very thin or absent in the apical dome area, except in structural lows, thus predating the main abrasion surface above. Onlap terminations are present along the slope of the dome (Fig. 3.5e).

3.4.1.8 Unit S7

S7 shows a lobe-like, transgressive pattern in paleobathymetric lows and along N-S oriented lines (Fig. 3.5e, f). This unit comprises the basal subunit S7a, defined by mainly transparent facies with interspersed high-amplitude continuous reflectors, displaying unconformable contact with the underlying sequence. On the other hand, a sharp change in seismic facies, which shifts toward higher amplitude and frequencies, is present within overlying subunit S7b, which displays continuous to chaotic reflectors. Moreover, in the eastern sector, in the Bagnoli valley, blocky to chaotic features characterize this subunit, reaching a maximum thickness of ~10m. (Fig. 3.5f).

3.4.1.9 Unit S8

In the basin, S8 overlies paraconformity H8, which evolves to an angular unconformity toward the dome area, producing a pronounced abrasion surface (Fig. 3.5g, area enclosed by dashed line in map inset of Figure 3.5). We divided this unit is into three subunits, as significant facies and geometric variations are recognized within the sequence. On N-S oriented lines (Figs. 3.2, 3.3), subunits S8a and S8b show prograding onlap terminations and lobate features (Fig. 3.5i).

The lowermost subunit S8a is marked by chaotic mid-amplitude and high-frequency reflectors showing a slight thickness increase from east to west. S8b is mainly composed of laterally discontinuous high amplitude reflectors. This unit has a flat-lying top surface, and on the western side, it pinches out on the Punta Pennata structure (Fig. 3.3a), whereas on the flank of the dome, it passes laterally to chaotic and irregular reflectors.

Finally, S8c, which represents a stratigraphic marker on both datasets, is composed of parallel stratified high frequency and amplitude reflectors that mantle the underlying sequences. Furthermore, this horizon was cored and calibrated by three gravity cores (Sacchi et al., 2014). To the west and east, its overall thickness increases toward Capo Miseno (Fig. 3.5j) and Nisida (Fig. 3.3), respectively.

3.4.1.10 Units S9-S10

Unit S9 features low amplitude, locally transparent reflectors with a high-amplitude, continuous reflector halfway its thickness, and includes the Vesuvius 79 CE and Ischia 60 CE tephras, as recognized by Sacchi et al. (2014). The overall thickness in the collar zone ranges between 4 and 7 m, reaching its maximum value in the Epitaffio and Bagnoli valleys (Fig. 3.4).

Laterally discontinuous high amplitude reflectors characterize S10 with internal geometries and valley-ponding features in the Epitaffio valley, where it reaches its maximum thickness. This sequence has been calibrated with gravity cores and correlated to the 1538 CE Monte Nuovo tephra (Fig. 3.5k).

Seismic unit	Seismic sub-unit	Seismic reflection pattern	Bounding horizon	Continuity	Seismic Amplitude	Reflection Configuration	Reference tephra/layer	Age range ka BP	La Starza Intervals
S10	S10b S10a		$H10_{ab}$	Variable	High	Subparallel to chaotic	MN	0-0.6	
			H10						
S9	S9b S9a	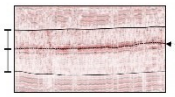	$H9_{ab}$	Reflection-free with interbedded continuous	Low with interbedded medium-amplitude reflections	Parallel to subparallel	AD 79	0.6-3.7	
			H9						
S8	S8c S8b S8a	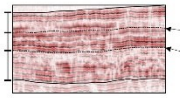	$H8_{bc}$ $H8_{ab}$	Variable	High	Subparallel	CM-NIS AST-FOL AV2-SOL	3.7-4.4	h3
			H8						
S7	S7b S7a	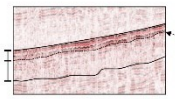	$H7_{ab}$	Discontinuous	Low to moderate	Subparallel to chaotic	PU	4.4-4.55	h2
			H7						
S6	S6c S6b S6a	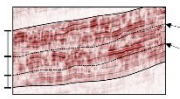	$H6_{bc}$ $H6_{ab}$	Variable	High	Subparallel to chaotic	AMS MSA-PA2 AV1-CIG AG1-2	4.55-5.5	g2-h1
			H6						
S5	S5b S5a	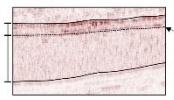	$H5_{ab}$	Reflection-free and continuous	Low to moderate	Chaotic to parallel	rizholites beds paleosol B	5.5-9.1	f-g1
			H5						
S4	S4c S4b S4a	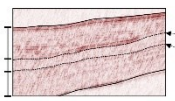	$H4_{bc}$ $H4_{ab}$	Continuous with interbedded reflection-free	Moderate to high	Subparallel to chaotic	CSD-PSN B-FdB	9.1-9.6	d-e
			H4						
S3		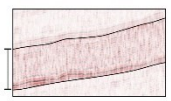		Continuous	Low to moderate	Parallel	paleosol A	9.6-10.46	c
			H3						
S2	S2c S2b S2a	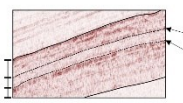	$H2_{bc}$ $H2_{ab}$	Continuous with interbedded reflection-free	Moderate to high	Parallel	So1-PP	10.46-12.3	a-b
			H2						
S1		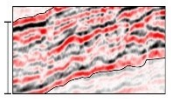		Continuous	Moderate to high	Subparallel	La Pigna Arch.AV	12.3-14.3	
			H1						
S0		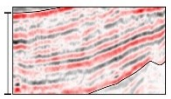		Continuous	Low with interbedded high-amplitude reflections	Parallel to subparallel	LaP-GAU MOF-BV	14.3-14.9	
			H0						
NYT		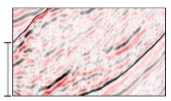		Discontinuous	Low with interbedded high-amplitude reflections	Chaotic	NYT	>14.9	

Table 3.1. Seismic units and seismic patterns of the last 15 ka fill of the Pozzuoli Gulf, and related age attribution, reference tephra and correspective La Starza intervals (Smith et al., 2011; Bevilacqua et al., 2016; Isaia et al., 2019). NYT: Neapolitan Yellow Tuff; BV: Bellavista; MOF: Mofete; GAU: Gauro; LaP: La Pietra; So1: Soccavo 1; PP: Pomici Principali; B-FdB: Baia-Fondi di Baia; CSD: Costa San Domenico; PSN: Pigna San Nicola; AG1-2; Agnano 1-2; AV1: Averno 1; CIG: Cigliano; A3: Agnano 3; MSA: Monte Sant'Angelo; PA2: Paleoastroni 2; AMS: Agnano Monte Spina; PU: Pozzuoli Unit; AV2-SOL: Averno 2 – Solfatara; AST: Astroni; CM: Capo Miseno; NIS: Nisida; MN: Monte Nuovo.

3.4.2 Deformation structures

Seismic images reveal that faults and intrusion-related structures thoroughly affect the caldera offshore. Two main fault systems are present: ring faults and dome high-angle faults (Fig. 3.1a). The ring fault zones, where numerous fault strands are present, are also the place of an intense fluid uprise (Figs. 3.2, 3.3). The inner ring faults displace the NYT unit and generally bound unit S0, whereas they are topped by S1 (Fig. 3.2). Nevertheless, in the western sector, these faults deform sediments up to unit S5 (Fig. 3.3). In concomitance with the ring faults, the signal is often blanked due to degassing (Figs. 3.2-3.4). Nearby Porto Miseno (Fig. 3.1a), a deformation structure occurs (Punta Pennata structure; Milia and Torrente, 2000). The latter is a complex intrusion in the footwall of the inner ring fault, likely related to a shallow intrusion (Steinmann et al., 2018). In fact, the caldera ring faults represent preferential pathways for the ascent of magma, promoting the emplacement of intrusions (Smith and Bailey, 1968; Saunders, 2004; Magee et al., 2013). Furthermore, in the eastern part of ~E-W profiles (Fig. 3.4), a well-defined anticlinal structure occurs, already interpreted by Sacchi et al. (2014) and Steinmann et al. (2016) as related to a sub-surficial intrusion.

The central dome, broadly included in the dashed circular area in Figure 3.1a, is affected by near-vertical faults that displace the seismostratigraphic succession up to unit S6. It is worth noting as the main abrasion surface associated with S7-S8 units cuts this fault system. These structures generally show smaller displacements than ring faults (Natale et al., 2020) and are also a favorable path for fluids escaping toward the seafloor (Carlino et al., 2016). These faults mainly strike NNE, NE-SW, and W-E and are defined by high dip angles (up to 80°) (Figs. 3.1, 3.3; Natale et al., 2020).

3.5 Discussion

3.5.1 Correlation of the seismo-stratigraphic units with the La Starza succession

We correlated the reconstructed stratigraphy of seismic units with the coeval La Starza succession exposed on-land. The latter represents the depocenter of the depositional basin ensuing the NYT collapse, whereas the offshore seismic units were formed in progressively more distal sectors. Figure 6 shows the proposed correlation between the eleven units identified in seismic profiles with the main stratigraphic intervals (a to h3 in Fig. 3.6b) defined for the La Starza unit by Isaia et al. (2019) and Vitale et al. (2019). Figure 7 shows a detailed visual

correlation between seismic sequences (Fig. 3.5) and their exposed counterparts observed at La Starza cliff and in a tunnel excavation (after Isaia et al., 2019).

The analysis of the La Starza succession indicates that, in the last 15 kyr, the proximal sector was characterized by alternating marine and subaerial environments (Isaia et al., 2019). In contrast, the Gulf of Pozzuoli has always been submerged during this time interval, including phases of prevailing net uplift of the seafloor when a sharp marine surface was formed in the inner shelf area. Therefore, to compare the seismic units with La Starza deposits, we use the interval names (a to h) of Isaia et al. (2019), as indicated in Figure 3.6b and reported in Table 3.1.

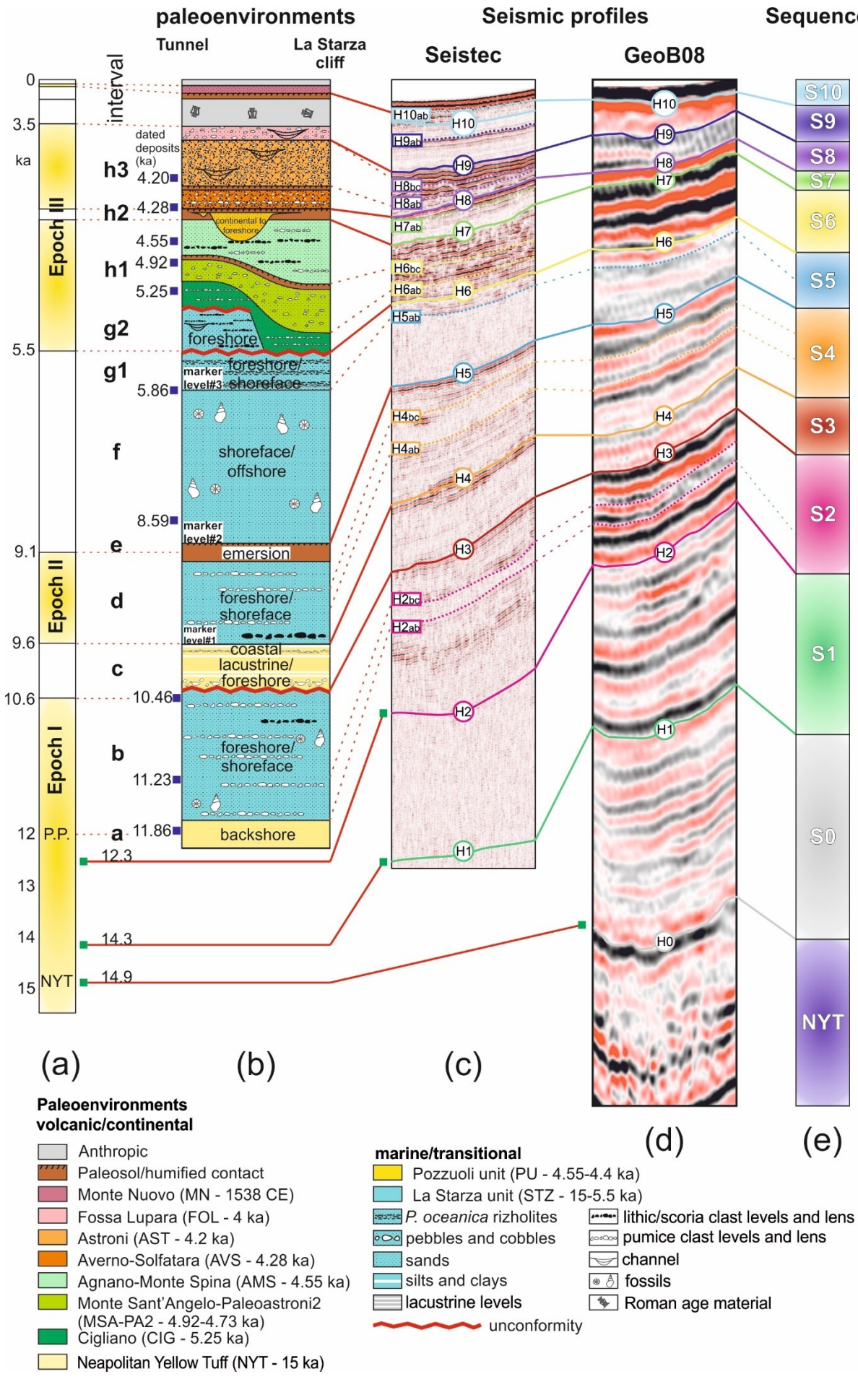
paleoenvironments
Seismic profiles
Sequences
Tunnel
La Starza cliff
Seistec
GeoB08
interval
dated deposits (ka)
0
3.5
ka
5.5
9.1
9.6
10.6
12
13
14
15
Epoch III
Epoch II
Epoch I
P.P.
NYT
h3
h2
h1
g2
g1
f
e
d
c
b
a
4.20
4.28
4.55
4.92
5.25
5.86
8.59
10.46
11.23
11.86
12.3
14.3
14.9
continental to foreshore
foreshore
foreshore/ shoreface
marker level#3
shoreface/ offshore
marker level#2
emersion
foreshore/ shoreface
marker level#1
coastal lacustrine/ foreshore
foreshore/ shoreface
backshore
H10ab
H9ab
H8bc
H8ab
H7ab
H6bc
H6ab
H5ab
H4bc
H4ab
H2bc
H2ab
H10
H9
H8
H7
H6
H5
H4
H3
H2
H1
H0
S10
S9
S8
S7
S6
S5
S4
S3
S2
S1
S0
NYT
(a)
(b)
(c)
(d)
(e)
Paleoenvironments volcanic/continental
Anthropic
Paleosol/humified contact
Monte Nuovo (MN - 1538 CE)
Fossa Lupara (FOL - 4 ka)
Astroni (AST - 4.2 ka)
Averno-Solfatara (AVS - 4.28 ka)
Agnano-Monte Spina (AMS - 4.55 ka)
Monte Sant'Angelo-Paleoastroni2 (MSA-PA2 - 4.92-4.73 ka)
Cigliano (CIG - 5.25 ka)
Neapolitan Yellow Tuff (NYT - 15 ka)
marine/transitional
Pozzuoli unit (PU - 4.55-4.4 ka)
La Starza unit (STZ - 15-5.5 ka)
P. oceanica rizholites
pebbles and cobbles
sands
silts and clays
lacustrine levels
unconformity
lithic/scoria clast levels and lens
pumice clast levels and lens
channel
fossils
Roman age material

Figure 3.6. (a) Chronostratigraphic log of the post-NYT volcanism. (b) La Starza stratigraphic intervals (modified after Isaia et al., 2019), (c) Seistec seismic type section with also indicated sub-horizons, (d) GeoB08 seismic type section. (e) Seismic sequences and corresponding color code adopted in the figures.

Based on the seismic stratigraphic analysis, we interpret the first intracaldera sedimentary unit (S0) above the NYT as a result of reworking of NYT volcaniclastics, the deposition of marine and volcaniclastic sediments, corresponding to tephras likely generated during the period of the early Epoch 1 (14.9-14.3 ka), when explosive eruptions mainly resulted in the building of monogenetic tuff edifices, such as Mofete, Gauro, Bellavista, and La Pietra (Figs. 3.1a; 3.2, 3.3, 3.6a, b, d). The Unit S0 becomes significantly thicker landward and shows some distinct reflectors corresponding to the La Pietra tuff cone (Fig. 3.2).

Likewise, in GeoB08 images, unit S1 is defined by the repeated alternation of transparent and reflective layers, suggesting a recurrent tephra input into the basin. We associate the reflective horizons of this unit with volcanic products generated mainly in the central northern sector of the caldera (Bevilacqua et al., 2015), such as La Pigna, Archiaverno, and Minopoli (14.3-12.3 ka; Smith et al., 2011). Because this unit shows no significant lateral thickness variations, in this time frame, the Pozzuoli Gulf behaved as a relatively more distal sedimentary sink, where volcaniclastic inputs dominantly filled the accommodation space created by the sea-level rise and previous NYT fault downthrowing. The highly reflective subunit S2a correlates with the basal interval a of the La Starza succession, with a constant thickness of ~8 m. We suggest that the stronger reflectors in the central upper part of the S2a subunit (Figs. 3.5a-c) correlate to Soccavo 1 tephra and the high magnitude eruption of Agnano-Pomici Principali (PP; 1 km^3 DRE) that occurred at 12.1 ka, in the central part of the caldera (Fig. 3.6; Di Vito et al., 1999; Smith et al., 2011; Bevilacqua et al., 2015). At this stage, the succession nowadays exposed at La Starza was formed in a coastal-marine transitional environment (Isaia et al., 2019), suggesting a balance between the volcaniclastic input and sea-level rise. As for the underlying unit S1, lateral thickness variations are not evident (Figs. 3.5a-c), possibly highlighting the absence and/or very low rates of ground deformation, both uplift or subsidence.

Weakly reflective subunits S2b and S2c display a landward (northward) increase in thickness and are correlated to the La Starza interval b, where a few intercalated tephra layers occur within the foreshore to shoreface marine sediments. This feature indicates the general subsidence of the central sector fed by mainly marine sediments and, to a lesser extent by tephra

deriving from minor eruptions in the northern sector, unable to balance the contemporaneous sea-level rise.

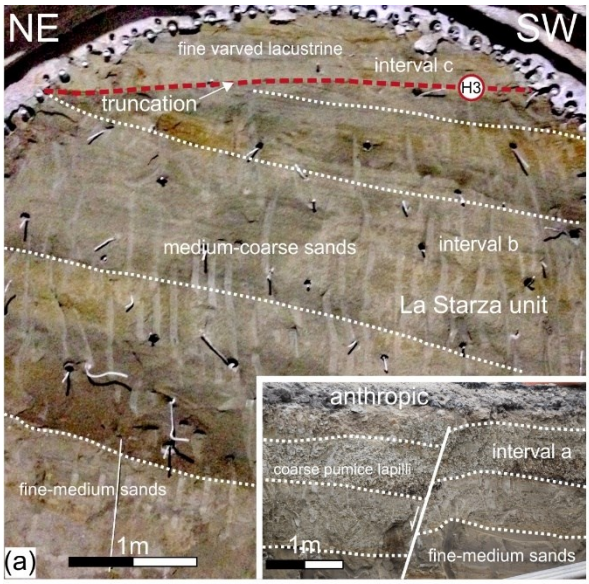
NE
SW
fine varved lacustrine
interval c
H3
truncation
medium-coarse sands
interval b
La Starza unit
fine-medium sands
1m
(a)
anthropic
interval a
coarse pumice lapilli
1m
fine-medium sands

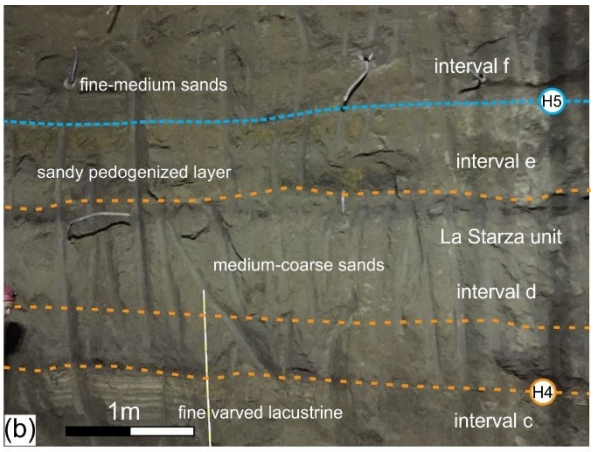
fine-medium sands
interval f
H5
sandy pedogenized layer
interval e
La Starza unit
medium-coarse sands
interval d
H4
1m
fine varved lacustrine
interval c
(b)

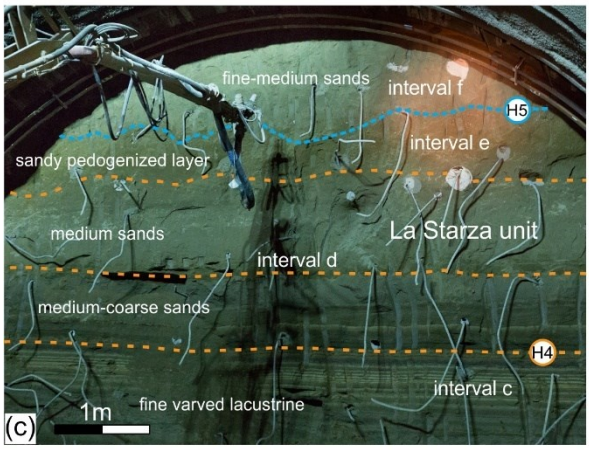
fine-medium sands
interval f
H5
interval e
sandy pedogenized layer
La Starza unit
medium sands
interval d
medium-coarse sands
H4
interval c
1m
fine varved lacustrine
(c)

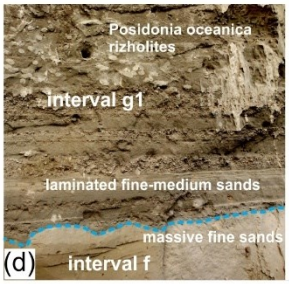
Posidonia oceanica
rizholites
interval g1
laminated fine-medium sands
massive fine sands
interval f
(d)

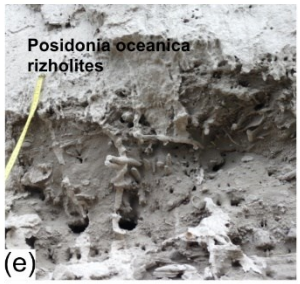
Posidonia oceanica
rizholites
(e)

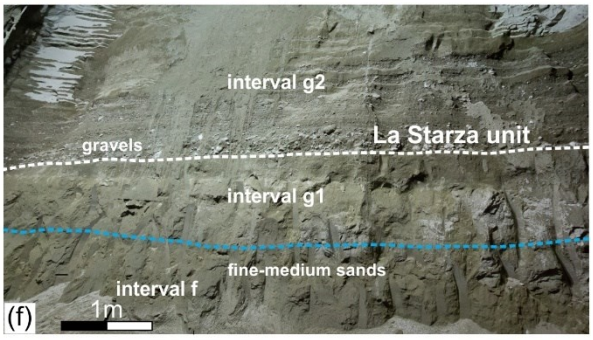
interval g2
La Starza unit
gravels
interval g1
fine-medium sands
interval f
1m
(f)

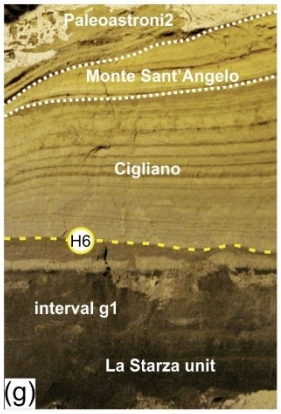
Paleoastroni2
Monte Sant'Angelo
Cigliano
H6
interval g1
La Starza unit
(g)


Astroni
Averno-Solfatara
paleosol
Agnano-Monte Spina
Paleoastroni2
Monte Sant'Angelo
Cigliano
H6
La Starza unit
(h)

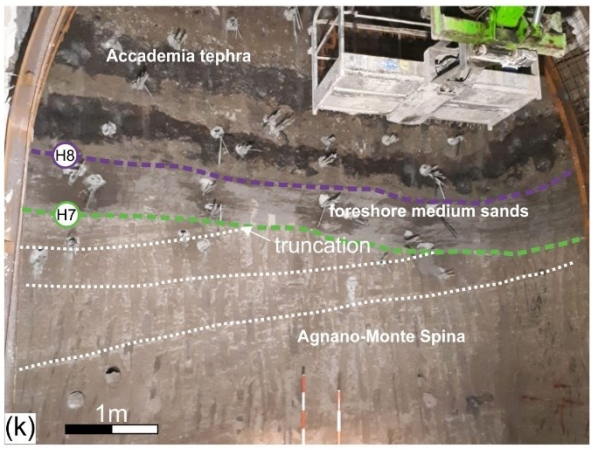
Accademia tephra
H8
H7
foreshore medium sands
truncation
Agnano-Monte Spina
1m
(k)

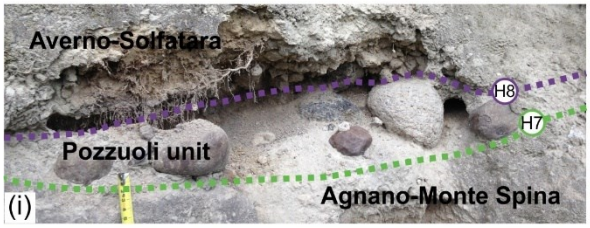
Averno-Solfatara
H8
H7
Pozzuoli unit
Agnano-Monte Spina
(i)

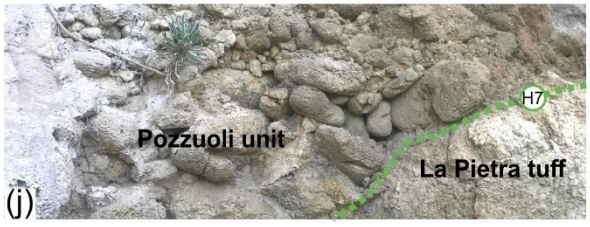
H7
Pozzuoli unit
La Pietra tuff
(j)


Gauro tuff cone
Fossa Lupara
Monte Nuovo
Astroni
Averno/Solfatara
Agnano-Monte Spina
Agnano-Monte Spina
Paleoastroni2
Monte Sant'Angelo
Cigliano
(l)

Figure 3.7. Excavation front within the La Starza unit, with angular unconformity H3 between units S2 (intervals a-b) and S3 (interval c), inset shows outcrop picture of interval a. (b) Starza interval c-d; (c) interval d, e, f at La Starza tunnel; (d-e) Detail of interval g1 at La Starza outcrops and (f) at the tunnel excavation front. (g) Epoch 3a pyroclastic deposits in contact with La Starza unit; (h) Epoch 3a tephra overlying La Starza Unit g1 and topped by a paleosol separating it from Epoch 3b tephra. (i-j) Chaotic and coarse transitional deposits located at 30 and 20 m a.s.l. at La Starza and La Pietra, respectively; (k) Abrasion surface (H8) observed on-land truncating AMS tephra and covered by marine sands and Accademia tephra; (l) Epoch 3 tephra exposed on top of La Starza terrace.

The overlying H3 surface is a paraconformity in the basin but evolves to an angular unconformity moving landward, truncating older reflectors (Fig. 3.5a-c). This surface correlates to the lowermost and well-developed angular unconformity visible on-land located at the base of interval c, which truncates the underlying marine sediments (Fig. 3.7a), whose top is dated at 10.46 ka (Isaia et al., 2019 and reference therein). This unconformity and the overlying lacustrine sediments indicate shallower sedimentary conditions compared to the underlying strata. This feature highlights the first clear evidence of ground uplift, likely related to doming. Consequently, we suggest that the onset of the inner caldera doming and the shallowing of the central sector, highlighted by the occurrence of lacustrine sediments at La Starza, occurred between 10.46 and 9.6 ka (interval c, Isaia et al., 2019, Figs. 3.6, 3.7a-c). It is not trivial to disclose whether this uplift phase lasted at least until 9.6 ka, or if the uplift pulse was shorter in time but large enough to preserve lacustrine conditions in the central sector despite the rapid sea level in this time interval (see Figure 3.9a for the sea level reference curve).

On the other hand, the occurrence of seismites in the same lacustrine beds suggests coeval seismo-tectonic activity, typical of doming-related unrests, as reported by Vitale et al. (2019). Furthermore, the presence of gravity flows in subunit S3 strengthens the hypothesis of protracted uplift. In this scenario, unit S3 is thus interpreted as the offshore counterpart of the lacustrine and coastal sediments of interval c, broadly corresponding to the short-lived absence of volcanic activity between Epochs 1 and 2. In some continental locations, this brief hiatus allowed the formation of the paleosol A (Di Vito et al., 1999).

The overlying S4 corresponds to interval d, characterized by foreshore marine sand intercalated with tephra beds related to Epoch 2 volcanic activity. In particular, the highly reflective reflectors alternating with sub-transparent seismic facies and westward increasing thickness suggest the correlation of unit S4a with the eruptive products of Baia-Fondi di Baia on the western side of the bay (Pistolesi et al., 2017). The volcaniclastic contribution from younger phreatomagmatic eruptions of Epoch 2, such as Costa San Domenico and Pigna San Nicola, might be responsible for the facies characteristics of subunits b and c. Moreover, the

S4c highly reflective facies and its stacking pattern are compatible with the culmination of uplift of Epoch 2, which resulted in increased coarser sedimentary input likely due to remobilization of volcaniclastic products testified by the emersion of the La Starza unit (interval e). This uplift has occurred around 9.1 ka (Isaia et al., 2019) and is constrained to at least before 8.59 ka, the age of a Cardium fossil shell at La Starza cliff located immediately above the interval e (Giudicepietro, 1993; Isaia et al., 2019).

The full transparent facies of thicker unit S5a suggests a close correlation with the interval f, characterized by fine-medium massive sands, which marks the reestablishment of progressively distal and deeper conditions between 9.1-5.86 ka, linked to a new submersion of La Starza. Unit S5b is correlated to interval g1, marked by a recurrent alternation of layers rich in Posidonia rizholiths and medium-size marine sands interpreted as having formed in a shoreface and offshore environment, respectively, within an overall shallowing pattern. In seismic images, this feature is reflected in alternating high amplitude and transparent reflectors (cf. Figs. 3.5d, 3.7d-f). This setting testifies a renewed doming with a cyclic shallowing of the paleoenvironment suggesting discontinuous increments of ground uplift, possibly linked to volcano-tectonic crises that predate the eruptive activity of Epoch 3 (Fig. 3.7b).

The strong amplitude reflectors within overlying S6a are interpreted as tephra layers associated with the eruptions that occurred at the onset of Epoch 3a (Averno 1, Agnano 1-2; Smith et al., 2011, Isaia et al., 2019) and included in interval g2. We suggest that the following subunits S6b and S6c, similarly characterized by very strong-amplitude reflectors, include pyroclastic/volcaniclastic products of the main eruptive units of Epoch 3a (from base to top: Cigliano, 5.25 ka; Agnano 3, 5.0 ka; Monte Sant'Angelo, 4.92 ka; PaleoAstroni 2, 4.73 ka; and Agnano-Monte Spina, 4.55 ka) (Figs. 3.5e, 3.6, 3.7g, h), which were deposited in a continental environment in the central sector of the caldera (Isaia et al., 2019; Vitale et al., 2019). In particular, subunit S6c is manifestly thicker, in line with the high magnitude of the AMS Plinian eruption (1.2 km^3 DRE; De Vita et al., 1999).

The overlying unit S7, which includes a well-visible transparent layer, represents a stratigraphic marker within the offshore area. S7 attains a significantly larger thickness within the collar zone depocenters than in the dome area and on-land. This marker correlates to shallow marine to coastal marine deposits of the Pozzuoli unit (interval h2), which testifies to a short-lived phase of ground subsidence that followed the Agnano-Monte Spina Plinian eruption and the associated caldera collapse of the Agnano Plain (Isaia et al., 2009). This subsidence allowed the coastline to shift northward up to the San Vito Plain (Sbrana et al., 2015) (Fig. 3.1a) and the

deposition of coastal sediments that now are exposed, uplifted, 20 m a.s.l. on La Pietra tuff (Isaia et al., 2009) (Fig. 3.7i, j). In the Bagnoli offshore, unit S7 displays chaotic and convoluted/slumped reflectors (Fig. 3.5f). This feature may be associated with gravity flows and landslides triggered by intense volcano- and seismotectonic activity, resulting in faulting, fracturing, and paleoliquefaction phenomena (Vitale et al., 2019).

A large (over 22 km^2) abrasion surface developed on the shelf above S7 and older sequences (map inset in Figure 5) and has been correlated to a truncation contact exposed on-land (Fig. 3.7k) that represents the proximal segment of H8 due to later subaerial exposure. It is worth noting that this large and preserved abrasion surface almost entirely wiped away the abrasion surface (H6) associated with the previous uplift phase, which is only preserved on the eastern part of the shelf (Fig. 3.5h), with its corresponding infralittoral prograding wedge (Hernandez-Molina et al., 2000).

Seismic facies of overlying unit S8, including strongly reflective layers, are interpreted as marine sediments embedding large amounts of eruptive products of Epoch 3b (Figs. 3.5i, 3.6c), emplaced during the Averno 2 - Solfatara (4.28 ka), Astroni (4.2 ka), Capo Miseno, and Nisida eruptions (3.9-3.7 ka; Figs. 3.5j, k, 3.7g, h, l). Pyroclastic products associated with volcanism younger than Solfatara eruption overlie abrasion surface H8 (Fig. 3.7k). In contrast, the sub-transparent facies of unit S9, calibrated by shallow coring by Sacchi et al. (2014), correlate to the centuries-long quiescence period between Epoch 3b and the Monte Nuovo eruption (1538 CE). Finally, the uppermost unit S10 reaches a maximum thickness of ~1.5m in the Epitaffio valley (Fig. 3.1a), but elsewhere it is only represented by a thin layer, correlated to Monte Nuovo tephra (Figs. 3.5k, 3.7l).

3.5.2 Seismic attributes and grain size comparison

To strengthen the proposed correlation, we compared the RMS (Root Mean Square) amplitude attribute of seismic units S2 to S5 to the grain size data of correlative sediments at La Starza provided by Isaia et al. (2019). The RMS amplitude attribute analysis is the post-stack evaluation of signal strength regardless of its polarity, and its visualization helps to identify the acoustic impedance contrast. In general, several factors such as cementation, change in bed thickness, porosity, and alteration might control the seismic amplitude. However, considering the relatively more undisturbed depositional environment of the caldera collar and

the characteristics of marine sediments at La Starza, generally consisting of loose sediments, we assume that the grain size and the sorting play the primary control.

Overall, a good fit exists between the RMS amplitude and sorting and grain size for transparent and reflective facies (Fig. 3.8). The two highest amplitude horizons correspond to poorly sorted, generally medium to coarse layers, whereas the transparent facies correspond to well-sorted, fine sands.

From bottom to top, the marine sediments of intervals b and c are constituted by fine to medium sand separated by angular unconformity H3, corresponding to a distinct emergence phase on-land (Fig. 3.8a, b). Sediments of interval b show a coarsening upward trend associated with a sorting decrease in correspondence of channelized beds, which peaks at H3 (Fig. 3.8 c-e). By contrast, interval c and overlying marine sands d show a fining upward trend and a good sorting until interval e, corresponding to a pedogenised horizon (paleosol B, marker level #2, Fig. 3.8a). The development of paleosol B indicates a subaerial exposure. It is represented in seismic images by the strongly reflective subunit S4c with a high RMS value, which is interpreted as the result of the uplift phase of the central sector and consequent sediment erosion and transport of poorly sorted material offshore.

The well-sorted fine sands (interval f at La Starza) corresponds to the transparent, low RMS amplitude of subunit S5a. The fine sands pass upward to less well-sorted and progressively coarser sands (interval g1), deposited in foreshore settings and topped by disconformity H5ab. Above this surface, coarse volcaniclastic deposits associated with a peak of poor sorting occur (Fig. 3.8d). The coarsening in interval g1 is reflected in seismic images by high amplitude reflections in subunit S5b.

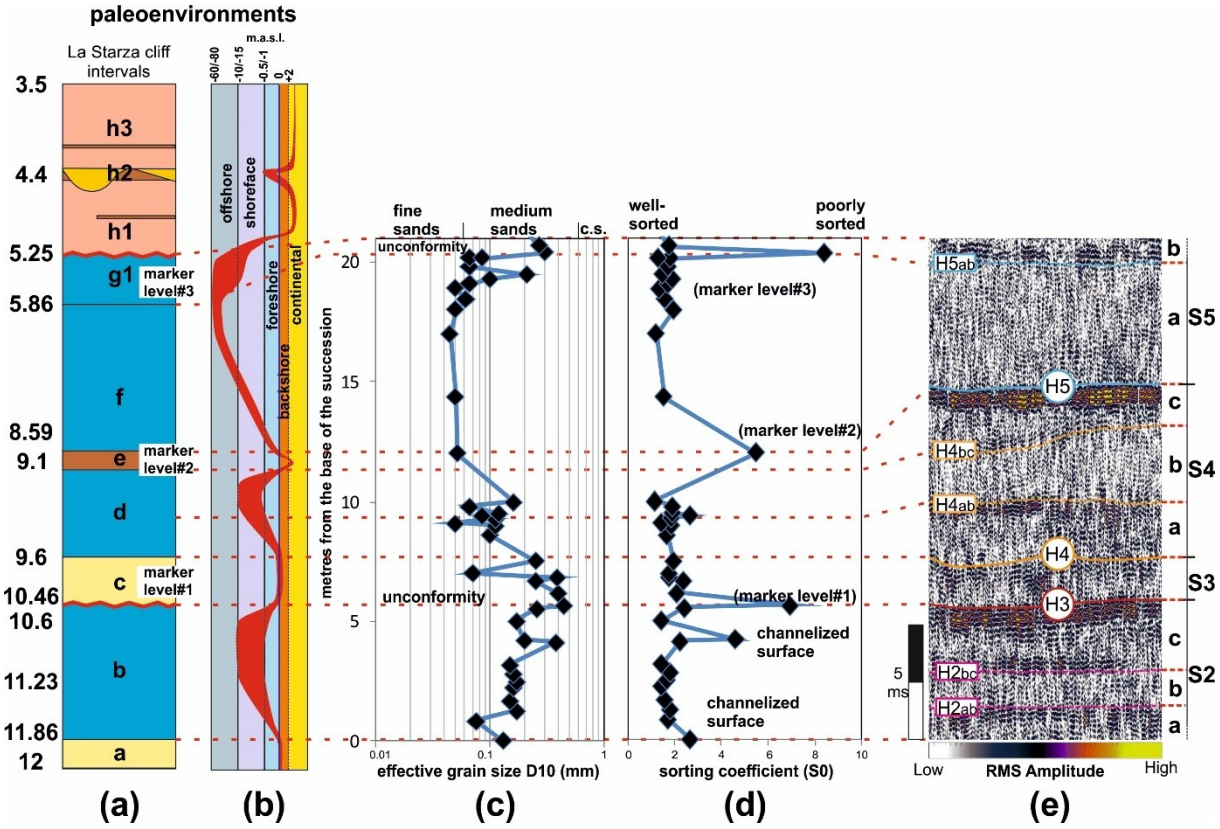

Figure 3.8. (a) Schematic stratigraphic section of La Starza cliff with available age determination and sedimentary intervals (modified after Isaia et al., 2019). (b) Adapted paleoenvironments reconstruction (modified after Isaia et al., 2019). (c) Effective grain size distribution and (d) sorting coefficient. (e) RMS Amplitude seismic attribute of the Seistec type section located in the collar zone. Red dotted lines highlight the proposed correlations.

3.5.3 Sedimentation rates

We estimated the time evolution of sedimentation rates in the CFc offshore sector based on the proposed stratigraphic reconstruction. This evaluation has to be considered a first approximation of the accumulation rate and does not include other factors such as sediment compaction. Subsequently, we compared our results with the sea-level change curve calculated by Lambeck et al. (2011) to qualitatively evaluate the contribution to sedimentation of Sea Level Rise (SLR; Fig. 3.9a) and with the erupted magma rates (Fig. 3.9c, Bevilacqua et al., 2016). A rapid SLR has occurred between ~15-7 ka but with significant variations in SLR rates, with peaks in velocity close to 18 mm/y (Fig. 3.9a; Lambeck et al., 2011). On the contrary, during the last ~7 ka, the sea level rose at a constantly decreasing rate (Fig. 3.9a).

We calculated sedimentation rates for the offshore (mm/yr; green dashed line Fig. 3.9b) and La Starza sections where data are available (blue dashed line in Figure 3.9b). Age uncertainty of data points representing individual rate estimates is indicated by horizontal error bars (details in the supplementary material). In addition, the curve of sedimentation rates for

the last 15 kyr was drawn, joining the points with a curve instead of straight lines to enhance the interpretation. Data points are placed at the end of the reference interval.

Following the peak of the NYT eruption (and early Epoch 1 tuff eruptions), the curve shows a millennial-scale decreasing trend inverted at ~12 ka. This peak (~15 mm/y) is related to the deposition of PP tephra, emplaced during the first large eruption following the NYT eruption (Fig. 3.9b, c), probably with the contribution of additional eruptions (e.g., the Soccavo 1 eruption).

After that, a sudden drop in both erupted volume and sedimentation rate is observed, with sedimentation rates falling to ~5 mm/y, a value broadly maintained until the start of Epoch 2 at 9.6 ka (Fig. 3.9b, c). The gentle increase observed at around 10.5 ka, and the peaks at 9.1 ka both on-land and offshore are interpreted as related to post-PP doming and Epoch 2 volcanism/doming contributions. The peaks in sedimentation rates offshore occur at ~9.4 ka and largely (~26 mm/y) at ~9.1 ka (Fig. 3.9b). Although minor volumes have been erupted in Epoch 2 compared to the ~12 ka peak, these peaks reasonably reflect the occurrence of eruptions more proximal to the gulf, such as Baia-Fondi di Baia, Costa San Domenico, and Pigna San Nicola, and also to an excess of sediment supply related to the doming that culminated at the end of Epoch 2 (Fig. 3.9b, c). In this time frame, a possible contribution of SLR-related erosion (Schwartz, 1967) is not excluded because of the ~18mm/y peak in SLR (Fig. 3.9a). Instead, a low (1.4 mm/y) sedimentation rate is estimated at La Starza for the same time interval when this sector emerged and a paleosol developed (Fig. 3.9b). This discrepancy is probably related to the erosion of coastal areas and the excess of sediment input in the offshore sector. On the other hand, a good correspondence exists between the rates of interval f (La Starza) and S5a (9.1-5.86 ka), with overlapping values around 1.6 mm/y (Fig. 3.9b). With the Epoch 2 uplift phase, the gulf became a relatively more proximal basin, but the ensuing long quiescence, joint to the subsidence, and slowing SLR rates led to lower sedimentation rates.

After a 2.7 ka-long quiescence, volcanic activity resumed with the onset of Epoch 3, resulting in increased sediment production (Fig. 3.9b, c), with a constantly declining SLR rate (Fig. 3.9a). Sedimentation rates, offshore and on-land, and erupted volume rates follow an increasing trend peaking at the end of Epoch 3a when the Agnano-Monte Spina eruption occurred (Fig. 3.9b). This event is the largest-volume eruption in the last 10 ka and is associated with a sedimentation peak at near 30 mm/y in the caldera collar. The following rate point is related to the sedimentation during the short-lived volcanic quiescence and rapid subsidence-uplift related to the Pozzuoli Unit. The surplus of sediment production (Fig. 3.9b) is related to

the intense ground deformation (Vitale et al., 2019), resulting in the deposition of material in the caldera depocenters (Figs. 3.4, 3.5f). The following sedimentation peak (~25 mm/y) couples with Epoch 3b volcanism at ~4.3 ka, and specifically, it may be associated with products of the Averno-Solfatara and Astroni eruptive sequence (Fig. 3.9c).

The lack of volcanic input after Epoch 3b is mirrored in a minimal sedimentation rate (~1.5 mm/y), which is only interrupted by the peak in correspondence of the Monte Nuovo eruption. We remark that the calculated sedimentary rate for unit S9, ~1.5 mm/y is comparable with the one calculated for other quiescence phases (i.e., interval f and subunit S5a), as shown in Figure 3.9b. In summary, an excellent agreement exists between erupted volumes, sedimentation rates, and resulting collar thickness, highlighting the coupling between sedimentation and volcanic activity (Fig. 3.9b-d).

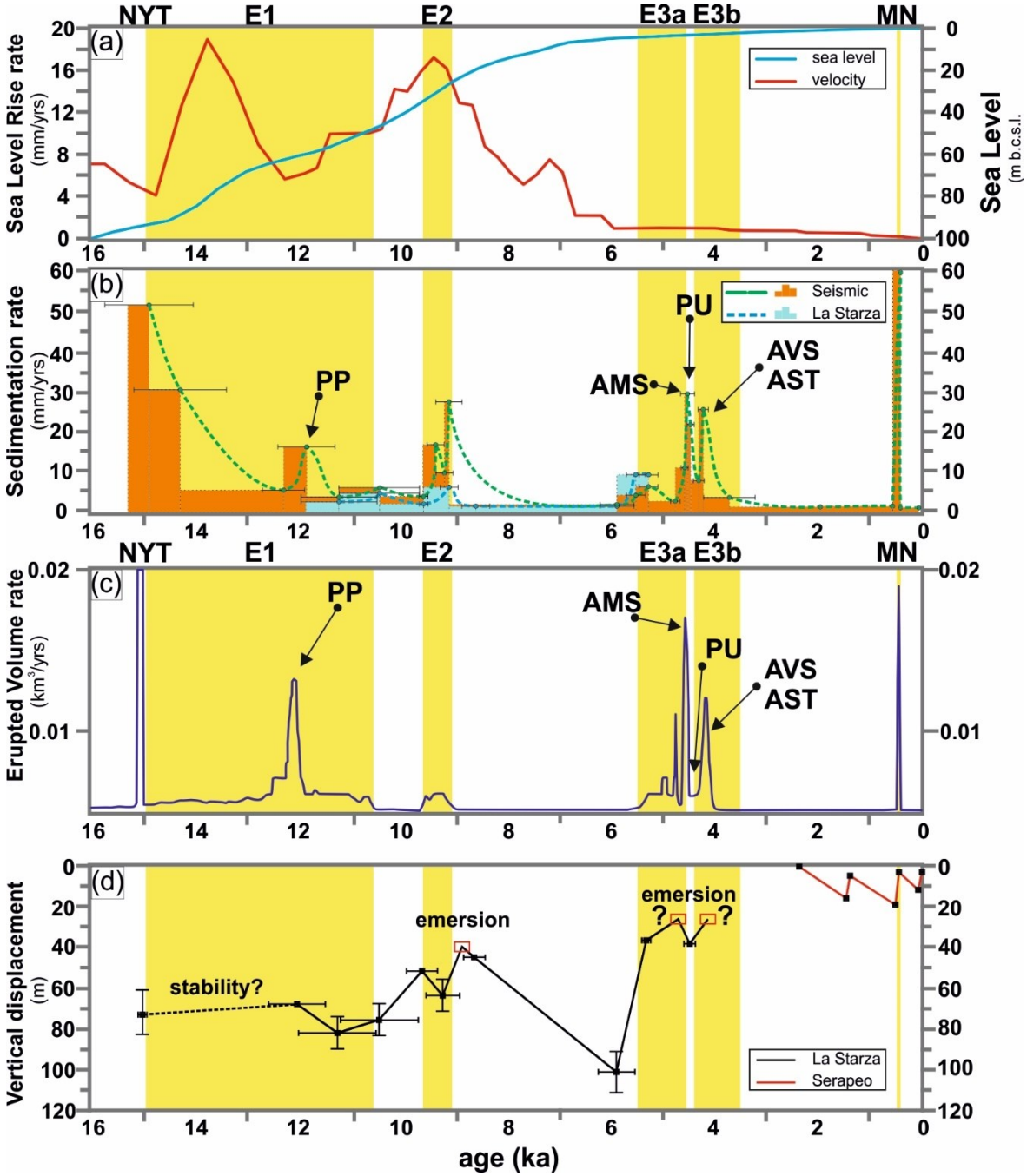

Figure 3.9. (a) Glacio-isostatic sea-level curve for the last 16 kyr, and its rate variations calculated after Lambeck et al. (2011). (b) Sedimentation rates calculated in this work from both seismic lines and La Starza section, error bars indicate age uncertainty. (c) Magma erupted volumes per year (after Bevilacqua et al., 2016). (d) Vertical displacement reconstruction for the on-land central sector of the caldera (after Isaia et al., 2019). NYT: Neapolitan Yellow Tuff. PP: Pomici Principali. AMS: Agnano-Monte Spina. PU: Pozzuoli Unit. AVS: Averno2-Solfatara. AST: Astroni. MN: Monte Nuovo.

3.5.4 Improving the stratigraphic position of coastal eruptions

The presented study is an up to date stratigraphic reconstruction which may allow us to improve the stratigraphic position of some eruptions along the coastline, which mainly produced tuff cones and rings such as Nisida, Capo Miseno, Nisida bank, Porto Miseno, and

Bacoli (Insinga et al., 2006; Di Renzo et al., 2011, Fedele et al., 2011; Smith et al., 2011). This feature has been debated in the literature, and analysis of seismic reflection profiles recently allowed Steinmann et al. (2018) better to define the relative chronology attribution of several vents and also to provide an updated erupted volume estimation that in some cases is significantly increased compared to previous estimations (Bevilacqua et al., 2015; 2016). Here, we present a further improvement to constrain the stratigraphic position of volcanic events using our fine-tuned offshore-on-land stratigraphic framework.

On the eastern side of the gulf, along the Bagnoli valley, we suggest that the anticlinal structure (Fig. 3.4), located offshore of Bagnoli, represents a locally deformed zone related to a small volume intrusion, in agreement with Steinmann et al. (2016). A bell-like shape is well visible on ~E-W seismic profiles (Figs. 3.4, 3.10c-e). On the other end, the deformation can also be observed on ~N-S lines (Fig. 3.10f-g), including the GeoB08-035 (Fig. 3.10g), which turns into a ~E-W direction in its northern end (Fig. 3.10a), allowing us to see the last clear evidence of deformation. With this in mind, considering the at least 800 m long NNE-SSW alignment of the crests and ~600 m width, as visible in the time-structure map (Fig. 3.10a), we interpret this structure as a forced fold *sensu* Jackson et al. (2013), related to a shallow magmatic intrusion (Fig 3.10b). The maximum amount of displacement is ~12-15 m (using 1650 m/s average velocity; Fig. 3.10c-g). It is interesting to note the occurrence of fluid uprise on the crest of the forced fold (Fig. 3.10c, f). Such as already suggested by some authors (Steinmann et al., 2016; Natale et al., 2018), the depth of this intrusion might be below the data penetration limit (300-350 ms). Approximating the volume underlying the forced fold as a triaxial hemi-ellipsoid, the minimum displaced volume is ~3 Mm^3. Moreover, the downlap terminations (Fig. 3.5f) of the S7 unit constrain the intrusion timing at around 4.4-4.3 ka, corresponding to the beginning of Epoch 3b similarly to other lava domes (Accademia dome 4.3 ka, Olibano dome 4.3 ka, Solfatara dome 4.4-4.28 ka) emplaced close to the coastline (Smith et al., 2011; Isaia et al., 2015; Bevilacqua et al., 2016; Fig. 3.1a). In support of this comparison, the estimated volume is in the same order of magnitude as these exposed domes (Bevilacqua et al., 2016). Another hypothesis considers such structure as a fold associated with a reverse fault. However, the vicinity of other lava domes of the same age, and the lack of evidence of such faults in the whole seismic dataset, lead us to consider the first interpretation as the most likely.

The two tuff cones of Nisida and Banco di Nisida similarly occur on the eastern sector within the caldera ring fault zone (Fig. 3.1a). The Island of Nisida is the subaerial emergence of a larger tuff cone complex which was already included by Steinmann et al. (2018) in the

volcanic Epoch 3 in agreement with the available literature age determinations (i.a. Di Renzo et al., 2011; 3.98 ± 0.53 ka for Nisida Island). The arrangement of the different volcanic mounds constituting the underwater complex suggests that volcanic activity occurred broadly aligned N-S, with the northward migration of the eruptive activity (Fig. 3.10h). Furthermore, our reconstruction allows us to define more precisely the stratigraphic position of the Nisida eruption within Epoch 3b since Nisida tephra is above S7 unit (Pozzuoli Unit, 4.4 ka) and within the upper part of unit S8, covered by the top of subunit S8c (Figs. 3.4a, 3.5j), resulting in a supposed age of 3.7 ka.

Banco di Nisida is a large tuff cone emplaced above the erosive head of the Canyon Dhorn, which drained sediments up to unit S2. Sediment drainage was halted from the volcanic bank eruption (Fig. 3.10h). The stratigraphic attribution of the cone to the upper part of unit S2 allowed to constrain its age to after the PP eruption (12 ka) and before unit S3 (10.5 ka), collocating it in the late-stage Epoch 1 (Fig. 3.10h) (e. g. Di Vito et al., 1999).

The western coast of the gulf is scattered with remnants of tuff cones and tuff rings. The stratigraphic position of these eruptions is non-trivial due to the lack of clear stratigraphic ties and the distance from the inner caldera basin. In correspondence with Porto Miseno, unit S2 has an anomalous thickness increase that we associate to the presence of the submerged flanks of the Bacoli tuff cone and Porto Miseno tuff ring, separated by an unconformable contact (Fig. 3.10i). This local increase in thickness is also observed by Steinmann et al. (2018) for their unit M2, which comprises our unit S2. The eruptions that built these two monogenetic edifices occurred short after PP (12 ka), placing these lithosomes at the end of Epoch 1, as hypothesized by Smith et al. (2011).

On the same line, we observe the main architectural elements (Bischoff et al., 2020) of the Capo Miseno tuff cone (Fig. 3.10i), which is, however, partially reworked moving toward SE. This eruption probably occurred in the late stage of Epoch 3b, almost at the same time as Nisida to the eastern part of the bay. The mutual relationships between these two lithosomes are not easy to disclose, but seismic horizons correlation suggests Nisida tephra be slightly younger than Capo Miseno. However, given the vertical resolution of the seismic dataset, the contemporaneity cannot be ruled out, as is a common feature in several caldera settings (e.g., Blong, 1994; Pistolesi et al., 2016).

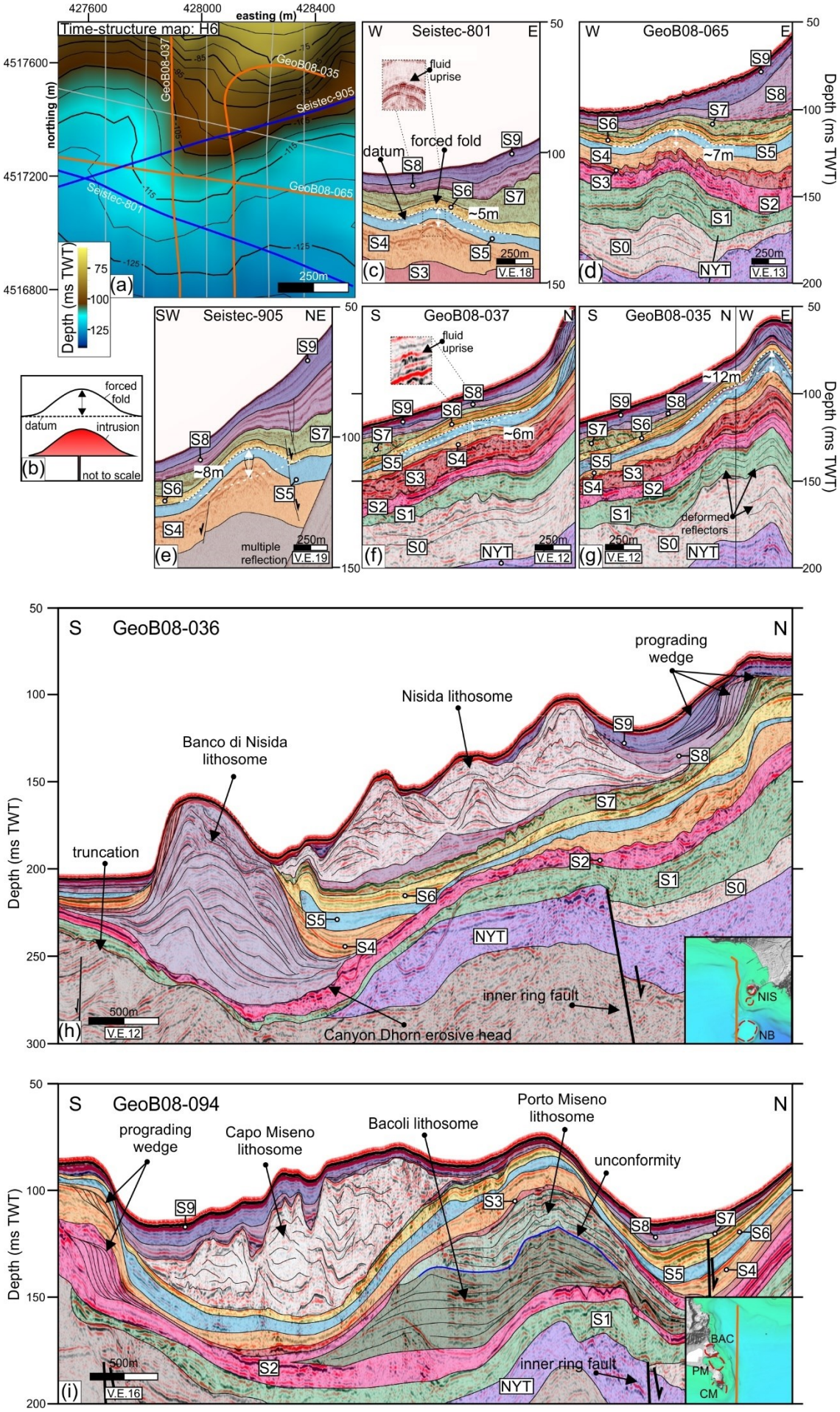
Time-structure map: H6
easting (m)
northing (m)
GeoB08-037
GeoB08-035
Seistec-905
GeoB08-065
Seistec-801
Depth (ms TWT)
(a)
(b)
forced fold
datum
intrusion
not to scale
W Seistec-801 E
fluid uprise
forced fold
datum
~5m
(c)
W GeoB08-065 E
~7m
(d)
SW Seistec-905 NE
~8m
multiple reflection
(e)
S GeoB08-037 N
fluid uprise
~6m
(f)
S GeoB08-035 N W E
~12m
deformed reflectors
(g)
S GeoB08-036 N
prograding wedge
Nisida lithosome
Banco di Nisida lithosome
truncation
inner ring fault
Canyon Dhorn erosive head
NIS
NB
(h)
S GeoB08-094 N
prograding wedge
Capo Miseno lithosome
Bacoli lithosome
Porto Miseno lithosome
unconformity
inner ring fault
BAC
PM
CM
(i)
NYT
S0
S1
S2
S3
S4
S5
S6
S7
S8
S9
250m
500m
V.E.18
V.E.13
V.E.19
V.E.12
V.E.16

Figure 3.10. (a) Time-structure map of H6 horizon above the Bagnoli bulge. Thin grey lines indicate 2D seismic lines used to reconstruct the time-structure map. Survey map location in Fig.1a. (b) Sketch of an intrusion-related forced fold (modified after Jackson et al., 2013). (c-e) ~E-W line Seistec-801, GeoB08-065, Seistec-905 showing the geometry of the forced fold close across sections orthogonal to the fold axis. (f-g) Interpreted ~N-S line GeoB08-037 and GeoB08-035 pointing out the deformation parallel to the fold axis. (h) Interpreted N-S trending line GeoB08-036 running along the coast of Nisida. Several features are present, like erosive truncations, inner ring fault, the two tuff complexes, and their relationships with the stratigraphic frame. (i) Interpreted N-S line GeoB08-094 running along the western coast sharpen the stratigraphic relationships between Bacoli and Porto Miseno volcanoes of the Epoch 2 and Capo Miseno of Epoch 3b. NIS: Nisida. BN: Banco di Nisida. CM: Capo Miseno. PM: Porto Miseno. BAC: Bacoli.

3.5.5 Insights into caldera deformation in the last 15 kyr

The integration of the reconstructed on-land stratigraphy with the offshore seismic stratigraphic architecture provides insights into the relationships between ground deformation, sea-level rise, and sedimentary evolution. This paragraph qualitatively summarizes the ground deformation history in the last 15 kyr. With the occurrence of the first post-caldera uplift at 10.5 ka, the deformation broadly followed a cyclic pattern between uplift and subsidence phases, broadly centered near Pozzuoli, likewise today. This cyclicity, among other features, is recorded offshore by alternating regressive and transgressive stacking patterns, respectively. However, in the long term, the uplift prevails, as testified by exhumed marine sequences.

To better highlight the impact of the ground deformation on the depositional system, we used lateral thickness changes, reflector terminations, and geometry (convergence or divergence) as indicators of volcano-tectonic perturbations at the basin scale. Finally, we summarize the ground evolution in a stratigraphic sketch showing periods of quiescence, doming, or stability with a different color referenced to individual seismic units/subunits and corresponding La Starza intervals (Fig. 3.11a).

Because seismic units S0, S1, and S2a do not show significant lateral thickness variations, they form a pre-doming sequence (Fig. 3.11a). Thus, they are considered sea-level-controlled, aggrading sequences deposited without significant/detectable volcano-tectonic deformation. On the contrary, in younger seismic units (S2b to S10), the depositional system adapts to deformation, resulting in various stratal termination and depositional features, such as onlaps and angular unconformities, erosive truncations, and gravity flows (Fig. 3.11b).

Following the PP eruption (12 ka), the system records a subsidence localized on-land. The landward thickness increase of subunits S2b and S2c suggests a subsidence stage that deepened the central caldera sector, as much as 15-20 m, between ~11.9 and 10.5 ka when interval b formed (Figs. 3.8a, 3.11a, 3.11b). Evidence of marine ingression following the PP eruption is reported at different on-land locations, including La Starza, San Vito Plain, and

several drill holes and excavations (i.a. Di Vito et al., 1999; Sbrana et al., 2015; Isaia et al., 2019).

The subsidence of the caldera central sector started at ~10.5 ka, has been inverted by an uplift event, testified by the unconformity H3, which evolved to an abrasion surface at La Starza. This uplift event, amounting up to 30-35m, is also corroborated by the occurrence of gravity flows and a shift of the depocenters, with the overlying unit S3 displaying an increasing thickness from the dome toward the collar area (Figs. 3.2, 3.3, 3.5a, b, 3.11b).

Between 9.6-9.1 ka, marine sediments of interval d were deposited at La Starza above the lacustrine beds of sequence c (Fig. 3.6a), suggesting that the rate of SLR (Fig. 3.9a) exceeded previous ground uplift of S4a, corroborated by ~10m of subsidence (Fig. 3.9d, Isaia et al., 2019), while the transparent subunit S4b, with probably indicating a stasis in volcaniclastic input. The following strongly reflective S4c. is associated with the forced marine regression, concurrently with the emersion of La Starza unit at around ~9.1 ka and no later than 8.6 ka (Isaia et al., 2019). The emergence of La Starza was likely accompanied by the formation of an abrasion surface that isolated the cliff, with not less than 20-25m of uplift at La Starza (Figs. 3.9d, 3.11a).

Nonetheless, between ~9.1-5.9 ka, when the sea level rose from -30 m to -5 m (Fig. 3.9a), the sedimentary facies at La Starza suggests a significant paleobathymetric depth increase (down to 60/80 m b.s.l. according to Isaia et al., 2019; Fig. 3.8a, b, d). This sequence event at La Starza corresponds to the full transparent facies of subunit S5a, which highlights the lack of primary pyroclastic input (Fig. 3.8e). Thus, with the development of an uplifted dome, the Pozzuoli Gulf has become a more proximal basin than the pre-doming conditions and is rather constant in the last 6 kyr. Hence, in this timeframe, we use the position of the on-lap terminations (labeled from 1 to 6 in Figure 3.11b) as indicative of regressive and transgressive sedimentation in a context of negligible (5 meters) SLR (Fig. 3.9a), compared to the decametric (up to 100 m) deformation reconstructed at La Starza by Isaia et al. (2019) (Fig. 3.9d).

Horizons H5a and H5b are truncated in the shelf area (point 1 in Fig. 3.11b); however, the same marine unit is exposed on-land at La Starza (interval f, g1; Fig. 3.5d-h). On the other hand, unit S6 onlaps above its basal unconformity within the present slope (point 2, Fig. 3.11b) due to marine regression caused by ground uplift. The La Starza unit remained in subaerial conditions from 5.25 to 4.4 ka, following the uplift phase that continued during deposition of unit S6 (Epoch 3a), which further developed an abrasion surface preserved from subsequent erosion in the eastern sector (Fig. 3.5h). The onlap at the base of unit S7 (point 3, Fig. 3.11b)

moves over 500 m landward, accompanying the marine transgression of the Pozzuoli Unit (Isaia et al., 2009), which deposited marine-transitional sediments on-land (Fig. 3.7i, j).

A large abrasion surface is associated with the subsequent regression phase. This structure is a distinctive morphological feature in the Gulf, which eroded the previous units and was associated with a well-developed prograding wedge (Sacchi et al., 2014; Fig. 3.7k). High-angle faults, which imply negligible horizontal extension, do not dislocate the abrasion surface, thus are not to be linked to the ground resurgence but likely to volcano-tectonic collapses (e.g., Ruch et al., 2012). The occurrence of gravity flows also testifies the regressive trend flows within unit S8 (Fig. 3.11b). This regression is associated with the uplift phase that accompanies the Epoch 3b activity (Vitale et al., 2019), with the corresponding onlap at the base of subunit S8b (point 4, Fig. 3.11b) located 400 m seaward, recording the Epoch 3b uplift, which recovered and exceeded the previous short-lived subsidence (Isaia et al., 2009; 2019). The relative stability of point 5, and later landward shift of point 6, indicating a subsiding trend, characterize the end of Epoch 3b (Fig. 3.11a, b). In summary, the aggregate vertical displacement since 10.5 ka, considering subunit S2a as the last pre-doming unit, is at least 100m between the caldera collar and the shelf. Most of this aggregate value is due to Epoch 3 uplifts (Fig. 3.9d, Isaia et al., 2019).

Nonetheless, not all the ground deformation visible in the infill of the last 15 kyr is related to the resurgent dome or the ring faults. In fact, in addition to the Bagnoli intrusion, a significant ground deformation occurred in the area east of Porto Miseno (Figs. 3.1a, 3.3). The Punta Pennata structure is characterized by an asymmetric ~700m N-S length with a tapered southern end and a sub-vertical, fault-bound northern edge (Fig. 3.11c). Here a ~20 m localized uplift occurs in the footwall of the inner ring fault, for over 1500m along the E-W direction (Fig. 3.11d; bysmalith, *sensu* Cruden et al., 2017, and references therein). This structure was active independently from the corresponding ring fault, as the depth of reference horizons in the hanging wall along strike is not downthrown, as visible from the time-structure map of Figure 11d. Using our detailed stratigraphic framework, we track the temporal evolution of the deformation occurring here (Fig. 3.11c). A first intrusion occurred around 10.5 ka, with the sharp displacement from subunit S2a to unit S3. Erosive unconformity probably formed concurrently with the uplift during the 9.6-9.1 ka time interval as testified by growth strata in unit S3. Weak continuous activity and differential compaction might explain thickness variation within units S5a and S6, whereas on-lap terminations within S8 unit suggest a renewed activation during Epoch 3b (Fig. 3.11c). In general, volcanic activity in the last 15 ka has often

clustered along the ring faults (Bevilacqua et al., 2016) and is already being considered in the recent work about hazard assessment (Bevilacqua et al., 2017). Moreover, continental deep drill holes (e.g., AGIP-ENEL joint-venture) have also encountered peripheral sub-volcanic bodies at different depths (Rosi and Sbrana, 1983).

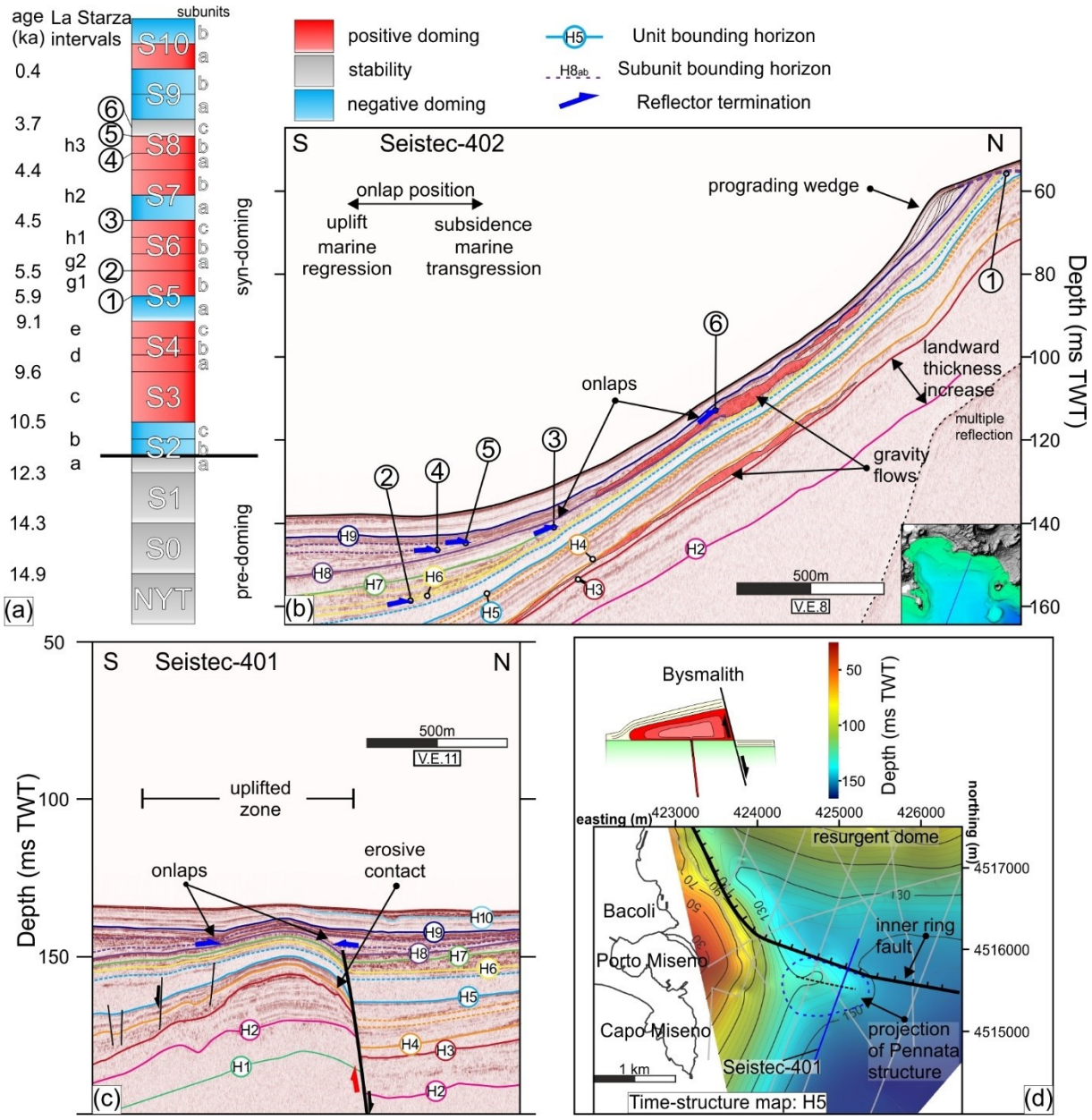

Figure 3.11. (a) Schematic stratigraphic section indicating the pre-doming and syn-doming sequences and relative age of reflector terminations. Letters to the right indicate subunits. Letters to the left indicate the corresponding La Starza intervals. (b) Onlaps stacking pattern on seismic line Seistec-402 showing seismo-stratigraphic indicators of ground deformation in the proximal caldera basin. (c) Zoomed section of Seistec-401 with indicated the Unit-bounding horizon, highlighting the uplifted Pennata structure. (d) Time-structure map of horizon H5, showing the extension of the Pennata structure and the relative position of the inner ring fault. The blue line is the location of the zoomed Seistec-401 section, and thin grey lines indicate the 2D seismic lines used to reconstruct the time-

structure map (contour interval of 10 ms, TWT). Top left corner: a sketch of bysmalith-like intrusion (modified after Cruden et al., 2017).

3.6 Conclusions

This paper provides an integrated on-land-offshore stratigraphy of the last 15 kyr for the Campi Flegrei caldera. The interpretation of 2D reflection seismic profiles allowed us to reconstruct a high-resolution stratigraphic framework of the offshore post-NYT caldera sedimentary record and better understand the complex interplay between the caldera floor deformation (uplift and subsidence), sea-level change, and volcanic activity. We correlated the main UBSUs with the marine-transitional sequence exposed on-land (La Starza unit). An excellent agreement exists between the seismic signature of the individual seismo-stratigraphic units and the sedimentological features of the exposed counterpart.

We identified eleven units above the NYT volcanic unit tested and fine-tuned by calculating the sedimentation rates for each unit/subunit and comparing them with the sedimentation rate of the corresponding intervals of La Starza sequence, calibrated with the sea-level rise. Results indicate that the sedimentation rate increases during the syn-eruptive volcaniclastic supply and uplift as more sediments are eroded from the dome apical region and transported seaward. This work highlights that the Campi Flegrei volcanic activity strongly controlled the sedimentation within the Pozzuoli Gulf, as supported by comparing sedimentation rates and estimations of erupted magma volumes. Furthermore, it is worth noting that the sedimentary system reacts and adapts to the deformation of the caldera floor, which systematically produces significant variations of the accommodation space and the localization of the depocenter over time.

Following the large-magnitude Pomici Principali eruption (12 ka), the sedimentation recorded the deformation affecting the caldera floor, resulting in the development of unconformities, lateral thickness variations, and variable onlap stacking patterns. Centuries-long subsidence was interrupted with the first intracaldera uplift at around 10.5 ka. The volcanic activity was generally coupled with the uplift, even though minor unrest phenomena not followed by eruptions cannot be excluded during the CF history of the last 15 kyr. The configuration of seismic stacking patterns and onlap terminations highlight the considerable uplift of the central part of the caldera that accompanied the Epoch 3 volcanism. This ground deformation stage was characterized by alternating uplift and subsidence phases, such as the transgressive event of the Pozzuoli Unit, following the large-magnitude Agnano-Monte Spina

eruption (4.55 ka). The subsequent volcanic activity has been accompanied by important ground uplift well-recorded by erosive surfaces. In addition, the seismic analysis allowed us to frame the relative stratigraphic position of coastal volcanic eruptions, such as Banco di Nisida, Nisida, Bacoli, Porto Miseno and Capo Miseno, and offshore intrusions, which contributes to refine an integrated post-caldera stratigraphic evolution.

This study underlines the benefit of a joint on-land-offshore approach to reconstruct the whole caldera stratigraphic framework and more comprehensively assess the long-term volcano-tectonic evolution, which is of the utmost importance in a highly inhabited, restless volcanic area such as Campi Flegrei caldera.

Chapter 4: Fault systems in the Campi Flegrei offshore sector: fault array geometry, nested caldera structure, dome resurgence and tectonic field influences

Abstract

We analyzed in detail the faults hosted in the marine and volcaniclastic succession in the offshore sector of the Campi Flegrei caldera (southern Italy). Through studying a dense seismic reflection dataset, we identified two main fault systems, including structures located along the caldera rims and at the top of the resurgent dome located in the center. The first system depicts an offshore nested caldera structure and comprises three main fault zones associated with concentric rims: the outer, medial, and inner ring fault zones. They formed during the largest eruption in Europe in the last 200 kyr, the Campanian Ignimbrite (CI) eruption (40 ka). The CI rims were reactivated during the Neapolitan Yellow Tuff eruption (15 ka), with the inner and medial fault zones accommodating most of the collapse and locally during inter-caldera periods. The second fault system occurs in the apical zone of the resurgent dome, which partially continues on-land, including high-angle normal and reverse structures related to a volcano-tectonic collapse that followed the Agnano-Monte Spina eruption (4.55 ka). The fault radial analysis suggests the existence of a volcano-centric strain field, which mainly controls fault orientations and highlights the role of old tectonic structures during volcano-tectonic collapses. However, a ~N-S-directed extensional tectonic field was present, becoming dominant during the inter-caldera periods. Finally, we provide a volcano-tectonic model of the Campi Flegrei caldera evolution in the last 40 kyr.

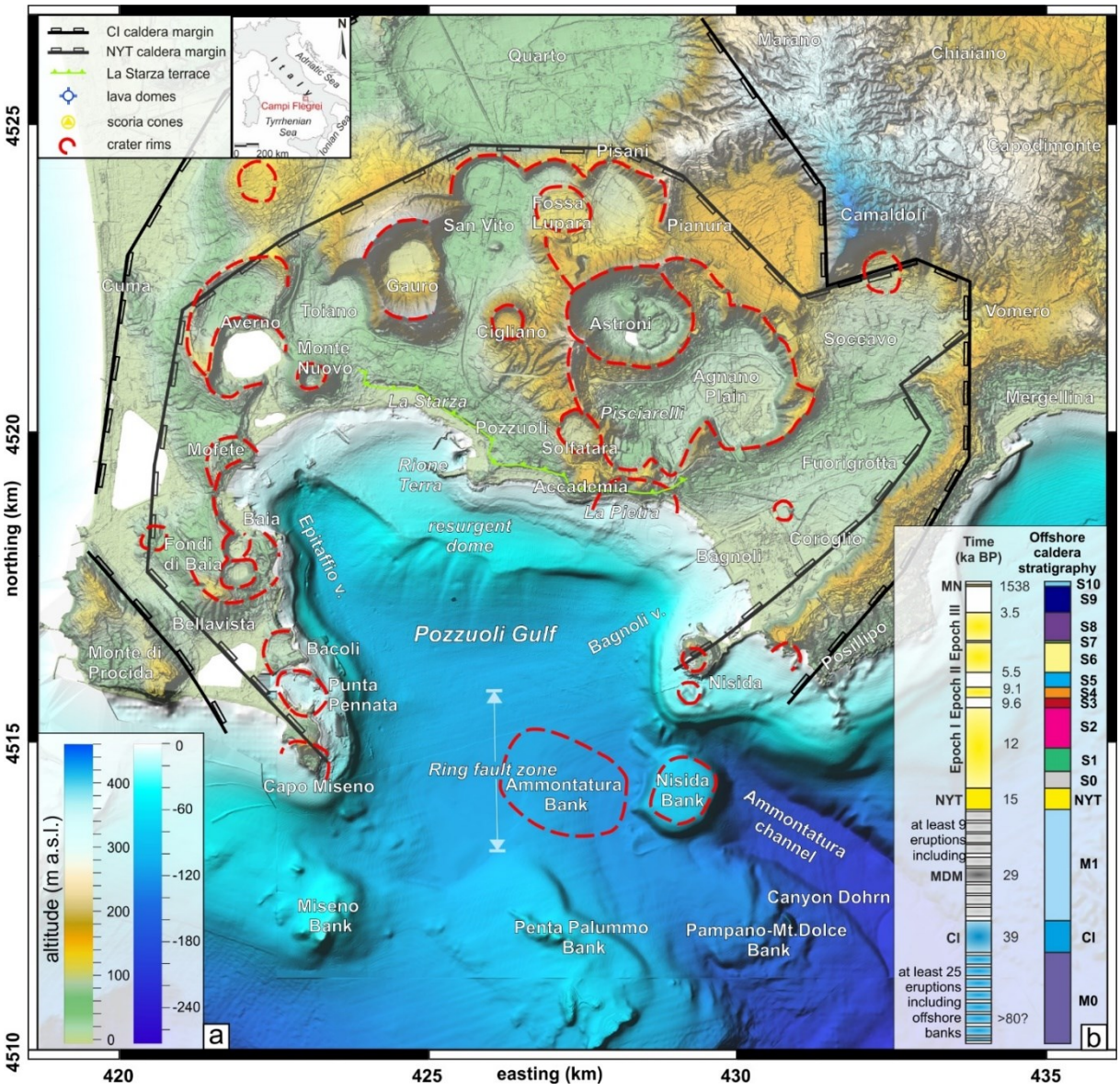

Figure 4.1. (a) Land-sea Digital Elevation Model of CFc, showing caldera and crater rims, scoria cone, and lava domes. (b) Simplified tephrostratigraphic logs of CF caldera in the last 80 kyr for the on-land and offshore (modified after Natale et al., 2021; Steinmann et al., 2016). Terrain shader rendered using Surfer 13 commercial software by Golden Software (**http://www.goldensoftware.com/products/surfer**).

4.1 Introduction

Calderas are morpho-structural depressions associated with large-volume volcanic eruptions (e.g., Cole et al., 2005; Branney and Acocella, 2015). Generally, the caldera collapse structures deeply control the long-lived volcanic activity, frequently hosting a complex hydrothermal/geothermal system. Thus, the comprehension of the structures, together with a detailed tephrostratigraphy, is relevant for hazard assessment of large volcanic areas and impacts the modern volcano monitoring techniques (Sparks et al., 2012). Among the many

examples of calderas worldwide, the Campi Flegrei (CF), in southern Italy, is probably one of the most studied due to its highly urbanized area, making it the highest volcanic risk in the world (e.g., Charlton et al., 2020). The CF caldera structural architecture is still a matter of debate; however, most of the authors agree about a nested structure (Rosi and Sbrana, 1983; 1987; Orsi et al., 1992; Acocella, 2008; 2010; Vitale and Isaia, 2014), resulting from at the least two caldera-forming eruptions, the Campanian Ignimbrite (CI, 39 ka; Giaccio et al., 2018) and the Neapolitan Yellow Tuff (NYT, 15 ka; Deino et al., 2004). The localization of the caldera boundaries (Fig. 4.1a) has been approximated by the distribution of younger volcanic vents (Scarpati et al., 1993; Orsi et al., 1996) or retrieved by direct observations in the field (e.g., Vitale and Isaia, 2014) and drill-hole (Rosi and Sbrana, 1983). Geophysical investigations also come to support the comprehension of complex volcanic settings (De Siena et al., 2018; Troiano et al., 2019), and the CF caldera has been the site of decades of research, such as gravity (Florio et al., 1999; Capuano et al., 2013), magnetic (Secomandi et al., 2003) and seismic (Zollo et al., 2004; De Siena et al., 2018; Pepe et al., 2019) investigations. Furthermore, more refined reflection seismic profiles have provided advanced pictures of the submerged caldera sector during the last decades, especially regarding the stratigraphic framework (Steinmann et al., 2018; Natale et al., 2021). The existence of the caldera lineaments offshore has been stressed out by recent works (Pescatore et al., 1984; Sacchi et al., 2014; Steinmann et al., 2016). On-land studies (i.a., Vitale and Isaia, 2014) allowed to conceive a conceptual model of the caldera, but similarly, accurate characterization is still lacking in the offshore sector, which might also provide insightful information applicable to the whole caldera structure. If the submerged sector hindered part of the evidence for understanding the caldera structure, conversely, more refined geophysical techniques allow envisaging an improved view of the volcano structure. Such knowledge might be important for the characterization of the geothermal potential of this area (Carlino et al., 2012) and helping the comprehension of unrest offshore seismicity (Orsi et al., 1999). With this in mind, we analyzed many high-resolution seismic reflection profiles acquired in the Gulf of Pozzuoli to characterize with unprecedented detail the main fault zones, that otherwise would inevitably be hindered in the continental sector, sheding light on the evolution of the nested caldera structure, and investigate the relationships with the regional tectonic field.

4.2 Geological setting

The CF caldera is located along the Tyrrhenian Sea margin of southern Italy (Fig. 4.1a; Vitale and Ciarcia, 2018 and reference therein). Volcanism in the CF caldera is older than 80 ka and

was characterized by a scattered volcanic activity with some volcanic edifices also located in the urban area of Naples (Sbrana et al., 2015). This area (Fig. 4.1a) hosted at least three large (>10 km3) eruptions: the CI (40 ka, up to 200 km3 DRE, Giaccio et al., 2017; Costa et al., 2012; Scarpati et al., 2016, 2020; Silleni et al., 2020); Masseria del Monte Tuff (29.3 ka, 16 km3 DRE; Albert et al., 2019) and NYT (15 ka, 40 km3 DRE, Orsi et al., 1992; Scarpati et al., 1993; Deino et al., 2004).

The present morphological depression primarily derives from the younger NYT caldera collapse, partially overriding the preexisting CI caldera (Rosi and Sbrana, 1987). After the large-scale event of NYT, intense and mostly explosive volcanism has occurred within and along the boundaries of the CF caldera, varying in style and magnitude (Bevilacqua et al., 2015, 2017). Eruptions occurred in closely spaced volcanic epochs, lasting from a few centuries to a few millennia, and were alternated with periods of quiescence lasting up to several millennia (e.g., Di Vito et al., 1999; Smith et al., 2011). Eruptions have mainly clustered on the principal structural discontinuities (Vitale and Isaia, 2014; Isaia et al., 2015). Furthermore, the volcanism was remarkably coupled to significant ground deformation and seismo-tectonic activity (e.g., Vitale et al., 2019), which continues nowadays (La Rocca and Galluzzo, 2019; Giudicepietro et al., 2020; Young et al., 2020; De Martino et al., 2021; Isaia et al., 2021). The long-term ground deformation of the caldera floor was recorded by the long studied marine-transitional sedimentary sequence of the La Starza unit (Isaia et al., 2019; Vitale et al., 2019), presently exposed along the Pozzuoli coast, and well recorded by the equivalent continuous infill in the Pozzuoli Gulf (Natale et al., 2021). Ongoing volcanic unrest shows a similar pattern to the long-term resurgence and other historical eruptive unrest (Guidoboni and Ciuccarelli, 2011; Di Vito et al., 2016), and non-eruptive (Del Gaudio et al., 2010; D'Auria et al., 2011).

4.3 Structural framework

Recent structural studies in the CF caldera, both inland (Isaia et al., 2015; Vitale and Isaia, 2014; Vitale et al., 2019; Isaia et al., 2021) and offshore (e.g., Natale et al., 2020), have documented that faults are located close to volcanic vents and caldera rims. These structures are associated with both eruptive and significant ground deformation (e.g., Bevilacqua et al., 2020). Generally, these structures show a prevalence of recurrent regional tectonic directions (NW-SE and NE-SW); Nonetheless, ~N-S and ~E-W trending faults are associated with the

youngest deformational episodes within the caldera (e.g., Vitale and Isaia, 2014; Vitale et al., 2019; Isaia et al., 2021). The former tectonic directions show significant displacement on-land, up to tens of meters, whereas the younger faults show metric displacements. Following Vitale and Isaia (2014), the fault orientation within the caldera results from the interplay between the regional tectonic field associated with the opening of the Tyrrhenian Sea (Vitale and Ciarcia, 2013) and the volcano-tectonic deformation. The high-angle N-S and E-W directed faults associated with the last volcano-tectonic activity frequently reactivated preexisting deep-seated faults (e.g., Vitale et al., 2019). The central sector is also characterized by intense degassing and hydrothermal activity (e.g., Chiodini et al., 2012; Cardellini et al., 2017; Young et al., 2020) and by the highest values of surface fractures and fault density, particularly around the town of Pozzuoli and in the Solfatara area (Bevilacqua et al., 2015; Bevilacqua et al., 2020). Historical and ongoing events have also been accompanied by meters of ground deformation, which was likely associated with the reactivation of main faults due to fluid overpressure, as already occurred during past deformation events (e.g., D'Auria et al., 2011; Di Luccio et al., 2015; La Rocca and Galluzzo, 2019; Vitale et al., 2019; Di Lieto et al., 2021).

4.4 Pozzuoli Gulf

The 6x7 km wide Pozzuoli Gulf hosts over one-third of the CF caldera surface. In the last 15 kyr, the interaction between sea-level rise, ground deformation, erosion, and sedimentation strongly affected its morphology (Natale et al., 2021). The resulting bathymetry consists of different morpho-structural features (Fig. 4.1a). The area close to the coastline is the offshore continuation of the resurgent dome located on the continental part. The inner continental shelf partially crosscuts the submerged dome, showing depths between 20 and 40 m b.s.l.

The gulf reaches depths down to 120 m b.s.l. in the sector between Capo Miseno and Nisida (Fig. 4.1a), occurring in correspondence with the caldera ring fault zone. This area is broadly 2.5 km wide, mainly composed of north-dipping faults. These faults displace the NYT unit and the older volcaniclastic rocks, including the CI. Southward, the most external caldera boundary is associated with the CI caldera collapse (Steinmann et al., 2016), bounding the pre-CI volcanic morpho-structural high in the footwall. These fault strands broadly join with the on-land lineaments associated with the CI caldera faults from Monte di Procida and Posillipo (Vitale and Isaia, 2014). The deformation structures and the stratigraphic framework of the offshore

caldera infill have been assessed by several works using seismic reflection datasets of different vintages and resolutions (Pescatore et al., 1984; Fusi et al., 1991; Milia, 1998; Milia et al., 2000; Aiello et al., 2012, 2016; Sacchi et al., 2014, 2019; Steinmann et al., 2016, 2018; Natale et al., 2020; 2021).

4.5 Offshore stratigraphy

We used the recent works of Natale et al. (2021) and Steinmann et al. (2016; 2018) to reconstruct the stratigraphic setting of the offshore successions. The stratigraphic architecture (Fig. 4.1b) helped us fully describe the relationships between the mapped faults and the caldera infill enclosed in the seismic penetration limit. In particular, from the sea bottom down to NYT unit, we used the high-resolution stratigraphy of Natale et al. (2021), whereas, for the deeper seismic units, we applied the stratigraphic framework described by Steinmann et al. (2016; 2018). For the sake of clarity, we applied the same names of the seismic units of Steinmann et al. (2016) for the post-CI deposits (M1 unit), including a large volcanic bank which herein is labelled as Ammontatura Bank. The pre-CI deposits are labeled M0. Pre-IC volcanic banks are labeled MB (Miseno Bank), PPB (Penta Palummo Bank), and MDB (Monte Dolce Bank). The timeframe of the rocks includes the pre-CI volcanic banks, located to the South of the study area (Fig. 4.1a), whose inferred ages range about 80-100 ka (Milia, 2010; Steinmann et al., 2016), similarly to the oldest dated tephras on-land (Pappalardo et al., 1999; Scarpati et al., 2013). The offshore succession passes upward to CI unit, pre-NYT marine and volcaniclastic units, NYT unit, and the post-NYT infill (Fig. 4.2a).

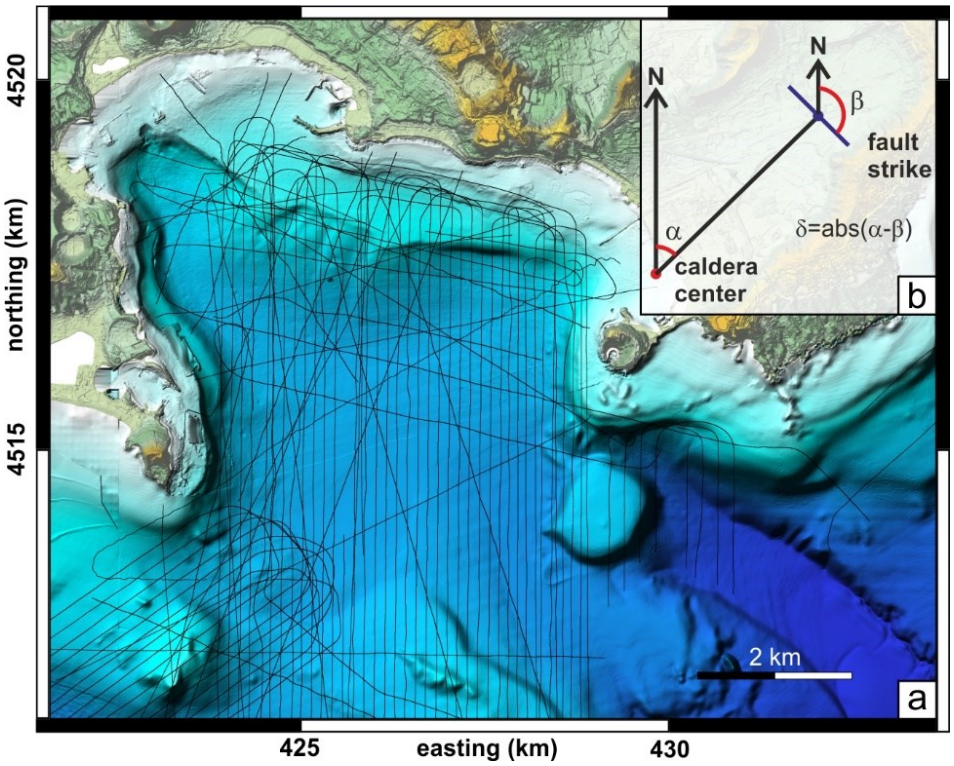

Figure 4.2. (a) Seismic dataset used in this work. (b) Geometric sketch of angles used to perform the radial analysis.

4.6 Materials and methods

The Pozzuoli Gulf volcano-tectonic architecture reconstruction was mainly based on three sets of high-resolution seismic profiles, namely Seistec_2013, Cafe GeoB08, Marisk (Fig. 4.2a). The Seistec dataset was acquired using the uniboom IKB-Seistec profiler (Simpkin and Davis, 1993, Mosher and Simpkin, 1999; Sacchi et al., 2019) by ISMAR-CNR of Naples in 2013. With a very high source frequency (central frequency 2kHz), it holds remarkably high spatial resolution (around 0.5 m). However, such high frequencies do not allow deep seismic penetration as is strongly influenced by the highly attenuating fluid-saturated volcaniclastic rocks, holding to Two Way Travel (TWT) depths between 100-150 ms.

Hence, to image the deeper reflectors and identify the marker NYT unit, we relied on the multichannel seismic lines from the GeoB08 dataset, acquired during the CAFE-7/3 expedition in 2008; Steinmann et al., 2016). The lower central source frequency of 250 Hz provides spatial resolutions around 1-2 meters with signal penetration exceeding 350 ms, with some local limitations linked to fluid uprise blanking and shallow water sea bottom multiple reflections (Steinmann et al., 2016). The Marisk sub-bottom chirp dataset, although the lower resolution

and investigated depth (signal penetration down to 40-50 ms), helped to constrain the geometry of faults in undersampled areas of the previous datasets. Seismic lines belonging to the three datasets were imported, analyzed through Eliis Paleoscan software packages (Eliis, 2018). To estimate the thickness of seismic units and gather information on the dipping angle of the faults, we used a two-way travel (TWT) time velocity of 1650 m/s, which is representative for shallow (<200 m), mostly unconsolidated volcaniclastic and marine deposits (Sacchi et al., 2014; Steinmann et al., 2018; Natale et al., 2021). Concerning this, we applied a correction to the measured dip angle values due to discrepancies between software velocity assumptions (2000 m/s TWT) and our applied velocity (1650 m/s TWT).

The lines from the three datasets are mainly N-S oriented with some oblique lines and a few ca. E-W oriented tie lines, covering the central part of the Pozzuoli Gulf (Fig. 4.2a). We identified over 1200 fault sticks (2D fault traces) in the whole dataset. To recover fault orientation data, we interpolate the fault sticks. Every fault segment has been interpolated by joining up to 3 fault sticks. As a result, we retrieved over 220 fault plane data, subsequently analyzed with Open Stereo (Grohmann and Campanha, 2010) and Tectonics FP (Reiter and Acs, 1996-2022) open-source software.

Moreover, fault plane data were also analyzed through the radial analysis method to determine how their azimuth relates with the caldera center, assumed to be close in the Pozzuoli town (Fig. 4.2b). This method (e.g., Tramparulo et al., 2018 and references therein) consists in measuring the following three angular parameters (α, β, and δ). α is the angle (from 0° to 360°) between the north direction and the strike of the line connecting the reference point (i.e., the caldera center) to the fault plane centroid position (Fig. 4.2b). β is the angle (from 0° to 180) between the north direction and the strike of the fault plane/dike (Fig. 4.2b). Finally, the angle δ, which is the absolute value of the difference between α and β, ranges between 0 and 90°, allows us to classify the analyzed structures as i) radial ($\delta \leq 30°$); ii) oblique ($30° \leq \delta \leq 60°$) and iii) tangential ($\delta \geq 60°$) groups. Through the α-β diagram and δ frequency histogram, the mutual relationship between faults and the caldera center is evaluated. These plot have been produced with designated Excel and Matlab scripts.

The fault mapping has been subjected to some limitations, especially in the dome area because, here, the individual fault segments have a limited strike length; furthermore, the ca. N-S-oriented faults might have been under-sampled due to the limited density of E-W trending

seismic profiles. Concerning the other deeper part of the gulf, the main limitations were fluid blanking and depth exceeding signal penetration.

4.7 Results

4.7.1 Stratigraphic framework

The multi-scale seismic reflection dataset analysis allowed us to identify four main fault zones, defined by more than 300 individual fault segments. We identify two main fault systems: (i) the ring faults and (ii) the dome faults. The former system occurs from Capo Miseno to Nisida, in a segmented, arc-shaped fashion, belonging to three main fault-controlled rims, broadly spaced 2.5 km on average, whereas the latter is located on the culmination of the dome (Fig. 4.1a), embracing an area from the shelf break to the coastline and beyond.

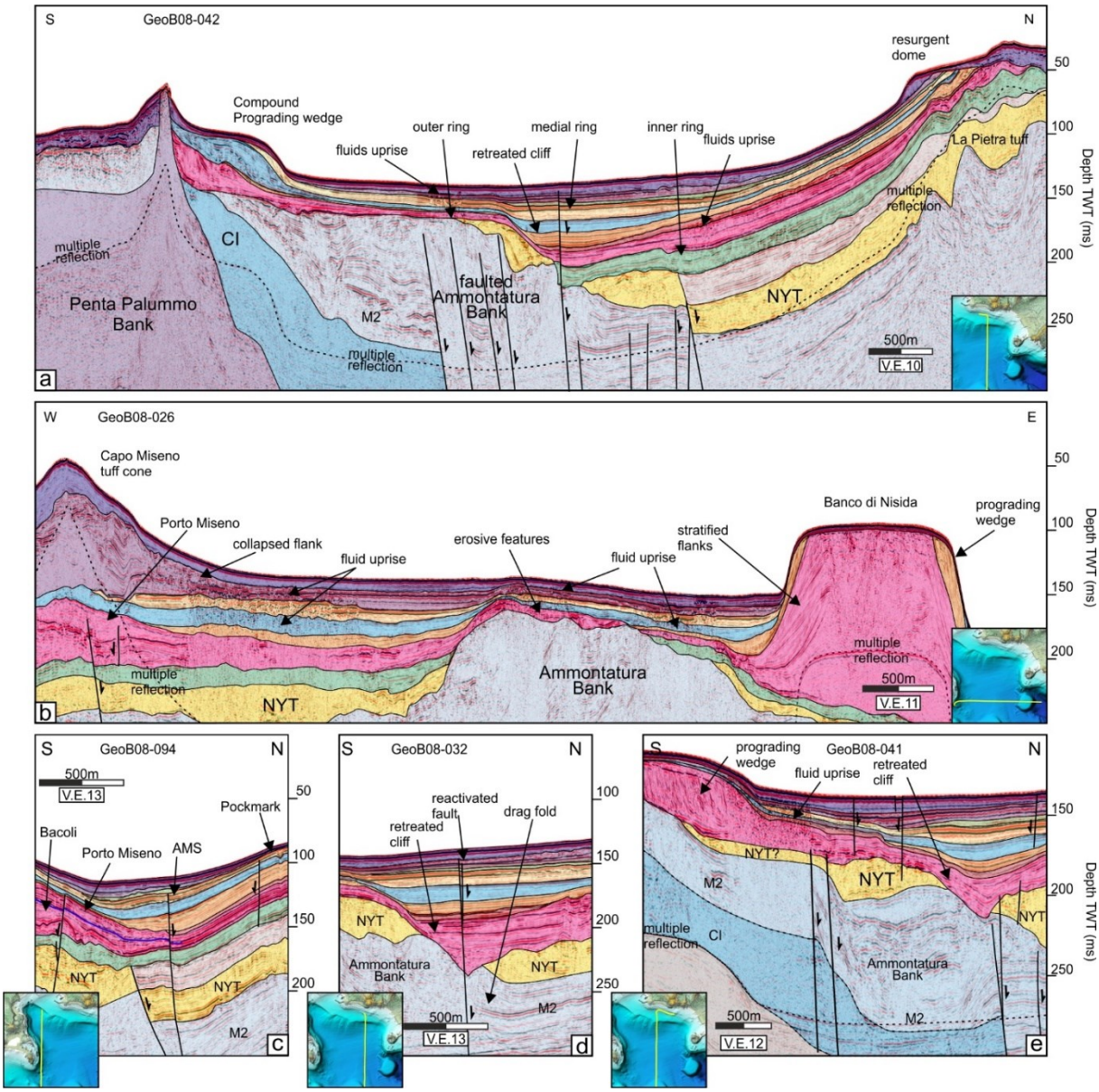

Figure 4.3. (a) 8 km long N-S oriented GeoB08-042 seismic profile illustrating the main features of the nested caldera ring fault zone and the uplifted dome. (b) E-W GeoB08-026 seismic profile showing the stratigraphic architecture of the caldera offshore, highlighting the stratigraphic position of different lithosomes (Capo Miseno to the West, the Ammontatura bank to the South, and Banco di Nisida to the East. (c) N-S GeoB08-094 seismic profile showing the reactivated inner ring fault zone. (d) N-S GeoB08-032 seismic profile showing the reactivated medial ring fault zone. (e) N-S GeoB08-041 seismic profile shows evidence of the medial and outer ring faults reactivation during NYT collapse.

Before deepening into details of the results, we briefly describe the general setting of the Pozzuoli Gulf as illustrated by the N-S and E-W profiles of Figure 4.3a and b, respectively. In the northern part of the N-S profile, the uplifted dome is well visible (Fig. 4.3a), with the stratal architecture characterizing the several phases of caldera floor deformation, thoroughly

described by Natale et al. (2021). The dome connects southward with the caldera collar, where the NYT unit onlap and covers older marine and volcaniclastic units. Among these, NYT unit tapers in contact with an older volcanic lithesome, herein labelled Ammontatura Bank (Natale et al., 2021), most visible on E-W lines (Fig. 4.3b), which is further eroded by a weakly inclined abrasion surface. In Figure 4.3a, is well visible the CI unit onlapping on the older volcanic bank of Penta Palummo. On the E-W line (Fig. 4.3b), from East to West, is distinctly displayed the submarine volcanic bank of Nisida Bank (~12 ka, Natale et al., 2021) with its variably steep stratified flanks (Bischoff et al. 2020), surmounting the erosive head of Ammontatura channel, which is the upper part of the tectonic Dhorn Canyon (Fig. 4.1a). The southwestern flank of Nisida bank lies on the eastern termination of a 2 km wide volcanic lithosome, overlying post-CI marine sediments and in turn covered by the NYT unit. Faults intensely affect this lithosome and locally convey uprising fluids, depicted by acoustic turbidity (Fig. 4.3b). On the western sector of Figure 4.3b, the submarine portion of the well-stratified tuff cone of Capo Miseno and its eastward collapsed sector are evident, all in turn covered by the post-Epoch 3b prevalently transparent units (Unit S9, Natale et al., 2021). Underneath Capo Miseno, it is worth noting the increase in thickness of the upper part of S2 unit, related to the buried southward propagation of Porto Miseno tuff ring (Fig. 4.3b). The span of marine infill between Capo Miseno and the southern bank is strongly affected by fluid uprise that makes the seismic signal extremely turbid (Fig. 4.3b). In the insets of Figure 4.3c, d, e, we display zoomed sections of the individual ring fault zones, here on labeled as inner, the medial, and the outer, respectively. NYT unit is generally clearly displaced across the inner ring, which is the site of intense degassing (Fig. 4.3a, c). Throw on the medial ring fault, on the NYT unit is around 35-40 meters (Fig. 4.3d). Locally, these faults displace also younger sequences (Figs. 4.3c, d). We have little direct evidence of faulted NYT unit on the outer ring faults, this is possibly due to the erosion of the older Ammontatura tuff cone and the acoustic turbidity that affects this investigated sectors (Fig. 4.3e).

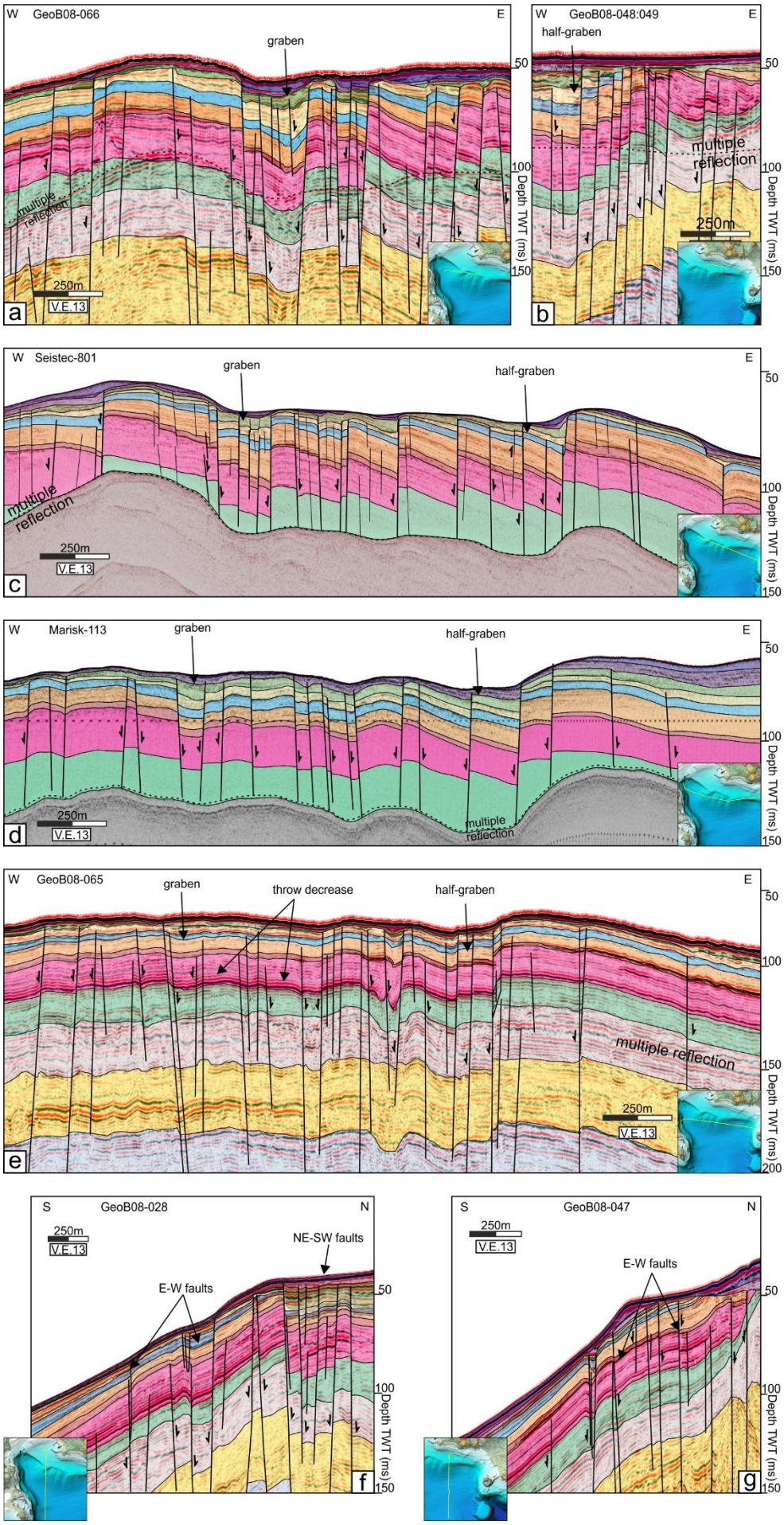
W GeoB08-066 E
graben
multiple reflection
250m
V.E.13
a
W GeoB08-048:049 E
half-graben
multiple reflection
250m
b
W Seistec-801 E
graben
half-graben
multiple reflection
250m
V.E.13
c
W Marisk-113 E
graben
half-graben
250m
V.E.13
multiple reflection
d
W GeoB08-065 E
graben
throw decrease
half-graben
multiple reflection
250m
V.E.13
e
S GeoB08-028 N
250m
V.E.13
NE-SW faults
E-W faults
f
S GeoB08-047 N
250m
V.E.13
E-W faults
g
50
100
150
200
Depth TWT (ms)

Figure 4.4. E-W and N-S seismic sections show the piece-meal collapse of the offshore part of the resurgent dome. (a) E-W GeoB08-066 seismic profile displaying the main faults tapped by the abrasion surface (b) E-W portion of two adjacent seismic profiles GeoB08-048-049 showing the north-eastern end of the dome fault zone (c) E-W high-resolution Seistec-801 profile showing the different fault zone affecting the resurgent dome. (d) E-W Marisk-113 profile showing the faults. (e) E-W GeoB08-065 profile displaying the southern end of the faults affecting the dome. (f) N-S GeoB08-028 profile showing the E-W and the NE trending faults affecting the western part of the shelf. (g) N-S GeoB08-047 profile showing the E-W trending faults affecting the eastern part of the shelf. For profile location, see the bottom right map inset.

As shown in the map inset of Figure 4.4, seven profiles cross the gulf. These selected lines well-illustrate the general structural setting of this area, which is composed of three main graben structures broadly oriented NE-SW and NNE-SSW. The first line (GeoB08-066; Fig. 4.4a) is located along the coast broadly oriented E-W and shows the high-angle fault system that affects a 4 km wide zone of the dome (Fig. 4.4a). This profile highlights the significant throw of the fault zone and the relationships with the erosive truncation associated with S7-8 units (Natale et al., 2021). The pervasive distribution of these faults is well observable on other lines located more to the NE on the compound lines GeoB08-048-49 (Fig. 4.4b), where the faults, apart from affecting marine and volcaniclastic sediments, involve La Pietra tuff (Natale et al., 2021). To the South, on lines Seistec-801, Marisk-113, GeoB08-065 (Fig. 4.4c, d, e), it is possible to follow the fault strands toward the South. Thanks to its very high resolution, the Seistec-801 profile (Fig. 4.4d) allows observing some fault zone features such as fault lenses and conjugate structures. Finally, on the N-S lines, we show the E-W graben faults and the NE-SW faults affecting the western part of the inner shelf (Fig. 4.4f), and the E-W faults affecting the eastern part of the inner shelf (Fig. 4.4g). The general architecture, fault plane orientations, and overall throw of the individual fault zones are described in the following paragraphs.

4.7.2 Fault systems

The following subsections describe the faults identified in the seismic dataset, divided into two main groups: the ring faults, forming a ~2.5 km wide belt comprising the offshore continuation caldera-related faults, and the dome faults located in the inner continental shelf.

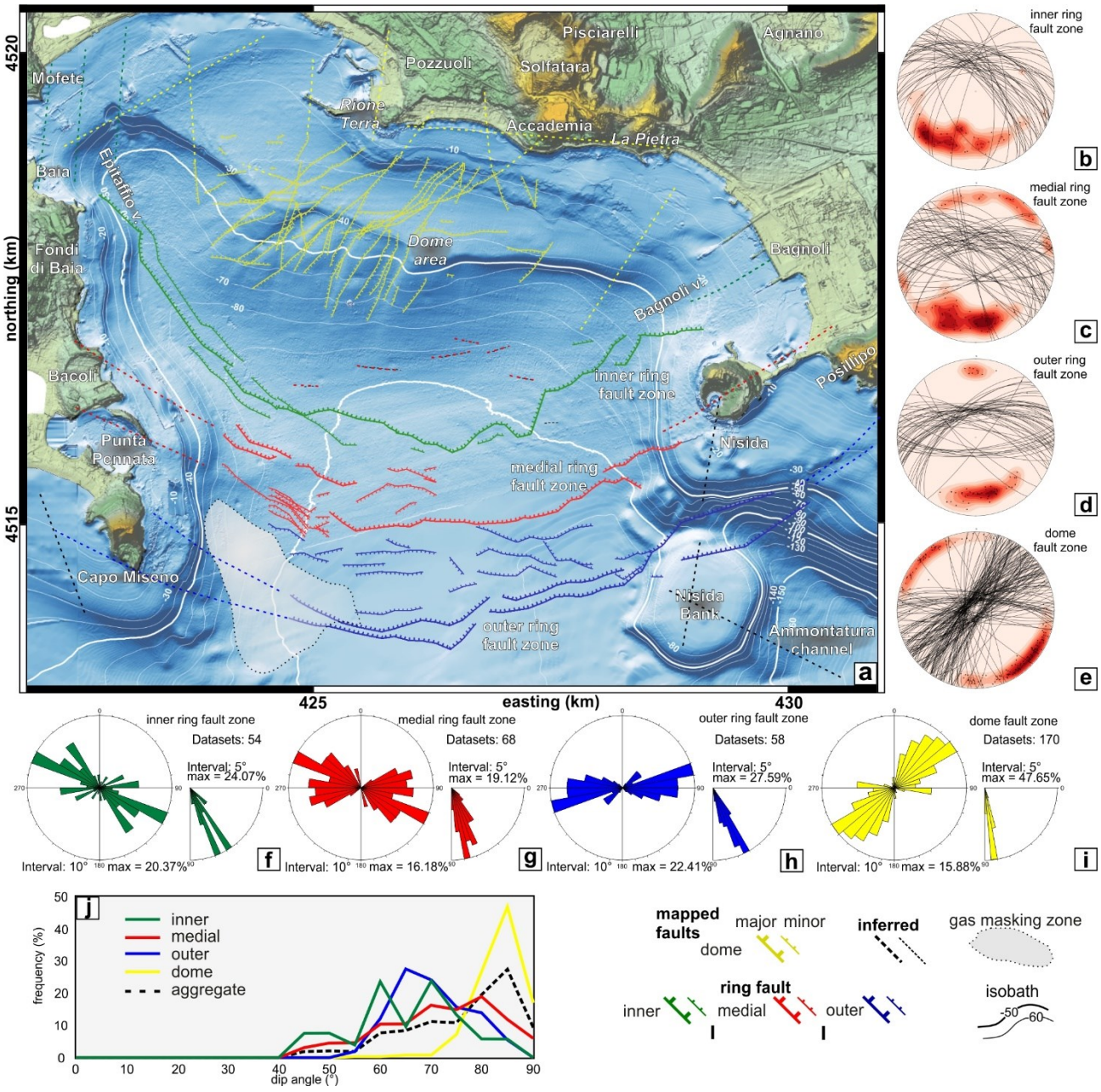

Figure 4.5. (a) Structural map of the Campi Flegrei offshore sector. Faults are color-coded according to the legend and structural plots. Barbs indicate downthrown block. Isobath contour interval is 10m, major contour interval 50 m. Stereographic projection of the faults mapped within the seismic dataset (equiareal net, lower hemisphere) (b) inner ring fault; (c) medial ring fault; (d) outer ring fault; (e) dome faults. Rose diagrams of fault strike and dip angle. (f) inner ring fault; (g) medial ring fault; (h) outer ring fault; (i) dome faults; (j) dip angle frequency plot of the mapped faults.

4.7.2.1 Ring fault system

The ring fault system runs arcuate from Bagnoli-Nisida on the East, toward Capo Miseno, Bacoli, and Baia to the West (Fig. 4.5a). We grouped the ring faults into three broadly

concentric structures since each consists of principal and secondary fault segments. We labeled them from the north (inside) toward the South (outside): (i) inner, (ii) medial, and (iii) outer ring fault systems (Fig. 4.5a). Overall, the whole ring fault zone is ~2.5 km wide, with the main segments averagely spaced less than 1 km apart from each other.

4.7.2.2 Inner Ring Fault System (IRFS)

All the mapped segments of the IRFS show normal kinematics with planes dipping toward the caldera center and a few antithetic segments, E-W to NE-SW directions in the eastern portion, E-W to NW-SE, and subordinately N-S directions, in the western end (Fig. 4.5b). Most dip angles show values between 60 and 80° (Fig. 4.5e), with the lowermost angles recorded among E-W oriented planes. These faults in some locations form complex fault structures such as relay zones (Fig. 4.5a). The IRF displace the NYT unit, with throw averagely around 40 m (Fig. 4.3a), maintained roughly along the whole fault system, whereas locally to the West, they cut the younger marine-volcanoclastic infill up to Unit S6 (Fig. 4.3c; Natale et al., 2021). Explicit morphological expressions of these faults are visible in the bathymetry, hosting the Epitaffio and Bagnoli valleys (Figs. 4.1a, 4.5a), the latter partially buried by the young lithosome of Nisida (Natale et al., 2021).

4.7.2.3 Medial Ring Fault System (MRFS)

The MRFS broadly shows the same arcuate shape of the IRFS, running from Nisida island to Bacoli (Fig. 4.5a), with prevalent E-W orientations (Fig. 4.5c). Some minor segments are located within the separation gap between IRFS and MRFS. The medial ring faults mainly dip toward the caldera center, with angles ranging between 70 and 80 degrees (Fig. 4.5f). Similar to the IRFS, this fault zone is locally segmented with articulate neutral relay zones. On the western part, it is worth noting the presence of a series of grabens broadly oriented E-W (Fig. 4.5a). Although clear cut-offs of NYT unit are only locally preserved from erosive features, these faults generally displace NYT and older units with an amount of throw comparable to the IRFS. Erosion strongly altered the morphology of this fault, with a receding scarp (Fig. 4.3a). Along a ~1 km long fault segment, the MRFS is reactivated, cutting younger sequences, almost reaching the sea bottom (Figs. 4.3d, 4.5a). NYT unit shows thickness variation between hanging wall and footwall.

4.7.2.4 Outer Ring Fault System (ORFS)

The outer ring fault zone runs from Posillipo to Capo Miseno, following the same arcuate attitude of the previously described structures (Fig. 4.5a). It is worth noting that, in the footwall of these faults, the Campanian Ignimbrite unit is at its most shallow depth of 150ms (Fig. 4.3a). In the area facing the eastern cliff of Capo Miseno, roughly covering 4 km^2, the seismic signal is strongly altered by a massive fluid-related blanking (Fig. 4.5a). Notwithstanding, we could map over 50 fault segments, mainly oriented E-W and NE-SW (Fig. 4.5d), mostly dipping between 60-70° (Fig. 4.5g), predominantly toward the north. Nonetheless, we report that many E-W elongated grabens exist in the intermediate zone with the medial ring fault zone. As well as for the medial ring fault, no explicit bathymetric expressions are visible related to these structures; instead, they are visible due to the long-lived prograding wedges (Fig. 4.5a).

4.7.3 Dome Fault System (DFS)

We reconstructed 170 individual fault segments in the dome area, which broadly form ~ 50 compound faults (Fig. 4.5a). These structures are mostly normal faults, with very few steep faults with reverse kinematics. All faults show a very high angle, greater than 80° on average, as shown by the dip-angle frequency plot showing that 69% of the mapped faults have values greater than 80° (Fig. 4.5i, j). Fault length ranges between 250 m to more than 4 km. Fault lengths smaller than the line spacing or in the undersampled area are listed as inferred. Describing the structure from the general architecture to the details, the Dome Fault System (DFS) forms a NE-SW to NNE-SSW (Fig. 4.5e) oriented structurally lowered zone, bounded by two main highs (Figs. 4.4 and 4.5a) that connect to two morphological tuff spurs on the coast, namely Rione Terra to the West and La Pietra to the East (Figs. 4.1a, 4.5a). From a morphological point of view, these faults have a bathymetric expression only south of the shelfbreak, often hosting channels streaming sediments down to the deeper depths (Fig. 4.5a).

On the contrary, these faults do not affect the flat-lying submerged terrace. In the depressed area, three fault sets are present: NE-SW, NNE-SSW, and E-W oriented structures (Fig. 4.5e, i). NE-SW trending faults mainly occur on the western end of the dome, forming a graben (Fig. 4.4); the NNE-SSW set is mainly on the central-eastern end of the lowered area, showing a half-graben structure dipping to the West, and finally, the E-W faults affect the whole area (Fig.

4.4f, g), mainly lowering toward the northern part, and linking to the NE-SW faults in a polygonal fashion (Cartwright et al., 2003). The throw of the faults averagely ranges between 5-10 m, with peaks of more than 20 m (Fig. 4.4).

4.7.4 Fault radial analysis

To highlight the geometric relationships between faults located in the dome area and the three caldera rims with the caldera center, we analyzed 350 fault planes using the radial analysis, as described in section 3. Figure 4.6a shows the centroid of each fault segment used in this analysis. As it stands, the overall orientations are mostly E-W, NE-SW, and subordinately NW-SE, with the majority of dip angles exceeding 80° (Fig. 4.6b). After calculating the three radial angles (α, β, and δ), we plotted the results of the α-β diagram (Fig. 4.6c) and δ-histogram (Fig. 4.6d). The results indicate that most ring faults are tangential to the caldera center, showing an arcuate trend crossing the tangential line around 80-100° β angle (Fig. 4.6c). On the other hand, dome faults range from radial to tangential, with a predominance of radial structures (Fig. 4.6d); also, these show an arcuate trend crossing the radial line at around 20-40° β angle, and subordinately 80-100° (Fig. 4.6c). In general, almost all the regional directions are found and represented in the α-β diagram; however, we can individuate two main horizontal clusters with β values of 45° (NE-SW) and ca. 90° (E-W), whereas 135° (NW-SE) cluster is less represented (Fig. 4.6c).

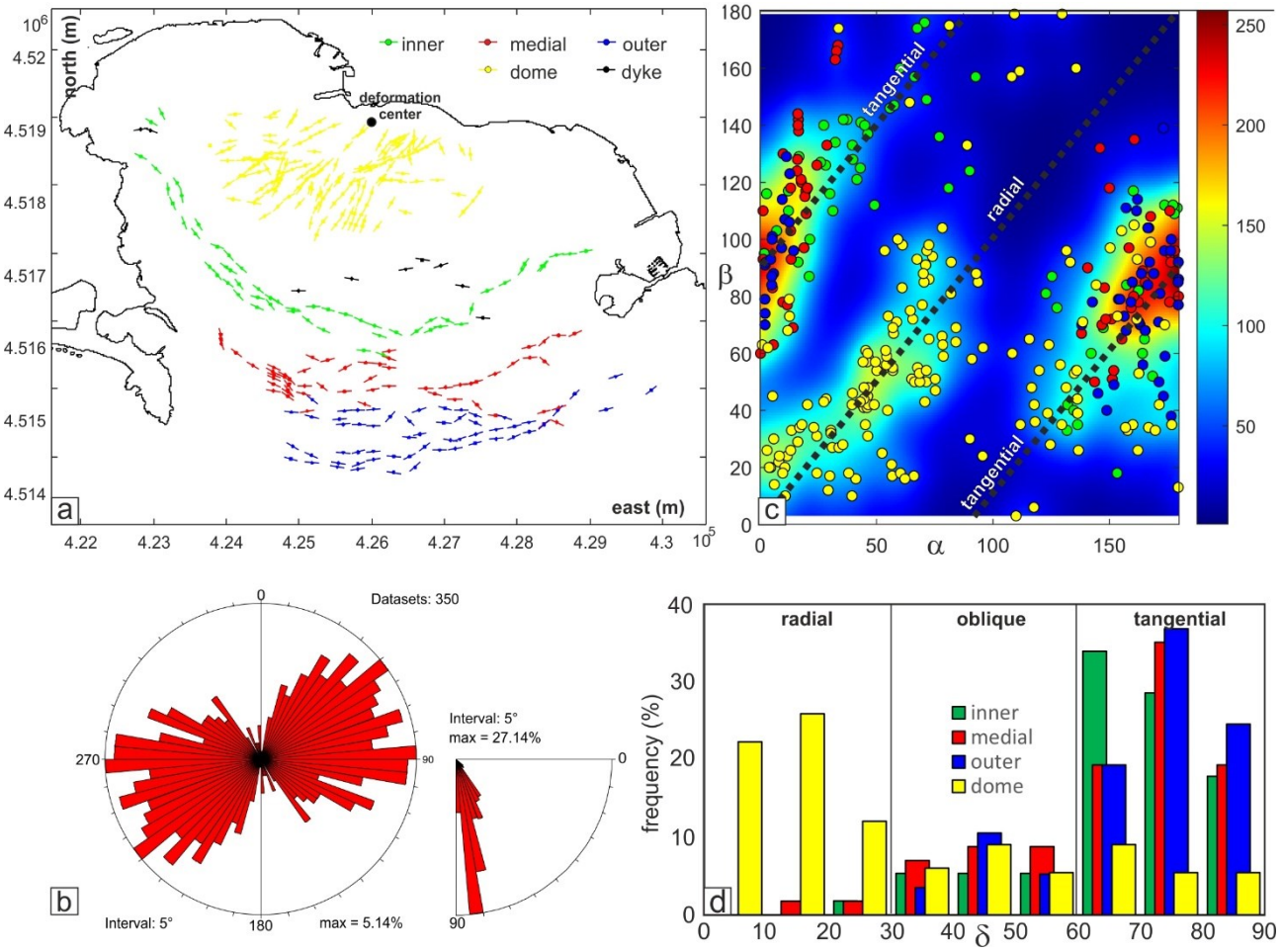

Figure 4.6. (a) Structural map indicating the centroid position of mapped fault planes used for the radial analysis. (b) Rose diagram of the mapped faults (n=350). (c) α-β diagram of ring and dome faults showing the distribution of angular parameters for each fault zone. (d) Histogram of the δ frequency for each fault array, highlighting the relative orientation compared to caldera deformation center.

4.8 Discussion

4.8.1 Ring fault system

The overall caldera structure can be summarized as formed by three concentric collapse depressions, which are nested into each other, in a telescopic geometry and with a spacing between major faults of ~1 km (Fig. 4.5a). In particular, the fault plane data extracted from seismic reflection profiles depict the general attitude of faults dipping toward the caldera center. In addition, each of the three rims and associated minor faults segments, both synthetic and antithetic, trace the complementary southern end of the caldera structure.

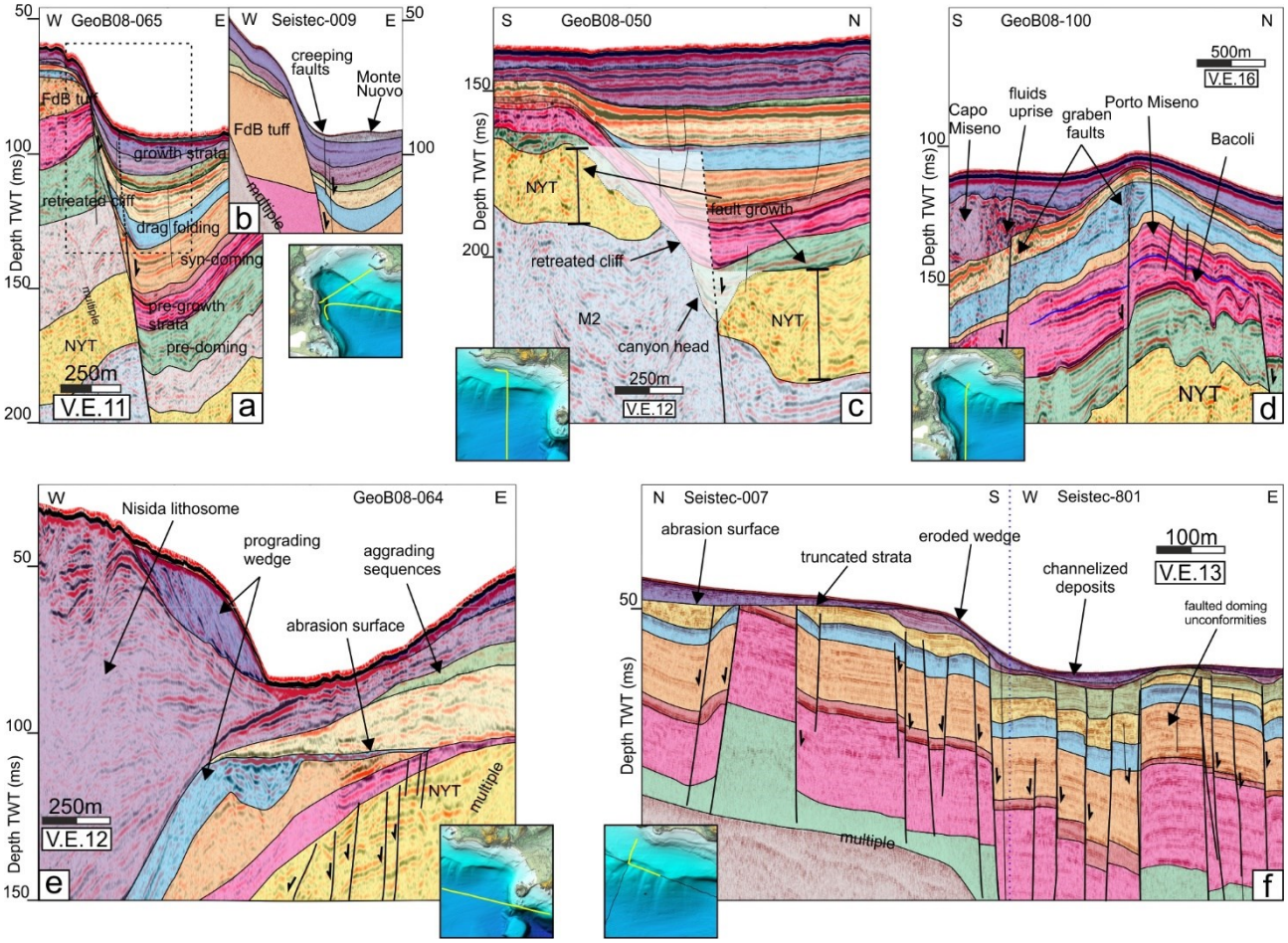

Figure 4.7. Zoomed sections of designated fault zones. (a) GeoB08-065 E-W shows the structural relationships between the hanging wall and the footwall of the western inner ring fault. (b) zoomed section Seistec-009 with a high-resolution image of fault activity. (c) GeoB08-050 N-S profile highlights the erosive features affecting the medial ring fault and thickness differences between hanging wall and footwall. (d) GeoB08-100 N-S profile showing the uplifted Pennata structure and the graben faults affecting S6 Unit. (e) E-W oriented GeoB08-064 showing the complex stratal architecture of the eastern outer ring fault. (f) Compound high-resolution Seistec profiles 007 (N-S) and 801 (E-W), showing the relationships between faults, abrasion surface, and channelized deposits.

4.8.1.1 Inner Ring Fault System

The IRFS is the innermost caldera rim identified offshore and can be followed from Nisida, on the East, to Baia, on the West (Fig. 4.5a). In fact, in addition to the southern part of this rim, the Pozzuoli Gulf also hosts the western portion of the IRFS, constraining the Epitaffio valley (Fig. 4.51a), the latter is well visible from the mapped structural data (Fig. 4.5a). It is worth noting that this system shows evidence of brittle (Fig. 4.3c) and syn-sedimentary plastic reactivation (Figs. 4.7a, b), displaying deformation and faulting features typical of footwall collapses (Fig. 4.7a, b; e.g., Hardy, 2013).

This motion has led to the subsidence of the hanging wall (Fig. 4.7a, b), promoting the accumulation of sediments along the Epitaffio valley due to the increased accommodation space. Stressing this matter, the footwall of the IRFS in its southwestern part hosts the Punta Pennata structure, which has been recently interpreted as a fault-bounded intrusion (Natale et al., 2021). Furthermore, on the eastern end of the gulf, the IRFS matches the position of the caldera faults identified from boreholes by Calderoni and Russo (1997). Overall, the geometry of segmentation of the IRFS suggests that the main segments are the reactivation of previously formed faults (Hardy, 2011; 2013; Vitale and Isaia, 2014), whereas the minor antithetic segments form as linkage strands with the cogenetic medial rim. It is significant to highlight that the inner rim runs to the East of the tuff cones of Baia, Mofete, Archiaverno and probably continues toward the Toiano plain, which hosts relevant thicknesses of post-NYT deposits (Fig. 4.1a; Di Vito et al., 1999). Along this fault system, the NYT unit consistently shows constant thickness on both hanging wall and footwall, and it is displaced ~40m on average along the mapped sections (Fig. 4.3a). This feature suggests that faulting on this system occurred late or after the deposition of NYT unit, as suggested by Wohletz et al. (1995).

4.8.1.2 Medial Ring Fault System

The MRFS develops from Nisida to the East, to Bacoli to the West (Fig. 4.5a), with the main fault dipping toward the center and minor synthetic and antithetic strands (Fig. 4.5a). It is composed of the main strand located below the subsequent paleovalley that extends along the fault scarp, putting in lateral contact NYT with the pre-NYT tuff cone (Fig. 4.3a). This scarp shows evidence of subsequent erosion and recession during the post-NYT inactivity and post-Last Glacial Maximum (LGM, ~22ka) sea-level rise (Fig. 4.7c). Unit NYT is 40 m of average thickness, an amount comparable to IRFS. Nonetheless, a difference in thickness between hanging wall and footwall is documented, as shown in Figure 4.7c. This feature agrees with the on-land evidence describing syn-erupting faulting in Coroglio (Scarpati et al., 1993; Wohletz et al., 1995). As well as the IRFS, the main faults are the reactivation of preexisting faults, and also, in this case, smaller synthetic and antithetic segments form as linkage strands with the cogenetic rims. The drag folding of the M2 reflectors underneath NYT unit underpins the motion along this main fault system during NYT collapse. Moreover, in the central part of this fault, a local reactivation occurs on an E-W segment ~1 km long (Figs. 4.3c, 4.5). Furthermore, South of the uplifted Pennata Structure (Fig. 4.5a), a complex array of E-W to WNW-ESE

normal faults is present, featuring an SW-dipping structure that cuts the strata younger than NYT up to S5 unit with a throw over 5 m (Fig. 4.7d). This fault likely connects to the WNW-ESE-directed fault cutting the lithosome of Bacoli. Similar to that separating Monte di Procida and Bellavista (Fig. 4.1a), the graben structure belongs to an antithetic structure to the main buried fault of the outer caldera (Vitale and Isaia, 2014).

4.8.1.3 Outer Ring Fault System

The ORFS forms the outermost caldera rim individuated in the seismic dataset, with faults mainly dipping toward the caldera center (Fig. 4.5a). CI unit is located in its footwall, emplaced in primary contact with older units like the older volcanic banks (Figs. 4.1a and 4.3a, e). This feature is the only occurrence of CI unit at shallow depth in the seismic dataset in the Pozzuoli Gulf. CI unit shows a primary contact with older units, just in a similar way as observed on-land on the extra caldera structural highs of Camaldoli, Quarto, and Monte di Procida (Fig. 4.1a; Rosi and Sbrana, 1987; Vitale and Isaia, 2014). The ORFS connects to the coastal structural highs of the caldera, including Monte di Procida to the West, running underneath the Capo Miseno tuff cone, Posillipo to the East, and the ~12 ka Banco di Nisida tuff cone (Fig. 4.5a; Natale et al., 2021), and connecting to the Coroglio cliff, which hosts the 21 ka inter-caldera ring vent of Trentaremi (Figs. 4.1a, 4.7d; Scarpati et al., 2013; Di Giuseppe et al., 2017). The presence of such important structural lineament is frequently marked by the extensive fluid uprise along the whole ring zone, with significant blanking East of Capo Miseno (Figs. 4.3b, 4.5a). As shown in Figure 4.3a, the ORFS also affects the post CI tuff cone suggesting a reactivation younger than CI.

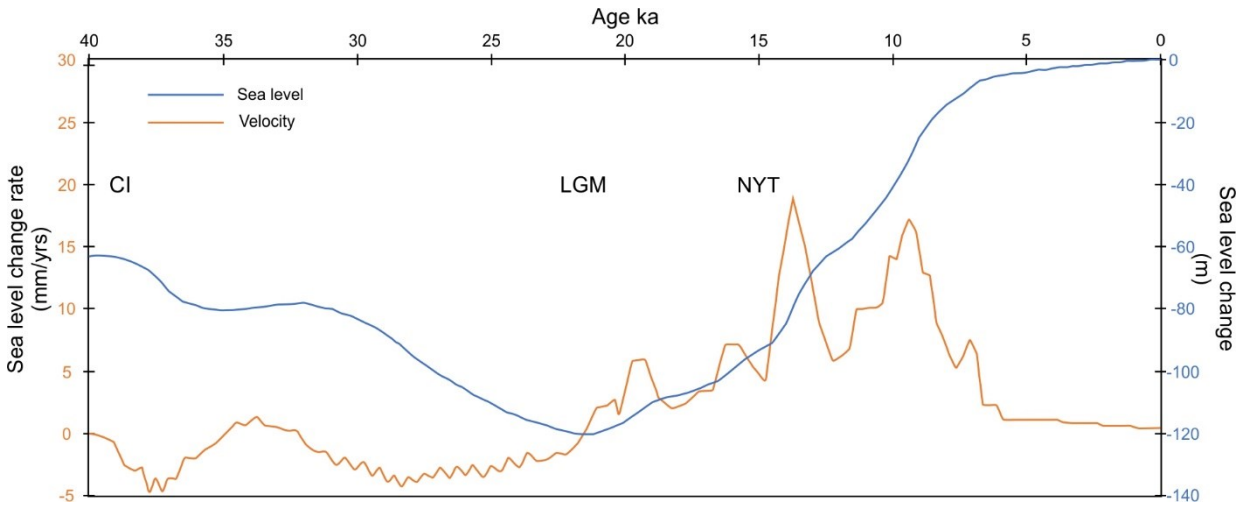

Figure 4.8. Sea level variation curve since 40 ka, featuring its 1st derivative, highlighting the change in velocity of SLR. 40-20 ka interval is from Waelbroek et al. (2002), 20-0 ka interval is from Lambeck et al. (2011). Main events are indicated. CI: Campanian Ignimbrite; LGM: Last Glacial Maximum; NYT: Neapolitan Yellow Tuff.

4.8.1.4 Insights on the telescopic collapse

To disclose whether and how the caldera faults acted during single collapse episodes, we analyzed the crosscutting relationships between faults and seismic units. We start discussing the CI caldera collapse. In the multi-scale seismic dataset, CI unit is not recognized both in the hanging wall of IRFS and MRFS. This observation agrees with the depth of CI observed in the deep borehole of Campi Flegrei Deep Drilling Project (CFDDP, De Natale et al., 2016), whose top is located at some 400 m b.s.l. in the hanging wall of the IRFS, beneath the Coroglio plain (Calderoni and Russo, 1997), which is, well below the seismic penetration limit of the dataset in the strongly attenuating volcaniclastic rocks (Steinmann et al., 2016). In fact, the CI unit is not imaged within the uppermost 300 ms inside both the IRFS and MRFS. Consequently, IRFS displaced the NYT unit just more than 40 m; hence such depth difference has to be related to a previous collapse, as suggested by Steinmann et al. (2016). This interpretation is supported by the evidence that CI unit is found in the seismic dataset only in the footwall of the ORFS, onlapping on the older volcanic banks of Penta Palummo at ~120 m depth, likewise on Monte di Procida, Quarto, and Camaldoli (Di Girolamo et al., 1984; Rosi and Sbrana, 1987; Orsi et al., 1996; Vitale and Isaia, 2014). Hence, the minimum aggregate amount of downthrow during the CI caldera formation on these offshore structures is at least 150-200 m, compared to the value of 100-120 m for NYT unit. This feature agrees with the aggradation process during deposition of M1 unit, which occurred despite the sea-level fall between 40 ka and the Last Glacial Maximum at around 20-22 ka (Figure 4.8; Waelbroek et al., 2002; Lambeck et al., 2011). We remark that the CI caldera collapse granted the observed and necessary accommodation space. Deepening into details of NYT collapse, the constant thickness of NYT unit on both fault blocks of the IRFS suggests no syn-depositional faulting but a late collapse near the end of the eruption (Wohletz et al., 1995). Unlike, we observe thickness differences of NYT unit between MRFS hanging wall and footwall, with more spotted records due to post-caldera erosion, exhibited as scrap recessions, and buried abrasion surfaces (Fig. 4.3a,b,d). This change in thickness might be linked to syn-depositional faulting of NYT unit (i.e., fault growth), coherently to what observed on the Coroglio cliff (Scarpati et al., 1993) and in agreement with Wohletz et al. (1995), which envisaged the collapse during the emplacement of the NYT Upper Member. Only a few observations of faulted Unit NYT are available on the ORFS (Fig. 4.3e).

Furthermore, a 4.5 km wide abrasion surface truncates the post-IC/pre-NYT Ammontatura tuff cone (Fig. 4.3e), and it is first covered by Unit S2, suggesting that the erosion took place between 15 and 12 ka (Natale et al., 2021). The presence of several faults dissecting the pre-NYT tuff cone, despite the common lack of NYT unit, suggests that faulting occurred after the formation of the tuff cone and before 12 ka, as the abrasion surface is not displaced. Hence, it follows that this faulting could be associated with the NYT collapse, supporting the nested telescopic caldera model (Smith, 1979; Spera and Crisp, 1981; Rosi and Sbrana, 1987; Orsi et al., 1996; Cole et al., 2005; Acocella, 2008; Vitale and Isaia, 2014). It is important to stress that outer ring faults were not recognized in previous works (Steinmann et al., 2016), and in addition, we attribute the reactivation of the whole caldera faults, but with smaller throw amounts, to the NYT eruption. Furthermore, it is important to highlight that we rarely identified reverse faults during the mapping of the fault strands. These reverse faults are found only in the dome area documenting near-vertical attitudes (Fig. 4.5f), typically associated with volcano-tectonic collapses (Ruch et al., 2012; Hardy et al., 2013; Vitale and Isaia, 2014). It follows that, despite multiple caldera rims and the occurrence of well documented post-NYT resurgence confined into the inner ring (Bevilacqua et al., 2020; Natale et al., 2021), there is no evidence of fault inversion as a mechanism for the caldera resurgence. This feature is supported by the evidence that the normalized displacement of caldera floor movements (both uplift and subsidence) becoming negligible toward the periphery of the radial deformation (Bevilacqua et al., 2020), suggesting that the IRFS plays as a peripheral clamp for the doming deformation, also during the long term dome resurgence (Marturano et al., 2018; Natale et al., 2021).

Results of this work indicate that the eastern margin of the CF caldera, subject to alternative interpretation by several authors (i.a. Lirer et al., 1987; Rosi and Sbrana, 1987; Orsi et al., 1996; Rolandi et al., 2003; Acocella, 2008, 2010; Vitale and Isaia, 2014; Sbrana et al., 2021) is likely the structural high of both CI and NYT collapses, with the younger NYT collapse reactivating the same faults but with smaller displacements. The outer rim of the CI caldera do not develop eastward of the Vomero hill but run underneath the Posillipo hill. Such results support the nested model of Rosi and Sbrana (1983) and Vitale and Isaia (2014). Furthermore, we observe that offshore, there are no vents younger than CI outside the ORFS and that the distribution of the post-NYT vents also follows this template. Nonetheless, we suggest that to the West, the innermost rim may connect to on-land via the Averno lake toward the Toiano plain (Fig. 4.1a), the medial to Miseno/Bacoli, and the outer passing beneath Miseno toward Monte di Procida.

The caldera collapse lowered the central part in a telescopic and concentric fashion. According to numerical and analogic models (e.g., Geyer and Martì, 2014 and references therein), the caldera formation is allowed by the simultaneous activity of normal and reverse faults that accommodate the downward roof collapse following a magmatic chamber emptying. The fault analysis provided in this work suggests that main ring faults dip of 80-70° to the caldera center and are characterized by normal kinematics. These features depict a caldera architecture different from the previous CF models that consider ring faults vertical (e.g., Orsi et al., 1996) or with reverse kinematics (e.g., Acocella, 2008). We suggest a simple model (Fig. 4.9) for the formation of the CI and NYT calderas. In the first step of the CI caldera formation (Fig. 4.9a), the downward movement of the magmatic chamber roof forms convex reverse faults on the top that initially lower the central sector of the forming caldera. The continuation of the roof sinking (Fig. 4.9b) triggers the formation of normal faults on the top while the CI deposits form; eventually, new deep-rooted reverse faults form in the center area to accommodate the horizontal component of the normal ring faults (Fig. 4.9b). In this case of the NYT caldera formation, new reverse faults form (Fig. 4.9d). Subsequently, the central area collapses and allows the extensional reactivation of the ring faults (Fig. 4.9e).

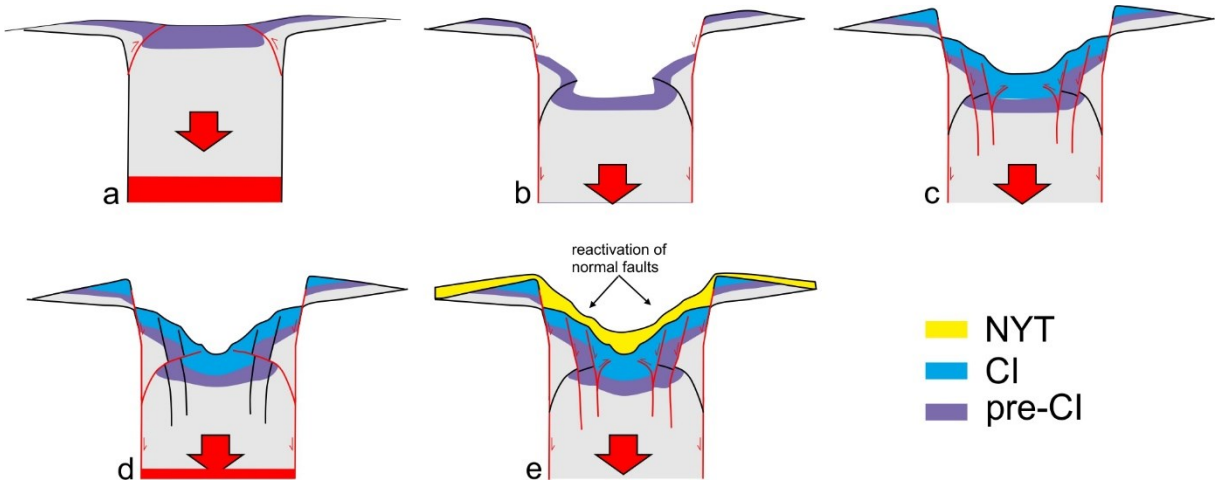

Figure 4.9. Cartoon showing a 2D model of the formation of CI (a-b) and NYT (c-d) calderas. See the text for the explanation. Abbreviations: CI, Campanian Ignimbrite; NYT, Neapolitan Yellow Tuff.

4.8.2 Dome faults

The offshore dome is highly affected by faults (Fig. 4.5a, f). In particular, the faults are mainly arranged in a NE-SW to NNE-SSW depressed structure (Fig. 4.5e), made up of a series of high-angle graben and half-graben that lower the culmination of the resurgent dome. Faults in this area of the gulf were mapped by several authors (Colantoni, 1972; Sacchi et al., 2014; Natale et al., 2020). Nonetheless, the detailed study provided in this work allows a much more comprehensive geological reconstruction. The central depressed zone is bounded by two structural highs, to the West and the East, corresponding to the Rione Terra tuff promontory and La Pietra tuff, respectively (Figs. 4.1a and 4.5a; Natale et al., 2021). It is important to remark on the correspondence between the morphostructures in the continental and offshore sectors. These faults propagate through the inner continental shelf to the coastal part, whereas vertical displacement gently decreases southward. On the other hand, the E-W faults acted simultaneously with the NE-SW/NNE-SSW sets, accommodating the volcano-tectonic collapse following the AMS eruption at 4.55 ka (Natale et al.; 2021), similarly to the on-land faults affecting Epoch 3 rocks (Vitale and Isaia, 2014; Isaia et al., 2019; Vitale et al., 2019; Bevilacqua et al., 2020; Natale et al., 2020; 2021). This important event was marked by the deposition of the transgressive Pozzuoli Unit, or locally to the formation of a paleosol (Isaia et al., 2009; 2019; Vitale et al., 2019; Natale et al., 2021). Furthermore, we cannot exclude that similar volcano-tectonic processes occurred earlier, given the resemblance with the ground deformation linked to Pomici Principali eruption (PP, 12 ka, Lirer et al., 1987; Di Vito et al., 1999; Smith et al., 2011), as evidenced by Natale et al. (2021). In fact, as described by Vitale and Isaia (2014) and Vitale et al. (2019), NW-SE and NE-SW fault sets are considered older and tectonic-inherited structures, which host the sediments of the La Starza unit, whose major thickness are recorded after the emplacement of PP tephra (Giudicepietro et al., 1993; Isaia et al., 2019). In this regard, we propose that such structures might be the surficial expression of lithostatic collapses at reservoir scale connected to large-volume explosive eruptions (> 1 km3 DRE), which is the case of Agnano-Pomici Principali and Agnano-Monte Spina eruption (Di Vito et al., 1999; De Vita et al., 1999; Smith et al., 2011).

Nonetheless, other authors (i.a., Corradino et al., 2021) refer to the faults due to resurgence-related extension on the dome apical zone, following the successful application to other caldera settings (e.g., Urbani et al., 2020). However, several features in the Campi Flegrei offshore indicate that this interpretation is geologically unapplicable. In fact, the authors associate these

faults to continuous resurgence, in analogy to analog model experiments (i.a., Brothelande and Merle, 2015). Nonetheless, the authors furnished no evidence of incremental displacement despite the documented long-term history of the ground uplift at CF (Isaia et al., 2019 and references therein). Furthermore, the near-vertical attitude of these faults (Fig. 4.5j) indicates a negligible or null layer-parallel extension. These features, among other indications, bring the interpretation toward the reactivation of sub-vertical fractures linked to inherited, well-known, tectonic structures (Vitale and Isaia, 2014; Vitale et al., 2019). On the other hand, the valley-ponding deposits occur along subsequent channels set on the NE-SW and NNE-SSW faults, also evident by the bathymetry (Figs. 4.1a, 4.4, 4.5a, 4.7f). Furthermore, faults do not crosscut the abrasion surface developed during the Epoch 3b dome activity (Fig. 4.7f; Natale et al., 2021).

4.8.3 Radial analysis

The radial analysis indicates that ring faults are mostly tangential to the caldera center (Fig. 4.6a, b). The clustering of both fault systems around the azimuth 90° could suggest that an N-S extension was active during the CF volcano-tectonic activity, affecting the geometry of the caldera ring and dome faults. Nonetheless, as it stands, we do not know if this extension had been synchronous to CI caldera collapse or subsequent. The map of Figure 4.5a shows some significant geometric kinks of the fault strands, especially for the IRF, which display NE-SW and NW-SE polygonal segments that diverge from the depocenter-like field. Moreover, this fault section of the fault zone is bypassed in the footwall by a tangential strand that is more adequately oriented to the depocentric field. In addition, structural analysis performed on-land (i.a., Vitale and Isaia, 2014) suggests that the N-S extension is younger than NE-SW and NW-SE extensions, such as observed in the Campania Plain (Cinque et al., 2000; Caiazzo et al., 2006). Furthermore, this orientation of the extensional field is similar to the recent deformation of the CF caldera, such as observed from the faults crosscutting the 3a and 3b Epoch deposits in the central sector (Vitale et al., 2019), the stress field carried out by the focal mechanisms inversion of the 1983-1984 unrest (Orsi et al., 1999), and current stress field (La Rocca and Galluzzo, 2019). The ~N-S extensional field is also marked by graben-like faults in the ring fault zone and the dome area (Figs. 4.5a and 4.7d), and by the motion of adequately oriented major caldera faults (i.e., E-W), as described for medial and outer ring fault zones (Fig. 4.3c,

d), which overlap with the computed focal mechanism of recorded deep earthquakes (INGV, 2022).

Furthermore, the faults affecting the dome area of the Pozzuoli Gulf are dominated by NE-SW-oriented structures and subordinately by E-W faults. Regarding NE-SW faults, we want to stress that these high-angle faults are likely related to the reactivation of older faults. Such behavior is also observed in other collapse-bounding structures like the Agnano caldera (De Vita et al., 1999; Isaia et al., 2021), where the mutual crosscutting relationships are also evident. Results of the structural analysis envisage the common occurrence of high-angle faults and the activation of former fractures and faults as suggested by Vitale and Isaia (2014) and documented in this study by the dip angle distribution of dome faults peaking around 85° (Fig. 4.5j).

4.8.4 Evolutionary model in the last 40 kyr

To summarize the interplay between the fault activity and the sedimentation, we provide a simplified 2D volcano-tectonic evolutionary model of the shallow part of the CF caldera where the normal faults formed according to the model of Figure 4.10. The proposed model considers the CF evolution from the Campanian Ignimbrite caldera formation (40 ka) to the Monte Nuovo eruption (1538 CE, Fig. 4.10).

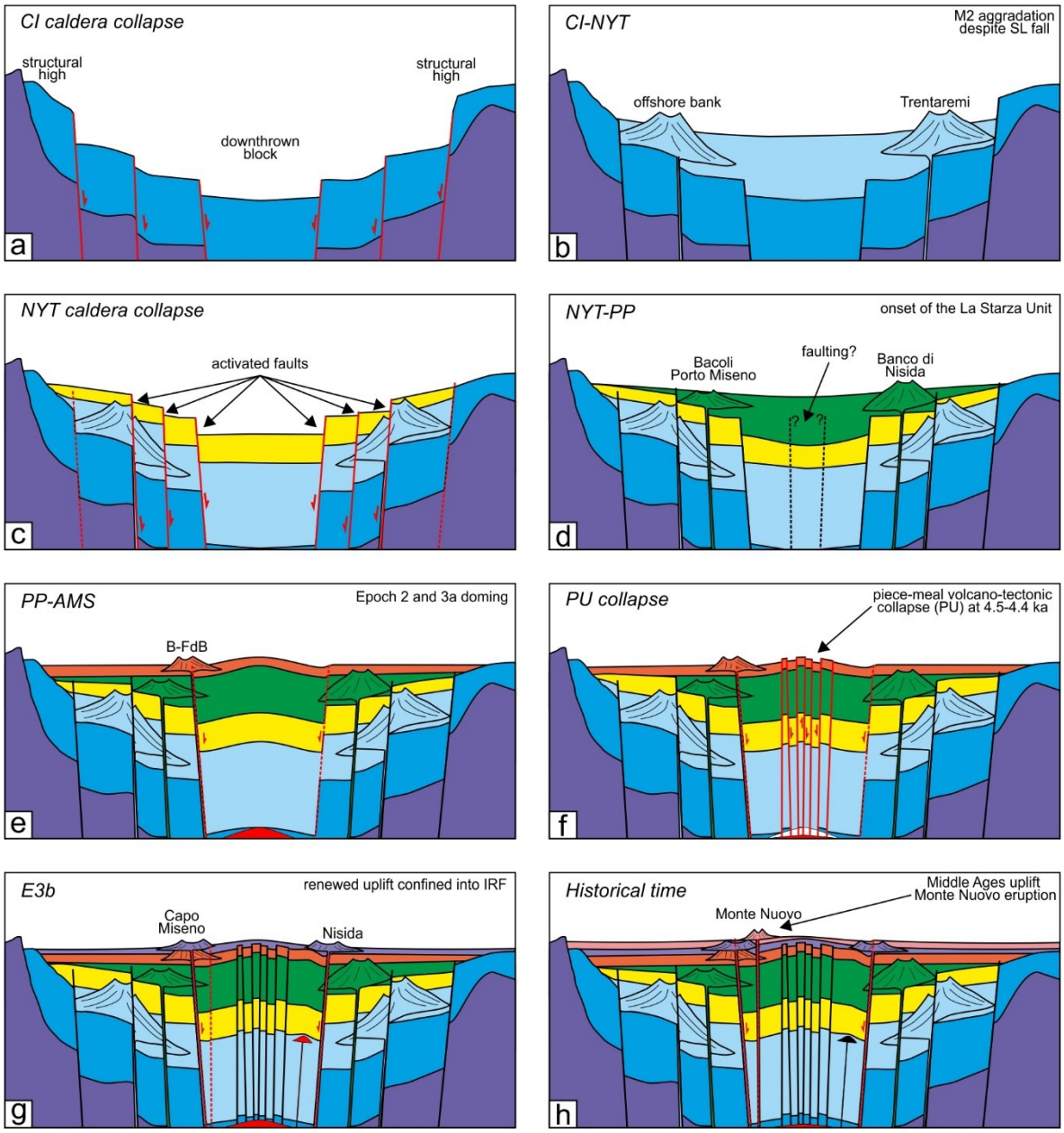

Figure 4.10. Multi-step 2D evolutionary model of the offshore caldera since the CI collapse. (a) CI caldera collapse. (b) Marine sedimentation despite sea-level fall and post-caldera ring volcanism. (c) NYT caldera collapse, with likely syn-eruptive collapse on outer and medial ring fault zones. (d) Ring eruptions during Epoch 1 and intra-caldera subsidence following PP eruption. (e) Ring eruptions and renewed intra-caldera doming during Epoch 3a. (f) Volcano-tectonic collapse following AMS eruption along inherited tectonic structures. (g) Rapid intra-caldera uplift during Epoch 3b with terminal ring eruptions. (h) Renewed intra-caldera uplift preceding Monte Nuovo eruption. Abbreviations: CI, Campanian Ignimbrite; NYT, Neapolitan Yellow Tuff; PP, Pomici Principali; AMS, Agnano-Monte Spina; PU, Pozzuoli Unit; E3b, Epoch 3b.

4.8.4.1 Stage 1 – Campanian Ignimbrite collapse

In the first step of the model (Fig. 4.10a), we reconstructed the CI collapse, with older rocks only exposed outside of the outermost structural highs, which in the offshore sector are represented by the old volcanic banks PentaPalummo, Miseno, and Pampano Mt Dolce. In the continental part, these are represented by the Monte di Procida and Acquamorta volcanoes, Punta Marmolite and Cuma lava domes and tephras, pre-CI rocks exposed at Camaldoli and the tuff cones and rings cropping out at Capodimonte, Vomero, C.so Vittorio Emanuele and Mt Echia (Sbrana, 2015).

4.8.4.2 Stage 2 – Intercaldera period

Following the CI eruption, the ORFS controlled the position of the post-CI vents, which are all located within or across the collapsed area (Fig. 4.10b). Despite the consistent sea-level fall proceeding toward the Last Glacial Maximum (Fig. 4.8), marine and volcaniclastic sediments have been deposited in the depocenter newly formed by the collapse. Among the visible post-CI centers near the coast are the Torregaveta volcano, Trentaremi tuff ring, and the Ammontatura tuff cone, described for the first time in this paper. Other inter-caldera eruptions are reported in literature, such as Monterusciello, Verdolino, Masseria del Monte, Monticelli and Lagno Amendolare (Sbrana et al., 2015).

4.8.4.3 Stage 3 – Neapolitan Yellow Tuff collapse

We have evidence that the NYT collapse has occurred on the same CI ring faults. According to the model of Figure 4.9c,d, the caldera collapse allowed the reactivation of CI faults proceeding from outside to inside, marked by the syn-depositional activation of the ORFS and MRFS ring faults and late activation of the inner (Fig. 4.10c).

4.8.4.4 Stage 4 – Pre-doming Post-NYT activity

Afterward, the post-NYT sedimentation can be divided into pre-doming (Fig. 4.10d) and syn-doming (Fig. 4.10e, f, g). Nonetheless, shortly after the NYT eruption, the volcanic activity clustered on the ring faults (Di Vito et al., 1999; Orsi et al., 2004; Bevilacqua et al., 2016). The Plinian eruption of Pomici Principali was quickly followed by a strong subsidence (Natale et

al., 2021), which probably activated several faults creating more accommodation space to host the sediments of the La Starza unit (Vitale et al., 2019).

4.8.4.5 Stage 5 – Syn-doming Post-NYT activity

The caldera resurgence that occurred during Epochs 2 and 3 (i.a., Isaia et al., 2019; Natale et al., 2021) is confined inside the IRF (Bevilacqua et al., 2020), promoting the creep reactivation of the IRF and clustering volcanism between IRF and MRF during Epoch 2 and 3a (Fig. 4.10e). This doming phase inverted the depocenter of the caldera and lasted until the AMS eruption. According to Isaia et al. (2019), a ca 60-80 m uplift of the central sector of the CF caldera occurred before Epoch 3a.

4.8.4.6 Stage 6 – Pozzuoli unit stage

Fault abuttal relationships and stratigraphic architecture allowed us to constrain the formation of the dome apical faults as directly linked to the AMS collapse (4.55 ka, Fig. 4.10f). Following this event, the caldera experienced strong subsidence with the deposition of the transgressive Pozzuoli unit (4.44 ka, Isaia et al., 2009).

4.8.4.7 Stage 7 – Epoch 3b rapid uplift

Renewed significant ground uplift, paired with seismo-volcanic crisis (Vitale et al., 2019), predates the volcanic eruptions during the Epoch 3b, with multiple dome intrusions and with the final eruptions (i.e., Nisida, Capo Miseno, and Fossa Lupara; Smith et al., 2011) clustered along the ring faults (Fig. 4.10g).

4.8.4.8 Stage 8 – Monte Nuovo eruption

Finally, after more than two millennia of quiescence, two centuries-long volcano-tectonic crises led to the last eruption of Monte Nuovo, in 1538 CE, again located on the ring zone (Fig. 4.10h), following a ground uplift centered at the caldera center (Di Vito et al., 2016).

4.9 Conclusions

The paper provides a detailed structural map of the Gulf of Pozzuoli, which encompasses one-third of the Campi Flegrei caldera. The interpretation of the seismic dataset from different vintages and resolutions allowed us to reconstruct the volcano-tectonic architecture of this caldera sector and image the structural evolution in the last 40 kyr. We combined the available seismo-stratigraphic reconstructions to describe the complex interplay between large caldera eruptions, caldera floor movements, volcanic activity, sea-level rise, and volcano-tectonic field. In the submerged part of the caldera, we described two main fault zones: caldera ring faults and resurgent dome faults. We identified three distinct caldera rims and associated fault zones that accommodated the CI caldera collapse at 40 ka. These rims join with the continental structural highs of Monte di Procida to the West and Posillipo to the East. Volcanic eruptions during inter-caldera periods generally occurred across the ring faults, which provided the necessary accommodation space in the caldera depocenter to accumulate the volcanic products despite the decreasing sea level.

The following caldera collapse, associated with the NYT eruption at 15 ka, differentially reactivated the preexisting caldera faults. The offshore collapse was accommodated mainly by the two innermost rims, which continue on-land in Coroglio to the East and Toiano to the West.

Considering that all ring faults show normal kinematics and generally are characterized by dip angles of 70-80°, the caldera formation models proposed in the literature for the CF caldera development do not fit this evidence (e.g. Acocella, 2010). Hence, we suggest a model for the CI caldera formation (Fig. 4.9a-d) that considers the early formation of convex reverse faults that allow the collapse of the central sector and subsequently trigger shallow normal faults. The NYT caldera formation model is similar to the previuìous CI model, with the formation of reverse faults and the subsequent reactivation of the normal ring faults (Fig. 4.9e, f).

Graben structures, multiple segmentation of the fault zones, and the reactivation of adequately oriented faults mark the occurrence of a secondary active N-S extensional tectonic field. The present-day fluid uprise along the ring faults highlights the pivotal role of these structures in conveying deep-seated hydrothermal fluids toward the surface. Furthermore, the resurgent dome faults are associated with at least one volcano-tectonic collapse that followed the Agnano-Monte Spina eruption, mainly accommodated by old NE-SW to NNE-SSW and neoformed E-W faults. Integrated geological observations suggest that these faults might also be active during precedent collapses that accommodate the sedimentation of the La Starza Unit. These faults

likely enucleate at depth and propagate upward during deflation stages, magma transfer, and large-volume eruptions.

Furthermore, understanding caldera structure and its impact on the distribution of post-caldera vents is of utmost importance to volcanic hazard assessment in such inhabited volcanic areas. As well as, observing fluid uprise across the faults, which transfer a large number of hydrothermal fluids, is of absolute importance. This feature may have implications for the geothermal potential of volcanic areas and volcano monitoring purposes. Finally, the characterization of the structural architecture of the Campi Flegrei provided in this study might also impact the provision of future scientific drilling research programs and help find the most suitable place to drill in.

Chapter 5: Volcano-tectonics in a carbonate ridge: the Middle-Late Pleistocene monogenetic eruption North-East of the Roccamonfina volcano (Taverna San Felice, Italy)

Abstract

We performed structural investigations on a magmatic dike hosted in Mesozoic carbonates and Pleistocene breccias in a quarry NE of Roccamonfina volcano (Mt Cesima ridge, southern Apennines). The dike crops out for over 250 m from the base to the top of the quarry, developing a meters-thick contact metamorphic aureole. In the upper part of the quarry, we described a stratigraphic succession made up of a series of paleosols and pumice-lapilli layers ascribable to the WTT eruptions of Roccamonfina, which is turn covered by the pyroclastic products of the feeding dike. These products consist of tens of meters thick strombolian pyroclastic sequence characterized by scoriaceous juvenile material. We measured the attitudes of dike boundaries and the fractures and faults hosted within the dike and the carbonate rocks through field survey and Virtual Outcrop Models analysis. Structural data indicate that the major dike is characterized by a segmented contact with the hosting carbonates showing a dominant E-W direction and a secondary NE-SW direction. The dike intruded within an E-W, north-dipping fault zone, active during an N-S extensional event. Before eventually reaching the surface, the dike trajectory was diverted by a pre-existing NE-SW fault zone, then fed a fissure eruption. The dike and pyroclastic sequences are furtherly dislocated by N-S and E-W trending faults, suggesting the existence of an important tectonic extensional pulse responsible for the late development of the Garigliano and Formicola grabens and resembling the pattern of rift-related extensional pulses. This dike intrusion event has to be considered independent from the dynamics of the nearby Roccamonfina and allows to postdate this monogenetic activity to be coeval to the latest stage of the volcano instead of the earliest.

5.1 Introduction

A large part of the volcanism worldwide occurs in extensional settings, including oceanic ridges, continental rift, and synorogenic back-arc basins, where the plate stress conditions favor the magma uprise (e.g., Gudmundsson, 1990; Gudmundsson et al., 1992; Rubin, 1995; Parsons

and Thompson, 1991; Favela and Anderson, 2000; Goldberg, 2010; Galindo and Gudmundsson, 2012). Volcanism in stretched crust areas can produce different kinds of volcanic structures, including fissure eruptions, vent alignments, and dikes, with a strong relationship with the tectonic features (e.g., Smets et al., 2015; De Matteo et al., 2018; Tibaldi et al., 2020, Trippanera et al., 2019, Ruch et al., 2016, Acocella, 2006; Cardello et al., 2020; Marra et al., 2021). However, understanding the interaction between volcanism and tectonics in time is challenging, especially in areas where volcanism, might be in complex interplay with the complex tectonic structures which makes non trivial to disclose volcano-tectonic interactions. Such is the case of the Pleistocene Italian volcanism localized along the margin of the Tyrrhenian Sea, a back-arc basin resulting from the subduction of the oceanic crust beneath the Europa plate starting the Serravallian (Scandone et al., 1991;Vitale and Ciarcia, 2013). The extension associated with the back-arc opening progressively migrated following the thrust front movement towards NE/E for the southern Apennines and towards SE/S for the Calabria-Peloritan Terrane (Vitale and Ciarcia, 2013 and references therein). In the Early Pliocene, the axial part of the orogen has been involved in a renewed Out-of-sequence collision phase that led to the overriding of platform units on the wedge-top basin (Vitale et al., 2020; Cardello et al., 2021). Starting from the Pleistocene, the extension affected the presently exposed chain (Bergomi et al., 1969; Nicotera and Civita 1969; Ippolito et al. 1973; Giordano et al., 1995; De Rita and Giordano, 1996; Tavani et al., 2021; Alessandri et al., 2021). This event formed different structural depressions between Lazio and Campania regions (Fig. 5.1a), hosting the volcanoes of the so-called co-magmatic Roman and Campanian Provinces (Washington, 1906, Peccerillo et al., 2017). Accordingly, geochemical and petrological properties indicate that the extensional tectonics drove their emplacement (Di Girolamo et al., 1988; Lustrino et al., 2011; Peccerillo et al., 2017). Amongst the structural depressions, the most significant structure is the Campania Plain, hosting the Campi Flegrei, Ischia, and Somma-Vesuvius active volcanoes (Fig. 5.1a). Furthermore, northward of the Campania Plain is localized the Garigliano Graben where the Roccamonfina volcano localizes, active in 546-50 ka (Tedesco, 1965).

Despite the vast volcanological and petrological literature about the Italian volcanoes, the knowledge of the structural mechanisms that acted during the early establishment of the Plio-Pleistocene central-southern Italy volcanic activity and the interplay between volcanism and tectonics in time has to be investigated (e.g., Giordano et al., 1995; Tramparulo et al., 2018; Isaia et al., 2019; Vitale et al., 2019; Cardello et al., 2020; Marra et al., 2021). Furthermore, we know little about the characteristics of the volcano emplacement mechanism with the formation

and evolution of the hosting structural depressions. Whit this in mind, this work aims to investigate the relation between the formation of the Garigliano Graben and the volcano-tectonic structures, and how faults may affect dike propagation paths (Gudmundsson, 1983; 2011; 2020) in analogy with hydraulic analogues (Davis et al., 2012; 2013; Lacazette and Geiser, 2013). Hence, we analyzed an example of a dike and a related vent hosted in Mesozoic carbonates, a few km North East of Roccamonfina. We focused particular attention was paid to the study of a 200 m long dike beautifully exposed in a quarry, representing the single example in the whole Pleistocene Italian volcanic area. We also investigated the role of tectonics in driving the intrusion and how this affected dike path (Gudmundsson, 2011; 2020), and dikes contact morphology (Poppe et al., 2020). Mode I fracture propagation is the main mechanism of the intrusion of magma within an elastic medium with the magma front breaking through the host rock as hydraulic fractures tapering forward anticipated by a tip cavity usually filled with fluids (Dahm, 2000; Delaney and Pollard, 1981; Lister, 1990; Pollard and Muller, 1976). Depending on the depth and width of the front dike tip, this kind of propagation mode may result in different surface deformation patterns and faulting (Trippanera et al., 2015).The other mechanism for magma sheet propagation are the mixed modes (Mode II and III), in which the blunt indenter, usually depending on high magma viscosity or from low-confining pressures, the dike propagation induces a shear folding and faulting of the host-rock, or even fluidization for organic-rich medium (Galland et al., 2019; Magee et al., 2019; 2021; Matiieu et al., 2008; Spacapan et al., 2017; Schofield et al., 2012). Dike swarm intrusions have often been used to proxy extensional events at a regional scale (Gudmundsson et al., 1990; Goldberg et al., 2010; Galindo and Gudmundsson, 2012; Bonali et al., 2019). The NW-SE and NE-SW extension directions are very common in the southern Apennine, the Garigliano Plain, Campania Plain and the Neapolitan volcanoes (Ortolani and Aprile, 1978; Ciaranfi et al., 1983; Bosi and Giordano, 1997; De Rita and Giordano, 1996; Cinque et al., 2000; Caiazzo et al., 2006; Vitale and Isaia, 2014; Boncio et al., 2016; Galderisi et al., 2017; Tramparulo et al., 2018).

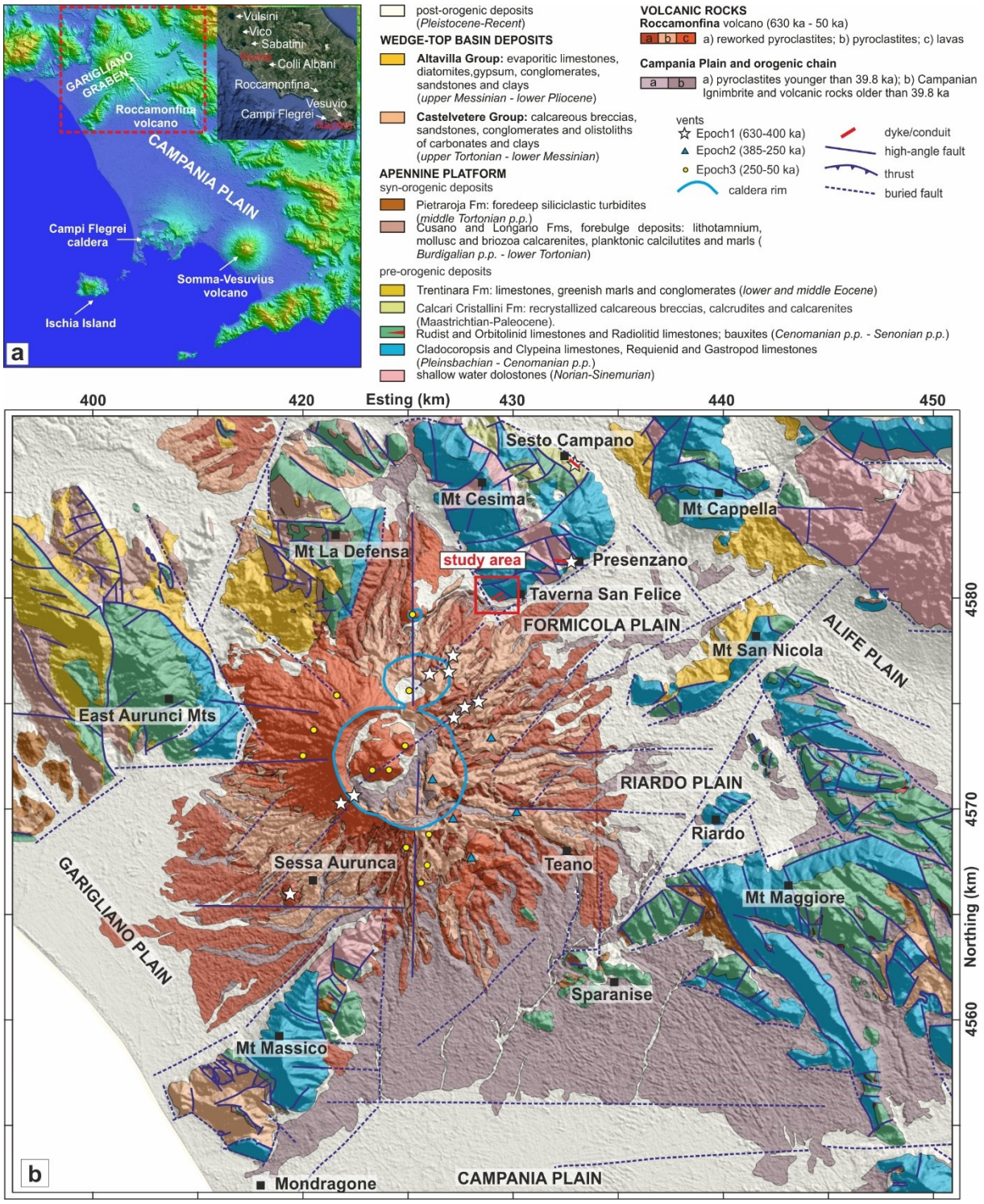

Figure 5.1. (a) DEM of the Campania Plain-Garigliano Graben area. (b) Geological map of the Garigliano Graben (modified after Vitale and Ciarcia, 2018).

5.2 Geological setting

The study area (Fig. 5.1b) is located within the NE-SW trending Garigliano Graben (Giordano et al., 1995; De Rita and Giordano, 1996), a structural depression bounded by some Meso-Cenozoic carbonate ridges to SW (Mt Massico), SE (Mt Maggiore), NW (Aurunci Mts), N (Mt La Defensa) and NE (Mt Cesima). These mountains are made of pre-orogenic shallow-water Triassic-Cretaceous carbonates and, locally, by Eocene and early-to-middle Miocene limestones. The southern part of Mt Cesima is a S-verging anticline made of calcareous succession, including Jurassic shallow-water oolitic limestones passing upward to Cretaceous rudist limestones finally Maastrichtian-Paleocene recrystallized calcarenites and breccias (Calcari Cristallini Fm; Vitale and Ciarcia, 2021). Finally, syn-extensional early Pleistocene continental sediments (Breccia Mortadella; Demangeot, 1965; D'Agostino et al., 1998), volcanic products of Roccamonfina (546-50 ka) and Campanian Ignimbrite (40 ka) seal the sedimentary pile. The Garigliano Graben formed in the middle Pleistocene (Giordano et al., 1995), including the plains of Garigliano, Riardo, and Formicola surrounding the Roccamonfina volcano edifice (Fig. 5.1b). NE-SW major high-angle faults and subordinately NW-SE faults bound the tectonic depression. Younger E-W and N-S faults crosscut the carbonate ridges around the graben and the Roccamonfina edifice (e.g., De Rita and Giordano, 1996).

Roccamonfina is a volcanic complex belonging to the Volsci (former Ernici) –Roccamonfina volcanic province on the Tyrrhenian margin of central-southern Italy, located between the Roman (to the north) and Campanian (to the south) magmatic provinces (Peccerillo, 2005). These provinces include the volcanic complexes of Vulsini (0.9-0.12 Ma), Vico (0.9-0.095 Ma), Sabatini (0.6-0.09 Ma), Colli Albani (0.7-0.03 Ma), Roccamonfina (0.63-0.05 Ma), Ischia (0.2 Ma-active), Campi Flegrei (0.08 Ma-active) and Somma-Vesuvius (0.3-active) (Fig. 5.1a). These volcanoes are classically associated with arc-tectonic calc-alkaline to ultra-potassic volcanism (Peccerillo, 2005). Before forming the Roccamonfina volcano in the middle Pleistocene, the area was interested in an intense eccentric magmatic activity along anti-Appeninic (NE-SW) lineaments (Sgrosso and Aiello, 1963; Di Girolamo, 1972, 1991; Bosi, 1994; De Rita and Giordano, 1996). The eruptive history of the Roccamonfina volcano consists of three main periods (called Epochs; Rouchon et al., 2008). In the first stage (546 and 358 ka; Giannetti, 2001), large volumes (about 100 km^3) of lava have been emplaced, interspersed with small volume ignimbrites, and Strombolian to Subplinian eruption deposits which formed the ancient stratovolcano (Tedesco, 1965). Contemporaneously, High-Potassic series (HKS)

products, such as phonolitic domes and scoria cones, were emplaced along NE-SW regional lineaments (Tedesco, 1965; De Rita and Giordano, 1996). The Brown Leucitic Tuff (BLT) emplacement, a 3-to-5 km^3 lithic-rich ignimbrite sequence with leucite-bearing pumices, also marks the transition to the second stage of activity (Luhr and Giannetti, 1987; De Rita and Giordano, 1996; Rouchon et al., 2008; Conticelli et al., 2009). This eruption, which occurred at 354 ka, produced a sector collapse of the volcano edifice toward NE and marked the transition from the HKS and Potassic series (KS) products. The Second Epoch (354-230 ka) is characterized by the formation of ca. 10 km^3 of trachytic and leucite-bearing trachy-phonolitic pyroclastic deposits of the White Trachytic Tuffs (WTT). These were produced in different explosive events mainly characterized by the emplacement of pyroclastic density currents (PDC) deposits and Plinian fallout units (Giannetti and Luhr, 1983; Ballini et al., 1989; Giannetti, 1990; Cole et al., 1993; De Rita et al., 1994; Giordano, 1995; De Rita and Giordano, 1996, Rouchon et al., 2008). WTT is furtherly divided into Lower and Upper WTT, separated by a number of monogenetic eruptions of trachybasaltic to shoshonitic compositions, including the Colle Friello cone (Rouchon et al., 2008). UWTT occurred at 230 ka. During the youngest Epoch (230-148 ka), the Roccamonfina volcano mainly produced effusive products such as basaltic-shoshonitic domes and flows of the KS magma series (Appleton, 1972), also forming the massive summit domes and many parasitic flows and cones (Giannetti and Luhr, 1983) along N-S lineaments. The major eruption in this time frame was the Yellow Trachytic Tuff (YTT), a 0.57 km^3 ignimbrite eruption, which has also produced a maar, dated at 227 ka (Giannetti, 1996) located in the northern part of the volcanic complex (Luhr and Giannetti, 1987; Cole et al., 1992; Rouchon et al., 2008). The volcanic successions of the Roccamonfina volcano are capped by the Campanian Ignimbrite (39 ka; Giaccio et al., 2017; Silleni et al., 2020) originated in the Campi Flegrei caldera.

In the areas surrounding the Roccamonfina, many examples of magmatic dike and vents are reported in the literature.

5.3 Materials and methods

The main outcrop area is the active cement quarry of Taverna San Felice, where access has been granted by local authorities during non-extraction days. Since 2019, we have repeatedly performed structural surveys of the area in accordance with the evolution of excavation fronts and accessible outcrops. For non-safe conditions, we replaced the on-site survey with

Unmanned Aerial Vehicle (UAV)-based photogrammetric surveys. We used a DJI Mavic Air 2 commercial drone using the necessary licenses and insurance to flight in the study area. The several surveys, conducted from September 2020 to January 2022, were conducted manually collecting multiple sets of images, to build the photogrammetric model of the quarry and surrounding areas. The UAV images were acquired using a DJI Mavic Air2 UAV with a 1/2" CMOS 12 MP sensor and 24 mm-equivalent focal length, with 4:3 aspect ratio in the 12 MP camera configuration to maximize camera resolution. The average front and side overlap of the pictures is around 80 %, in accordance to the best practice for UAV surveys (James et al., 2012; USGS, 2017).

We analyzed dike contacts, faults, and fractures hosted in the dike, associated products, and Mesozoic carbonates. Fault data, including fault plane attitude, striation orientation, and kinematics, have been analyzed with Tectonics FP and Open Stereo Open software. Furthermore, we analyzed and processed aerial images captured by UAV to build photogrammetric Virtual Outcrop Models (VOMs) via Agisoft Metashape software, whereas the structural data on reconstructed VOMs were performed with the GeoVis3D Open software.

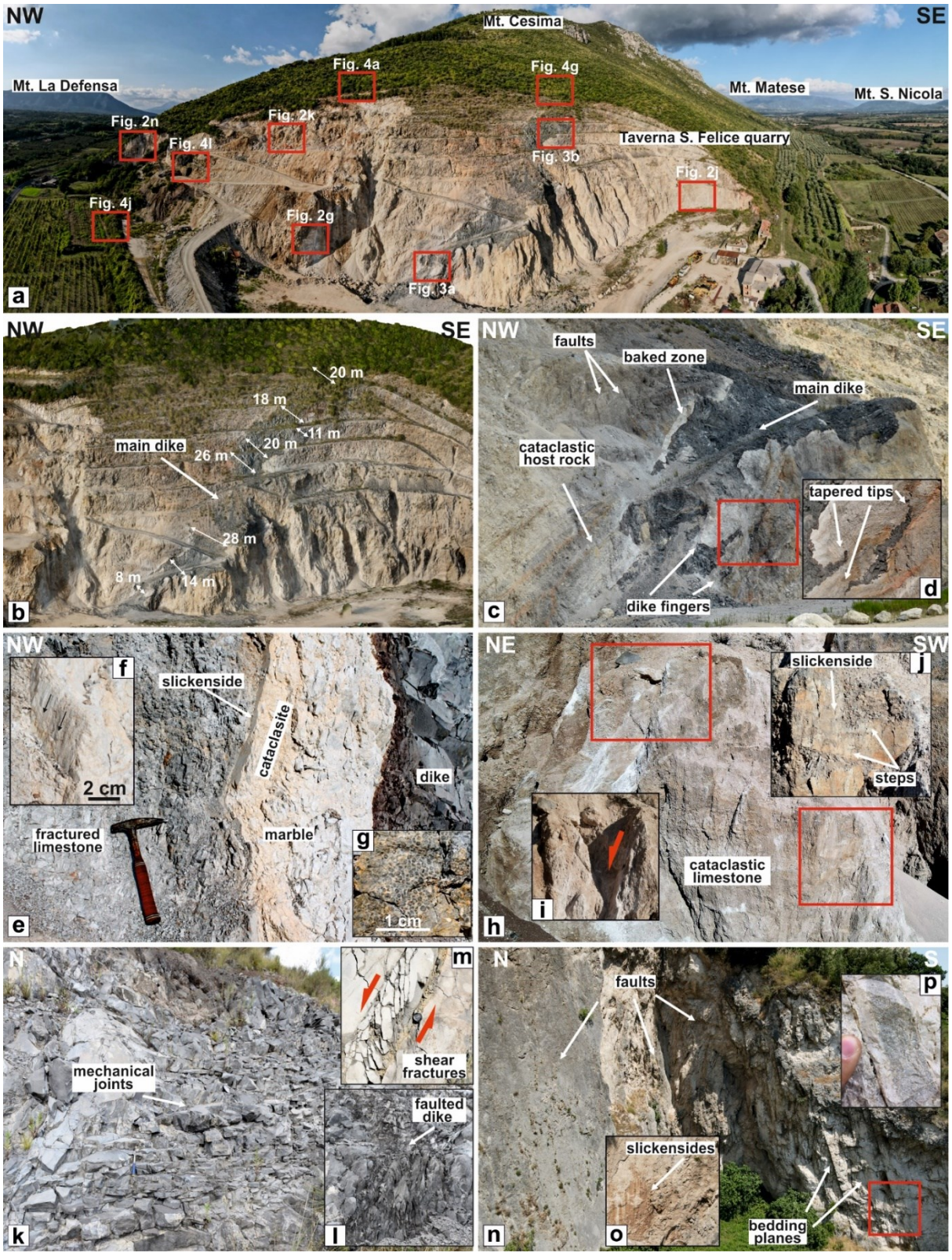

Figure 5.2. (a) UAV wideangle picture of the Taverna San Felice quarry showing the main study area, red boxes indicate the zoomed sections (b) Texturized UAV Photogrammetic 3D model of the quarry, documenting dike thickness measurement along its visible strike. (c) Picture broadly taken parallel to dike stike in the basal portion, where the main dike is hosted in a cataclastic limestone forming a marble contact aureole. (d) Zoomed photo showing an isolated dikelet with both lateral tip showing tapered ends. (e-g) Zoomed field pictures showing the marble contact aureole and the polished fault planes. (h) UAV picture indicating some North-dipping E-W normal

faults (j), and NE-SW normal faults (i). (k) Severe jointing in the medial part of the dike showing further faulting and fracturing (l-m). (n) UAV photo taken in the abandoned quarry showing the nearly vertical South-dipping limestone beds affected by both E-W and NE-SW faults.

5.4 Geological and structural survey

5.4.1 Quarry – Dike and host rock

In the quarry, the excavation activity, operating since 1981, has progressively exposed for a length of over 250m, a large magmatic dike (here on called the main dike), which is a rare example in the Italian peninsula of a Pleistocene magmatic sheet hosted in a sedimentary succession (Fig. 5.2a). This structure crops out in the central part of the quarry, developing with a W-E orientation at its base, whereas it is orientated mainly along the NE-SW direction from the middle toward the topmost exposition. The main dike also shows some N-S/NW-SE trending bends. Figures 5.2 and 5.3 show the general features of excavation fronts and some details. Figure 5.2a illustrates the main excavation fronts and steps, with the red boxes indicating some detailed pictures. The main dike shows a variable thickness ranging between 5 and 28 m (Fig. 5.2b), with a smaller aperture at the base, as retrieved by VOMs. (Fig. 5.2b). In general, the thickness varies sharply along the dike strike. The dike dips by ca. 55° toward NNW at the base, where are also well visible some minor dikes (Fig. 5.2c), also displaying both lateral tips. The host rock (Fig. 5.2c) is characterized by a thermometamorphic marble aureole in its basal part. In particular, along the contact, polished fault planes (Fig. 5.2e) with kinematic indicators (Fig. 5.2f) occur; these faults are parallel to the dike-host rock contact. Relicts of sedimentary features of the oolitic Jurassic limestone are present (Fig. 5.2g). Both limestones and dikes are affected by several faults and fractures. In particular, the limestone is pretty damaged and affected by cataclasis, and the bedding planes are barely recognizable. Faults (Fig. 5.2h) are visible as polished surfaces (Fig. 5.2j) or fine-grained deformation bands (Fig. 5.2i). The main dike shows diffuse jointing (Fig. 5.2k), faulting (Fig. 5.2l), and related shear fractures (Fig. 5.2m). Fortunately, in the nearby abandoned quarry (Fig. 5.2a), the bedding planes are visible and steeply dipping toward the south (Fig 5.2n), with many high-angle faults with a similar attitude (Fig. 5.2o). Stratigraphic polarity retrieved by sedimentary indicators (Fig. 5.2p) suggests an upward younging.

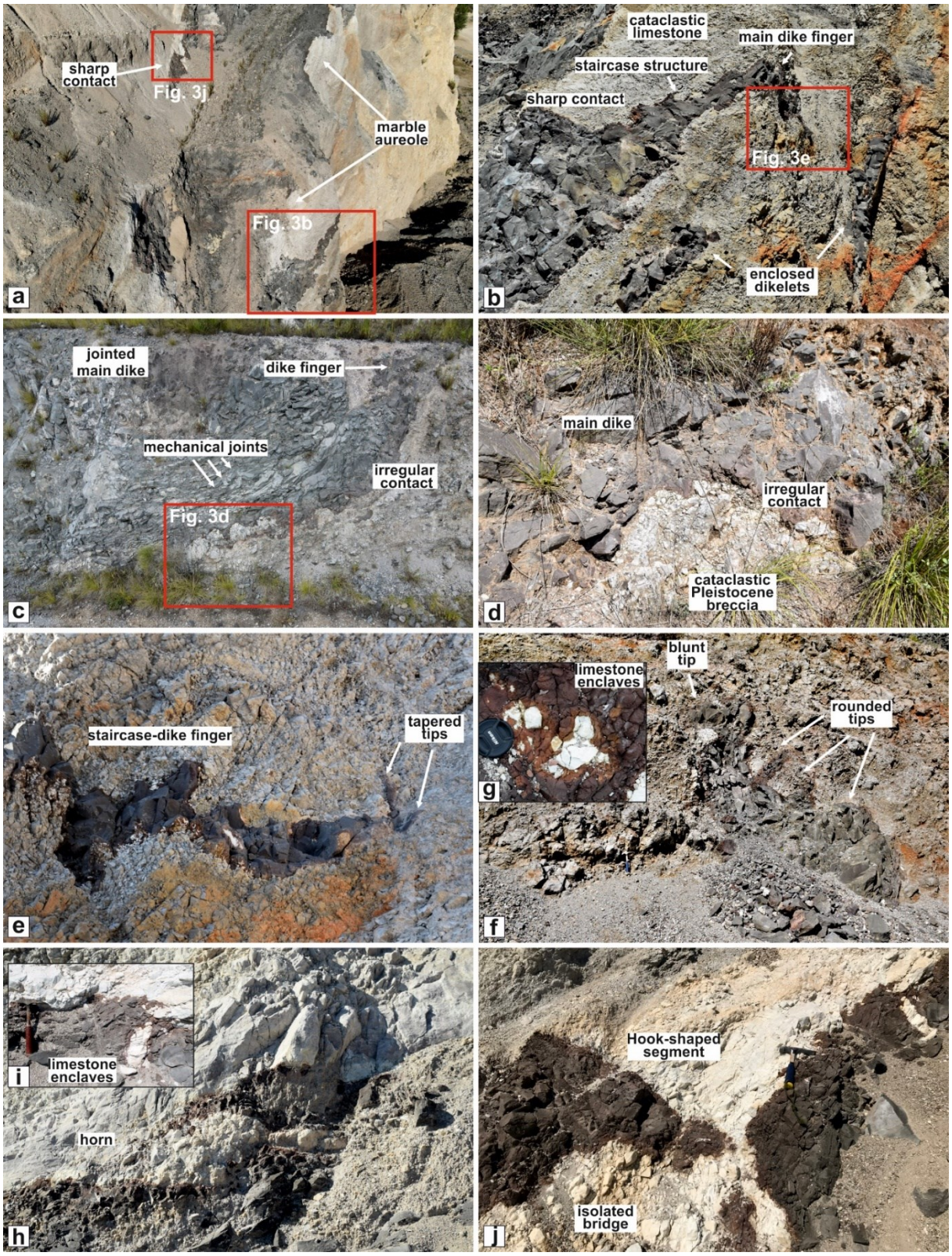

Figure 5.3. (a) UAV oblique view of the main dike showing the sharp contact between the dike and the host rock at the base of the quarry. (b) UAV picture of the upper portion of the dike, hosted in the Pleistocene breccia, with a well-developed jointing and an irregular contact. (c) Dike fingers and enclosed dikelets with rounded to tapered tips. (d) Zoom field photograph of the irregular dike-host rock contact withinh the Pleistocene breccia. (e, f) Detail pictures of the dike terminations showing sensible differences between cataclastic limestone and Pleistocene

breccia country rocks, resulting in sharp staircase-like contacts and wedge-like tip in the lower part of the quarry and, irregular contact and rounded tips in a embedded dikelet in the upper part of the quarry, respectively. (g) Detailed picture of calcinated carbonate enclaves with reddish oxidized aureole. (h) Incomplete (soft linked) dike horn (failed magma path) almost insulating a carbonate bridge. (i) Detail field photograph showing large carbonate enclave. Carbonatic enclaves in the lava producing an oxidation aureole. (j) Almost hard-linked hook-shaped magma segment enclosing the carbonatic host rock.

In general, the contact characteristics between the dike and the host rock vary significantly along its length. A sharp marble aureole occurs along the boundary between the dike and the cataclastic carbonates (Fig. 5.3a), whose thickness varies between 1 and 4 m. The main dike also features many minor finger-like dikelets that depart from the main sheet or are enclosed in the host rock (Fig. 5.3b). On the contrary, when the dike intrudes the Pleistocene breccia (Fig. 5.3c), the margin is irregular and blunt (Fig. 5.3d). In the basal section of the quarry, these minor dikes show a length varying between 2 and 7 m, with an average thickness of 80 cm, pinching out toward the tips. The dike terminations can vary from wedge-like to rounded tips (Fig. 5.3 e, f). Some smaller dikelets show staircase-like shape. Frequently, host-rock enclaves occur along the margin (Fig. 5.3g, i). Some other features, such as dike failed-path (horns), occur both as a partial linkage (soft-linked, Fig. 5.3h) or as complete linkage (hard-linked; fig. 5.3j). It is common to find along the margin limestone enclaves (Fig. 5.3i) and kinematic flow indicators such as stretched vesicles and preferentially oriented phenocrysts (Fig. 5.3g and k).

5.4.2 Quarry – Strombolian deposits and vent area

Within the topmost portion of the quarry (Fig. 5.4a) and preserved in the topographic lows (Fig. 5.4b), we document the finding of a pyroclastic succession up to 15m thick. The most significant thicknesses occur in the top-right corner of the quarry. These deposits cover the cataclastic limestones and the Pleistocene breccia, which are in turn covered by a 3-4 m thick altered, pedogenized reddish pyroclastic material, interspersed to variably altered clast supported pumice lapilli. This deposit of 60 cm thick clast-supported white to grey pumice lapilli layer (Fig. 5.4c) is located on top of up to 2.8m thick profoundly altered and pedogenized layer. This layer of pumice-lapilli passes upward to a 1.6 m thick reworked and altered sequence evolving upward to a mature red paleosol (Fig. 5.4a, f).

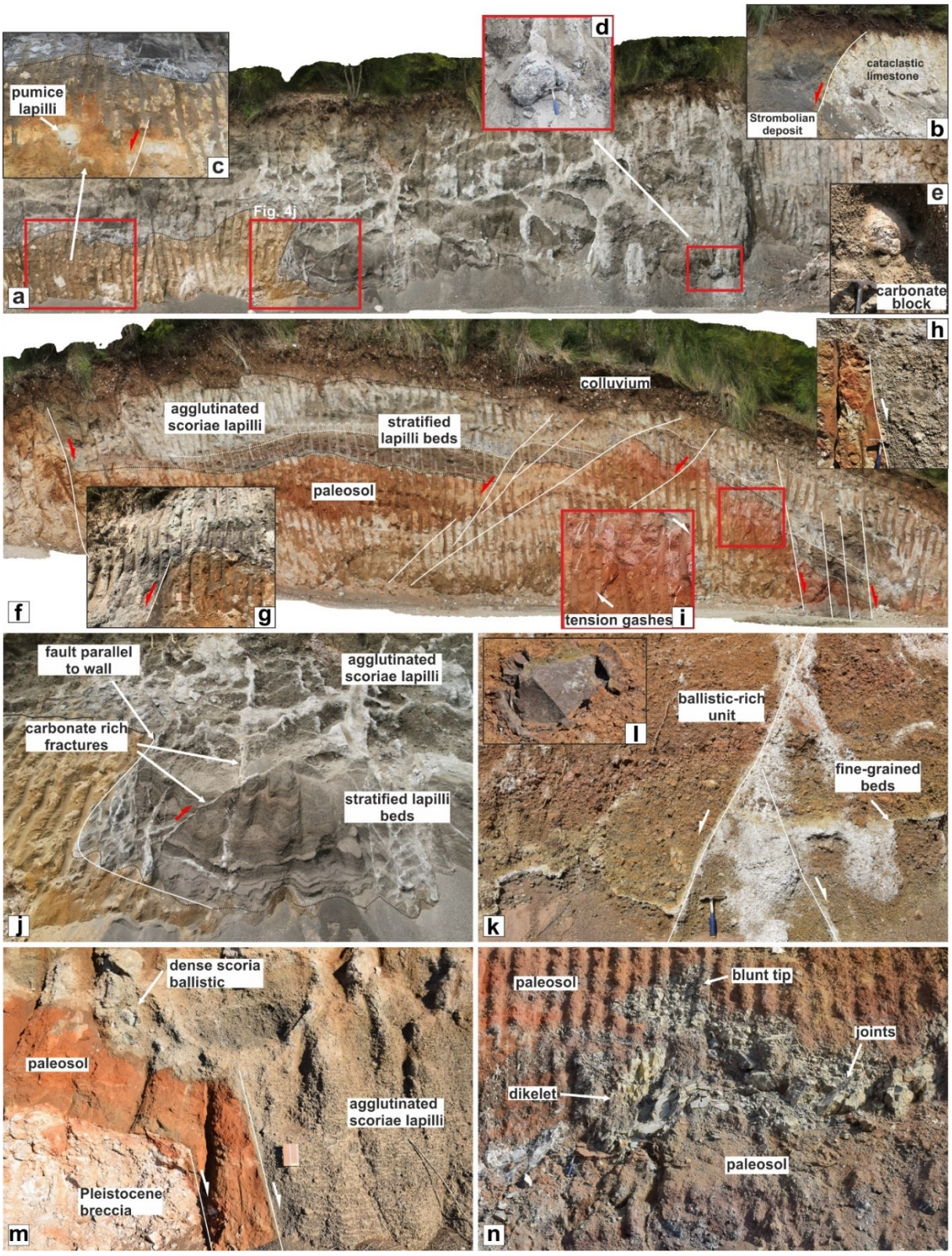

Figure 5.4. (a) Texturized UAV Photogrammetic 3D model of the uppermost excavation front showing the strombolian pyroclastic sequences, preserved in structural lows. Inset shows the pumice-lapilli layer enclosed in the thick paleosol. (b) N-S fault putting in structural contact the pyroclastic deposits and the limestone. (c) carbonatic ballistics enclosed in the pyroclastic succession. (d) Detail of structural contact between stratified scoriaceous lapilli beds and underlying paleosol sequence, fault is nearly parallel to the front. (e) Conjugate faults affecting the upper Strombolian succession, characterized by the alternance of massive bomb-rich and fine grained

beds. (f) Large lava block enclosed in a round-shaped crust within the upper strombolian unit. (g) Texturized UAV Photogrammetic 3D model showing a condensed stratigraphic section of the Strombolian units and undelying paleosols. (g-i) E-W faults lowering toward the south. (j) 3 meters thick paleosol intruded by a minor dike with a very articulated geometry and shape of the terminations. (k) N-S faults cutting the whole Strombolian succession.

On top of this paleosol, a thick scoria-lapilli and bomb-bearing pyroclastic deposit occurs characterized by Strombolian scoriae lapilli, bombs, and limestone blocks (Fig. 5.4 d-e). Two main units form this succession: the Lower and the Upper Strombolian units (Fig. 5.4j, k, k). The former unit shows thicknesses varying from 2 to 10 m (Fig. 5.5b). It is characterized by well-defined beds of loose scoriae lapilli with locally ballistic bombs and blocks of lava, dense scoriae, and carbonate clasts. The Upper unit is massive, showing no clear bedding surfaces, made up of agglutinated scoriae lapilli, spatters with ballistics ejecta made up of lava, dense scoriae, and carbonates (Fig. 5.4d, e, l). The thickness is generally of 5-6 m with a maximum of 10 m in the most preserved sections (Fig. 5.4k, m). The whole succession hosts faults, fractures, and carbonate-filled veins (Fig. 5.4). The faults are parallel or oblique to the excavation fronts (e.g., Fig. 5.4). Noteworthy, close to the nearest occurrence of the main dike, we also document a minor dike intruding the paleosol succession resulting in an articulate morphology.

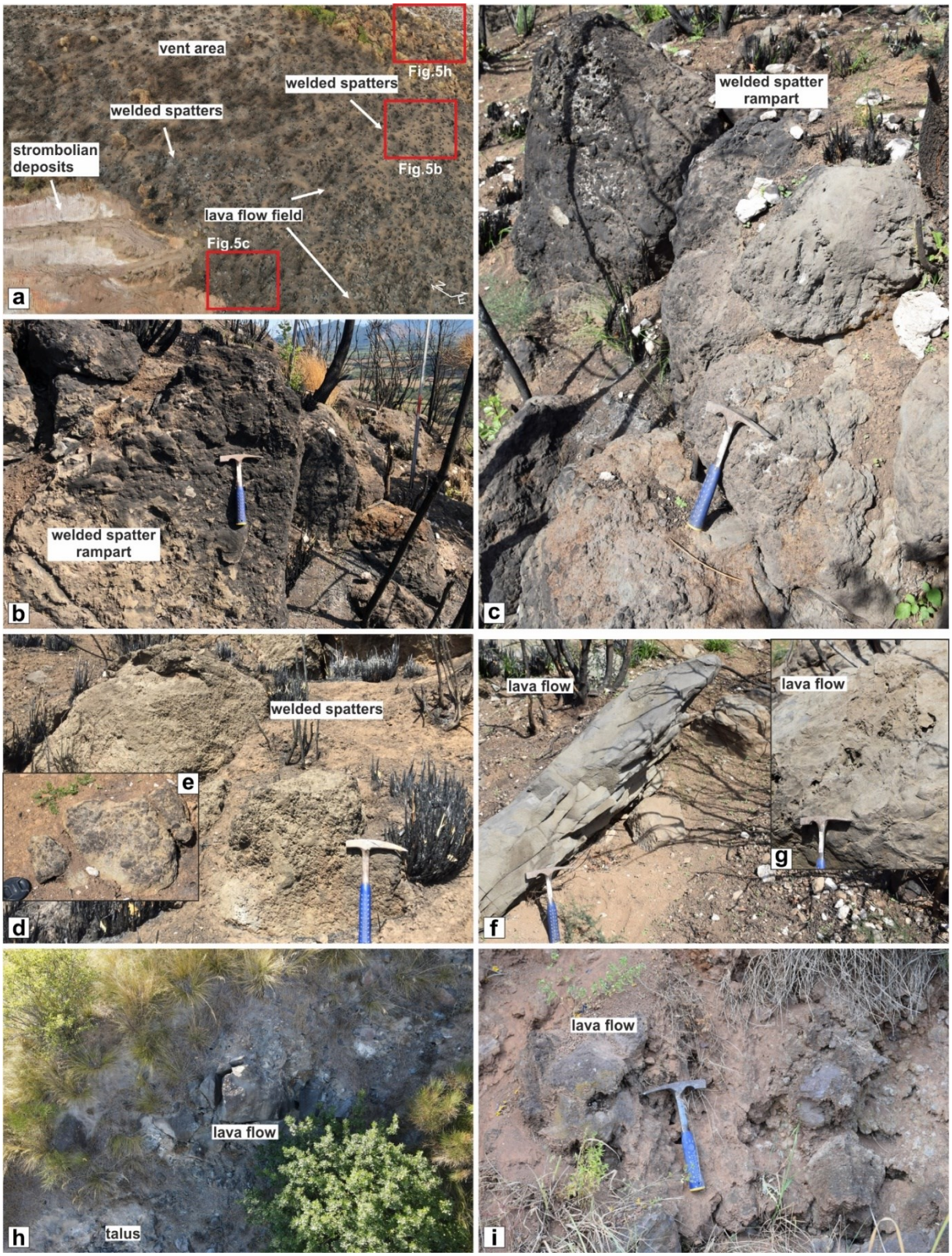

Figure 5.5. (a) Texturized UAV Photogrammetic 3D model oblique view of the Eastern part of the quarry, site of the remnants of vent ramparts. (b) Field picture of welded-spatter ramparts. (c) Detail of welded-spatter rampart. (d-e) Detail field picture of welded scoria-lapilli and spatters. (f-g) Field pictures of lava flows with both shear foliation and degassing structures. (h-i) Outcrops of lava flow fronts at the base of the slope.

Outside of the quarry, to the East of the upper excavation steps (Fig. 5.5a), we found welded deposits made up of scoriaceous spatters, at least 2m thick (Fig. 5.5b, c). The distribution of those ramparts shown in Figure 5.5a resembles the same trend of the uppermost portion of the dike. More scattered in this area, we found many examples of welded lapilli and spatters (Fig. 5.5d – g), laterally passing to lava flow deposits (Fig. 5.5h, i). Also, these deposits are affected by faults, with the most visible also showing surface expression (Fig. 5.5j, k).

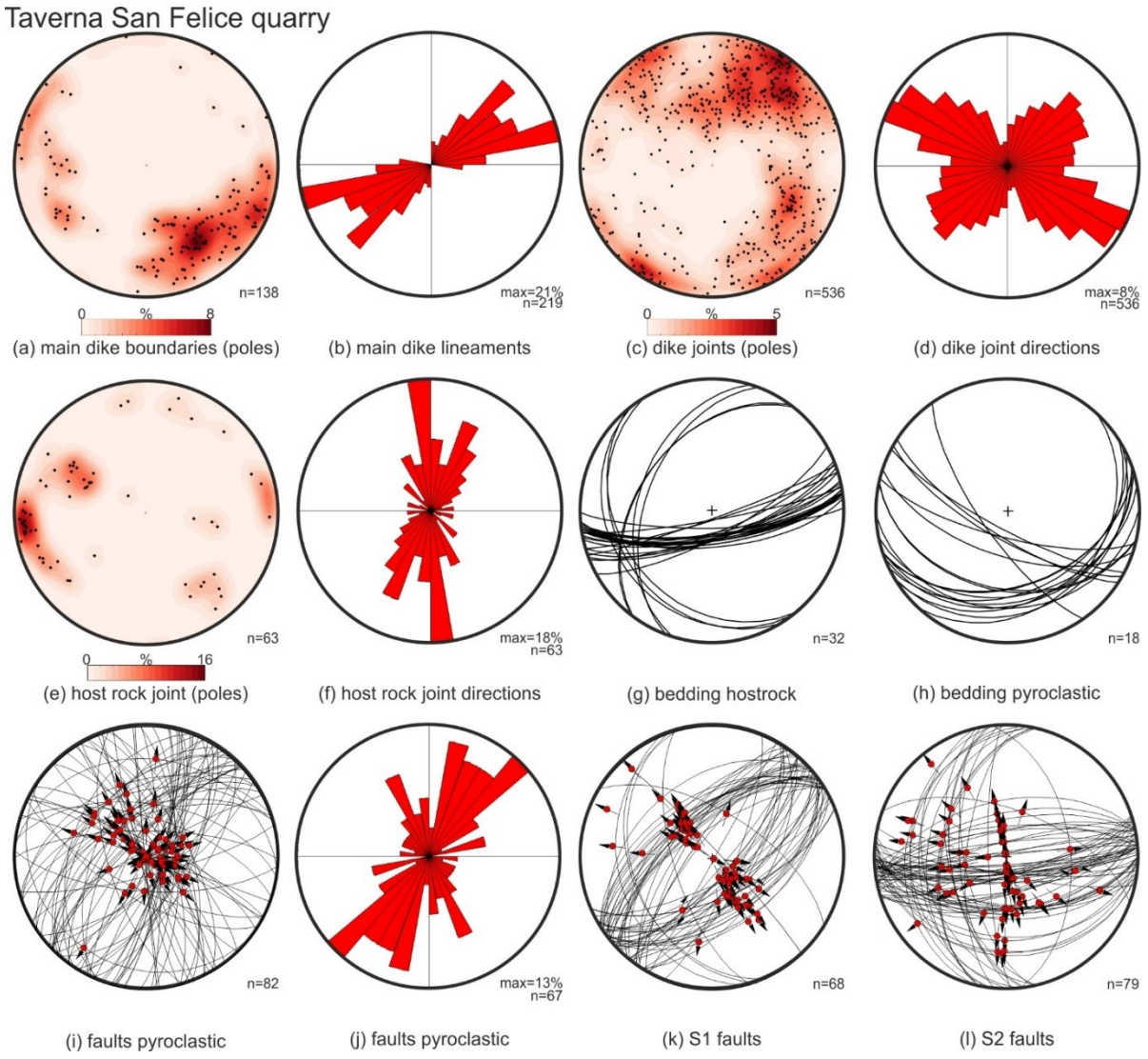

Figure 5.6. Stereographic projections of poles to lineaments, joints, faults and bedding surface (lower hemisphere, equiareal net), corresponding contour plots, rose diagrams and great circles. (a-b) contour plot and rose diagram of main dike lineaments and measured contacts with the host rock. (c-d) contour plot and rose diagram of dike joints. (e-f) contour plot and rose diagram of host rock joints. (g) great circle plot of bedding attitude of the carbonate host-rock. (h) great circle plot of bedding attitude of the carbonate host-rock. (i) great circle and slip vector of faults in strombolian deposits. (j) rose diagram of the fault directions. (k) great circle and slip vector of S1 fault system measured in the host-rock. (l)) great circle and slip vector of S2 fault system measured in the host-rock.

5.4.3 Structural analysis

We present the orientation analysis of structures exposed in the Taverna San Felice quarry. Poles of main dike boundaries (Fig. 5.6a) form a cluster indicating a 324/56 mean plane. The rose diagram of map lineaments carried out on UAV-derived nadir-view orthomosaic indicates preferred E-W and NE-SW directions, with the former mainly observed in the lower part of the quarry and the latter in the latter topmost (Fig. 5.6b). Fractures hosted in the main dike (Fig. 5.6c) show two main clusters of the poles, indicating mean 223/62 and 202/82 planes. The joint direction highlighted in the rose diagram (Fig. 5.6d) shows dominant NE-SW and secondary WNW-ESE directions. Poles to fractures within the host rock (Fig. 5.6e) show two clusters with 085/82 and 119/62 mean planes, respectively. The rose diagram (Fig. 5.6f) indicates the main N-S and a secondary NE-SW direction. The bedding attitude of the limestone host-rock is barely visible within the quarry and has been measured in nearby locations, with two main sets, high-angle south-dipping attitude, and sub-horizontal west-dipping attitude, respectively (Fig. 5.6g). Strombolian units dip at around 40° toward SW following the slope angle (Fig. 5.6h). Faults with different orientations affect the pyroclastic deposits (Fig. 5.6i); the dominant fault directions are deductable from the rose diagram (Fig. 5.6j), showing dominant NE-SW and subordinate N-S and E-W directions. Finally, we recognized two main fault systems, both made up of two fault sets. The former, named S1, is characterized by the well-known NE-SW direction with conjugate planes and a few NW-SE directions, with dominant normal and subordinate transtensive kinematics (Fig. 5.6k). The latter system, labeled S2 (Fig. 5.6l), includes normal and transtensive faults that indicate dominant E-W and subordinate N-S directions.

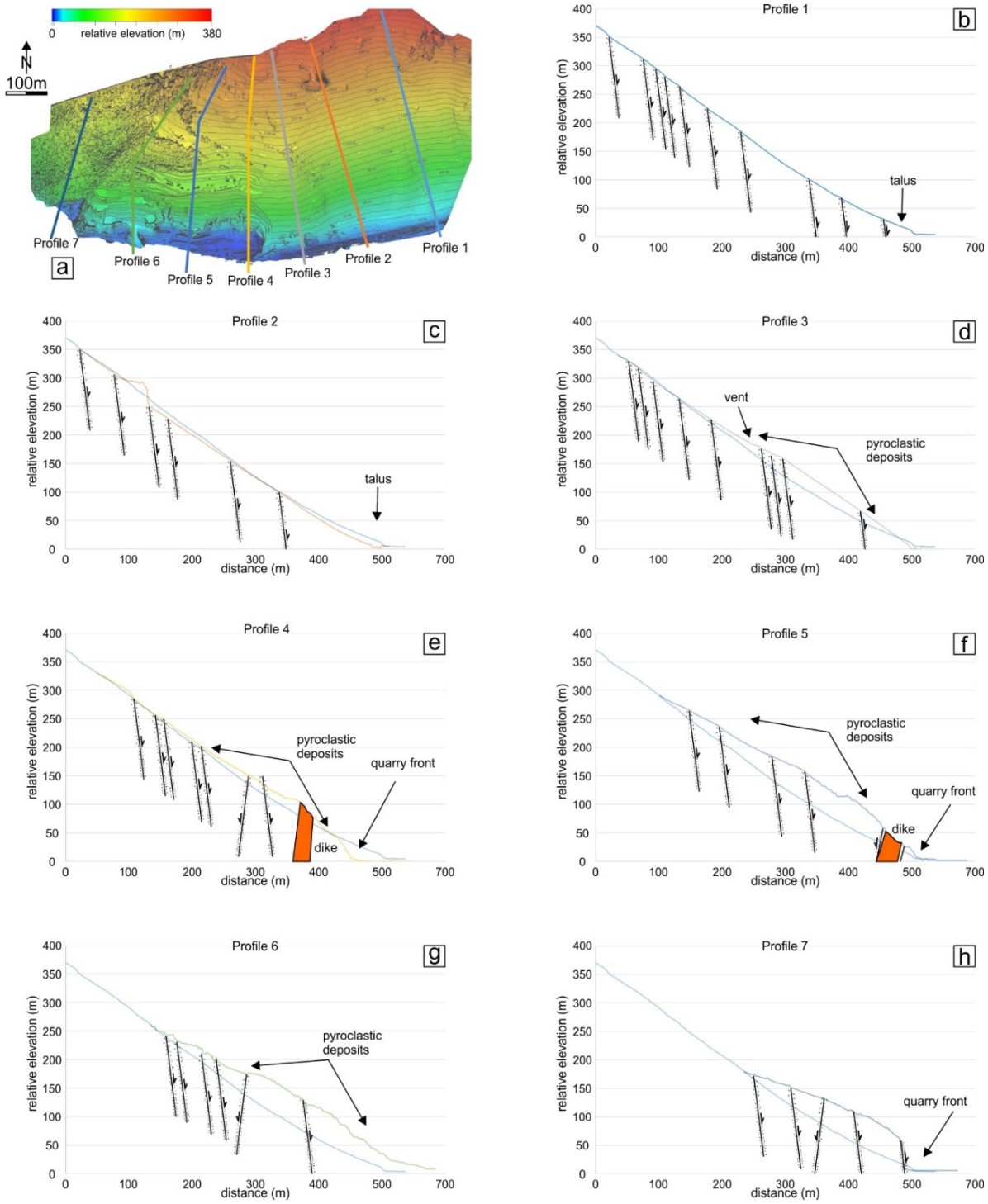

Figure 5.7. (a) Topographic profiles displayed on the UAV-derived Photogrammetric DSM of the study area. (b-h) color-coded topographic profiles, broadly NNW oriented. Mapped faults and the area covered by pyroclastic deposits are indicated. For profiles from c to h, the profile 1 has been projected for comparison.

5.4.4 Topographic profiles

To retrieve significant morphological features about the position of the magmatic dike within the host rock and to map the distribution of associated pyroclastic/effusive products, we

analyzed a high resolution (0.1 m) Digital Surface Model (DSM), built using Structure from Motion (SfM) technique starting from UAV pictures. The survey allowed to build a DSM up to relative height of 350 m above quarry base, with the approach described in the methods section. Seven topographic profiles, about orthogonal to the contour lines, were traced along the southern flank of Mt Cesima, reaching up to 350m above the main quarry level, from East to West, labeled from 1 to 7 (Fig. 5.7a). Profiles 1 and 2 are located outside the quarry and away from the area affected by the deposition and/or preservation of the pyroclastic material (Fig. 5.7b, c). They both show well-rectified slopes with a break toward the lower part linked to the debris talus/fan. In addition, some fault-line scarps and fault scarps are recognizable along the slope. Profile 3 (Fig. 5.7d) is still outside the quarry but records a marked bulge-like shape below 200m, having a remarkably more convex shape. Profiles 4 and 5 (Fig. 5.7e, f) crosscut the quarry excavation fronts and steps, but we traced the position of the main dike, the faults, and the approximate location of pyroclastic deposits. Profiles 6 and 7 (Fig. 5.7g, h) are strongly affected by extraction operations and are less representative of surface expression of faults and pyroclastic material.

5.5 Discussion

In this section, we discuss the results of the geological and structural surveys, both on the field and assisted by UAV, of an active cement quarry on whose excavation front we studied one of the most impressive examples of magmatic dike intruded within a carbonate host rock.

5.5.1 Dike emplacement mechanisms

To reconstruct the tectonic stress field that acted during the dike emplacement, we have to consider some geological and geometric features. First of all, the exposition of the dike and the associated pyroclastic deposits indicates that the dike exposed in the quarry represents the shallowest part of the intrusion. Second, the uppermost part of the dike shows very high thickness values compared to similar dikes documented in the literature (Gudmundsson, 1990; Tramparulo et al., 2018; Scudero et al., 2019; Drymoni et al., 2020; 2021; Geshi et al., 2020). This evidence suggests again that the exposed dike was close to the topographic surface during the emplacement, characterized by very low to null confining pressure. Only the lowermost part of the dike (at 100 m below the former topographic surface) shows typical thicknesses and the

occurrence of some fingers. It follows that the stress field at the time of the intrusion has to be estimated by the geometrical features of the lower part of the dike, where the confining pressure was more significant than the upper portion. With this in mind, all geometric elements suggest that the orientation of the least stress (σ3) at the time of intrusion was broadly N-S oriented.

On the contrary, the dike geometry in the upper part of the quarry, namely close to the topographic surface at the time of the intrusion, shows a NE-SW orientation. Analysis of crosscutting relationships and structural data suggest that the upper part of the dike has propagated within a pre-existing NE-SW fault zone. In general, the whole host rock is strongly damaged by faults and the dike intrusion itself, which also has promoted an intense fluid circulation. Furthermore, no geological and structural evidence (e.g. multiple joint rows, internal chilled margins) exists indicating a multiple magma intrusion.

In addition, remarkable differences among recognized dike geometries have been observed. The low-porphiricity of magma and the sharp contact at the base suggest a low viscosity, compatible with the leucite-bearing tephrite composition of these rocks (Di Girolamo et al., 1991). In this perspective, the sharp contacts and tapering tips of the main dike and of the dikelets exposed at the quarry base indicate that the magma flowed obliquely upward, with the lateral and frontal tips propagated through the Mode I fracturing. According to other literature examples, the presence of pervasive fractures and faults in the host rock also promoted the formation of peculiar geometries such as stair-case tips and hook-shaped horns (e.g., Poppe et al., 2020). Differently, in the upper portion of the quarry the dike has intruded the lower Pleistocene breccia. The host rock lithology and texture favored the occurrence of strongly irregular contacts and blunt-like lateral tips. Gudmundsson (1990) suggests that relevant thickness changes may reflect the drop in stiffness of the host rock, which may be a factor in this case, and/or to lateral propagation drop-like dike thickening (Geshi et al., 2020). However, the dike thickness significantly increases upward, as usually reported in the literature (Geshi et al., 2010), reaching almost 30m of thickness. This value is quite out of scale, so other physical factors may have to be called into question. In fact, since this dike intrusion is related to an extensional event, this considerable thickness may be related to the dilatant effect of normal faults during rifting events (Weismuller et al., 2019). Hence, extension and low-confining pressure must be the principal factors controlling the passive dike intrusion (Cervelli et al., 2002). This interpretation is supported by the very low magma vesicularity of the dike index of a low overpressure (Geshi et al., 2020).

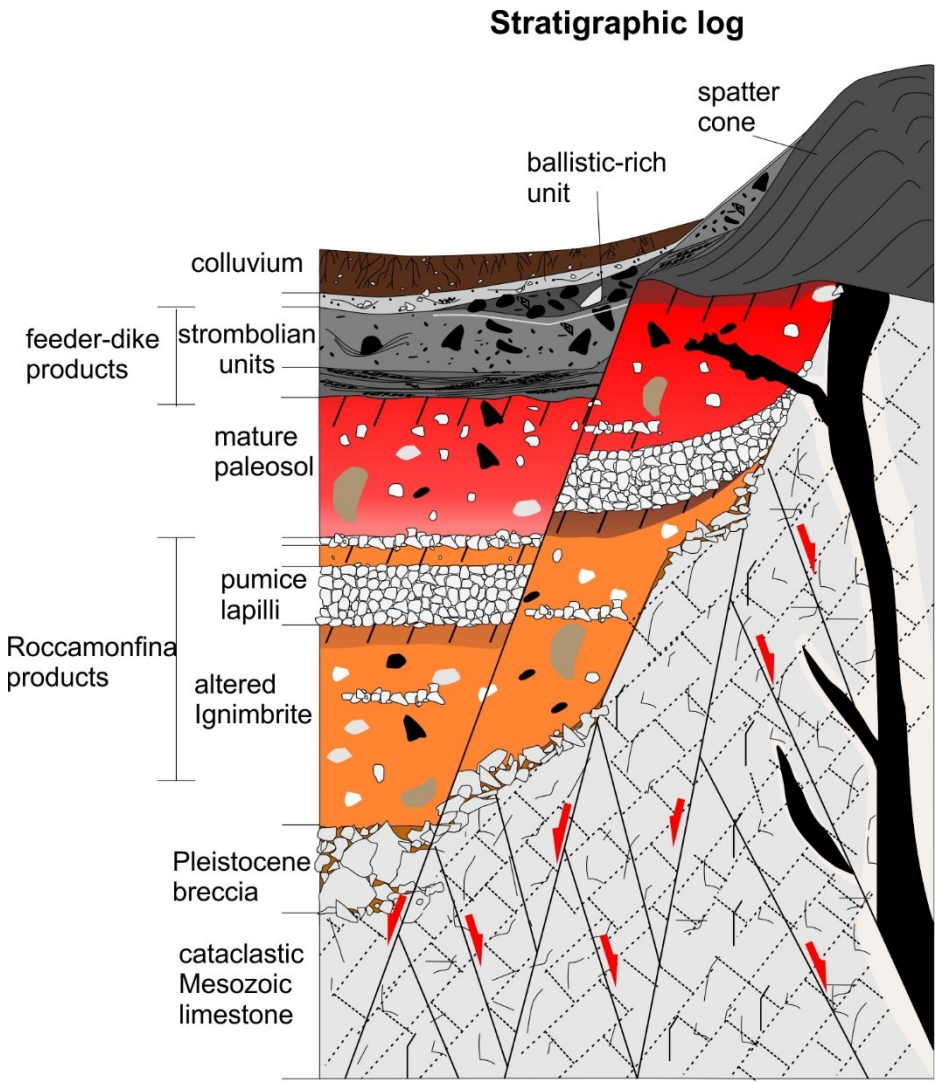

Figure 5.8. Comprehensive stratigraphic log of the different sedimentary and pyroclastic succession cropping out in the quarry.

5.5.2 Volcano-tectonic evolution of the study area

The Roccamonfina volcano history has to be considered to reconstruct the volcano-tectonic evolution of the study area. The formation and evolution of the Garigliano graben strongly affected the Roccamonfina volcano evolution. In fact, several tectonic pulses have conditioned the eruptive vent distribution, resulting in a central stratovolcano and several NE-SW-aligned parasitic vents (Bergomi, 1969; De Rita and Giordano, 1996; Rouchon et al., 2008). In particular, the origin of the summit caldera of the Roccamonfina has been linked to an important tectonic extensional phase that preceded the BLT eruption (De Rita and Giordano, 1996). The NE-SW faults controlled both the collapse of Roccamonfina and the distribution of parasitic vents (Bergomi et al., 1969; De Rita and Giordano, 1996). These faults have been active at least

in the last 300 kyr, down throwing about 50 m the Garigliano and the Formicola plains (De Rita and Giordano, 1996). In this regard, other parasitic or, more generally monogenetic activities are reported in the area (Sgrosso and Aiello, 1963; Bergomi et al., 1969; Di Girolamo et al., 1972; Di Girolamo et al., 1991; Giordano et al., 1995; De Rita and Giordano, 1996), in the central Apennines (Cardello et al., 2020). In particular, the area of Mt Cesima ridge is the site of at least three examples of monogenetic eruptions within the carbonatic rocks: near Sesto Campano, in Presenzano town, and, finally, in the quarry of Taverna San Felice. The last area was indicated by Di Girolamo et al. (1991) as the location of a possible vent. The excavation activities exposed the dike and related pyroclastic products, confirming the Authors' hypothesis. Furthermore, the geological survey allowed clarifying the dike geometry and characterize the stratigraphic relationships with the well-known pyroclastic products erupted by the nearby Roccamonfina. In Figure 5.8, we summarize the stratigraphic position of each of the recognized units. The main dike is hosted in the cataclastic Mesozoic limestone, whereas in the upper part, it crosscuts the Pleistocene Breccia and paleosols (Fig. 5.8). In particular, these paleosols showing variable thickness were formed at the expenses of Roccamonfina volcano pyroclastic deposits, including pumice-lapilli fall associated with the WTT eruption (De Rita and Giordano, 1996; De Rita et al., 1997). A further reddish paleosol occurs on top of this clast-supported pumice-lapilli layer (Fig. 5.8). Proximal dike-related products cover the paleosol. Considering that the paleosol locally shows up to 1.5 m in thickness and a high soil maturity, it is reasonable to suppose that the dike-fed eruption occurred much later.

The pyroclastic products of the dike have been grouped in Lower and Upper Strombolian units. The dike-fed eruption opened with scoria lapilli and ash deposition, resulting in a stratified deposit, locally interested by ballistic impacts. This Strombolian unit shows rhythmic alternation of coarse and fine-grained lapilli and ash beds associated with lava fountaining. A sharp hydrothermalized contact, probably associated with short-lived phreatomagmatic explosions, marks the transition to a more violent eruption phase (Fig. 5.5), resulting in massive coarse-grained, agglutinated scoria lapilli, and suggesting higher emplacement temperature from sustained lava fountains. Up to 1 m in sized ballistics, formed mainly by lava blocks, large spindly-shaped bombs, dense scoriae, and carbonate boulders, frequently occur. Upward, these deposits pass to an even coarser, bomb, and lithic rich sequence that closes the eruption (Fig. 5.5), suggesting increasing energy of the eruption toward its end. In the eastern side of the quarry, these deposits are generally thicker and laterally pass to the welded scoria and spatter found in the preserved section of the vent area. The latter depicts the classic morphology of the

eruptive fissures, defined by aligned foci building a series of ramparts and levees. According to the position of these ramparts, they seem to be open toward the south, feeding the lava flows found south and downhill of the rampart system. The excavation activity of the quarry clarified the stratigraphic relationships between dike, related products, paleosols, and the Roccamonfina pyroclastics. However, it probably erased the former vents distribution and dike-related products, as also suggested by the topographic analysis and by the occurrence of lava and scoria at both sides of the quarry. These features suggest that the dike fed the eruption along an up to ~200m long fissure.

The structural survey shows as the pyroclastic strombolian succession is pervasively faulted (Figs. 5.5 and 5.6i). The complex array of faults does not allow us to recognize the direct expression of dike-induced faulting (Rubin, 1992; Trippanera et al., 2015; 2019); nonetheless, we have no clues to exclude that such process took place. It is important to stress that some of the strombolian pyroclastic deposits were analyzed in the past by Di Girolamo et al. (1991), who sampled some a scattered outcrop of lavas and scoria. The results of the chemical analysis on those samples allowed to constrain its composition to an lc-tephrite, which composition resembles and overlaps with the HKS volcanics of the pre-BLT products of the Roccamonfina volcano (Conticelli et al., 2004). By inference, using the petrologic criteria, those rocks were associated with the earliest period of activity of the older Roccamonfina stratovolcano (Di Girolamo et al., 1991). However, the results of this study provide a different interpretation suggesting that this eruption has occurred well-after the WTT eruption, whose younger age is at around 230 ka. Furthermore, the dike intrusion event has to be considered independent from the dynamics of the nearby Roccamonfina as suggested by the kinematic indicators suggesting that the magma flow was obliquely coming from below the Mt Cesima ridge.

With this in mind, the structural evolution of this area is discussed. The structural survey and the previous considerations about the dike emplacement mechanisms support the interpretation of a dike driven by a regional N-S extension. As concern the dike joints, these are mainly clustered in two main systems, one parallel to the dike-host-rock contact, formed due to the competence contrast and the temperature gradient, and other orthogonal to it, characterized by different sets of cooling-joints (e.g., Gudmundsson, 1984). Furthermore, the crosscutting relationships between faults observed in the quarry point out that E-W faults are younger than NE-SW faults, in agreement with the existing literature (e.g., Giordano, 1995 and references therein). From a morphostructural point of view, the general aspect of the outcrop of the dike and its related products and the intense subsequent faulting suggest that the dike intruded in a

different morphostructural setting compared to today. It is worth noting as the paleosol and the overlying pumice lapilli layers lack calcareous clasts, suggesting the absence of a carbonatic relief close to the dike. Moreover, the presence of solidified lava within the uppermost part of the dike suggests that the former topographic surface was about flat or formed by small highs and lows. However, the current morphology of the Mt Cesima SW side is characterized by a slope where the dike is located. The pervasive occurrence of normal and transtensive E-W faults characterized by a few meters of displacements suggests that the Mt Cesima was exhumed after the dike emplacement. To summarize, a cartoon showing the volcano-tectonic evolution of the area is proposed (Fig. 5.9). Structural data collected in the quarry and in nearby areas suggest that the near vertical bedding attitude is the result of south verging thrusting (Fig. 5.9a), likely the result of out-of-sequence thrusting in the Early Pliocene, in agreement with Vitale et al. (2020). During the Early Pliocene, the well-documented NE-SW and NW-SE extension resulted in the formation of the main structural lineaments of the Garigliano graben and the deposition of detrital talus made up of cemented Breccia Mortadella (Fig. 5.9b). These rocks are, in turn, covered by the pyroclastic deposits of Roccamonfina volcano, including the WTT tephra, with the tectonic activity favouring the preservation of these deposits in structural lows, whereas a thick paleosol develops on top of these tephra (Fig. 5.9c). With a N-S strong extension, magma rises through the crust reaching the surface within a E-W fault zone, diverging its path to NE-SW before reaching the surface (Fig. 5.9d). Ultimately, the dike fed a fissure Strombolian eruption, that built a series of aligned vents and ramparts (Fig. 5.9e). Following the monogenetic eruption, tectonic activity continued, as testified by extensive faulting affecting the strombolian sequences, and exhuming the ridge of Mt Cesima, strongly eroding and altering the morphology compared to the time of the eruption (Fig. 5.9f). Finally, the recent extraction activity in the quarry allowed to access the several outcrops that have been studied (Fig. 5.9g).

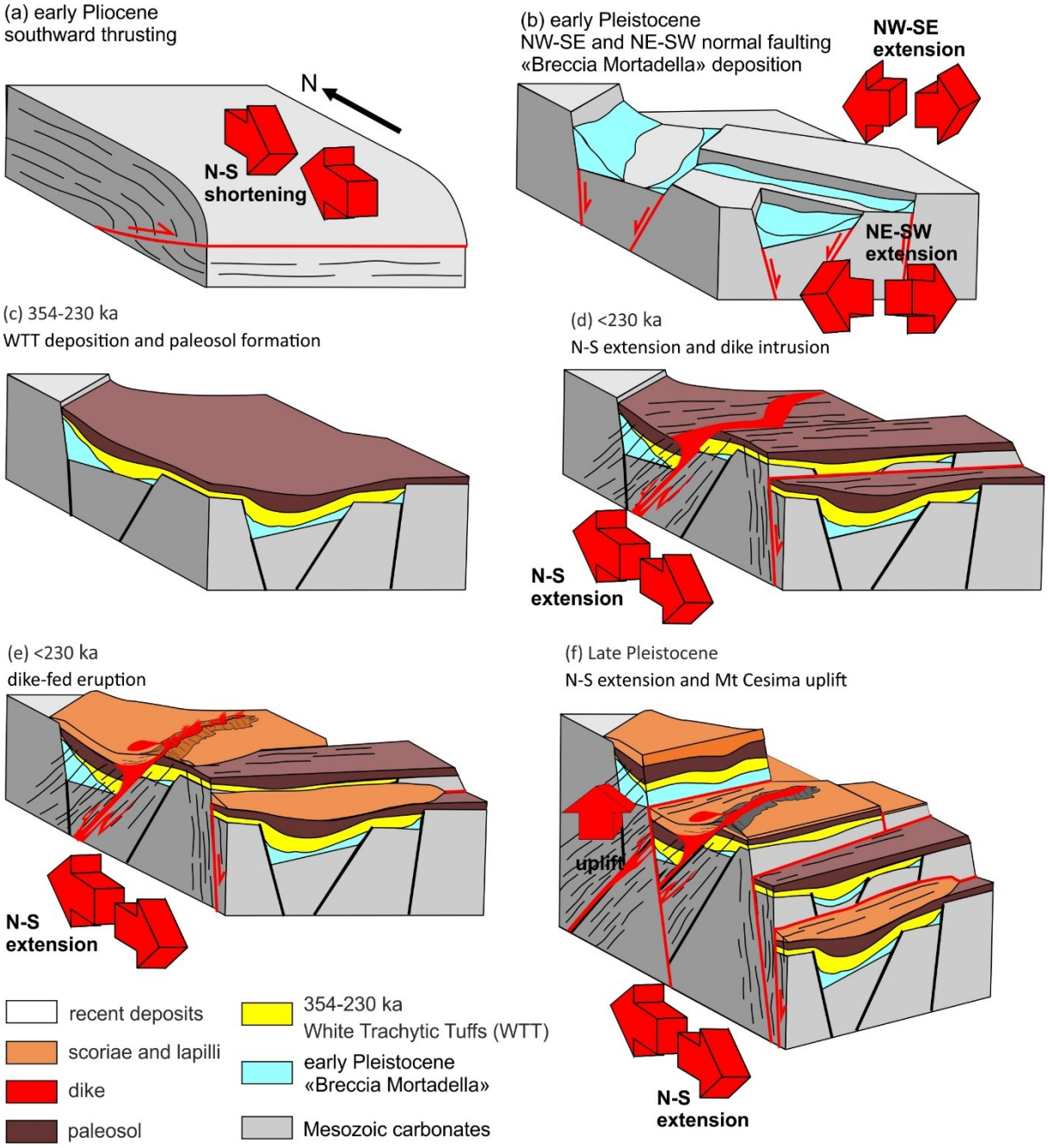

Figure 5.9. Cartoon showing the volcano-tectonic evolution of the southern sector of Mt Cesima. See the text for the explanation.

5.6 Conclusions

This study focuses on the structural and stratigraphic analysis of a magmatic dike hosted within Mesozoic carbonates and Pleistocene breccia. The dike is exposed along the excavation front of the cement quarry of Taverna San Felice, Northeast of Roccamonfina volcano. Several

field campaigns and UAV surveys allowed the reconstruction of the dike geometry and of the relationships with the regional tectonic evolution of the area. Furthermore, this study investigated the stratigraphic relationships between the pyroclastic products associated with the dike and the nearby Roccamonfina. The main results of this study are the following:

(i) The Mesozoic carbonate host-rock has undergone several tectonic events, including an Early Pliocene shortening that produced a South-verging anticline that resulted in steeply-dipping bedding; Early Pleistocene extensional stages defined by NE-SW and NW-SE trending normal faults to which a calcareous breccia (Breccia Mortadella) is associated. A subsequent N-S extension affected the area by forming conjugate E-W normal faults.

(ii) As retrieved from the cross-cutting relationships, this study reconstructed the kinematics of the dike intrusion event. In the lower portion of the quarry, the emplacement of the dike and the associated minor segments resulted from an N-S extension, intruding within an N-dipping cataclastic E-W fault zone. In contrast, as depicted by a sudden thickness increase, the dike diverted its path toward the surface, making its way possibly within a pre-existing NE-SW fault zone. Along its contact with the host rock, the dike induced the formation of a meters-thick metamorphic aureole, displaying sharp to undulose contacts in the lower and in the upper part of the quarry, respectively.

(iii) The dike eventually made it to the surface, feeding a fissure Icelandic/Strombolian-type eruption. Up to 30 m thick Strombolian pyroclastic deposits were emplaced during the eruption, building a series of aligned welded-spatter ramparts. Also, a lava flow was fed by the eruption. The juvenile material is mainly composed of lc-tephrite scoriae lapilli.

(iv) Stratigraphic studies point out that the dike products emplaced on top of a succession of several paleosols and greyish pumice-lapilli layers, ascribed to the last Plinian eruption cycle, the WTT, of the nearby Roccamonfina volcano. Hence, this event of dike intrusion has to be considered at least younger than the WTT stage of the Roccamonfina. Disproving the literature inference that such monogenetic eruptions belong to the earliest phase of the volcano.

(v) The whole sequence is strongly affected by south-dipping normal faults, mainly E-W and N-S oriented, that lowered the southern part and uplifted the Mt Cesima ridge. Thus, an important tectonic extensional phase is responsible for the late

development of the Garigliano and Formicola grabens, and resembles the pattern of rift-related extensional pulses.

Chapter 6: Conclusions and Outlook

Within this thesis, a variety of techniques were applied to investigate two different study areas connected by a mutual link which is volcano-tectonic interactions at different scales/magnitudes. First, for the Campi Flegrei offshore sector, high-resolution single and multi-channel reflection seismic data were used to examine both the evolution of the stratal architecture of post-caldera infill as a response to volcano-tectonic processes in interplay with sea-level change and volcanism, and ultimately to reconstruct in detail the structure of the nested caldera system characterizing this restless volcanic area. Understanding the formation of such large calderas and their post-collapse evolution is crucial to improve the assessment of the hazards related to volcano-tectonic and volcanism to foresee future potential hazard scenarios. Regarding the other study area, near Roccamonfina, field geological and structural survey had a primary role in investigating a quarry exposing an outstanding example of a magmatic dike intruded in a carbonatic host rock.

The main aim of this thesis was to investigate and possibly significantly improve the knowledge on several research fields in two main study areas, namely the Campi Flegrei caldera and the monogenetic vents NE of the Roccamonfina volcano.

For Campi Flegrei caldera, this research was focused on studying a set of over 100 single-channel and multi-channel reflection seismic data, which were utilized to examine the offshore portion of the caldera the surrounding areas. For this matter, in this thesis, two main research strands were followed to (1) Understanding the evolution of ground deformation since the Neapolitan Yellow Tuff eruption, investigating the role of pre-existing caldera structures on constraining the deformation field, and understanding how the interplay between volcano-tectonic processes and sea-level rise, affect the sedimentation record. This goal was achieved through a novel approach to match for the first time the offshore seismic data with the uplifted and outcropping marine-continental succession of the La Starza unit. (2) Exploring the room for improvements of the current caldera models by taking advantage of the possibilities offered by the use of the multiscale seismic dataset and reconstructing the heretofore most detailed structural map of the Campi Flegrei offshore, which allows disentangling the formation and evolution of nested caldera structure and, understand the post-caldera deformation due to volcano-tectonic collapses. For the NE sector of Roccamonfina, (3) several field surveys allowed to shed light on the relationship between the tectonic extensional regime and rift volcanism in the Garigliano graben, giving clues on the rejuvenation of the volcanism along

tectonic lineaments, and suggesting the mechanism of the onset of volcanism along tectonic structures.

The main findings of this doctoral study have been presented in three standalone research manuscripts, listed in Chapters 3 to 5. Chapter 3 focused on the development of an integrated offshore-on-land stratigraphy for Campi Flegrei in the last 15 kyr. Chapter 4 focused on the reconstruction of the structural setting of the caldera offshore and the evolution in the last 40 kyr. Chapter 5 deals with reconstructing volcano-tectonic and regional tectonic events leading to monogenetic volcanic activity along carbonatic ridges. The main outcomes of these three manuscripts are summarized in the following sections.

6.1 Integrated offshore-on-land stratigraphy of Campi Flegrei caldera in the last 15 kyr

Chapter 3 discussed the novel integration of the recently detailed reconstruction of La Starza unit, cropping out along the coastal central sector of the caldera, and the sedimentary record of the offshore infill as depicted by the high-resolution seismic profiles. The main aim was to overwhelm the lack of direct age/stratigraphic information in the Pozzuoli Gulf, and taking advantage of the almost complete record of volcanic activity and ground deformation stored in the sediments in the offshore sector. Therefore, sequence unconformities were correlated to the continental marker levels, such as paleosols, transgressive marine units, well-dispersed tephras, and structures. Considering the relationship between the sea-level change and the tephrostratigraphic record, all this has been done. More specifically, eleven units were recognized above the NYT unit, starting from three constraint levels. These units have underpinned the volcano-tectonic evolution since the NYT eruption. The stages can be broadly divided into pre-doming and syn-doming sequences. After 5 ka of volcanism clustered along the ring faults, the Plinian eruption of Agnano-Pomici Principali triggered millennia-long subsidence that favored the aggradation of marine and volcaniclastic sediments in the nowadays central sector. This phase was soon after replaced by a rapid uplift that led to the Epoch 2 volcanism, during which the emersion of the central sector occurred. Over 3000 years of quiescence and subsidence centered in Pozzuoli preceded the Epoch 3 volcanism, which was strongly dominated by the Plinian eruption of Agnano-Monte Spina at 4.55 ka. The ground deformation pattern resembled the same behavior of the previous Pomici Principali eruption, with subsequent subsidence then followed by new ground uplift. This phase separates Epochs

3a and 3b, and differently from the previous event, the time frame of oscillating ground deformation was shorter in time. The evolution of ground deformation and volcanism is well-recorded by the proposed stratigraphy, providing indirect age estimations for some debated coastal eruptions, namely Banco di Nisida and Nisida on the East, and Bacoli, Porto Miseno, and Miseno on the West. Finally, some sub-surficial features such as the Bagnoli cryptodome and the Punta Pennata structure were described and discussed. The results of this study represent the most elaborated attempt to tie the offshore stratigraphy with continental knowledge and is an important contribution towards the comprehensive understanding of the evolution of this restless caldera system. Such advancements will unravel the volcano-tectonic processes and further improve the volcanic hazard assessment.

6.2 Fault systems in the Campi Flegrei offshore sector

Chapter 4 focused on the reconstruction of the most updated structural map of the offshore sector of the caldera, which strongly improves previous studies and also discusses the debated existence of the caldera and its geometry, highlighting the presence of a complex array of caldera ring fault zone, which acted in interplay with the regional tectonic stress field. Two main fault systems have been recognized, namely the caldera ring fault system and the dome fault system, using a multiscale reflection seismic dataset of different vintages and resolutions. Overall, more than 200 individual fault segments have been mapped within the seismic dataset, with the majority being normal faults, dipping between 80 to 60°. The ring fault system has been grouped into Inner, Medial, and Outer ring faults, with associated fault zones. For the first time, three caldera rims were identified and related to the Campanian Ignimbrite eruption, at 40 ka, the most energetic and voluminous volcanic eruption in Europe in the last 200 kyr. The Outer caldera fault geometry links with the on-land structural high of Posillipo and Monte di Procida, to the East and to the West, respectively. Volcanism during the CI-NYT stage also took place on the southern ring fault zone and enclosed the position of the vents younger than CI. The recent most large caldera-forming eruption of Neapolitan Yellow Tuff at 15 ka mainly reactivated the Inner and the Medial ring faults, and only locally the Outer. The Inner ring fault zone binds with the continental sector in Bagnoli and to Averno, to the East and the West, respectively. The ring faults have a marked control on the post-collapse ascent of hydrothermal fluids and magma, as pointed out by the presence of extensive fluid uprise, submarine vents, and intrusions. The arrangement of these ring faults and their relationship with the caldera

center depicts that their formation is influenced by an N-S tectonic field, which also forces the caldera geometry to be slightly elliptical. The reactivation of adequately oriented normal faults suggests that this tectonic field is still acting. The other fault system is the Dome fault system, which is the offshore prosecution of the fault zone affecting the central sector of the resurgent dome. These faults have been described as apical extensional faults in literature, furnishing a simplified view of an indeed complex system.

In contrast, in this study, the driving processes and the activation timeframe of these faults has been a constraint to be related to near-vertical volcano-tectonic collapses associated with the large intra-caldera Plinian eruptions, with the drop in magmatic pressure accommodated by the reactivation of tectonic-inherited structures that downthrown the central part of the resurgent dome in response to reservoir pressure changes. The results of this study represent a significant advancement in the understanding of the caldera structure at Campi Flegrei, which can be used as a template to reconstruct the overall caldera. Furthermore, it highlights that the caldera ring faults control the ascent of hydrothermal fluids, which is a site prone to volcanic activity, despite the current consideration.

6.3: Monogenetic eruption during extensional pulse NE of Roccamonfina volcano

Chapter 5 focused on the study of a magmatic dike that intruded within a Mesozoic carbonate ridge North East of Roccamonfina volcano. Several field campaigns and UAV surveys, performed during the extraction activities of the cement quarry of Taverna San Felice, North East of Roccamonfina, allowed us to describe the outstanding exposure of a Pleistocene magmatic dike, which fed a monogenetic eruption along the master fault of the Garigliano-Formicola graben. In particular, the dike and minor segments geometry allowed to constraint the main propagation path of the dike swarm, to have occurred within an E-W fault zone before being deflected by a pre-existing NE-SW fault zone. The dike propagated within the Mesozoic limestones of the Mt Cesima ridge, whereas in the upper, near-surface, portion has intruded within the Lower Pleistocene cemented breccia. This dike fed a small volume fissure eruption that emplaced a 30-40m thick Strombolian pyroclastic sequence, made up of scoria lapilli and spatters, with metric ballistics of lava, spatters, and carbonate blocks. The remnants of a spatter cone/rampart system have withstood the erosion east of the quarry. The stratigraphic analysis constrains this eruption to be younger than the last Plinian eruptions of Roccamonfina, namely

the White Trachytic Tuffs, whose younger age is 230 ka. A thick reddish paleosol on top of the WTT tephra suggests that considerable time has passed before the Strombolian monogenetic eruption. The entire quarry front exposes many faults, with the E-W set cross-cutting the NE-SW set. Also, the pyroclastic deposits of the Strombolian eruption are intensely faulted and presently preserved in structural depressions. Significant uplift occurred shortly after the eruption, resulting in a radical morpho-structural change leading to the uplift of the Mt Cesima carbonate ridge. This study focused on one example of monogenetic eruptions, among the several reported in the literature, which occurred with the tectonic extensional pulse that fueled the evolution of peri-Tyrrhenic half-graben depressions.

6.4 Research outlook

This thesis aimed to contribute to the overall understanding of the complex evolution of the caldera of Campi Flegrei, which involves large caldera collapses in response to large-volume ignimbrite eruptions and post-collapse dome-resurgence. Furthermore, this thesis attempted to shed light on the rift-related graben volcanism in the late Pleistocene, describing the relationships between dike intrusion and extensional tectonic pulses. Nevertheless, numerous scientific questions need to be addressed in the future to improve the structural characterization of complex caldera systems and link the take-home messages of rift-related passive diking mechanisms to the formation of central compositive volcanoes, such as the Somma-Vesuvius. At Campi Flegrei, after matching the stratigraphy of the last 15kyr between on-land and offshore, the detailed structural framework built off-shore also needs to be adequately detailed on-land. A general, comprehensive caldera model has to be formulated, learning from the limitations and advantages of many techniques that can be applied. The structural template developed for the offshore caldera may provide insightful indications toward a fitful reconstruction of the longly debated caldera. The results of this study furnished a key to disentangling the interplay between tectonic/external and volcano-tectonic/internal forces. Volcanic activity at Campi Flegrei seem to have a strong relationship with the structural heritage of the area, and this might help understand the behavior of one of the most cryptic volcanic area in the world. So, the outlook of this research is to reconstruct at caldera-scale the geometry of fault zones in the different sectors and characterize the impact of deep-seated faults in conveying the ascent of magmatic fluids from the hydrothermal system toward the surface.

This would be critical to assess the geothermal potential of the area in the renewed vision of sustainable energy sources.

Regarding the Garigliano graben area, further studies and developments have to be pursued to unravel the occurrence of rift-like monogenetic volcanism as a proxy to describe various pulses of strong tectonic activity that shaped the Tyrrhenian margin of the Campania Plain. In this view, the studies on the Mt Cesima ridge, and other horst ridges along the Garigliano and Campana coastal plains, have to be carried out. Such scattered volcanism may represent the embryonic stage of more mature central volcanism, hence representing the opportunity to study the opening stages of volcanic activity onset in rift-like environments. A detailed mapping of the area, aided by indirect investigations (geophysical methods), may help to understand the complete picture of the evolution of early-stage volcanism.

Acknowledgements

This thesis has benefitted from the thorough comments and corrections of Guido Giordano and Giovanni Luca Cardello which helped to improve the previous version of the manuscript.

References

Acocella, V. (2008). Activating and reactivating pairs of nested collapses during caldera-forming eruptions: Campi Flegrei (Italy). Geophysical Research Letters, 35(17).

Acocella, V. (2010). Evaluating fracture patterns within a resurgent caldera: Campi Flegrei, Italy. Bulletin of Volcanology, 72(5), 623-638.

Acocella, V. (2019). Bridging the Gap From Caldera Unrest to Resurgence. Front. Earth Sci. 7:173. doi: 10.3389/feart.2019.00173

Acocella, V., Funiciello, R. (2006). Transverse systems along the extensional Tyrrhenian margin of central Italy and their influence on volcanism. Tectonics, 25(2).

Acocella, V., R. Di Lorenzo, C. Newhall, R. Scandone (2015), An overview of recent (1988 to 2014) caldera unrest: Knowledge and perspectives, Rev. Geophys., 53, 896–955, doi:10.1002/2015RG000492.

Aiello, G., Marsella, E., Di Fiore, V. (2012). New seismo-stratigraphic and marine magnetic data of the Gulf of Pozzuoli (Naples Bay, Tyrrhenian sea, Italy): inferences for the tectonic and magmatic events of the Phlegrean Fields volcanic complex (Campania). Marine Geophysical Research, 33(2), 97-125.

Aiello, G., Giordano, L., Giordano, F. (2016). High-resolution seismic stratigraphy of the Gulf of Pozzuoli (Naples Bay) and relationships with submarine volcanic setting of the Phlegrean Fields volcanic complex. Rendiconti Lincei, 27(4), 775-801.

Albert, P.G., Giaccio, B., Isaia, R., Costa, A., Niespolo, E. M., Nomade, S., Pereira, A., Renne, P.R., Hinchliffe, A., Mark, D.F., Brown, R.J., Smith, V. C. (2019). Evidence for a large-magnitude eruption from Campi Flegrei caldera (Italy) at 29 ka. Geology, 47(7), 595-599.

Albini, A., Cristofolini, R., Di Girolamo, P., Stanzione, D. (1980). Rare-earth and other trace-element distributions in the calc-alkaline volcanic rocks from deep boreholes in the Phlegrean Fields, Campania (south Italy). Chemical Geology, 28, 123-133.

Amore, F., Barra, D., Ciampo, G., Ruggiero Taddei, E., Russo G, F., Sgarrella, F. (1988). Il terrazzo de La Starza: associazioni fossili e batimetria.

Amoruso, A., Crescentini, L., Sabbetta, I. (2014). Paired deformation sources of the Campi Flegrei caldera (Italy) required by recent (1980–2010) deformation history. Journal of Geophysical Research: Solid Earth, 119(2), 858-879.

Amoruso, A., Crescentini, L., D'Antonio, M., Acocella, V. (2017). Thermally-assisted magma emplacement explains restless calderas. Scientific reports, 7(1), 1-9.

Appleton, J. D. (1972). Petrogenesis of potassium-rich lavas from the Roccamonfina Volcano, Roman Region, Italy. Journal of Petrology, 13(3), 425-456.

Aprile, F., Ortolani, F. (1978). Nuovi dati sulla struttura profonda della Piana Campana. Boll. Soc. Geol. It., 97, 591-608.

Ascione, A., Cinque, A., Miccadei, E., Villani, F., Berti, C. (2008). The Plio-Quaternary uplift of the Apennine chain: new data from the analysis of topography and river valleys in Central Italy. Geomorphology, 102(1), 105-118.

Ballini, A., Barberi, F., Laurenzi, M. A., Mezzetti, F., Villa, I. M. (1989). Nuovi dati sulla stratigrafia del vulcano di Roccamonfina. Boll. Gnv, 5, 533-555.

Barbieri, M., Di Girolamo, P., Locardi, E., Lombardi, G., Stanzione, D. (1979). Petrology of the calc-alkaline volcanics of the Parete 2 well (Campania, Italy). Periodico di Mineralogia, 48, 53-74.

Bellucci, F., Woo, J., Kilburn, C. R., Rolandi, G. (2006). Ground deformation at Campi Flegrei, Italy: implications for hazard assessment. Geological Society, London, Special Publications, 269(1), 141-157.

Beltrando, M., Compagnoni, R., Lombardo, B. (2010). (Ultra-) High-pressure metamorphism and orogenesis: an Alpine perspective. Gondwana Research, 18(1), 147-166.

Bergomi, C., Catenacci, V., Cestari, G., Manfredini, M., Manganelli, V. (1969). Note illustrative del F. 171 Gaeta e vulcano di Roccamonfina. Serv Geol It, 140.

Bevilacqua, A., Isaia, R., Neri, A., Vitale, S., Aspinall, W. P., Bisson, M., Flandoli, F., Baxter, P.J., Bertagnini, A., Ongaro, T.E., Iannuzzi, E., Pistolesi, M., Rosi, M. (2015).

Quantifying volcanic hazard at Campi Flegrei caldera (Italy) with uncertainty assessment: 1. Vent opening maps. Journal of Geophysical Research: Solid Earth, 120(4), 2309-2329.

Bevilacqua, A., Flandoli, F., Neri, A., Isaia, R., Vitale, S. (2016). Temporal models for the episodic volcanism of Campi Flegrei caldera (Italy) with uncertainty quantification. Journal of Geophysical Research: Solid Earth, 121(11), 7821-7845.

Bevilacqua, A., Neri, A., Bisson, M., Esposti Ongaro, T., Flandoli, F., Isaia, R., Rosi, M., Vitale, S. (2017). The effects of vent location, event scale, and time forecasts on pyroclastic density current hazard maps at Campi Flegrei caldera (Italy). Frontiers in Earth Science, 5, 72.

Bevilacqua, A., Neri, A., De Martino, P., Isaia, R., Novellino, A., Tramparulo, F. D. A., Vitale, S. (2020). Radial interpolation of GPS and leveling data of ground deformation in a resurgent caldera: application to Campi Flegrei (Italy). Journal of Geodesy, 94(2), 24.

Bischoff, A., Planke, S., Holford, S., Nicol, A. (2021). Seismic geomorphology, architecture and stratigraphy of volcanoes buried in sedimentary basins. In Volcanoes-Updates in Volcanology. IntechOpen.

Blong, R. (1994). The Rabaul eruption, 1994. The Australian Geographer, 25(2), 186-190.

Bonali, F. L., Tibaldi, A., Marchese, F., Fallati, L., Russo, E., Corselli, C., Savini, A. (2019). UAV-based surveying in volcano-tectonics: An example from the Iceland rift. Journal of Structural Geology, 121, 46-64.

Bonardi, G., Ciarcia, S., Di Nocera, S., Matano, F., Sgrosso, I., Torre, M. (2009). Carta delle principali unità cinematiche dell'Appennino meridionale. Nota illustrativa. Bollettino della Società Geologica Italiana, 128(1), 47-60.

Boncio, P., Dichiarante, A. M., Auciello, E., Saroli, M., Stoppa, F. (2016). Normal faulting along the western side of the Matese Mountains: Implications for active tectonics in the Central Apennines (Italy). Journal of Structural Geology, 82, 16-36.

Bosi, V. (1994). Evoluzione neotettonica del Lazio meridionale Campania settentrionale, in corrispondenza della terminazione meridionale della linea tettonica 'Ortona-Roccamonfina'. PhD thesis, Universitfi 'La Sapienza', Roma, Italia.

Bosi, V., Giordano, G. (1997). Stress field evolution in central Italy during middle-late Pleistocene: new information from southern Latium. Il Quaternario, 10(2), 631-636.

Branney, M., Acocella, V. (2015). Calderas. In The encyclopedia of volcanoes (pp. 299-315). Academic Press.

Caiazzo, C., Ascione, A., Cinque, A. (2006). Late Tertiary–Quaternary tectonics of the Southern Apennines (Italy): new evidences from the Tyrrhenian slope. Tectonophysics, 421(1-2), 23-51.

Calderoni, G., Russo, F. (1998). The geomorphological evolution of the outskirts of Naples during the Holocene: a case study of the Bagnoli-Fuorigrotta depression. The Holocene, 8(5), 581-588.

Cardello, G. L., Consorti, L., Palladino, D. M., Carminati, E., Carlini, M., Doglioni, C. (2020). Tectonically controlled carbonate-seated maar-diatreme volcanoes: The case of the Volsci Volcanic Field, central Italy. Journal of Geodynamics, 139, 101763.

Cardello, G. L., Vico, G., Consorti, L., Sabbatino, M., Carminati, E., Doglioni, C. (2021). Constraining the passive to active margin tectonics of the internal central Apennines: insights from biostratigraphy, structural, and seismic analysis. Geosciences, 11(4), 160.

Carlino, S., Somma, R., Troise, C., De Natale, G. (2012). The geothermal exploration of Campanian volcanoes: Historical review and future development. Renewable and Sustainable Energy Reviews, 16(1), 1004-1030.

Carminati, E., Doglioni, C. (2012). Alps vs. Apennines: the paradigm of a tectonically asymmetric Earth. Earth-Science Reviews, 112(1-2), 67-96.

Cartwright, J., James, D., Bolton, A. L. (2003). The genesis of polygonal fault systems: a review. Geological Society, London, Special Publications, 216(1), 223-243.

Casero, P., Roure, F., Endignoux, L., Moretti, I., Muller, C. (1988). Neogene geodynamic evolution of the Southern Apennines. Memorie della Società Geologica Italiana, 41, 109-120.

Cashman, K. V., Giordano, G. (2014). Calderas and magma reservoirs. Journal of Volcanology and Geothermal Research, 288, 28-45.

Catalano, S., Monaco, C., Tortorici, L., Paltrinieri, W., Steel, N. (2004). Neogene-Quaternary tectonic evolution of the southern Apennines. Tectonics, 23(2).

Cavazza, W., Wezel, F. C. (2003). The Mediterranean region-a geological primer. Episodes, 26(3), 160-168.

Cavazza, W., Roure, F., Ziegler, P. A. (2004). The Mediterranean area and the surrounding regions: active processes, remnants of former Tethyan oceans and related thrust belts. In The Transmed Atlas. The Mediterranean Region from Crust to Mantle (pp. 1-29). Springer, Berlin, Heidelberg.

Chiodini, G., Caliro, S., De Martino, P., Avino, R., Gherardi, F. (2012). Early signals of new volcanic unrest at Campi Flegrei caldera? Insights from geochemical data and physical simulations. Geology, 40(10), 943-946.

Cervelli, P., Segall, P., Amelung, F., Garbeil, H., Meertens, C., Owen, S., Miklius, A., Lisowski, M. (2002). The 12 September 1999 upper east rift zone dike intrusion at Kilauea volcano, Hawaii. Journal of Geophysical Research: Solid Earth, 107(B7), ECV-3.

Chiodini, G., Paonita, A., Aiuppa, A., Costa, A., Caliro, S., De Martino, P., Acocella, V., Vandemeulebrouck, J. (2016). Magmas near the critical degassing pressure drive volcanic unrest towards a critical state. Nature Communications, 7(1), 1-9.

Ciaranfi, N., Guida, M., Turco, E., Scarpa, R., Cuscito, M. (1983). Elementi sismotettonici dell'Appennino meridionale. Bollettino della Società geologica italiana, 102(2-3), 201-222.

Cinque, A., Rolandi, G. T., Zamparelli, V. (1985). L'estensione dei depositi marini olocenici nei Campi Flegrei in relazione alla vulcano-tettonica. Bollettino della Società Geologica Italiana, 104(2), 327-348.

Cinque, A., Ascione, A., Caiazzo, C. (2000). Distribuzione spazio-temporale e caratterizzazione della fagliazione quaternaria in Appennino meridionale. Le ricerche del GNDT nel campo della pericolosità sismica, 203-218.

Cipollari, P., Cosentino, D., Gliozzi, E. (1999). Extension-and compression-related basins in central Italy during the Messinian Lago-Mare event. Tectonophysics, 315(1-4), 163-185.

Colantoni, P., M. Del Monte. "Ricerche geologiche nel Golfo di Pozzuoli." (1972).

Cole, P. D., Guest, J. E., Duncan, A. M., Chester, D. K., Bianchi, R. (1992). Post-collapse volcanic history of calderas on a composite volcano: an example from Roccamonfina, southern Italy. Bulletin of volcanology, 54(4), 253-266.

Cole, P. D., Guest, J. E., Duncan, A. M. (1993). The emplacement of intermediate volume ignimbrites: a case study from Roccamonfina Volcano, Southern Italy. Bulletin of Volcanology, 55(7), 467-480.

Cole, J. W., Milner, D. M., Spinks, K. D. (2005). Calderas and caldera structures: a review. Earth-Science Reviews, 69(1-2), 1-26.

Conticelli, S., Melluso, L., Perini, G., Avanzinelli, R., Boari, E. (2004). Petrologic, geochemical, and isotopic characteristics of potassic and ultrapotassic magmatism in Central-Southern Italy: inferences on its genesis and on the nature of mantle sources. Periodico di Mineralogia, 73(1), 153-164.

Conticelli, S., Marchionni, S., Rosa, D., Giordano, G., Boari, E., Avanzinelli, R. (2009). Shoshonite and sub-alkaline magmas from an ultrapotassic volcano: Sr–Nd–Pb isotope data on the Roccamonfina volcanic rocks, Roman Magmatic Province, Southern Italy. Contributions to Mineralogy and Petrology, 157(1), 41-63.

Corradino, M., Pepe, F., Sacchi, M., Solaro, G., Duarte, H., Ferranti, L., Zinno, I. (2021). Resurgent uplift at large calderas and relationship to caldera-forming faults and the magma reservoir: New insights from the Neapolitan Yellow Tuff caldera (Italy). Journal of Volcanology and Geothermal Research, 411, 107183.

Cosentino, D., Cipollari, P., Pipponzi, G., (2003). Il sistema orogenico dell'Appennino centrale:

vincoli stratigrafici e cronologia della migrazione. In: Cipollari, P., Cosentino, D. (Eds.), Evoluzione cinematica del sistema orogenico dell'Appennino centro-meridionale: caratterizzazione stratigrafico-strutturale dei bacini sintettoniciStudi Geologici Camerti, Numero Speciale 2003, 85–99.

Cosentino, D., Cipollari, P., Marsili, P., Scrocca, D. (2010). Geology of the central Apennines: a regional review. Journal of the virtual explorer, 36(11), 1-37.

Costa, A., Folch, A., Macedonio, G., Giaccio, B., Isaia, R., Smith, V. C. (2012). Quantifying volcanic ash dispersal and impact of the Campanian Ignimbrite super-eruption. Geophysical Research Letters, 39(10).

Cruden, A. R., McCaffrey, K. J., Bunger, A. P. (2017). Geometric scaling of tabular igneous intrusions: Implications for emplacement and growth. In Physical Geology of Shallow Magmatic Systems (pp. 11-38). Springer, Cham.

D'Agostino, N., Chamot-Rooke, N., Funiciello, R., Jolivet, L., Speranza, F. (1998). The role of pre-existing thrust faults and topography on the styles of extension in the Gran Sasso range (central Italy). Tectonophysics, 292(3-4), 229-254.

D'Auria, L., Giudicepietro, F., Aquino, I., Borriello, G., Del Gaudio, C., Lo Bascio, D., Martini, M., Ricciardi, G.P., Ricciolino, P., Ricco, C. (2011). Repeated fluid-transferepisodes as a mechanism for the recent dynamics of Campi Flegrei caldera (1989-2010). Journal of Geophysical Research: Solid Earth 116, B04313.

Dahm, T. (2000). Numerical simulations of the propagation path and the arrest of fluid-filled fractures in the Earth. Geophysical Journal International, 141(3), 623-638.

Davies, R.J., Mathias, S.A., Moss, J., Hustof, S., Newport, L., (2012). Hydraulic fractures: how far can they go? Marine and Petroleum Geology 37, 1e6

Davies, R. J., Foulger, G. R., Mathias, S., Moss, J., Hustoft, S., Newport, L. (2013). Reply: Davies et al.(2012), Hydraulic fractures: How far can they go. Marine and Petroleum Geology, 43, 519-521.

DeCelles, P. G., Busby, C. (2012). Foreland basin systems revisited: Variations in response to tectonic settings. Tectonics of sedimentary basins: Recent advances, 405-426.

Dewey, J. F., Helman, M. L., Knott, S. D., Turco, E., Hutton, D. H. W. (1989). Kinematics of the western Mediterranean. Geological Society, London, Special Publications, 45(1), 265-283.

De Lorenzo, G. (1904). The history of volcanic action in the Phlegraean Fields. Quarterly Journal of the Geological Society, 60(1-4), 296-315.

De Matteo, A., Corti, G., de Vries, B. V. W., Massa, B., Mussetti, G. (2018). Fault-volcano interactions with broadly distributed stretching in rifts. Journal of Volcanology and Geothermal Research, 362, 64-75.

De Natale, G., Troise, C., Mark, D., Mormone, A., Piochi, M., Di Vito, M. A., Isaia, R., Carlino, S., Barra, D., Somma, R. (2016). The Campi Flegrei Deep Drilling Project (CFDDP): New insight on caldera structure, evolution and hazard implications for the Naples area (Southern Italy). Geochemistry, Geophysics, Geosystems, 17(12), 4836-4847.

De Rita, D., Giordano, G., Milli, S. (1994). A stratigraphic-sedimentological approach to the volcanic risk evaluation: an example from Roccamonfina volcano (Southern Italy). EGS 19th General Assembly, Grenoble, 25-29 April 1994 (abstract).

De Rita, D., Giordano, G. (1996). Volcanological and structural evolution of Roccamonfina volcano (Italy): origin of the summit caldera. Geological Society, London, Special Publications, 110(1), 209-224.

De Rita, D., Giordano, G., Milli, S. (1997). Forestepping-backstepping stacking pattern of volcaniclastic successions: Roccamonfina volcano, Italy. Journal of volcanology and Geothermal Research, 78(3-4), 267-288.

De Siena, L., Chiodini, G., Vilardo, G., Del Pezzo, E., Castellano, M., Colombelli, S., Tisato, N., Ventura, G. (2017). Source and dynamics of a volcanic caldera unrest: Campi Flegrei, 1983–84. Scientific reports, 7(1), 1-13.

De Vita, S., Orsi, G., Civetta, L., Carandente, A., D'Antonio, M., Deino, A., di Cesare, T., Di Vito, M.A., Fisher, R.V., Isaia, R., Marotta, E., Necco, A., Ort, M., Pallalardo, L., Piochi, M., Southon, J. (1999). The Agnano–Monte Spina eruption (4100 years BP) in the restless Campi Flegrei caldera (Italy). Journal of Volcanology and Geothermal Research, 91(2-4), 269-301.

De Vivo, B., Rolandi, G., Gans, P. B., Calvert, A., Bohrson, W. A., Spera, F. J., Belkin, H. E. (2001). New constraints on the pyroclastic eruptive history of the Campanian volcanic Plain (Italy). Mineralogy and Petrology, 73(1), 47-65.

Deino, A. L., Orsi, G., de Vita, S., Piochi, M. (2004). The age of the Neapolitan Yellow Tuff caldera-forming eruption (Campi Flegrei caldera–Italy) assessed by 40Ar/39Ar dating method. Journal of Volcanology and Geothermal Research, 133(1-4), 157-170.

Delaney, P. T., Pollard, D. D. (1981). Deformation of host rocks and flow of magma during growth of minette dikes and breccia-bearing intrusions near Ship Rock, New Mexico (No. 1202). USGPO.

Demangeot, J. (1965). Géomorphologie des Abruzzes adriatiques (Vol. 1). Éditions du Centre national de la recherche scientifique.

Dewey, J.F., Helman, M.L., Turco, E., Hutton, D.H.W., Knott, S.D. (1989). Kinematics of the western Mediterranean, in Coward, M.P., Dietrich, D., Park, R.G. (Eds.), Alpine tectonics. Geological Society of London, Special Publications 45, 265-283.

Di Girolamo, P. (1972): II cono di scorie eccentrico di Sesto Campana (Isernia) (vulcano di Roccamonfina). - Boll. Soc. Nat. Napoli 81: 31-50.

Barbieri, M., Di Girolamo, P., Locardi, E., Lombardi, G., Stanzione, D., Nicoletti, M. (1976). Geothermal research in Western Campania (Italy): stratigraphy of the Parete exploratory well and new data on the volcanic sequence. In Proceedings of the Int. Conf.«Thermal Waters, Geothermal Energy and Volcanism of the Mediterranean Area», Athens.

Di Girolamo, P., Ghiara, M. R., Lirer, L., Munno, R., Rolandi, G., Stanzione, D. (1984). Vulcanologia e petrologia dei Campi Flegrei: Bollettino Società Geologica Italiana, v. 123.

Di Girolamo, P., Morra, V., Ortolani, F., Pagliuca, S. (1988). Osservazioni petrologiche e geodinamiche sul magmatismo orogenico transizionale della Cammpania nell'evoluzione della fascia tirrenica della catena appenninica. Bollettino della Societa Geologica Italiana, 107(3-4), 561-578.

Di Girolamo, P., Melluso, L. Morra, V. (1991). Magmatic activity northeast of Roccamonfina volcano (Southern Italy): Petrology, geochemistry and relationship with campanian volcanics. Neues Jahrbuch ffir Mineralogie Abhunellurgen, 163, 271-289.

Di Giuseppe, M. G., Troiano, A., Di Vito, M. A., Somma, R., Matano, F. (2017). Definition of small-scale volcanic structures by Electrical Resistivity Tomography: the Trentaremi cone, an example from the Campi Flegrei Caldera (Italy). Annals of Geophysics, 60(5), 0552.

Di Renzo, V., Arienzo, I., Civetta, L., D'Antonio, M., Tonarini, S., Di Vito, M. A., Orsi, G. (2011). The magmatic feeding system of the Campi Flegrei caldera: architecture and temporal evolution. Chemical Geology, 281(3-4), 227-241.

Di Vito, M. A., Isaia, R., Orsi, G., Southon, J. D., De Vita, S., d'Antonio, M., Pappalardo, L., Piochi, M. (1999). Volcanism and deformation since 12,000 years at the Campi Flegrei caldera (Italy). Journal of Volcanology and Geothermal Research, 91(2-4), 221-246.

Di Vito, M. A., Acocella, V., Aiello, G., Barra, D., Battaglia, M., Carandente, A., Del Gaudio, C., de Vita, S., Ricciardi, G.P., Ricco, C., Scandone, R., Terrasi, F. (2016). Magma transfer at Campi Flegrei caldera (Italy) before the 1538 AD eruption. Scientific reports, 6(1), 1-9.

Doglioni, C. (1991). A proposal for the kinematic modelling of W-dipping subductions-possible applications to the Tyrrhenian-Apennines system. Terra Nova, 3(4), 423-434.

Doglioni, C., Harabaglia, P., Martinelli, G., Mongelli, F., Zito, G. (1996). A geodynamic model of the Southern Apennines accretionary prism. Terra Nova 8, 540-547

Drymoni, K., Browning, J., Gudmundsson, A. (2020). Dyke-arrest scenarios in extensional regimes: Insights from field observations and numerical models, Santorini, Greece. Journal of Volcanology and Geothermal Research, 396, 106854.

Drymoni, K., Browning, J., Gudmundsson, A. (2021). Volcanotectonic interactions between inclined sheets, dykes, and faults at the Santorini Volcano, Greece. Journal of Volcanology and Geothermal Research, 107294.

Eliis Paleoscan (2021). https://www.eliis-geo.com/

EMODnet Bathymetry Consortium. (2018). EMODnet Digital Bathymetry (DTM 2018).

Faccenna, C., Funiciello, F., Giardini, D., Lucente, P., (2001). Episodic back-arc extension during restricted mantle convection in the Central Mediterranean. Earth and Planetary Science Letters 187, 105-116.

Favela, J., Anderson, D. L., Boschi, E. (2000). Extensional tectonics and global volcanism. Problems in geophysics for the new millennium, 463-498.

Fedele, L., Insinga, D. D., Calvert, A. T., Morra, V., Perrotta, A., Scarpati, C. (2011). 40Ar/39 Ar dating of tuff vents in the Campi Flegrei caldera (southern Italy): toward a new chronostratigraphic reconstruction of the Holocene volcanic activity. Bulletin of Volcanology, 73(9), 1323-1336.

Florio, G., Fedi, M., Cella, F., Rapolla, A. (1999). The Campanian Plain and Phlegrean Fields: structural setting from potential field data. Journal of Volcanology and Geothermal Research, 91(2-4), 361-379.

Fusi, N., Mirabile, L., Camerlenghi, A., Ranieri, G. (1991). Marine geophysical survey of the Gulf of Naples (Italy): Relationship between submarine volcanic activity and sedimentation. Mem. Soc. Geol. It. 47, 95-114, 13

Galderisi, A., Galli, P., Mazzoli, S., Peronace, E. (2017). Kinematic constraints of the active northern Matese Fault System (southern Italy). Bollettino di Geofisica Teorica ed Applicata, 58(4).

Galindo, I., Gudmundsson, A. (2012). Basaltic feeder dykes in rift zones: geometry, emplacement, and effusion rates. Natural Hazards and Earth System Sciences, 12(12), 3683-3700.

Galland, O., Spacapan, J. B., Rabbel, O., Mair, K., Soto, F. G., Eiken, T., Schiuma, M., Leanza, H. A. (2019). Structure, emplacement mechanism and magma-flow significance of igneous fingers–Implications for sill emplacement in sedimentary basins. Journal of Structural Geology, 124, 120-135.

Geo Marine Survey Systems B.V. (2012). https://www.geomarinesurveysystems.com/

GeoVis3D software package. (2022). https://www.ausgeol.org\geovis3d

Geshi, N., Kusumoto, S., Gudmundsson, A. (2010). Geometric difference between non-feeder and feeder dikes. Geology, 38(3), 195-198.

Geshi, N., Browning, J., Kusumoto, S. (2020). Magmatic overpressures, volatile exsolution and potential explosivity of fissure eruptions inferred via dike aspect ratios. Scientific reports, 10(1), 1-9.

Giaccio, B., Isaia, R., Fedele, F. G., Di Canzio, E., Hoffecker, J., Ronchitelli, A., Sinitsyn, A.A., Anikovich, M., Lisitsyn, S.N., Popov, V. V. (2008). The Campanian Ignimbrite and Codola tephra layers: two temporal/stratigraphic markers for the Early Upper Palaeolithic in southern Italy and eastern Europe. Journal of Volcanology and Geothermal Research, 177(1), 208-226.

Giaccio, B., Hajdas, I., Isaia, R., Deino, A., Nomade, S. (2017). High-precision 14 C and 40Ar/39Ar dating of the Campanian Ignimbrite (Y-5) reconciles the time-scales of climatic-cultural processes at 40 ka. Scientific Reports, 7(1), 1-10.

Giannetti, B., Luhr, J. F. (1983). The white trachytic tuff of Roccamonfina volcano (Roman region, Italy). Contributions to Mineralogy and Petrology, 84(2), 235-252.

Giannetti, B. (1990). Strutture neotettoniche presenti nel tufo trachitico bianco del vulcano di Roccamonfina. Boll Ser Geol Ital, 109, 195-206.

Giannetti, B., Luhr, J. F. (1990). Phlogopite-clinopyroxenite nodules from high-K magmas, Roccamonfina Volcano, Italy: evidence for a low-pressure metasomatic origin. Earth and Planetary Science Letters, 101(2-4), 404-424.

Giannetti, B. (2001). Origin of the calderas and evolution of Roccamonfina volcano (Roman Region, Italy). Journal of Volcanology and Geothermal Research, 106(3-4), 301-319.

Giordano, G., Naso, G., Trigari, A. (1995). Evoluzione Tettonica Di Un Settore Particolare Del Margine Tirrenico: L'area Al Confine Tra Lazio E Campania. Prime Considerazioni.

Giudicepietro, F. (1993). La dinamica recente dell'area vulcanica flegrea (Doctoral dissertation, Ph. D. Thesis, Napoli, 179 pp).

Goldberg, A. S. (2010). Dyke swarms as indicators of major extensional events in the 1.9–1.2 Ga Columbia supercontinent. Journal of Geodynamics, 50(3-4), 176-190.

Grohmann, C. H., Campanha, G. A. (2010). OpenStereo: open source, cross-platform software for structural geology analysis. In AGU Fall Meeting abstracts (Vol. 2010, pp. IN31C-06).

Gudmundsson, A. (1983). Form and dimensions of dykes in eastern Iceland. Tectonophysics, 95(3-4), 295-307.

Gudmundsson, A. (1984). Formation of dykes, feeder-dykes, and the intrusion of dykes from magma chambers. Bulletin Volcanologique, 47(3), 537-550.

Gudmundsson, A. (1990). Emplacement of dikes, sills and crustal magma chambers at divergent plate boundaries. Tectonophysics, 176(3-4), 257-275.

Gudmundsson, A. (1995). The geometry and growth of dykes. Physics and chemistry of dykes, 23-34.

Gudmundsson, A. (2011). Rock fractures in geological processes. Cambridge University Press.

Gudmundsson, A. (2020). Volcanotectonics: Understanding the structure, deformation and dynamics of volcanoes. Cambridge University Press.

Gueguen, E., Doglioni, C., Fernandez, M. (1998). On the post-25 Ma geodynamic evolution of the western Mediterranean. Tectonophysics, 298(1-3), 259-269.

Guidoboni, E., Ciuccarelli, C. (2011). The Campi Flegrei caldera: historical revision and new data on seismic crises, bradyseisms, the Monte Nuovo eruption and ensuing earthquakes (twelfth century 1582 AD). Bulletin of volcanology, 73(6), 655-677.

Hardy, S. (2011). Cover deformation above steep, basement normal faults: Insights from 2D discrete element modeling. Marine and Petroleum geology, 28(5), 966-972.

Hardy, S. (2013). Propagation of blind normal faults to the surface in basaltic sequences: Insights from 2D discrete element modelling. Marine and Petroleum Geology, 48, 149-159.

INGV (2021). Volcano monitoring monthly bulletin

Insinga, D., Calvert, A. T., Lanphere, M. A., Morra, V., Perrotta, A., Sacchi, M., Scarpati, C., Saburomaru, J., Fedele, L. (2006). The Late-Holocene evolution of the Miseno area (south-western Campi Flegrei) as inferred by stratigraphy, petrochemistry and 40Ar/39Ar geochronology. In Developments in Volcanology (Vol. 9, pp. 97-124). Elsevier.

Ippolito, F. (1973). Struttura marginale tirrenica dell'Appennino Campano: reinterpretazione di dati di antiche ricerche di idrocarburi.

Isaia, R., D'Antonio, M., Dell'Erba, F., Di Vito, M., Orsi, G. (2004). The Astroni volcano: the only example of closely spaced eruptions in the same vent area during the recent history of the Campi Flegrei caldera (Italy). Journal of Volcanology and Geothermal Research, 133(1-4), 171-192.

Isaia, R., Marianelli, P., Sbrana, A. (2009). Caldera unrest prior to intense volcanism in Campi Flegrei (Italy) at 4.0 ka BP: Implications for caldera dynamics and future eruptive scenarios. Geophysical Research Letters, 36(21).

Isaia, R., Vitale, S., Di Giuseppe, M. G., Iannuzzi, E., Tramparulo, F. D. A., Troiano, A. (2015). Stratigraphy, structure, and volcano-tectonic evolution of Solfatara maar-diatreme (Campi Flegrei, Italy). GSA Bulletin, 127(9-10), 1485-1504.

Isaia, R., Vitale, S., Marturano, A., Aiello, G., Barra, D., Ciarcia, S., Iannuzzi, E., Tramparulo, F. D. A. (2019). High-resolution geological investigations to reconstruct the long-

term ground movements in the last 15 kyr at Campi Flegrei caldera (southern Italy). Journal of Volcanology and Geothermal Research, 385, 143-158.

Isaia, R., Di Giuseppe, M. G., Natale, J., Tramparulo, F. D. A., Troiano, A., Vitale, S. (2021). Volcano-tectonic setting of the Pisciarelli fumarole field, Campi Flegrei caldera, southern Italy: Insights into fluid circulation patterns and hazard scenarios. Tectonics, 40, e2020TC006227. https://doi.org/10.1029/2020TC006227

Jackson, C. A., Schofield, N., Golenkov, B. (2013). Geometry and controls on the development of igneous sill–related forced folds: A 2-D seismic reflection case study from offshore southern Australia. Bulletin, 125(11-12), 1874-1890.

James, M. Robson, S. (2012). Straightforward reconstruction of 3D surfaces and topography with a camera: Accuracy and geoscience application. J. Geophys. Res. Space Phys. 117, 03017.

Jolivet, L., Faccenna, C., D'Agostino, N., Fournier, M., Worrall, D. (1999). The kinematics of back-arc basins, examples from the Tyrrhenian, Aegean and Japan Seas. Geological Society, London, Special Publications, 164(1), 21-53.

Kennedy, B. M., Holohan, E. P., Stix, J., Gravley, D. M., Davidson, J. R. J., Cole, J. W. (2018). Magma plumbing beneath collapse caldera volcanic systems. Earth-Science Reviews, 177, 404-424.

Lacazette, A., Geiser, P. (2013). Comment on Davies et al., 2012—Hydraulic fractures: How far can they go?. Marine and Petroleum Geology, 43, 516-518.

Lambeck, K., Antonioli, F., Anzidei, M., Ferranti, L., Leoni, G., Scicchitano, G., Silenzi, S. (2011). Sea level change along the Italian coast during the Holocene and projections for the future. Quaternary International, 232(1-2), 250-257.

Lirer, L., Luongo, G., Scandone, R. (1987). On the volcanological evolution of Campi Flegrei. Eos, Transactions American Geophysical Union, 68(16), 226-234.

Lister, J. R. (1990). Buoyancy-driven fluid fracture: the effects of material toughness and of low-viscosity precursors. Journal of Fluid Mechanics, 210, 263-280.

Lucchi, F., Tranne, C. A., Calanchi, N., Rossi, P. L., Keller, J. (2007). The stratigraphic role of marine deposits in the geological evolution of the Panarea volcano (Aeolian Islands, Italy). Journal of the Geological Society, 164(5), 983-996.

Lucchi, F. (2019). On the use of unconformities in volcanic stratigraphy and mapping: Insights from the Aeolian Islands (southern Italy). Journal of Volcanology and Geothermal Research, 385, 3-26.

Luhr, J. F., Giannetti, B. (1987). The brown leucitic tuff of Roccamonfina Volcano (Roman region, Italy). Contributions to Mineralogy and Petrology, 95(4), 420-436.

Lustrino, M., Duggen, S., Rosenberg, C. L. (2011). The Central-Western Mediterranean: Anomalous igneous activity in an anomalous collisional tectonic setting. Earth-Science Reviews, 104(1-3), 1-40.

Magee, C., Jackson, C. A. L., Schofield, N. (2013). The influence of normal fault geometry on igneous sill emplacement and morphology. Geology, 41(4), 407-410.

Magee, C., Muirhead, J., Schofield, N., Walker, R. J., Galland, O., Holford, S., Spacapan, J., Jackson, C. A-L, McCarthy, W. (2019). Structural signatures of igneous sheet intrusion propagation. Journal of Structural Geology, 125, 148-154.

Magee, C., Jackson, C. A. L. (2021). Can we relate the surface expression of dike-induced normal faults to subsurface dike geometry?. Geology, 49(4), 366-371.

Marra, F., Gaeta, M., Giaccio, B., Jicha, B. R., Palladino, D. M., Polcari, M., Sottili, G., Taddeucci, J., Florindo, F., Stramondo, S. (2016). Assessing the volcanic hazard for Rome: 40Ar/39Ar and In-SAR constraints on the most recent eruptive activity and present-day uplift at Colli Albani Volcanic District. Geophysical Research Letters, 43(13), 6898-6906.

Marra, F., Florindo, F., Jicha, B. R., Nomade, S., Palladino, D. M., Pereira, A., Sottili, G., Tolomei, C. (2019). Volcano-tectonic deformation in the Monti Sabatini Volcanic District at the gates of Rome (central Italy): evidence from new geochronologic constraints on the Tiber River MIS 5 terraces. Scientific reports, 9(1), 1-14.

Marra, F., Castellano, C., Cucci, L., Florindo, F., Gaeta, M., Jicha, B. R., Palladino, D. M., Sottili, G., Tertulliani, A., Tolomei, C. (2020). Monti Sabatini and Colli Albani: the dormant twin volcanoes at the gates of Rome. Scientific reports, 10(1), 1-17.

Marra, F., Jicha, B., Palladino, D. M., Gaeta, M., Costantini, L., Di Buduo, G. M. (2020). 40Ar/39Ar single crystal dates from pyroclastic deposits provide a detailed record of the 590–240 ka eruptive period at the Vulsini Volcanic District (central Italy). Journal of Volcanology and Geothermal Research, 398, 106904.

Marra, F., Cardello, G. L., Gaeta, M., Jicha, B. R., Montone, P., Niespolo, E. M., Nomade, S., Palladino, D. M., Pereira, A., De Luca, G., Florindo, F., Frepoli, A., Renne, P. R., Sottili, G. (2021). The Volsci Volcanic Field (central Italy): eruptive history, magma system and implications on continental subduction processes. International Journal of Earth Sciences, 110(2), 689-718.

Marsh, B. D. (1984). On the mechanics of caldera resurgence. Journal of Geophysical Research: Solid Earth, 89 (B10), 8245-8251.

Martí, J., Groppelli, G., da Silveira, A. B. (2018). Volcanic stratigraphy: A review. Journal of Volcanology and Geothermal Research, 357, 68-91.

Marturano, A., Isaia, R., Aiello, G., Barra, D. (2018). Complex dome growth at Campi Flegrei caldera (Italy) in the last 15 ka. Journal of Geophysical Research: Solid Earth, 123(9), 8180-8197.

Mathieu, L., De Vries, B. V. W., Holohan, E. P., Troll, V. R. (2008). Dykes, cups, saucers and sills: Analogue experiments on magma intrusion into brittle rocks. Earth and Planetary Science Letters, 271(1-4), 1-13.

Mazzoli, S., Aldega, L., Corrado, S., Invernizzi, C., Zattin, M. (2006). Pliocene-quaternary thrusting, syn-orogenic extension and tectonic exhumation in the Southern Apennines (Italy): Insights from the Monte Alpi area. Special Papers-Geological Society Of America, 414, 55.

Mazzoli, S., D'errico, M., Aldega, L., Corrado, S., Invernizzi, C., Shiner, P., Zattin, M. (2008). Tectonic burial and "young"(< 10 Ma) exhumation in the southern Apennines fold-and-thrust belt (Italy). Geology, 36(3), 243-246.

Noguera, A. M., Rea, G. (2000). Deep structure of the Campanian–Lucanian arc (southern Apennine, Italy). Tectonophysics, 324(4), 239-265.

Milia A. (1998): Stratigrafia, strutture deformative e considerazioni sull'origine delle unità deposizionali oloceniche del Golfo di Pozzuoli (Napoli). Boll. Soc. Geol. Ital., 117, 777-787.

Milia A., Torrente M.M., Giordano F. (2000): Active deformation and volcanism offshore Campi Flegrei, Italy: new data from high-resolution seismic reflection profiles. Mar. Geol., 171, 61-73.

Milia, A., Torrente, M. M. (2003). Late-Quaternary volcanism and transtensional tectonics in the Bay of Naples, Campanian continental margin, Italy. Mineralogy and Petrology, 79(1), 49-65.

Milia, A. (2010). The stratigraphic signature of volcanism off Campi Flegrei (Bay of Naples, Italy). Geological Society of America Special Papers, 464, 155-170.

Morhange, C., Marriner, N., Laborel, J., Todesco, M., Oberlin, C. (2006). Rapid sea-level movements and noneruptive crustal deformations in the Phlegrean Fields caldera, Italy. Geology, 34(2), 93-96.

Mosher, D. C., Simpkin, P. G. (1999). Status and trends of marine high-resolution seismic reflection profiling: Data acquisition. Geoscience Canada, 26, 174–188.

Merlini, S., Mostardini, F. (1986). Appennino centro-meridionale: sezioni geologiche e proposta di modello strutturale. In Geologia dell'Italia centrale. Congresso nazionale. 73 (pp. 147-149).

Natale, J., Ferranti, L., Scarpati, C., Marino, C., Sacchi, M. (2018). Structural features of the Neapolitan Yellow Tuff (NYT) collapse caldera-resurgent dome system in the Campi

Flegrei offshore sector, Southern Italy. In AGU Fall Meeting Abstracts (Vol. 2018, pp. V31H-0218).

Natale, J., Ferranti, L., Marino, C., Sacchi, M. (2020). Resurgent dome faults in the offshore of the Campi Flegrei caldera (Pozzuoli Bay, Campania): Preliminary results from high-resolution seismic reflection profiles. Bollettino di Geofisica Teorica ed Applicata, 61(3), 333–342.

Natale, J., Ferranti, L., Isaia, R., Marino, C., Sacchi, M., Spiess, V., Steinmann, L., Vitale, S. (2021). Integrated on-land-offshore stratigraphy of the Campi Flegrei caldera: new insights into the volcano-tectonic evolution in the last 15 kyr. Basin Research.

Neri, A., Bevilacqua, A., Esposti Ongaro, T., Isaia, R., Aspinall, W. P., Bisson, M., Flandoli, F., Baxter, P.J., Bertagnini, A., Iannuzzi, E., Orsucci, S., Pistolesi, M., Rosi, M., Vitale, S. (2015). Quantifying volcanic hazard at Campi Flegrei caldera (Italy) with uncertainty assessment: 2. Pyroclastic density current invasion maps. Journal of Geophysical Research: Solid Earth, 120(4), 2330-2349.

Newhall, C. G., Dzurisin, D. (1988). Historical unrest at the large calderas of the world (Vol. 2, No. 1855). Department of the Interior, US Geological Survey.

Nicotera, P., Civita, M. (1969). Ricerche idrogeologiche per la realizzazione delle opere di presa delle sorgenti Mercato e Palazzo in Sarno (Campania). Mem. e Note Ist. Geol. Appl. Napoli, 13.

Orsi, G., D'Antonio, M., de Vita, S., Gallo, G. (1992). The Neapolitan Yellow Tuff, a large-magnitude trachytic phreatoplinian eruption: eruptive dynamics, magma withdrawal and caldera collapse. Journal of Volcanology and Geothermal Research, 53(1-4), 275-287.

Orsi, G., De Vita, S., Di Vito, M. (1996). The restless, resurgent Campi Flegrei nested caldera (Italy): constraints on its evolution and configuration. Journal of Volcanology and Geothermal Research, 74(3-4), 179-214.

Orsi, G., Civetta, L., Del Gaudio, C., De Vita, S., Di Vito, M. A., Isaia, R., Petrazzuoli, S. M., Ricciardi, G. P., Ricco, C. (1999). Short-term ground deformations and seismicity in the

resurgent Campi Flegrei caldera (Italy): an example of active block-resurgence in a densely populated area. Journal of Volcanology and Geothermal Research, 91(2-4), 415-451.

Orsi, G., Di Vito, M. A., Isaia, R. (2004). Volcanic hazard assessment at the restless Campi Flegrei caldera. Bulletin of Volcanology, 66(6), 514-530.

Palladino, D. M., Simei, S., Sottili, G., Trigila, R., Groppelli, G. (2010). Integrated approach for the reconstruction of stratigraphy and geology of Quaternary volcanic terrains: an application to the Vulsini Volcanoes (central Italy). Stratigraphy and Geology of Volcanic Areas. The Geological Society of America Special Paper, 464, 63-84.

Palmiotto, C., Loreto, M. F. (2019). Regional scale morphological pattern of the Tyrrhenian Sea: New insights from EMODnet bathymetry. Geomorphology, 332, 88-99.

Pappalardo, L., Civetta, L., d'Antonio, M., Deino, A., Di Vito, M., Orsi, G., Carandente, A., de Vita, S., Isaia, R., Piochi, M. (1999). Chemical and Sr-isotopical evolution of the Phlegraean magmatic system before the Campanian Ignimbrite and the Neapolitan Yellow Tuff eruptions. Journal of Volcanology and Geothermal Research, 91(2-4), 141-166.

Parascandola, A. (1947). I fenomeni bradisismici del Serapeo di Pozzuoli. Stabilmento tipografico G. Genovese.

Parsons, T., Thompson, G. A. (1991). The role of magma overpressure in suppressing earthquakes and topography: Worldwide examples. Science, 253(5026), 1399-1402.

Patacca, E., Scandone, P. (2007). Geology of the southern Apennines. Bollettino della Società Geologica Italiana, 7, 75-119.

Peccerillo, A. (2005). Plio-quaternary volcanism in Italy (Vol. 365). New York: Springer-Verlag Berlin Heidelberg.

Peccerillo, A., Association internationale de volcanologie et de chimie de l'intérieur de la Terre. (2017). Cenozoic volcanism in the Tyrrhenian Sea region (p. 399). Berlin: Springer.

Penta, F., Conforto, B. (1951). Results of exploratory drilling in Campi Flegrei region and of prospecting for vapor, thermal water, and endogenous forces. Ann. Geofis.(Rome), 4(3).

Perini, G., Francalanci, L., Davidson, J. P., Conticelli, S. (2004). Evolution and genesis of magmas from Vico Volcano, Central Italy: multiple differentiation pathways and variable parental magmas. Journal of Petrology, 45(1), 139-182.

Pescatore T., Diplomatico G., Senatore M., Tramutoli M., Mirabile L. (1984): Contributi allo studio del Golfo di Pozzuoli: aspetti stratigrafici e strutturali. Mem. Soc. Geol. Ital., 27, 133-149.

Pistolesi, M., Bertagnini, A., Di Roberto, A., Isaia, R., Vona, A., Cioni, R., Giordano, G. (2017). The Baia–Fondi di Baia eruption at Campi Flegrei: stratigraphy and dynamics of a multi-stage caldera reactivation event. Bulletin of Volcanology, 79(9), 1-18.

Pistolesi, M., Isaia, R., Marianelli, P., Bertagnini, A., Fourmentraux, C., Albert, P. G., Tomlinson, E.L., Menziers, M.A., Rosi, M., Sbrana, A. (2016). Simultaneous eruptions from multiple vents at Campi Flegrei (Italy) highlight new eruption processes at calderas. Geology, 44(6), 487-490.

Pollard, D. D., Muller, O. H. (1976). The effect of gradients in regional stress and magma pressure on the form of sheet intrusions in cross section. Journal of Geophysical Research, 81(5), 975-984.

Poppe, S., Galland, O., de Winter, N. J., Goderis, S., Claeys, P., Debaille, V., Boulvais, P., Kervyn, M. (2020). Structural and geochemical interactions between magma and sedimentary host rock: The Hovedøya case, Oslo Rift, Norway. Geochemistry, Geophysics, Geosystems, 21(3), e2019GC008685.

Radicati di Brozolo, F., Di Girolamo, P., Turi, B., Oddone, M. (1988). 40Ar-39Ar and K-Ar dating of K-rich rocks from the Roccamonfina Volcano, Roman Comagmatic Region, Italy. Geochimica et Cosmochimica Acta, 52(6), 1435-1441.

Reiter, F., Acs, P., (1996-2022). TectonicsFP ©1996-2020 Help version 1.7.14, 2020-02-02

Rittmann, A. (1950). Sintesi geologica dei Campi Flegrei. Boll. Soc. Geol. Ital, 69(2).

Rodriquez, A. (1964). Contributo alla conoscenza delle faune fossili dei Campi Flegrei (La Starza). Boll. Soc. Nat., Napoli 73, 102-138

Rolandi, G., Bellucci, F., Heizler, M. T., Belkin, H. E., De Vivo, B. (2003). Tectonic controls on the genesis of ignimbrites from the Campanian Volcanic Zone, southern Italy. Mineralogy and Petrology, 79(1), 3-31.

Romano, C., Vona, A., Campagnola, S., Giordano, G., Arienzo, I., Isaia, R. (2020). Modelling and physico-chemical constraints to the 4.5 ka Agnano-Monte Spina Plinian eruption (Campi Flegrei, Italy). Chemical Geology, 532, 119301.

Rosi, M., Sbrana, A., Principe, C. (1983). The Phlegraean Fields: structural evolution, volcanic history and eruptive mechanisms. Journal of Volcanology and Geothermal Research, 17(1-4), 273-288.

Rosi, M., Sbrana, A. (1987). Phlegrean fields. Quaderni de la ricerca scientifica, 9(114).

Rouchon, V., Gillot, P. Y., Quidelleur, X., Chiesa, S., Floris, B. (2008). Temporal evolution of the Roccamonfina volcanic complex (Pleistocene), Central Italy. Journal of Volcanology and Geothermal Research, 177(2), 500-514.

Roure, F., Casero, P., Addoum, B. (2012). Alpine inversion of the North African margin and delamination of its continental lithosphere. Tectonics, 31(3).

Royden, L. H. (1993). The tectonic expression slab pull at continental convergent boundaries. Tectonics, 12(2), 303-325.

Rubin, A. M. (1992). Dike-induced faulting and graben subsidence in volcanic rift zones. Journal of Geophysical Research: Solid Earth, 97(B2), 1839-1858.

Rubin, A. M. (1995). Getting granite dikes out of the source region. Journal of Geophysical Research: Solid Earth, 100(B4), 5911-5929.

Ruch, J., Acocella, V., Geshi, N., Nobile, A., Corbi, F. (2012). Kinematic analysis of vertical collapse on volcanoes using experimental models time series. Journal of Geophysical Research: Solid Earth, 117(B7).

Sabbatino, M., Vitale, S., Tavani, S., Consorti, L., Corradetti, A., Cipriani, A., Arienzo, I., Parente, M. (2020). Constraining the onset of flexural subsidence and peripheral bulge extension in the Miocene foreland of the southern Apennines (Italy) by Sr-isotope stratigraphy. Sedimentary Geology, 401, 105634.

Sabbatino, M., Tavani, S., Vitale, S., Ogata, K., Corradetti, A., Consorti, L., Arienzo, I., Cipriani, A., Parente, M. (2021). Forebulge migration in the foreland basin system of the central-southern Apennine fold-thrust belt (Italy): New high-resolution Sr-isotope dating constraints. Basin Research, 33(5), 2817-2836.

Sacchi, M., Caccavale, M., Corradino, M., Esposito, G., Ferranti, L., Hámori, Z., Horvath, F., Insinga, D., Marino, C., Matano, F., Molisso, F., Natale, J., Passaro, S., Pepe, F., Tóth, T. (2019). The use and beauty of ultra-high-resolution seismic reflection imaging in Late Quaternary marine volcaniclastic settings, Napoli Bay, Italy. Földtani Közlöny, 149(3, 4), 371-371.

Sacchi, M., Pepe, F., Corradino, M., Insinga, D. D., Molisso, F., Lubritto, C. (2014). The Neapolitan Yellow Tuff caldera offshore the Campi Flegrei: Stratal architecture and kinematic reconstruction during the last 15 ky. Marine Geology, 354, 15-33.

Saunders, S. J. (2004). The possible contribution of circumferential fault intrusion to caldera resurgence. Bulletin of Volcanology, 67(1), 57-71.

Savelli, C., (2002). Time–space distribution of magmatic activity in the western Mediterranean and peripheral orogens during the past 30 Ma (a stimulus to geodynamic considerations). Journal of Geodynamics 34, 99–126.

Sbrana, A., Isaia, R., Iannuzzi, E., Marianelli, P. (2015). Carta Geologica d'Italia alla scala 1:50.000, Foglio 446-447 Napoli (aree emerse). https://www.isprambiente.gov.it/Media/carg/447_NAPOLI/Foglio.html

Scandone, R., Bellucci, F., Lirer, L., Rolandi, G. (1991). The structure of the Campanian Plain and the activity of the Neapolitan volcanoes (Italy). Journal of Volcanology and Geothermal Research, 48(1-2), 1-31.

Scarpati, C., Cole, P., Perrotta, A. (1993). The Neapolitan Yellow Tuff—a large volume multiphase eruption from Campi Flegrei, southern Italy. Bulletin of Volcanology, 55(5), 343-356.

Scarpati, C., Perrotta, A., Lepore, S., Calvert, A. (2013). Eruptive history of Neapolitan volcanoes: constraints from 40Ar–39Ar dating. Geological Magazine, 150(3), 412-425.

Scarpati, C., Perrotta, A. (2016). Stratigraphy and physical parameters of the Plinian phase of the Campanian Ignimbrite eruption. Bulletin, 128(7-8), 1147-1159.

Scarpati, C., Sparice, D., Perrotta, A. (2020). Dynamics of large pyroclastic currents inferred by the internal architecture of the Campanian Ignimbrite. Scientific reports, 10(1), 1-13.

Schofield, N. J., Brown, D. J., Magee, C., Stevenson, C. T. (2012). Sill morphology and comparison of brittle and non-brittle emplacement mechanisms. Journal of the Geological Society, 169(2), 127-141.

Schwartz, M. L. (1967). The Bruun theory of sea-level rise as a cause of shore erosion. The journal of Geology, 75(1), 76-92.

Scrocca D., Doglioni C., Innocenti F., Manetti P., Mazzotti A., Bertelli L., Burbi L., D'offizi S. (Eds.) (2003) - CROP Atlas: seismic reflection profiles of the Italian crust. Mem. Descr. Carta Geol. d'It., 62: pp. 194.

Scrocca, D. (2010). Southern Apennines: structural setting and tectonic evolution. Journal of the Virtual Explorer, 36(14).

Secomandi, M., Paoletti, V., Aiello, G., Fedi, M., Marsella, E., Ruggieri, S., D'Argenio, B., Rapolla, A. (2003). Analysis of the magnetic anomaly field of the volcanic district of the Bay of Naples, Italy. Marine Geophysical Researches, 24(3), 207-221.

Serpelloni, E., Casula, G., Galvani, A., Anzidei, M., Baldi, P. (2006). Data analysis of Permanent GPS networks in Italy and surrounding region: application of a distributed processing approach. Annals of Geophysics, 49(4-5).

Sgrosso, I., Aiello, R. (1963): Bocca eruttiva presso Presenzano (Caserta). - Boll. Soc. Nat. Napoli 72: 285-293.

Shiner, P., Beccacini, A., Mazzoli, S. (2004). Thin-skinned versus thick-skinned structural models for Apulian carbonate reservoirs: constraints from the Val d'Agri Fields, S Apennines, Italy. Marine and Petroleum Geology, 21(7), 805-827.

Silleni, A., Giordano, G., Isaia, R., Ort, M. H. (2020). The Magnitude of the 39.8 ka Campanian Ignimbrite Eruption, Italy: Method, Uncertainties and Errors. Front. Earth Sci, 8, 543399.

Simpkin, P. G., Davis, A. (1993). For seismic profiling in very shallow water, a novel receiver. Sea Technology, 34, 21–28.

Smets, B., Kervyn, M., d'Oreye, N., Kervyn, F. (2015). Spatio-temporal dynamics of eruptions in a youthful extensional setting: Insights from Nyamulagira Volcano (DR Congo), in the western branch of the East African Rift. Earth-Science Reviews, 150, 305-328.

Smith, R. L., Bailey, R. A. (1968). Resurgent cauldrons. Memoir of the Geological Society of America, 116, 613-662.

Smith, R. L. (1979). Ash-flow magmatism. Ash-flow tuffs: Geological Society of America Special Paper, 180, 5-27.

Smith, V. C., Isaia, R., Pearce, N. J. G. (2011). Tephrostratigraphy and glass compositions of post-15 kyr Campi Flegrei eruptions: implications for eruption history and chronostratigraphic markers. Quaternary Science Reviews, 30(25-26), 3638-3660.

Somma, R., Iuliano, S., Matano, F., Molisso, F., Passaro, S., Sacchi, M., Troise, C., De Natale, G. (2016). High-resolution morpho-bathymetry of Pozzuoli Bay, southern Italy. Journal of Maps, 12(2), 222-230.

Spacapan, J. B., Galland, O., Leanza, H. A., Planke, S. (2017). Igneous sill and finger emplacement mechanism in shale-dominated formations: a field study at Cuesta del Chihuido, Neuquén Basin, Argentina. Journal of the Geological Society, 174(3), 422-433.

Spera, F. J., Crisp, J. A. (1981). Eruption volume, periodicity, and caldera area: relationships and inferences on development of compositional zonation in silicic magma chambers. Journal of Volcanology and Geothermal Research, 11(2-4), 169-187.

Steinmann, L., Spiess, V., Sacchi, M. (2016). The Campi Flegrei caldera (Italy): formation and evolution in interplay with sea-level variations since the Campanian Ignimbrite eruption at 39 ka. Journal of Volcanology and Geothermal Research, 327, 361-374.

Steinmann, L., Spiess, V., Sacchi, M. (2018). Post-collapse evolution of a coastal caldera system: Insights from a 3D multichannel seismic survey from the Campi Flegrei caldera (Italy). Journal of Volcanology and Geothermal Research, 349, 83-98.

Storti, F., McClay, K. (1995). Influence of syntectonic sedimentation on thrust wedges in analogue models. Geology, 23(11), 999-1002.

Tedesco, C. (1965). Main lines of the history of the Roccamonfina volcano. Bulletin Volcanologique, 28(1), 119-137.

Tibaldi, A., Corti, N., Bonali, F. L., Mariotto, F. P., Russo, E. (2020). Along-rift propagation of Pleistocene-Holocene faults from a central volcano. Journal of Structural Geology, 141, 104201.

Townsend, M., Huber, C., Degruyter, W., Bachmann, O. (2019). Magma chamber growth during intercaldera periods: Insights from thermo-mechanical modeling with applications to Laguna del Maule, Campi Flegrei, Santorini, and Aso. Geochemistry, Geophysics, Geosystems, 20, 1574–1591. https://doi.org/10.1029/2018GC008103

Tozer, R.S.J., Butler, R.W.H., Corrado, S., Geologiche, S., Tre, R., San, L., Murialdo, L., (2002). Comparing thin- and thick-skinned thrust tectonic models of the Central Apennines, Italy. EGU Stephan Mueller Special Publication Series 1, pp. 181–194.

Tramparulo, F. D. A., Vitale, S., Isaia, R., Tadini, A., Bisson, M., Prinzi, E. P. (2018). Relation between alternating open/closed-conduit conditions and deformation patterns: An example from the Somma-Vesuvius volcano (southern Italy). Journal of Structural Geology, 112, 138-153.

Trippanera, D., Ruch, J., Acocella, V., Rivalta, E. (2015). Experiments of dike-induced deformation: insights on the long-term evolution of divergent plate boundaries. Journal of Geophysical Research: Solid Earth, 120(10), 6913-6942.

Trincardi, F., Zitellini, N. (1987). The rifting of the Tyrrhenian Basin. Geo-marine letters, 7(1), 1-6.

Trippanera, D., Ruch, J., Passone, L., Jónsson, S. (2019). Structural mapping of dike-induced faulting in Harrat Lunayyir (Saudi Arabia) by using high resolution drone imagery. Frontiers in Earth Science, 7, 168.

Turco, E., Schettino, A., Pierantoni, P. P., Santarelli, G. (2006). The Pleistocene extension of the Campania Plain in the framework of the southern Tyrrhenian tectonic evolution: morphotectonic analysis, kinematic model and implications for volcanism. In Developments in Volcanology (Vol. 9, pp. 27-51). Elsevier.

USGS (2017), USGS National UAS Project Office. Unmanned Aircraft Systems Data Post-Processing: Structure-from-Motion Photogrammetry. Available online: https://uas.usgs.gov/nupo/pdf/USGSAgisoftPhotoScanWorkflow.pdf

Versino, L. (1972). Relazione sui rilievi effettuati nell'area flegrea nel 1970–71. Quaderni Ricerca Scientifica, (83).

Vitale S., Ciarcia, S., (2013). Tectono-stratigraphic and kinematic evolution of the southern Apennines/Calabria-Peloritani Terrane system (Italy). Tectonophysics 583, 164-182

Vitale, S., Isaia, R. (2014). Fractures and faults in volcanic rocks (Campi Flegrei, southern Italy): insight into volcano-tectonic processes. International Journal of Earth Sciences, 103(3), 801-819.

Vitale S., Tramparulo F.D.A., Ciarcia S., Amore F.O., Prinzi E.P., Laiena F. (2017). The northward tectonic transport in the southern Apennines: Examples from the Capri Island and western Sorrento Peninsula (Italy). International Journal of Earth Sciences, 106, 97-113.

Vitale, S., Ciarcia, S. (2018). Tectono-stratigraphic setting of the Campania region (southern Italy). Journal of Maps, 14(2), 9-21.

Vitale, S., Isaia, R., Ciarcia, S., Di Giuseppe, M. G., Iannuzzi, E., Prinzi, E. P., Tramparulo, F.D.A., Troiano, A. (2019). Seismically induced soft-sediment deformation phenomena during the volcano-tectonic activity of Campi Flegrei caldera (southern Italy) in the last 15 kyr. Tectonics, 38(6), 1999-2018.

Vitale S., Prinzi E.P., Tramparulo F.D.A., De Paola C., Di Maio R., Piegari E., Sabbatino M., Natale J., Notaro P., Ciarcia S. (2020). Late Miocene-early Pliocene out-of-sequence thrusting in the southern Apennines (Italy). Geosciences, 10(8), 301.

Vitale, S., Prinzi, E. P., Monda, M., Tramparulo, F. D. A., Ciarcia, S. (2020). Structural and stratigraphic setting of campagna and giffoni tectonic windows: New insights on the orogenic evolution of the Southern Apennines (Italy). Geosciences, 10(10), 405.

Vitale S., Ciarcia S. (2021). The dismembering of the Adria platforms following the Late Cretaceous-Eocene abortive rift: A review of the tectono-stratigraphic record in the southern Apennines. Journal of Geology Review. DOI:10.1080/00206814.2021.2004559)

Waelbroeck, C., Labeyrie, L., Michel, E., Duplessy, J.C., McManus, J.F., Lambeck, K., Balbon, E., Labracherie, M. (2002). Sea-level and deep water temperature changes derived from benthic foraminifera isotopic records. Quat. Sci. Rev. 21, 295–305.

Washington, H. S. (1906). The Roman comagmatic region (No. 57). Carnegie Institution of Washington.

Weismüller, C., Urai, J. L., Kettermann, M., von Hagke, C., Reicherter, K. (2019). Structure of massively dilatant faults in Iceland: lessons learned from high-resolution unmanned aerial vehicle data. Solid Earth, 10(5), 1757-1784.

Wohletz, K., Orsi, G., De Vita, S. (1995). Eruptive mechanisms of the Neapolitan Yellow Tuff interpreted from stratigraphie, chemical, and granulometric data. Journal of Volcanology and Geothermal Research, 67(4), 263-290.

Woo, J. Y., Kilburn, C. R. (2010). Intrusion and deformation at Campi Flegrei, southern Italy: sills, dikes, and regional extension. Journal of Geophysical Research: Solid Earth, 115(B12).

Zitellini, N., Ranero, C. R., Loreto, M. F., Ligi, M., Pastore, M., D'Oriano, F., Sallares, V., Grevemeyer, I., Moeller, S., Prada, M. (2020). Recent inversion of the Tyrrhenian Basin. Geology, 48(2), 123-127.

Zollo, A., Judenherc, S., Auger, E., D'Auria, L., Virieux, J., Capuano, P., Chiarabba, C., de Franco, R., Makris, J., Michelini, A., Musacchio, G. (2003). Evidence for the buried rim of Campi Flegrei caldera from 3-d active seismic imaging. Geophys. Res. Lett. 30, 2002.